



JOHANNES GUTENBERG
UNIVERSITÄT MAINZ

Self-organization of active matter: The role of interactions

Dissertation

zur Erlangung des Grades

„Doktor der Naturwissenschaften“

am Fachbereich Physik, Mathematik und Informatik
der Johannes Gutenberg-Universität Mainz

vorgelegt von

Andreas Fischer

geboren am 17.12.1990
in Nürnberg

Mainz, den 17. März 2020

Abstract

Active matter has received considerable attention in recent years. Its constituents, active particles, have the ability to convert free energy into directed motion by which they drive themselves out of thermal equilibrium. The field of active matter encompasses a multitude of biological systems on different length scales: from running, flying or swimming macroscopic animals down to motile bacteria and sperm cells. Moreover, synthetic microscopic active particles that either draw inspiration from biological microswimmers or propel via novel mechanisms have been devised. The combination of self-propelled motion and interactions between active particles gives rise to a wealth of fascinating self-organized collective behaviors, such as the formation of flocks of birds, collective cell migration and the motility-induced phase separation of active Janus colloids.

In this thesis, we investigate several self-organized phenomena in systems of active particles via numerical simulations and analytical theory. A major goal of this work is to elucidate how the properties of interactions (e.g., their strength and range) affect the emergent collective behavior. We first deal with the motility-induced phase separation of active particles that interact via short-ranged repulsive potentials. In contrast to the conventional model of active Brownian particles, we take into account the self-propulsion mechanism via a chemical reaction in a thermodynamically consistent way. This influences the resulting phase behavior, especially for soft particles. In a second system, inspired by bacterial quorum sensing, we study active particles that discontinuously change their motility at a threshold concentration of self-generated chemical signals. This interaction leads to a separation of the system into regions of different motility. Via numerical simulations, we show that the densities and sizes of the phases sensitively depend on the concentration threshold, the interaction range and the self-propulsion speed. We compare our results to experiments of light-activated Janus colloids and develop a mean-field theory that yields quantitative agreement with the simulations. Finally, we investigate active colloidal clusters that self-assemble from passive building blocks. Using the approach speeds of particle pairs obtained from experiments as input, we develop a model that disentangles the interplay of reciprocal and nonreciprocal effective interactions giving rise to self-propulsion and quantitatively predicts the motion of larger clusters.

Zusammenfassung

Aktive Materie hat in den letzten Jahren erhebliche Aufmerksamkeit erregt. Sie besteht aus aktiven Teilchen, welche die Fähigkeit haben, freie Energie in gerichtete Bewegung umzuwandeln, wodurch sie sich selbst aus dem thermischen Gleichgewicht bringen. Das Feld der aktiven Materie umfasst eine Vielzahl biologischer Systeme auf verschiedenen Längenskalen: Von laufenden, fliegenden oder schwimmenden makroskopischen Tieren bis hin zu motilen Bakterien und Spermien. Darüber hinaus wurden synthetische mikroskopische aktive Teilchen entwickelt, die entweder von biologischen Mikroschwimmern inspiriert sind oder neuartige Antriebsmechanismen verwenden. Die Kombination von Selbstantrieb und Interaktionen zwischen aktiven Teilchen ruft eine Vielzahl faszinierender selbstorganisierter kollektiver Phänomene hervor, wie die Bildung von Vogelschwärmen, kollektive Zellmigration oder die motilitätsinduzierte Phasenseparation von aktiven Janus-Kolloiden.

In dieser Arbeit werden verschiedene selbstorganisierte Vorgänge in Systemen aktiver Teilchen mithilfe numerischer Simulationen und analytischer Theorie untersucht. Ein Hauptziel dieser Arbeit ist zu klären, wie die Eigenschaften von Interaktionen (beispielsweise ihre Stärke und Reichweite) das emergente kollektive Verhalten beeinflussen. Zunächst wird die motilitätsinduzierte Phasenseparation aktiver Teilchen behandelt, die über kurzreichweitige, abstoßende Potentiale wechselwirken. Im Gegensatz zum herkömmlichen Modell aktiver Brownscher Teilchen wird der Selbstantriebsmechanismus mittels einer chemischen Reaktion thermodynamisch konsistent einbezogen. Insbesondere für weiche Teilchen wird das Phasenverhalten dadurch merklich beeinflusst. Im Anschluss werden aktive Teilchen untersucht, die, inspiriert von bakteriellem Quorum sensing, ihre Motilität beim Erreichen einer Konzentrationsschwelle von selbst generierten chemischen Signalen diskontinuierlich ändern. Diese Wechselwirkung führt zu einer Separation des Systems in Regionen unterschiedlicher Motilität. Mithilfe numerischer Simulationen wird gezeigt, dass die Dichten und Ausdehnungen der Phasen empfindlich von der Konzentrationsschwelle, der Wechselwirkungsreichweite und der Selbstantriebsgeschwindigkeit abhängen. Die Resultate werden mit Experimenten an Licht-aktivierten Janus-Kolloiden verglichen und es wird eine Mean-Field-Theorie ausgearbeitet, die quantitative Übereinstimmung mit den Simulationen erzielt. Zuletzt werden aktive kolloidale Cluster untersucht, die sich aus passiven Bausteinen selbst-assemblieren. Es wird ein Modell entwickelt, das, ausgehend von im Experiment gemessenen Relativgeschwindigkeiten von Teilchenpaaren, das zum Selbstantrieb führende Zusammenspiel von reziproken und nicht-reziproken effektiven Interaktionen beschreibt, sowie die Dynamik größerer Cluster quantitativ voraussagt.

Contents

1. Introduction	1
2. Theoretical Background	7
2.1. Brownian motion	7
2.1.1. Langevin equation	7
2.1.2. Rotational Brownian motion	9
2.1.3. Overdamped dynamics	10
2.2. Self-diffusiophoretic particles	11
2.3. Active Brownian particles	13
2.3.1. Single-particle properties	14
2.3.2. Interacting active Brownian particles	16
2.3.3. Phase separation of active Brownian particles	19
2.4. Numerical and analytical methods	22
2.4.1. Brownian dynamics simulations	22
2.4.2. Smoluchowski equation	24
2.4.3. One-body Smoluchowski equation	25
2.4.4. Mean-field approximations and effective speed	28
2.4.5. Moment expansion of the one-body density	29
3. Phase separation of active Brownian particles at constant affinity	31
3.1. Background: Active Brownian particles at constant affinity	31
3.2. Effective propulsion speed	34
3.3. Hard discs	36
3.3.1. Brownian dynamics simulations	36
3.3.2. Mean-field theory	41
3.4. Soft discs	45
3.4.1. Constant speed	46
3.4.2. Constant affinity	48
4. Self-organization of active particles by quorum sensing rules	51
4.1. Quorum-sensing active particles	52
4.1.1. Coarse-grained concentration field	54
4.1.2. Experimental realization	56
4.1.3. Simulation scheme	57

4.2. Simulations with periodic boundary conditions	58
4.3. Circularly confined system	62
5. Mean-field theory for quorum-sensing active particles	69
5.1. Derivation of the one-body Smoluchowski equation	70
5.2. Moment expansion	72
5.3. Jump conditions	74
5.4. No orientational coupling: Phase separation	77
5.4.1. Planar interface	78
5.4.2. Circular interface	83
5.4.3. Simulations	87
5.5. With orientational coupling: Vortex clusters	95
5.5.1. Simulations	95
5.5.2. Theory	97
6. Dynamics of binary active clusters driven by ion-exchange particles	101
6.1. Experimental setup	103
6.2. Particle interactions	104
6.2.1. A cationic IEX and a passive particle	105
6.2.2. A cationic IEX and an anionic IEX	108
6.3. Larger clusters	110
6.3.1. Cationic-passive clusters	111
6.3.2. Cationic-anionic clusters	113
7. Conclusion and outlook	117
A. Appendix	121
A.1. Supplementary Figures	121
A.2. Concentration profile of a radially symmetric density distribution . .	122
Bibliography	123

List of Publications

This thesis is in parts a recapitulation of ideas published in the following articles by the author during the course of the PhD program:

- [9] T. Bäuerle*, **A. Fischer***, T. Speck, and C. Bechinger. “Self-organization of active particles by quorum sensing rules”. In: *Nat. Commun.* 9 (1), 3232 (2018), *: equal contribution

Own contribution: I developed the simulation code, performed the simulations, analyzed the numerical data and helped analyzing the experimental data. I obtained the analytical results together with T. Speck and contributed to the writing of the manuscript. I created figures 3, 4, 8 as well as all supplementary figures.

- [105] R. Niu, **A. Fischer**, T. Palberg, and T. Speck. “Dynamics of binary active clusters driven by ion-exchange particles”. In: *ACS Nano* 12 (11), 10932–10938 (2018)

Own contribution: I developed the interaction model with input from T. Speck, extracted the input parameters for the model from experimental data and developed the scheme to predict linear and angular velocities of larger clusters. Moreover, I created figures 2 to 5 and contributed to the writing of the manuscript.

- [47] **A. Fischer**, A. Chatterjee, and T. Speck. “Aggregation and sedimentation of active Brownian particles at constant affinity”. In: *J. Chem. Phys.* 150 (6), 064910 (2019)

Own contribution: I implemented active Brownian particles at constant affinity into an existing simulation code, performed the simulations, analyzed the data and obtained the analytical results for the section about aggregation. Moreover, I supervised A. Chatterjee, an exchange student, who performed the calculations for sedimentation. I created figures 2 to 6 and contributed to the writing of the section about aggregation.

- [48] **A. Fischer**, F. Schmid, and T. Speck. “Quorum-sensing active particles with discontinuous motility”. In: *Phys. Rev. E* 101 (1), 012601 (2020)

Own contribution: I wrote the simulation code, performed the simulations, analyzed the data, obtained the majority of the analytical results and conceived the orientational coupling leading to vortex formation. Moreover, I created all figures and wrote most of the manuscript.

Other publications of the author published during or prior to the PhD program:

- P. Krinninger, **A. Fischer**, and A. Fortini. “Order-disorder transition in swirled granular disks”. In: *Physical Review E* 90 (1), 012201 (2014)
- J. Plagge, **A. Fischer**, and C. Heussinger. “Viscoelasticity of reversibly crosslinked networks of semiflexible polymers”. In: *Phys. Rev. E* 93 (6), 062502 (2016)
- H. E. Amuasi, **A. Fischer**, A. Zippelius, and C. Heussinger. “Linear rheology of reversibly cross-linked biopolymer networks”. In: *J. Chem. Phys.* 149 (8), 084902 (2018)
- A. Jayaram, **A. Fischer**, and T. Speck. “From scalar to polar active matter: Connecting simulations with mean-field theory”. In: *Phys. Rev. E* 101 (2), 022602 (2020)

List of Figures

1.1.	Examples of motile organisms and their collective behavior	2
2.1.	Self-diffusiophoresis of colloidal Janus particles	13
2.2.	Active Brownian particles in two dimensions	15
2.3.	Weeks-Chandler-Andersen potential	17
2.4.	Clustering of active Brownian particles	19
2.5.	Phase diagrams of the liquid-gas transition and of active Brownian particles	21
2.6.	Visualization of periodic boundary conditions	23
2.7.	Two-body correlations of active Brownian particles	29
3.1.	Model of the self-propulsion mechanism of self-diffusiophoretic Janus particles	32
3.2.	Speed distributions for hard discs propelled at constant affinity	37
3.3.	Phase behavior of hard discs propelled at constant affinity	38
3.4.	Profiles of propulsion speed and force	39
3.5.	Forces and speeds versus density	40
3.6.	Mean-field spinodals and critical points	44
3.7.	Comparison of the harmonic and the WCA potential	45
3.8.	Soft discs with constant propulsion speed	47
3.9.	Soft discs at constant affinity	49
4.1.	Quorum sensing response	53
4.2.	Finite-size transitions of quorum-sensing active particles	59
4.3.	Phase separation of quorum-sensing active particles	61
4.4.	Quorum sensing and motility-induced phase separation	61
4.5.	Quorum-sensing active particles under circular confinement	62
4.6.	Experimental results for quorum-sensing active particles	64
4.7.	$\bar{c} - \lambda$ phase diagram	65
4.8.	Cluster fluctuations and stability	67
4.9.	Finite-size behavior	67
4.10.	Interfacial fluctuations and interfacial width	68
5.1.	Jump conditions	74

5.2.	Phase separation with a planar interface	80
5.3.	$v_0 - \rho$ phase diagrams for MIPS and for discontinuous motility response	82
5.4.	Phase separation with a circular interface	85
5.5.	Simulation results for circular clusters	88
5.6.	Fitting via effective diffusion coefficient D_{eff}	90
5.7.	Fitted effective diffusion coefficients	91
5.8.	Cluster stability and phase diagrams for circular clusters	93
5.9.	Quorum-sensing active particles with orientational coupling	95
5.10.	Analysis of vortex clusters	97
5.11.	Maximum of the average angular particle orientation versus torque strength	100
6.1.	Binary active clusters composed of IEXs	102
6.2.	Flow generation of a cationic IEX	103
6.3.	Pair of a cationic IEX and a passive particle	106
6.4.	Cationic-anionic IEX pair	109
6.5.	Larger cationic-passive clusters	112
6.6.	Larger cationic-anionic clusters	114
A.1.	Radial density profiles for different motility update intervals	121
A.2.	Vortex cluster in a system with periodic boundary conditions	121

List of Symbols and Abbreviations

\mathbf{r}	position
t	time
\mathbf{F}	force
D_0, D_r	translational, rotational diffusion coefficient
ξ, ξ_r	translational, rotational noise
μ_0	translational mobility
d	particle diameter
v_0	free self-propulsion speed
φ	particle orientation
\mathbf{e}	particle orientation vector
U	potential energy
$u(r)$	pair potential
N	particle number
ψ	N -particle distribution function
ψ_1	one-particle distribution function
ρ	number density
\mathbf{p}	polarization
\mathbf{Q}	nematic tensor
ϕ	packing fraction
ρ_0, ϕ_0	global number density, packing fraction
c	concentration of a molecule
λ	particle step length / decay length of chemical profile
\bar{c}	threshold concentration
ω	interfacial width / angular velocity
ABP	active Brownian particle
MIPS	motility-induced phase separation
WCA	Weeks-Chandler-Andersen (potential)
IEX	ion-exchange particle

Introduction

Motility, the ability “to exhibit motion and to perform mechanical work at the expense of metabolic energy” [3], is a characteristic of a plethora of living systems on all length scales. Most animals of the macroscopic world are capable of autonomous locomotion, e.g., by running, flying or swimming. On the microlevel, a great number of prokaryotic and eukaryotic cells, e.g., *E. coli* bacteria and sperms [Fig. 1.1(a,b)], are able to swim via beats of their cilia and flagella [21]. Moreover, many eukaryotic cells perform a crawling-like motion pattern [1] (“amoeboid movement”), with the help of their actin cytoskeleton. Motility is an essential feature of these organisms, as it allows them, e.g., to explore their environment in the search of food or a partner, to escape from predators or to move towards the egg cell (in the case of sperms). When encountered in large numbers, motile organisms often exhibit intriguing collective behavior, such as the formation of flocks of birds [44] or schools of fish [133], swarming bacterial colonies [77] and collective cell migration [123], see Fig. 1.1(c-e). Interestingly, these phenomena are typically self-organized [28], i.e., they solely arise from the combination of motility and the interactions between individuals in the absence of any external control.

Not attempting to capture the intricate interactions between living organisms in every detail (which apart from physical interactions involve behavioral and social rules requiring complex internal information processing), physicists have started to develop simplified models aiming to unveil unifying principles governing these fascinating collective phenomena. In the seminal Vicsek model introduced in 1995 [159], where a collection of particles is propelled at constant speed and aligns with the average direction of the particles in their local neighborhood, the formation of a polarized flock occurs due to a phase transition from a homogeneous disordered state similar to the ferromagnetic phase transition.¹ This finding, among others, paved the way for a new field of physics, *active matter* [118, 97], which tries to understand collective phenomena in systems of motile living systems with tools from statistical physics. However, concepts from equilibrium statistical physics cannot be confidently applied to active matter as its constituents, *active particles* [130], constantly drive themselves out of equilibrium by converting free energy into directed

¹The very first model to simulate animal flocks was already introduced by Reynolds in 1987 for computer graphics applications [121].

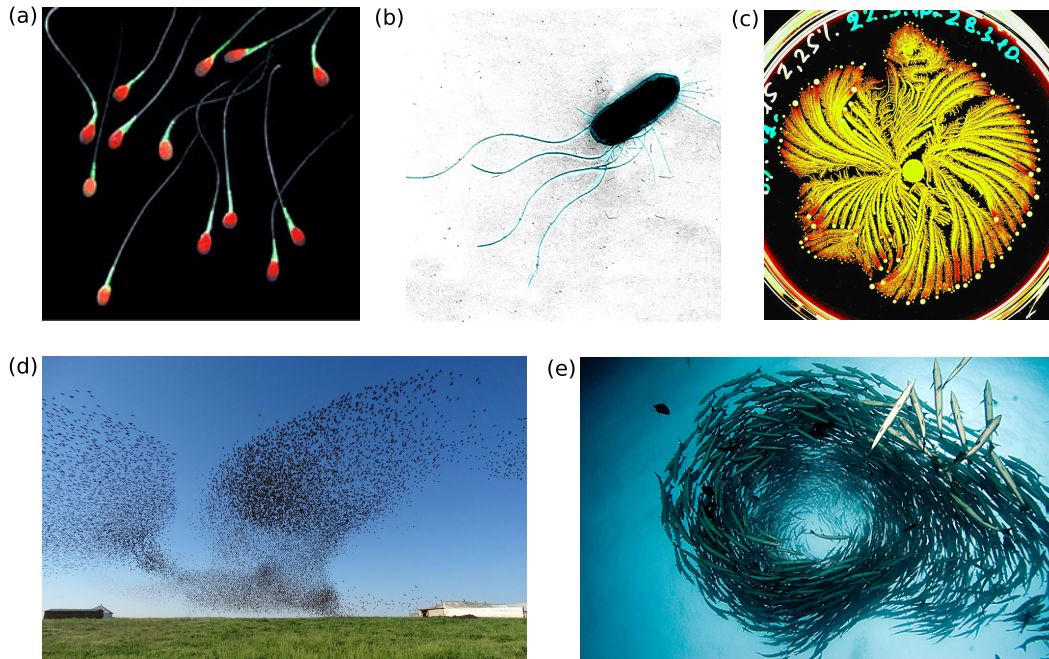


Fig. 1.1. Examples of motile organisms and their collective behavior. (a) Photomicrograph of fluorescently stained sperm cells. Taken from [168]. (b) Flagellated *Escherichia Coli* bacterium. Adapted from [49]. (c) Pattern formed by a colony of swarming *Paenibacillus vortex* bacteria. Taken from [170]. (d) Flock of starlings. Taken from [169]. (e) Vortex pattern formed by a school of barracudas. Taken from [50]. Pictures used in accordance with Creative Commons licenses (a) CC BY 2.0 (b,e) CC BY-SA 2.0, (c) CC BY-SA 3.0, (d) CC BY-SA 4.0.

motion. This local energy injection on the level of each particle is a distinctive feature of active matter compared to other non-equilibrium systems like, for example, sheared systems (where the energy input takes place at the system's boundaries), giving rise to, e.g., giant number fluctuations [101, 177], turbulence [167] and unusual rheological properties [139, 90]. While elucidating these phenomena poses a wealth of theoretical challenges [118, 97], various potential applications of active matter exist, such as bacteria-driven micromotors [160] and materials built from active building blocks with novel properties [102].

Inspired by biological microswimmers like motile bacteria and sperms, various types of artificial microscopic particles capable of self-propulsion have been devised in recent years [38, 10], which has opened up the field of synthetic active matter. One approach is to make use of nature-inspired mechanisms, e.g., by equipping microparticles with synthetic flagella driven by external magnetic fields [36] or cardiomyocytes [171]. Apart from that, novel self-propulsion mechanisms have been conceived, e.g., based on driving via chiral propellers [57], ultrasound [164]

or Maragani flows [74]. The most prevalent experimental technique, however, are Janus colloids, micron-sized spheres or rods consisting of two halves with different surface properties. The asymmetry of the particles induces phoretic motion [4] due to self-generated gradients of, e.g., temperature (thermophoresis) [76], electric potential (electrophoresis) [114] or the concentration of a neutral molecular solute (diffusiophoresis) [72]. The gradients necessary for self-diffusiophoresis are typically generated by the decomposition of hydrogen peroxide [72, 109] or the demixing of a critical mixture triggered by light [161, 27]. These particles are propelled along their symmetry axis and undergo random orientational changes due to rotational diffusion. In total, this leads to directed motion over significant time [72, 161].

A widely studied model system that well describes the motion of self-phoretic Janus colloids are active Brownian particles (ABPs) [122], combining self-propulsion with short-ranged repulsive interactions and Brownian motion. In numerical simulations, at high enough propulsion speeds and densities large collections of ABPs separate into a dense and a dilute phase due to self-trapping [46, 119, 26], a phenomenon that also has been observed in experiments with active Janus particles [26]. The large-scale behavior of this so-called motility-induced phase separation (MIPS) [31] strongly resembles passive liquid-gas phase separation [146], which, in contrast, requires attractive particle interactions. However, many distinct features of MIPS exist that disagree with an effective equilibrium picture: the phase equilibrium is not determined by the Maxwell construction [140], the interfacial tension is negative [15] and the critical fluctuations do not seem to follow Ising universality [134]. A lot of work has been put into establishing a general framework founded on statistical physics that allows to predict the phase behavior of ABPs [173, 146, 140, 81]. Since ABPs are a non-equilibrium system in which detailed balance is broken, their entropy production also received attention recently. However, various attempts to quantitatively describe the entropy production have lead to conflicting results [54, 51, 143, 96]. The reason is that the ABP model only describes the effective motion of the particles, but neglects the physical mechanisms causing directed motion, which precludes an unambiguous identification of the heat exchanged with the environment along trajectories. In Ref. [144], the ABP model has been extended by incorporating the self-propulsion mechanism via the reaction of an abundant chemical, which allows to consistently identify the entropy production. In Chapter 3, we study the implications of this modified model for MIPS via computer simulations and mean-field theory for different inter-particle potentials.

In contrast to synthetic active particles, many biological microorganisms are capable of gathering information about their environment and regulating their motion in response to it. An important class of such mechanisms is “taxis” [37], the ability of

some bacteria and cells to sense and direct their motion along gradients of, e.g., light (phototaxis), oxygen (aerotaxis) or the concentration of chemicals (chemotaxis). For example sperm cells exploit the mechanism of chemotaxis by detecting and following the gradient of signaling molecules secreted by the oocyte [42]. Chemical sensing, however, is not only involved in the response to external stimuli, but also plays an important role in a widespread cell-to-cell communication mechanism, called quorum sensing [98]. The members of a quorum-sensing bacterial population produce and release signaling molecules (“autoinducers”), which leads to a concentration of chemicals that increases as a function of cell density. When the concentration sensed by a bacterium surpasses a threshold (when the density of bacteria is high enough), the expression of certain genes is triggered, which facilitates the synchronized behavior of the bacterial population required, e.g., for virulence [178], bioluminescence [93], biofilm formation [112] and motility control [147].

Apart from understanding the collective behavior arising from these communication mechanisms in biological systems, it would be interesting to transfer some of these strategies to synthetic microswimmers in order to enable them to fulfill more complex tasks. While on macroscopic scales collections of robots have been equipped with behavioral interaction rules that facilitate their programmable self-assembly into various functional structures [64, 124], for microscopic systems such approaches are even more challenging, as they require control over the motion of individual particles. For phoretic Janus particles triggered by light, recent advances in experimental techniques in the group of Prof. Clemens Bechinger (Fachbereich Physik, Universität Konstanz) allow for the control of the propulsion speed at the particle level by imposing dynamical light patterns. In Chapter 4, we present an interaction rule motivated by above-described quorum sensing, that can be implemented in this experimental setup: particles switch between two discrete states of motility (active and passive), when a threshold value of a (virtual) self-generated concentration field of autoinducers is reached. This rule induces the separation of the system into regions of different motility, the densities and dimensions of which can be controlled by tuning the particle response. We analyze this emergent collective phenomenon via numerical simulations based on the ABP model and compare to experimental results. In Chapter 5, we extend the quantitative analysis of the observed phase separation and develop a mean-field theory that yields very good agreement with simulations and reveals important distinctive features of this transition compared to MIPS. Moreover, we show that introducing an additional coupling of particle orientations to the gradient of the concentration field triggers the formation of vortex clusters.

Chapter 6, is devoted to a novel type of synthetic microswimmer developed in the group of Prof. Thomas Palberg (Institut für Physik, Johannes Gutenberg-Universität Mainz). These swimmers consist of immotile ion-exchange particles that self-assemble into small aggregates (“colloidal clusters”) due to long-ranged hydrodynamic interactions [108]. In contrast to other approaches where clusters typically contain active building blocks [40, 162, 136], here, in suspensions of particles of different types the formed clusters perform self-propelled motion due to non-reciprocal interactions between unlike particles. Depending on their composition and structure, the aggregates undergo either linear or circular motion with different speeds and angular velocities. In this chapter, we develop a framework to quantitatively predict this motion using (effective) interaction potentials that we extract from experimental measurements of speeds of particle pairs.

Theoretical Background

We start out by introducing the major theoretical concepts and methods on which the results presented in the subsequent chapters are founded. After discussing classical Brownian motion, we describe the propulsion mechanism of self-diffusiophoretic particles. Thereafter we introduce the active Brownian particle (ABP) model and highlight some of the individual properties of ABPs as well their motility-induced phase separation (MIPS). This is followed by an overview over the main numerical and analytical techniques we employ throughout this thesis: Brownian dynamics simulations and (many-body and mean-field) Smoluchowski equations.

2.1 Brownian motion

Microscopic particles suspended in a fluid typically undergo stochastic motion as a result of irregular collisions with the fluid molecules, which is named Brownian motion after the botanist Robert Brown who discovered this phenomenon in 1827 when studying pollen grains immersed in water [25]. In order to perform *directed* motion on microscopic scales, biological and synthetic microswimmers have to overcome the limitations of Brownian motion, which randomizes their trajectories. Therefore, to understand the physics of microswimmers, it is important to first recapitulate the theory of Brownian motion.

2.1.1 Langevin equation

The motion of a spherical particle (with position \mathbf{r}) of radius a and mass m in a fluid medium with viscosity η at temperature T can be described by Newton's equation of motion

$$m\ddot{\mathbf{r}} = \mathbf{F}_{\text{total}}(t), \quad (2.1)$$

with $\mathbf{F}_{\text{total}}(t)$ the total force exerted by the surrounding medium on the particle at time t . In principle this force would be deterministic, if one knew the degrees of freedom of the fluid molecules as functions of time. However, due to the vast number of fluid molecules it is not practical to look for an exact expression for

$\mathbf{F}_{\text{total}}(t)$. Phenomenologically, it is known that the collisions with the molecules on average cause a frictional force $-\gamma\dot{\mathbf{r}}$ with friction coefficient $\gamma = 6\pi\eta a$, known as Stokes' drag, slowing down the particle [152]. An additional random force $\mathcal{F}(t)$ arises due to the irregular collisions of the particle with the fluid molecules. All in all, this leads to the equation of motion [83]

$$m\ddot{\mathbf{r}} = -\gamma\dot{\mathbf{r}} + \mathcal{F}(t), \quad (2.2)$$

which is known as the Langevin equation of a Brownian particle. It was pointed out by Ornstein and Uhlenbeck [158] that the random force should be Gaussian distributed with mean $\langle \mathcal{F}(t) \rangle = 0$ ($\langle \dots \rangle$ denotes the ensemble average) and autocorrelation function

$$\langle \mathcal{F}_\alpha(t) \mathcal{F}_\beta(t') \rangle = 2B \delta_{\alpha\beta} \delta(t - t'), \quad (2.3)$$

where the indices α, β run over the different spatial coordinates, $\delta_{\alpha\beta}$ is the Kronecker delta and $\delta(t - t')$ the Dirac delta function. Equation (2.3) states that the components of $\mathcal{F}(t)$ are independent and its correlation time is infinitesimally short, with its strength determined by the parameter B . For a particle with mass much larger than the colliding molecules, the Gaussian assumption is very reasonable, since its motion arises from a great number of successive collisions, which is a prerequisite for the central limit theorem. In this situation, property (2.3) is justified as well, since correlations between different impacts only persist for the timescale of molecular motion, which is much shorter than the timescale of Brownian motion [82].¹

From Eq. (2.2), the mean-square velocity can be calculated as [181]

$$\langle |\mathbf{v}(t)|^2 \rangle = e^{-2t\gamma/m} \langle |\mathbf{v}(0)|^2 \rangle + \frac{n_d B}{\gamma m} (1 - e^{-2t\gamma/m}). \quad (2.4)$$

Irrespective of the initial velocity $\mathbf{v}(0)$, in the long-time limit it should approach its equilibrium value $\langle |\mathbf{v}|^2 \rangle_{\text{eq}} = n_d \frac{k_B T}{m}$ (with n_d the number of spatial dimensions and Boltzmann constant k_B) determined by the equipartition theorem [113]. This leads to the fluctuation-dissipation theorem

$$B = \gamma k_B T, \quad (2.5)$$

¹Note that there exist situations in which these assumptions may be not appropriate, e.g., when the mass of the suspended particle is comparable to the molecular mass, leading to an overlap of the timescales of molecular and particle motion [82]. Then finite correlation times of $\mathcal{F}(t)$ have to be taken into account, leading to memory effects in the friction force, which enter into the “generalized” Langevin equation [99, 182]. However, for the situations we will encounter in this thesis, the description via Eqs. (2.2), (2.3) is sufficient.

first stated by Einstein in 1905 [41], which relates the strength B of the fluctuating force to the magnitude γ of the dissipative force.

In thermal equilibrium, i.e., when $\langle |\mathbf{v}(t)|^2 \rangle$ has relaxed to $\langle |\mathbf{v}|^2 \rangle_{\text{eq}}$, the mean-square displacement is given by (for an initial position $\mathbf{r} = 0$) [181]

$$\langle |\mathbf{r}(t)|^2 \rangle = 2n_d \frac{k_B T}{\gamma} \left[t - \frac{m}{\gamma} (1 - e^{-t\gamma/m}) \right]. \quad (2.6)$$

At small times ($t \ll m/\gamma$) one finds $\langle |\mathbf{r}(t)|^2 \rangle = \langle |\mathbf{v}|^2 \rangle_{\text{eq}} t^2$ implying *ballistic* motion (here the inertial response to the random force dominates). For long times ($t \gg m/\gamma$) it is

$$\langle |\mathbf{r}(t)|^2 \rangle = 2n_d \frac{k_B T}{\gamma} t, \quad (2.7)$$

showing that there is a transition to a *diffusive* regime (signified by the $\propto t$ dependence) in which the viscous response is dominant. Defining the translational diffusion coefficient as

$$D_0 = \frac{k_B T}{\gamma}, \quad (2.8)$$

yields the well-known Einstein relation [41]. Note that in equilibrium, however, the mean displacement has to vanish due to symmetry reasons, i.e., $\langle \mathbf{r}(t) \rangle = 0$.

2.1.2 Rotational Brownian motion

The fluid not only exerts forces on the Brownian particle, but also torques, which leads to random particle rotations. In analogy to Eq. (2.2), the Langevin equation for the particle's rotation around a fixed axis (described by the angle φ) reads

$$I\ddot{\varphi} = -\gamma_r \dot{\varphi} + \mathcal{T}(t), \quad (2.9)$$

with moment of inertia I , rotational friction coefficient γ_r and fluctuating torque $\mathcal{T}(t)$. For a sphere the friction coefficient is given by $\gamma_r = 8\pi\eta a^3$ for every axis of rotation [69]. The fluctuating torque satisfies $\langle \mathcal{T}(t) \rangle = 0$ and

$$\langle \mathcal{T}(t)\mathcal{T}(t') \rangle = 2B_r \delta(t - t'). \quad (2.10)$$

The corresponding fluctuation-dissipation theorem

$$B_r = \gamma_r k_B T \quad (2.11)$$

can be derived analogously to Eq. (2.5), since the equipartition theorem also applies to rotational degrees of freedom. For times $t \gg I/\gamma_r$ the rotational dynamics is diffusive ($\langle [\varphi(t) - \varphi(0)]^2 \rangle = 2D_r t$) with rotational diffusion coefficient

$$D_r = \frac{k_B T}{\gamma_r}, \quad (2.12)$$

which can be related to the translational diffusion coefficient as (using the expressions for the friction coefficients γ and γ_r)

$$D_r = \frac{3}{d^2} D_0, \quad (2.13)$$

with particle diameter $d = 2a$.

2.1.3 Overdamped dynamics

It is important to notice that for the systems we will consider in this thesis inertial and viscous forces are not equally relevant. The Langevin equation (2.2) implies the mean particle velocity

$$\langle \mathbf{v}(t) \rangle = \langle \mathbf{v}(0) \rangle e^{-t/(\frac{m}{\gamma})}, \quad (2.14)$$

describing the decay of the initial velocity due to friction on the “momentum relaxation” timescale $\tau_m = m/\gamma$ (above we have already seen that the ballistic and diffusive regime are separated by the same timescale). For a spherical particle with radius a and density ρ_p this timescale can be calculated as

$$\tau_m = \frac{m}{\gamma} = \frac{(4/3)\pi\rho_p a^3}{6\pi\eta a} = \frac{2\rho_p a^2}{9\eta}. \quad (2.15)$$

For typical systems we are dealing with in this thesis τ_m is very small. For example, for a colloidal particle made of silica with $a = 1 \mu\text{m}$ suspended in water at room temperature, we can estimate $\tau_m \approx 4 \cdot 10^{-7} \text{ s}$ (using $\rho_p \approx 2 \text{ g/cm}^3$ and $\eta = 0.001 \text{ Pa s}$ [70]), which is much shorter than the timescales of the particle dynamics we are typically interested in. Therefore we make the limit $\tau_m \rightarrow 0$ (instantaneous decay of any initial velocity) which is equal to saying that inertial forces are negligibly small compared to viscous forces. In this so called *overdamped* limit, the Langevin equation (2.2) simply becomes

$$\gamma \dot{\mathbf{r}} = \mathcal{F}(t). \quad (2.16)$$

Similar arguments for the rotational motion lead to

$$\gamma_r \dot{\varphi} = \mathcal{T}(t). \quad (2.17)$$

Note that Eqs. (2.16) and (2.17) describe purely diffusive motion (with diffusion coefficients given by Eq. (2.8) and (2.12)) without the initial ballistic regime.

2.2 Self-diffusiophoretic particles

As explained above, for microscopic objects in suspension, typically, any initial velocity decays very fast due to strong viscous drag forces, with the remaining motion being determined by equilibrium fluctuations. In order to overcome these bounds and to move in a directed way in the absence of an external force, particles have to drive themselves out of equilibrium. Motile microorganisms such as bacteria or spermatozoa achieve this by converting stored energy (in the form of the molecule ATP) into intricate beating patterns of their flagella or cilia [43], which due to the absence of inertial effects have to occur in a nonreciprocal way to trigger self-propulsion [117]. While synthetic active particles inspired by biological microswimmers exist [36, 171], some of the most established propulsion mechanisms are based on phoretic effects. Generally, phoretic motion of a colloidal particle is caused by the interaction of external fields with the particle's interfacial boundary region [4] and can be observed, e.g., in gradients of temperature (thermophoresis), electric potential (electrophoresis) or concentration of a molecular solute (diffusiophoresis). This phenomenon is exploited for *self*-phoretic particles which move in self-generated local field gradients. Although there exist realizations of thermophoretic [76] and electrophoretic [114] self-propulsion schemes, in the following, we focus in more detail on particles driven by diffusiophoresis as these are closest to the systems we consider throughout this thesis.

A colloidal particle that is placed in a concentration gradient ∇c of a neutral molecular solute moves via diffusiophoresis when interactions of the solutes with the surface of the particle induce a pressure difference in the hydrodynamic boundary layer [4]. This pressure gradient drives a flow tangential to the surface characterized by the phoretic slip velocity \mathbf{v}_s (the solvent velocity at the edge of the boundary layer) which is proportional to the local concentration gradient of the solute. The slip velocity at position \mathbf{r}_s on the edge of the boundary layer is given by [4]

$$\mathbf{v}_s(\mathbf{r}_s) = \mu_s(\mathbb{1} - \mathbf{n} \otimes \mathbf{n}) \cdot \nabla c(\mathbf{r}_s) \quad (2.18)$$

with local surface normal \mathbf{n} , \otimes the outer vector product and phoretic mobility μ_s . The mobility depends on the details of the interaction between solute and the particle's

surface and can be either positive or negative. Force balance implies that the particle in response moves in the opposite direction with speed [4]

$$\mathbf{v}_p = -\frac{1}{A_s} \int d\mathbf{r}_s \mathbf{v}_s(\mathbf{r}_s), \quad (2.19)$$

where the integral is over the surface enclosing the particle plus its boundary layer with area A_s . Note that this process also generates a flow field in the surrounding fluid, which can be computed using $\mathbf{v}_s(\mathbf{r}_s)$ as boundary condition [4].

The concept of self-diffusiophoretic particles that move due to a self-generated concentration gradient was introduced theoretically by Golestanian *et al.* [60]. Most experimental realizations employ *Janus* particles whose surface is divided in (typically two) regions with distinct physical properties. In the following, we give a brief overview of the two most established experimental implementations of self-diffusiophoretic Janus colloids. Quantitative theoretical descriptions of their propulsion mechanisms can be found, e.g., in Refs. [78, 174, 145].

Decomposition of hydrogen peroxide

Howse *et al.* [72] pioneered the concept of particles generating a chemical gradient via a chemical reaction that takes place selectively on one side of the particle. Spherical particles made of polystyrene with one hemisphere coated with platinum are suspended in a hydrogen peroxide (H_2O_2) solution. The platinum catalyzes the reduction of hydrogen peroxide to oxygen and water. Since the reaction only takes place on the coated hemisphere, this results in a local gradient of product molecules around the particle, triggering diffusiophoretic motion (typically towards lower product concentrations [39]), see Fig. 2.1(a). Increasing the H_2O_2 -concentration induces a stronger local gradient of products (due to the rising number of reactions), leading to a higher propulsion speed.

Critical demixing

An alternative approach is based on spherical Janus particles, made of silica (SiO_2) with one hemisphere coated with gold, suspended in a binary mixture of lutidine and water [161, 27], see Fig. 2.1(b). The mixture exhibits a lower critical point [see the schematic phase diagram Fig. 2.1(c)]. It is prepared at the critical mass fraction of lutidine $\phi_c = 0.286$ and maintained at a temperature slightly below the critical value $T_c = 307$ K [62]. The suspension is illuminated with green light at wavelength

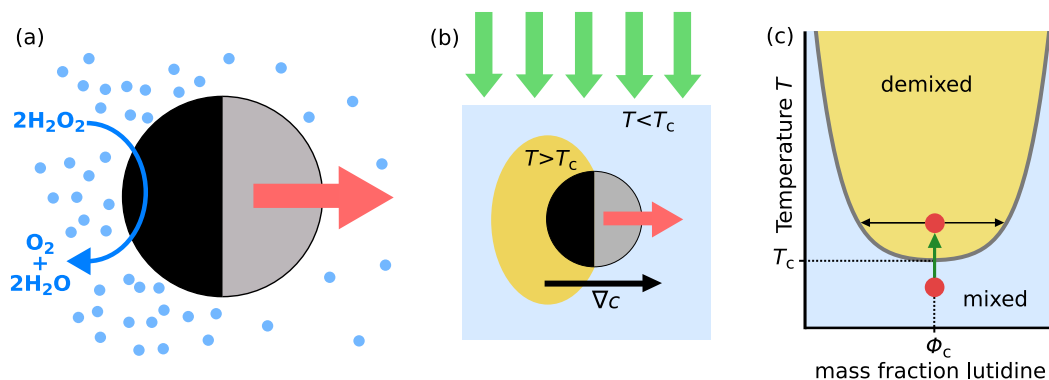


Fig. 2.1. Self-diffusiophoresis of colloidal Janus particles. (a) Polystyrene sphere with one side covered with platinum (black) in H_2O_2 solution [72]. Platinum catalyzes the reduction of H_2O_2 into O_2 and H_2O , which generates a local concentration gradient of product molecules (blue disks) inducing diffusiophoretic particle motion. (b) Silica particle with hydrophilic gold cap (black) suspended in a near-critical water-lutidine mixture [161, 27]. When illuminated with green light, the gold heats above the critical temperature and the solution locally demixes, which induces a local concentration gradient ∇c of lutidine. In response the particle moves via diffusiophoresis. (c) Phase diagram of the water-lutidine solution exhibiting a lower critical point (ϕ_c, T_c) .

$\lambda = 532 \text{ nm}$, which is near the plasmonic absorption peak of gold [111]. Due to light absorption, the gold cap heats above T_c at high enough intensity, whereas the silica side is not heated as it does not absorb the light. Hence, in the vicinity of the cap, the solution demixes into a lutidine-rich and a water-rich phase via spinodal decomposition, cf. Fig. 2.1(c). Importantly, the gold cap is rendered either hydrophilic or hydrophobic by chemical functionalization. In case of a hydrophilic cap, the lutidine-rich phase is depleted from the cap, which creates a gradient of lutidine pointing from the gold to the silica hemisphere. The interaction of lutidine with the particle surface is such that it triggers diffusiophoretic motion in the direction of the lutidine gradient [27], see Fig. 2.1(b).² As in the case of catalytic self-phoretic particles, the particle speed can be controlled: Higher light intensities heat up the cap to higher temperatures and, thus, increase the strength of the lutidine gradient. This, in turn, leads to a higher speed of particles.

2.3 Active Brownian particles

A model that is commonly used to describe the dynamics of self-phoretic colloids is the *active Brownian particle* (ABP) model [122, 46, 26, 119]. It treats a particle

²For a hydrophobic cap the lutidine gradient points in the opposite direction which leads to a reverted propulsion direction.

as a sphere with an internal orientation vector \mathbf{e} along which it is propelled at constant speed v_0 , see Fig. 2.2(a). The interaction with the solvent (assuming that it is not modified by the self-propulsion mechanism) is modeled in the same way as for Brownian particles (Sec. 2.1), providing friction plus (equilibrium) fluctuating forces and torques. The equation of motion for the particle's position $\mathbf{r}(t)$ then reads (Eq. (2.16) divided by γ with the additional propulsion term)

$$\dot{\mathbf{r}} = v_0 \mathbf{e} + \boldsymbol{\xi}. \quad (2.20)$$

The translational noise is related to the random force via $\boldsymbol{\xi}(t) = \gamma^{-1} \mathcal{F}(t)$ and thus has zero mean and autocorrelation $\langle \xi_\alpha(t) \xi_\beta(t') \rangle = 2D_0 \delta_{\alpha\beta} \delta(t - t')$.

In the following, we assume that the particle's motion is restricted to the xy -plane, i.e., \mathbf{r} , \mathbf{e} and $\boldsymbol{\xi}$ are two-dimensional vectors. This is the case in many experimental studies where self-phoretic particles move on a substrate [156, 110] (onto which they sediment due to gravity) or are confined between two plates [26]. Moreover, we only allow for particle rotations in that plane (around the z -axis). Then, the orientation vector can be written as $\mathbf{e}(t) = (\cos \varphi(t), \sin \varphi(t))$ with $\varphi(t)$ the angle enclosed by the particle's orientation vector with the x -axis, undergoing rotational diffusion via [Eq. (2.17) divided by γ_r]

$$\dot{\varphi} = \xi_r. \quad (2.21)$$

The rotational noise is given by $\xi_r(t) = \gamma_r^{-1} \mathcal{T}(t)$ with zero mean and autocorrelation $\langle \xi_r(t) \xi_r(t') \rangle = 2D_r \delta(t - t')$. Since we consider spherical particles, relation (2.13) between the diffusion coefficients D_r and D_0 is applicable.

2.3.1 Single-particle properties

Figures 2.2(b-d) show examples of trajectories of an ABP with two different propulsion speeds v_0 and of a Brownian particle ($v_0 = 0$). Clearly, with increasing v_0 the trajectories explore more space and exhibit longer segments of directed motion. More quantitative statements can be made by calculating the mean displacement of the particle given by [66]

$$\langle \mathbf{r}(t) - \mathbf{r}(0) \rangle = \frac{v_0}{D_r} \left[1 - e^{-D_r t} \right] \mathbf{e}(0). \quad (2.22)$$

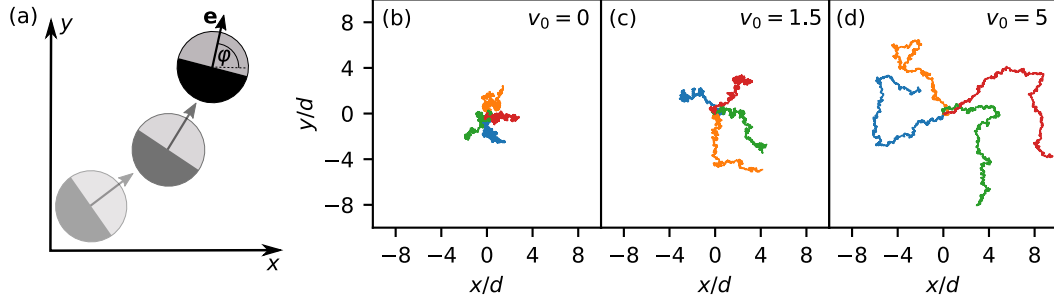


Fig. 2.2. Active Brownian particles (ABPs) in two dimensions. (a) An ABP is propelled along its orientation vector \mathbf{e} (parametrized by the angle φ) which changes due to rotational diffusion. Comparison of trajectories of Brownian particles (b) and active Brownian particles (c,d) for two different propulsion speeds v_0 starting at the origin with different initial orientations $\mathbf{e}(0)$ (obtained via the integration scheme introduced in Sec. 2.4.1). The particles have equal diameter d , translational and rotational diffusion coefficients D_0 and $D_r = (3/d^2)D_0$ [Eq. (2.13)], respectively. Propulsion speeds are given in units of dD_r . The colors indicate independent trajectories over the same time interval $\Delta t = 3D_r^{-1}$.

This shows that on average an ABP moves along its initial orientation $\mathbf{e}(0)$ for a finite persistence length

$$\ell_p = \lim_{t \rightarrow \infty} \langle |\mathbf{r}(t) - \mathbf{r}(0)| \rangle = \frac{v_0}{D_r}, \quad (2.23)$$

before its direction is randomized due to rotational diffusion. This is in contrast to ordinary Brownian particles for which no preferred direction of motion exists ($\ell_p = 0$).

Moreover, the mean-square displacement of an ABP (in 2 dimensions) is given by [66]

$$\langle |\mathbf{r}(t) - \mathbf{r}(0)|^2 \rangle = \left[4D_0 + 2\frac{v_0^2}{D_r} \right] t + 2\frac{v_0^2}{D_r^2} [e^{-D_r t} - 1] \quad (2.24)$$

$$= \begin{cases} 4D_0 t + v_0^2 t^2, & t \ll D_r^{-1} \\ 4(D_0 + \frac{1}{2}v_0^2 D_r^{-1})t, & t \gg D_r^{-1} \end{cases}, \quad (2.25)$$

indicating ballistic motion $\propto t^2$ on timescales that are small compared to the reorientation time, D_r^{-1} , due to rotational diffusion.³ As a result of randomization of the particle's orientation, at long times the dynamics of the particle becomes diffusive with enhanced (long-time) diffusion coefficient $D_0 + \frac{1}{2}v_0^2 D_r^{-1}$ due to self-propulsion. Expression (2.24) has been confirmed in several experiments with self-phoretic

³At even smaller times $t \ll 4D_0/v_0^2$, the mean-square displacement is equal to $4D_0 t$, i.e., purely diffusive.

active particles [72, 161], which is one reason why the ABP model has been widely used to describe their dynamics. The relative importance of directed and diffusive motion can be quantified via the dimensionless Péclet number, usually defined as [149, 135]

$$\text{Pe} = \frac{3v_0}{D_r d}. \quad (2.26)$$

in the context of ABPs. While the ABP model is typically used to describe the motion of self-phoretic Janus colloids, it does not fully capture the dynamics of many biological microswimmers. For example, for motile bacteria such as *E. coli*, the dominant reorientation mechanism is not rotational diffusion, but so-called “tumble” events - sudden changes of the propulsion direction occurring at a certain rate - inbetween periods of almost straight motion (“runs”) [127, 11]. However, although the reorientation dynamics of run-and-tumble motion is different from that of ABPs, it has been shown that their long-time diffusion properties are equivalent [30].

2.3.2 Interacting active Brownian particles

Going from a single particle to a collection of N ABPs, inter-particle interactions have to be taken into account. Here, we only consider interactions that can be represented as pair potentials u (i.e., conservative forces), which for spherical particles typically only depend on the distance r between two particles. The total potential energy is then given by

$$U(\{\mathbf{r}_k\}) = \sum_{k=1}^N \sum_{l>k}^N u(|\mathbf{r}_l - \mathbf{r}_k|) \quad (2.27)$$

and the resulting force on a single particle is $\mathbf{F}_k = -\nabla_k U(\{\mathbf{r}_k\})$, with Nabla operator $\nabla_k = (\partial_{x_k}, \partial_{y_k})$. Adding the forces to the equations of motion (2.20) of all particles, one obtains the $3N$ coupled equations

$$\dot{\mathbf{r}}_k = v_0 \mathbf{e}_k - \mu_0 \nabla_k U + \boldsymbol{\xi}_k, \quad (2.28)$$

$$\dot{\varphi}_k = \xi_{r,k}, \quad (2.29)$$

with mobility $\mu_0 = D_0/(k_B T)$. The translational and rotational noise have the same properties as introduced above for a single ABP, without any cross-correlations between particles.

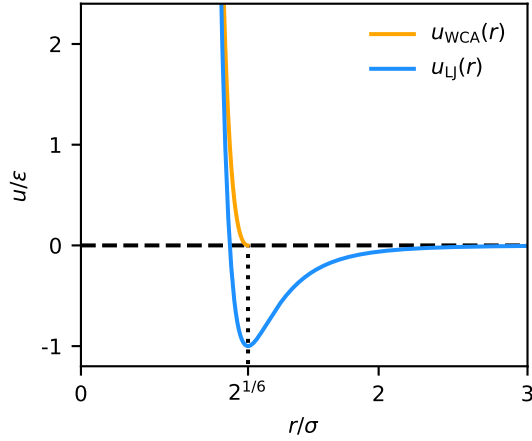


Fig. 2.3. The Weeks-Chandler-Andersen potential $u_{\text{WCA}}(r)$ (orange) can be constructed from the Lennard-Jones potential $u_{\text{LJ}}(r) = 4\epsilon \left[\left(\frac{\sigma}{r}\right)^{12} - \left(\frac{\sigma}{r}\right)^6 \right]$ (blue) by truncating it at its minimum $r/\sigma = 2^{1/6}$ and adding an offset ϵ .

Interaction potential and effective diameter

Many options for the choice of a pair potential u exist, differing in their strength, range and sign. Here, we consider short-ranged repulsive interactions modeling volume exclusion of colloidal particles (in general, repulsiveness can be ensured by $\partial_r u(r) \leq 0 \forall r > 0$). While some studies employ steep Yukawa-like potentials [17, 175], in the context of ABPs the Weeks-Chandler-Andersen (WCA) potential is most commonly used [26, 119, 149, 134]. It is defined as [166]

$$u_{\text{WCA}}(r) = \begin{cases} 4\epsilon \left[\left(\frac{\sigma}{r}\right)^{12} - \left(\frac{\sigma}{r}\right)^6 + \frac{1}{4} \right] & (r/\sigma < 2^{1/6}) \\ 0 & (r/\sigma \geq 2^{1/6}) \end{cases}, \quad (2.30)$$

consisting of the repulsive part of the well-known Lennard-Jones potential with a constant offset ensuring that it goes to zero smoothly at the cutoff-distance $r_{\text{cut}} = 2^{1/6}\sigma$, see Fig. 2.3. The interaction range is controlled by σ and the interaction strength by ϵ . Due to its widespread usage, the WCA potential will be our default choice throughout this thesis (Chaps. 3, 4, 5). As in various previous studies [15, 135, 134], we employ $\epsilon = 100k_{\text{B}}T$, which only allows for small particle overlaps.

An important control parameter of a system of interacting ABPs is the packing fraction $\phi_0 = NA_{\text{p}}/A$ with A being the total area of the system and A_{p} the area covered by a particle. In order to calculate $A_{\text{p}} = \pi(d/2)^2$, the particle diameter d has to be known. Calculating the rotational diffusion coefficient D_{r} via Eq. (2.13), requires knowledge of the diameter as well. Since for the WCA potential the amount

of possible particle overlap varies depending on the choice of ϵ , neither σ nor the cutoff distance $2^{1/6}\sigma$ can be a reliable measure for the diameter. Nevertheless, in thermal equilibrium, an *effective* diameter can be determined through a mapping of a soft potential (which allows for particle overlap) on hard disks ($u(r) = \infty$ for $r \leq d$ and $u(r) = 0$ otherwise) via the Barker-Henderson diameter [8]. For the WCA potential, it can be calculated as

$$d_{\text{BH}} = \int_0^{r_{\text{cut}}} dr \left[1 - \exp\left(-\frac{u(r)}{k_{\text{B}}T}\right) \right], \quad (2.31)$$

yielding $d_{\text{BH}} \approx 1.10688\sigma$ for $\epsilon = 100k_{\text{B}}T$. The higher kinetic energy of self-propelled particles compared to passive ones can, in principle, lead to larger particle overlaps [149]. However, due to the strong repulsiveness of the WCA potential with $\epsilon = 100k_{\text{B}}T$, we neglect corrections to d_{BH} arising from this. In contrast, for ABPs with softer interaction potentials, the impact of self-propulsion on the ability to overlap can be very relevant in order to understand their collective behavior, as we will see in Sec. 3.4.

Additional interactions

In real systems of self-propelled particles, volume exclusion is often not the only relevant interaction. As already mentioned in Sec. 2.2, the phoretic propulsion mechanism of active colloids generates a flow field in the surrounding fluid, determined by the slip velocity profile on the particle surface. These flows can induce *hydrodynamic* interactions between individual particles, affecting their velocities and angular velocities [43, 180]. Moreover, the self-produced chemical concentration gradient around a phoretic swimmer can disturb the concentration field around neighboring particles that in turn leads to additional drift and reorientations of particles [85, 148]. In experiments with self-phoretic particles driven by the decomposition of hydrogen peroxide (as introduced in Sec. 2.2), these *phoretic* interactions presumably play an important role [156, 110]. In contrast, for swimmers based on the demixing of a water-lutidine solution, these interactions have found to be negligible [26]. Models including either hydrodynamic [179, 18] or phoretic interactions [116, 87] have shown their potential importance on the many-body dynamics of self-propelled particles. Simulations including both types of interactions are very costly and still restricted to small systems [73]. Apart from that, it is still under discussion how important the different types of interactions are in specific experimental situations [86].

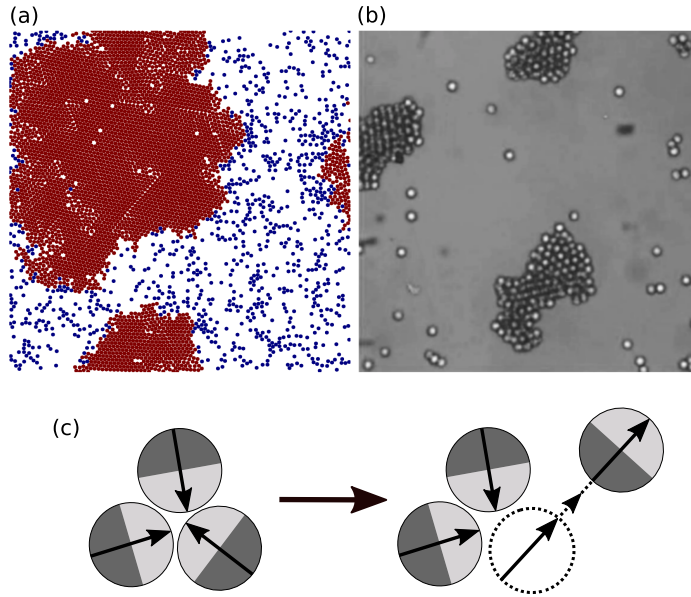


Fig. 2.4. System of active particles separated into a dense cluster phase and a dilute gas phase in (a) simulations of ABPs with short-ranged repulsive interactions and (b) in experiments with light-activated self-phoretic colloids. Reprinted with permission from Ref. [26]. Copyright 2013 by the American Physical Society. (c) Sketch illustrating the self-trapping mechanism leading to cluster formation (adapted from Ref. [26]): Particles that collide head-on are trapped (left) and can only leave when their orientation has rotated outward due to rotational diffusion (right).

On the other hand, the ABP model [as described by Eqs. (2.28), (2.29)], with a relatively small set of parameters, exhibits interesting collective phenomena, as we will see in the next section. Not primarily aiming to model experiments in every detail, throughout this thesis, we stick to the idealized situation of the ABP model and neglect hydrodynamic and phoretic interactions. In the specific system we consider in Chap. 4, this minimal approach even turns out to be sufficient to achieve quantitative agreement with experimental results of self-phoretic colloids.

2.3.3 Phase separation of active Brownian particles

Numerical simulations of ABPs with volume-exclusion interactions have shown that at sufficiently high propulsion speeds v_0 and global densities $\rho_0 = \phi_0/A_p$, phase separation into a dense cluster and a dilute phase of freely moving particles occurs [46, 119, 26], see Fig. 2.4(a). The same phenomenon has been observed in experiments with self-phoretic active particles [26], see Fig. 2.4(b) for a snapshot. Intriguingly, this transition occurs without attractive particle interactions (as required, e.g., for the liquid-gas transition of passive particles), but solely arises from the combina-

tion of directed particle motion and excluded volume, which renders it a genuine non-equilibrium transition.

The formation of clusters can be understood via a self-trapping mechanism [26] [see Fig. 2.4(c) for a sketch]: when two or more particles collide head-on, their motion is inhibited and they form a small cluster. A particle can only leave this configuration, when, after some time, due to rotational diffusion its orientation points outward, such that it can swim away. Thus, the waiting time is $\sim D_r^{-1}$ and independent of v_0 and ρ_0 . However, the mean time between collisions rises with increasing v_0 and ρ_0 , which facilitates cluster growth. When the mean collision time falls below a certain value, phase separation can occur.

On a coarse-grained scale, clustering can be regarded to arise from an effective propulsion speed $v(\rho)$ that decreases with the local particle density ρ due to the higher frequency of collisions, i.e., $v'(\rho) < 0$. Since in regions of lower speed, particles will accumulate, this leads to a positive feedback between accumulation-induced slowing and slowing-induced accumulation. This can trigger a “motility-induced” phase separation (MIPS) when the coupling between v and ρ is strong enough [30, 31].

Similarities to passive liquid-gas phase separation

Despite its non-equilibrium nature, many similarities between the phase separation of ABPs with repulsive interactions and the liquid-gas transition of passive particles with attractive interactions have been identified. Below a critical temperature T_c , a passive fluid with attractive interactions can undergo phase separation into a gas and a liquid phase with different densities when its global density ρ_0 and temperature T are located within the liquid-gas coexistence region [see Fig. 2.5(a) for a schematic phase diagram]. The latter is enclosed by the *binodal* line, which can be determined via a common-tangent construction to the free energy F , as, in phase equilibrium, the pressure $p = -\frac{\partial F}{\partial V}|_{T,N}$ and the chemical potential $\mu = \frac{\partial F}{\partial N}|_{T,V}$ have to be equal in both phases [129]. The binodal also determines the coexisting densities ρ_{gas} and ρ_{liq} in the $T - \rho$ diagram.

The region of coexistence can be further subdivided via the *spinodal* curve, which separates two regions with different phase separation kinetics [32]. When a gas is quenched into the region between the binodal and spinodal (e.g., by rapidly increasing its temperature), it becomes metastable, meaning that it now is in a local minimum of the free energy landscape with the phase-separated state being the global minimum. Small droplets of the liquid phase form due to thermal

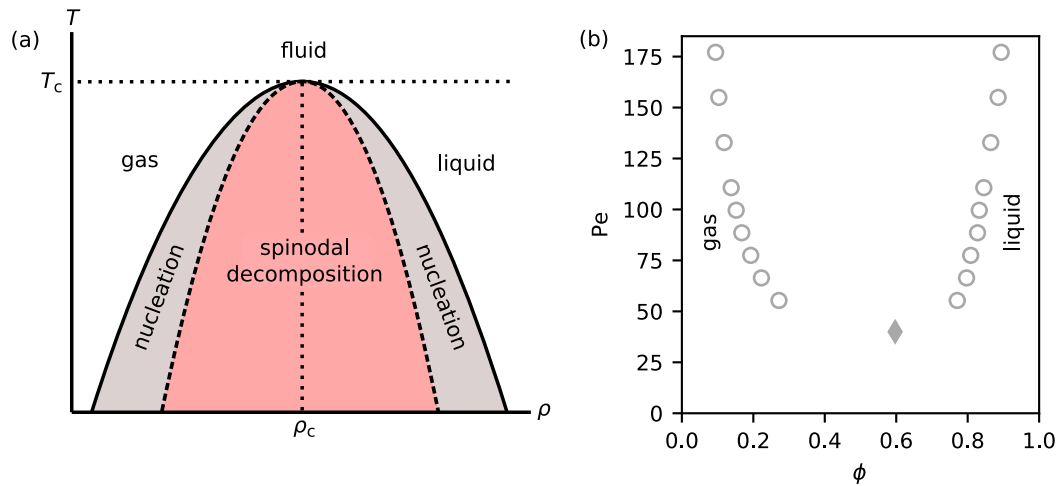


Fig. 2.5. Phase diagrams of the liquid-gas transition and of active Brownian particles. (a) Schematic temperature-density ($T - \rho$) diagram of the liquid-gas transition for passive systems with attractive interactions. Below the binodal (solid line) the fluid phase separates into a gas and a liquid phase, with the coexisting densities lying on the binodal. Between binodal and spinodal (dashed line) the fluid is metastable and phase separation occurs via nucleation. Spinodal decomposition takes place inside the spinodal where the fluid is unstable. Binodal and spinodal meet at the critical point (T_c, ρ_c) . (b) Phase diagram of active Brownian particles with repulsive WCA interactions obtained from simulations by Siebert *et al.* [134] with Péclet number Pe [as defined in Eq. (2.26)] on the y -axis and packing fraction ϕ on the x -axis. Circles depict the coexisting “gas” and “liquid” densities and the diamond indicates the critical point.

fluctuations, which can only grow - and thus initiate phase separation - above a critical droplet size.⁴ Therefore, phase separation only starts after a finite waiting time, when a strong enough fluctuation has occurred. The formation of a critical droplet (nucleus) is called *nucleation* [32]. In contrast, for a quench below the spinodal curve, the system is globally unstable and regions of the liquid phase start to form instantaneously throughout the system, coarsening over time. This process is known as *spinodal decomposition*. Note that in real systems, where fluctuations are important, the boundary separating nucleation from spinodal decomposition is not perfectly sharp, since the spinodal curve is a mean-field concept [32].

For ABPs with purely repulsive interactions, a similar phase diagram as for liquid-gas phase separation has been found with the propulsion speed v_0 playing the role of inverse temperature. The binodal [119, 15, 141, 135] and the critical point [134] have been determined in simulations, see Fig. 2.5(b). Moreover, the two phase separation scenarios, nucleation and spinodal decomposition, have been identified [119, 16]. Further links to liquid-gas separation can be made via an

⁴In two dimensions, liquid droplets of radius a lower the bulk free energy $\propto a^2$ but increase the interfacial free energy $\propto a$. Thus, only for droplets larger than a critical droplet size, further droplet growth leads to a reduction of the total free energy.

effective free energy functional, which has been found to describe the large-scale behavior of ABPs (although no rigorous free energy exists, as ABPs are driven out of equilibrium) [31, 146]. The phase equilibrium and thus the binodal, however, cannot be constructed via a common-tangent construction [173]. Further differences to liquid-gas separation exist, such as negative interfacial tension [15] and critical fluctuations that do not follow Ising universality [134].

2.4 Numerical and analytical methods

In the following, the main numerical and analytical methods used throughout this thesis are presented using the example of ABPs with volume exclusion interactions. In Chaps. 3, 4, 5, where we study extended versions of the ABP model, we apply these techniques in slightly modified form.

2.4.1 Brownian dynamics simulations

The Langevin equations (2.28) and (2.29) can be written as Itô stochastic differential equations [56]

$$d\mathbf{r}_k(t) = [v_0 \mathbf{e}_k - \mu_0 \nabla_k U] dt + \sqrt{2D_0} d\mathbf{W}_k(t), \quad (2.32)$$

$$d\varphi_k(t) = \sqrt{2D_r} dW_{r,k}(t). \quad (2.33)$$

Here, $d\mathbf{W}_k(t)$ and $dW_{r,k}(t)$ are increments of a two-dimensional and a one-dimensional Wiener process $\mathbf{W}_k(t)$ and $W_{r,k}(t)$, respectively. Using finite differences, the stochastic differential equations can be integrated forward in time via the Euler-Maruyama scheme as [71]

$$\mathbf{r}_k(t_{i+1}) = \mathbf{r}_k(t_i) + [v_0 \mathbf{e}_k(\varphi_k(t_i)) - \mu_0 \nabla_k U(\{\mathbf{r}_k(t_i)\})] \delta t + \sqrt{2D_0 \delta t} \mathbf{R}_k(t_i), \quad (2.34)$$

$$\varphi_k(t_{i+1}) = \varphi_k(t_i) + \sqrt{2D_r \delta t} R_{r,k}(t_i), \quad (2.35)$$

with time step $\delta t = t_{i+1} - t_i$ and $\tilde{\mathbf{R}}_k = (\mathbf{R}_k, R_{r,k})$ a three-dimensional vector of independent random numbers from a Gaussian distribution with zero mean and variance 1 (for every particle, new random numbers are drawn at every time step). The time step δt has to be chosen small enough to ensure numerical stability. Based on this simulation scheme, the particle trajectories $\{\mathbf{r}_k(t), \varphi_k(t)\}$ can be calculated numerically.

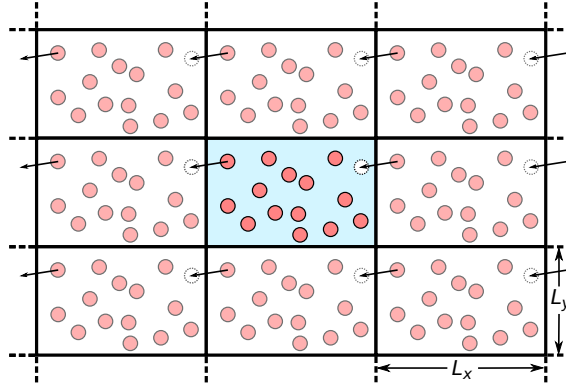


Fig. 2.6. Visualization of periodic boundary conditions. The central simulation box (blue) with dimensions L_x and L_y is replicated throughout space. A particle leaving a box through one side, reenters through the opposite side.

Boundary conditions

Since systems simulated on a computer (due to finite resources) always have to be finite, it is important to employ suitable boundary conditions. One possibility is to impose a confinement on the particles, e.g., due to a wall potential. However, when one is interested in the bulk behavior of a system, surface effects due to confinement are not desirable. In order to simulate a finite system with bulk properties, the method of choice is periodic boundary conditions [2]. This means that one simulates a single “central” box (and only stores the properties of particles in this box), e.g., of rectangular dimensions L_x and L_y , that is replicated throughout space, see Fig. 2.6. This results in an infinite lattice of boxes, with the image particles moving in exactly the same way as those in the central box. Consequently, when a particle leaves the central box, one of its images will enter through the opposite surface. Equivalently, the position $\mathbf{r}_k = (x_k, y_k)$ of the leaving particle itself can be shifted, according to (assuming the origin to be located at the center of the simulation box)

$$x_k(t_{i+1}) \rightarrow \begin{cases} x_k(t_{i+1}) + L_x, & \text{if } x_k(t_{i+1}) < -L_x/2 \\ x_k(t_{i+1}) - L_x, & \text{if } x_k(t_{i+1}) > L_x/2 \end{cases} \quad (2.36)$$

and analogously for the y -component. In principle, a particle in the central box interacts with all particles from all boxes, which would be infinitely many contributions. However, for pair-interactions with interaction range shorter than the box lengths L_x and L_y (which is typically true for the short-ranged repulsive interactions of ABPs), a particle k in the central box can only interact with the single closest

realization of a particle l . Their distance vector can be calculated from the distance vector of their realizations in the central box $\mathbf{r}_{kl} = (x_{kl}, y_{kl}) = (x_l - x_k, y_l - y_k)$ as

$$x_{kl} \rightarrow x_{kl} - L_x \lfloor 2x_{kl}/L_x \rfloor, \quad (2.37)$$

$$y_{kl} \rightarrow y_{kl} - L_y \lfloor 2y_{kl}/L_y \rfloor, \quad (2.38)$$

where $\lfloor \cdot \rfloor$ denotes the floor operation. Topologically, the central two-dimensional simulation box can be regarded to form the surface of a three-dimensional torus [2]. We take this into account, e.g., for the determination of the center of mass of the simulated system via the method given in Ref. [7].

2.4.2 Smoluchowski equation

A useful alternative to stochastic differential equations, which treat the stochastic dynamics of each particle individually, is the Fokker-Planck equation which describes the system in terms of a single probability density. In general, a system of Itô stochastic differential equations for a vector of n variables $\mathbf{q}(t) = (q_1(t), \dots, q_n(t))$ can be defined as [56]

$$d\mathbf{q}(t) = \mathbf{a}(\mathbf{q}, t)dt + \mathbf{B}(\mathbf{q}, t)d\mathbf{W}(t), \quad (2.39)$$

with vector of drift coefficients $\mathbf{a}(\mathbf{q}, t)$, matrix of diffusion coefficients $\mathbf{B}(\mathbf{q}, t)$ and n -dimensional Wiener process $\mathbf{W}(t)$. The corresponding Fokker-Planck equation is given by [56]

$$\partial_t \psi = - \sum_{i=1}^n \partial_i [a_i(\mathbf{q}, t)\psi] + \frac{1}{2} \sum_{i=1}^n \sum_{j=1}^n \partial_i \partial_j \left\{ [\mathbf{B}(\mathbf{q}, t) \cdot \mathbf{B}^T(\mathbf{q}, t)]_{ij} \psi \right\}, \quad (2.40)$$

where $\psi \equiv \psi(\mathbf{q}, t)$ is the joint time-dependent probability density of all n degrees of freedom. In case of ABPs, $\mathbf{q}(t)$ is a $3N$ -dimensional vector consisting of all particle positions $\mathbf{r}_k(t) = (x_k(t), y_k(t))$ and orientations $\varphi_k(t)$ whose dynamics is given by Eqs. (2.32) and (2.33). Identifying the coefficients

$$a_i = \begin{cases} v_0 \cos \varphi_k - \mu_0 \partial_{x_k} U, & i \in \{x_k\} \\ v_0 \sin \varphi_k - \mu_0 \partial_{y_k} U, & i \in \{y_k\} \\ 0, & i \in \{\varphi_k\} \end{cases} \quad (2.41)$$

and

$$[\mathbf{B} \cdot \mathbf{B}^T]_{ij} = \begin{cases} 2D_0, & i = j \in \{x_k, y_k\} \\ 2D_r, & i = j \in \{\varphi_k\} \\ 0, & i \neq j \end{cases}, \quad (2.42)$$

the Fokker-Planck equation (2.40) is given by

$$\partial_t \psi = \sum_{k=1}^N \left\{ -\nabla_k \cdot [(v_0 \mathbf{e}_k - \mu_0 \nabla_k U) \psi] + D_0 \nabla_k^2 \psi + D_r \partial_{\varphi_k}^2 \psi \right\}, \quad (2.43)$$

with N -particle probability density $\psi(\{\mathbf{r}_k, \varphi_k\}, t)$. In the following, we refer to this specific type of Fokker-Planck equation as the *Smoluchowski equation* in reference to the related Fokker-Planck equation describing a Brownian particle in an external potential formulated by Marian von Smoluchowski in 1915 [138].

2.4.3 One-body Smoluchowski equation

Due to its explicit dependence on all particle positions and orientations, an analytical solution of Eq. (2.43) is out of reach. However, as shown by Bialké *et al.* [14], progress can be made by deriving a coarse-grained, one-body description from the microscopic N -body equation (2.43). In this and the next section, we recapitulate their approach as it forms the basis of our analytical considerations in Chaps. 3 and 5.

Generally, if one is interested only in the properties of a subset of $n < N$ particles, one can eliminate the degrees of freedom of the other $N - n$ particles by integrating them out. This leads to the definition of the reduced distribution function [67]

$$\psi_n(\mathbf{r}_1, \dots, \mathbf{r}_n, \varphi_1, \dots, \varphi_n, t) = \frac{N!}{(N-n)!} \int d\mathbf{r}_{n+1} \dots d\mathbf{r}_N \int d\varphi_{n+1} \dots d\varphi_N \psi(\{\mathbf{r}_k, \varphi_k\}, t), \quad (2.44)$$

where $\psi_n d\mathbf{r}_1 \dots d\mathbf{r}_n d\varphi_1 \dots d\varphi_n$ is the probability to find any subset of n particles in the configuration space element $d\mathbf{r}_1 \dots d\mathbf{r}_n d\varphi_1 \dots d\varphi_n$. The factor $N!/(N-n)!$ is equal to the number of possibilities to choose n out of N indistinguishable particles. The positional integrals are evaluated over the whole (two-dimensional) space and the angular integrals from 0 to 2π .

Here, the main quantity of interest is the one-body density

$$\psi_1(\mathbf{r}_1, \varphi_1, t) = N \int d\mathbf{r}_2 \dots d\mathbf{r}_N \int d\varphi_2 \dots d\varphi_N \psi(\{\mathbf{r}_k, \varphi_k\}, t), \quad (2.45)$$

where now $\psi(\mathbf{r}_1, \varphi_1, t)d\mathbf{r}_1d\varphi_1$ is the probability to find an arbitrary particle inside the element $d\mathbf{r}_1d\varphi_1$. In order to obtain a dynamical equation for ψ_1 , the same integration as in Eq. (2.45) can be performed over both sides of Eq. (2.43). The integrals of the different terms on the right-hand side can be evaluated individually. The propulsion term yields⁵

$$\begin{aligned}
& - \int d\mathbf{r}_2 \dots d\mathbf{r}_N \int d\varphi_2 \dots d\varphi_N N \sum_{k=1}^N \nabla_k \cdot (v_0 \mathbf{e}_k \psi) \\
& = - \nabla_1 \cdot (v_0 \mathbf{e}_1 \psi_1) - \sum_{k=2}^N \int d\mathbf{r}_2 \dots d\mathbf{r}_{k-1} d\mathbf{r}_{k+1} \dots d\mathbf{r}_N \int d\varphi_2 \dots d\varphi_N N \underbrace{[v_0 \psi \mathbf{e}_k \cdot \mathbf{n}_k]_{|\mathbf{r}_k| \rightarrow -\infty}^{|\mathbf{r}_k| \rightarrow \infty}}_{=0} \\
& = - v_0 \mathbf{e}_1 \cdot \nabla_1 \psi_1,
\end{aligned} \tag{2.46}$$

with \mathbf{n}_k the normal vector of the boundary curve of the \mathbf{r}_k -integration area (the divergence theorem for the \mathbf{r}_k -integral has been applied). The second term in line two vanishes, since the probability distribution ψ has to go to zero for $|\mathbf{r}_k| \rightarrow \pm\infty$ in order to be normalizable. Along the same lines, considering $\nabla_k \psi \rightarrow 0$ for $|\mathbf{r}_k| \rightarrow \pm\infty$, the translational diffusion term can be evaluated as

$$\int d\mathbf{r}_2 \dots d\mathbf{r}_N \int d\varphi_2 \dots d\varphi_N N D_0 \sum_{k=1}^N \nabla_k^2 \psi = D_0 \nabla_1^2 \psi_1. \tag{2.47}$$

For the rotational diffusion term, one obtains⁶

$$\begin{aligned}
& \int d\mathbf{r}_2 \dots d\mathbf{r}_N \int d\varphi_2 \dots d\varphi_N N D_r \sum_{k=1}^N \partial_{\varphi_k}^2 \psi \\
& = D_r \partial_{\varphi_1}^2 \psi_1 + D_r \sum_{k=2}^N \int d\mathbf{r}_2 \dots d\mathbf{r}_N \int d\varphi_2 \dots d\varphi_{k-1} d\varphi_{k+1} \dots d\varphi_N N \underbrace{[\partial_{\varphi_k} \psi]_{\varphi_k=0}^{\varphi_k=2\pi}}_{=0} \\
& = D_r \partial_{\varphi_1}^2 \psi_1,
\end{aligned} \tag{2.48}$$

because ψ has to be 2π -periodic in φ_k . Starting out to evaluate the interaction term yields

$$- \int d\mathbf{r}_2 \dots d\mathbf{r}_N \int d\varphi_2 \dots d\varphi_N N \sum_{k=1}^N \nabla_k \cdot \left\{ -\mu_0 \nabla_k \left[\sum_{l \neq k} u(|\mathbf{r}_l - \mathbf{r}_k|) \right] \psi \right\}$$

⁵ $\int d\mathbf{r}_2 \dots d\mathbf{r}_{k-1} d\mathbf{r}_{k+1} \dots d\mathbf{r}_N$ always denotes an integration over all particle coordinates except \mathbf{r}_1 and \mathbf{r}_k . Thus for $k=2$ it is $\int d\mathbf{r}_3 \dots d\mathbf{r}_N$ and for $k=N$ it is $\int d\mathbf{r}_2 \dots d\mathbf{r}_{N-1}$.

⁶ $\int d\varphi_2 \dots d\varphi_{k-1} d\varphi_{k+1} \dots d\varphi_N$ denotes an integration over all particle orientations except φ_1 and φ_k . Thus for $k=2$ it is $\int d\varphi_3 \dots d\varphi_N$ and $\int d\varphi_2 \dots d\varphi_{N-1}$ for $k=N$.

$$\begin{aligned}
&= -\mu_0 \nabla_1 \cdot \int d\mathbf{r}_2 \dots d\mathbf{r}_N \int d\varphi_2 \dots d\varphi_N N \sum_{l=2}^N [-\nabla_1 u(|\mathbf{r}_l - \mathbf{r}_1|)] \psi \\
&\quad + \mu_0 \sum_{k=2}^N \int d\mathbf{r}_2 \dots d\mathbf{r}_{k-1} d\mathbf{r}_{k+1} \dots d\mathbf{r}_N \int d\varphi_2 \dots d\varphi_N N \underbrace{\left\{ \nabla_k \left[\sum_{l \neq k} u(|\mathbf{r}_l - \mathbf{r}_k|) \right] \cdot \mathbf{n}_k \psi \right\}}_{=0} \Bigg|_{|\mathbf{r}_k| \rightarrow +\infty}^{\Big|_{|\mathbf{r}_k| \rightarrow -\infty}}.
\end{aligned}$$

Again, the last term vanishes because $\psi \rightarrow 0$ at infinity. Since the particles are indistinguishable, the first term is a sum of $N - 1$ identical integrals. Without loss of generality, in the following, we rename $(\mathbf{r}_1, \varphi_1) \rightarrow (\mathbf{r}, \varphi)$ and $\nabla_1 \rightarrow \nabla$, as well as $(\mathbf{r}_2, \varphi_2) \rightarrow (\mathbf{r}', \varphi')$. Continuing with the evaluation of the interaction term, one arrives at

$$\begin{aligned}
&-\mu_0 \nabla \cdot N(N-1) \int d\mathbf{r}' d\mathbf{r}_3 \dots d\mathbf{r}_N \int d\varphi' d\varphi_3 \dots d\varphi_N [-\nabla u(|\mathbf{r}' - \mathbf{r}|)] \psi \\
&= -\mu_0 \nabla \cdot \int d\mathbf{r}' \int d\varphi' [-\nabla u(|\mathbf{r}' - \mathbf{r}|)] \psi_2(\mathbf{r}, \mathbf{r}', \varphi, \varphi', t). \tag{2.49}
\end{aligned}$$

Thus, the dynamical equation for $\psi_1(\mathbf{r}, \varphi, t)$ reads

$$\partial_t \psi_1 = -\nabla \cdot [\mu_0 \mathbf{f} + (v_0 \mathbf{e} - D_0 \nabla) \psi_1] + D_r \partial_\varphi^2 \psi_1, \tag{2.50}$$

with the force density

$$\mathbf{f}(\mathbf{r}, \varphi, t) = \int d\mathbf{r}' \int d\varphi' [-\nabla u(|\mathbf{r}' - \mathbf{r}|)] \psi_2(\mathbf{r}, \mathbf{r}', \varphi, \varphi', t) \tag{2.51}$$

containing all information about the particle interactions. However, since \mathbf{f} depends on the two-body density ψ_2 , Eq. (2.50) is not a closed equation for ψ_1 . Similarly, integrating Eq. (2.43) over the degrees of freedom of $N - 2$ particles, yields a dynamical equation for ψ_2 which is coupled to the three-body density ψ_3 . Consequently, one obtains a hierarchy of coupled equations, known as the Bogoliubov–Born–Green–Kirkwood–Yvon (BBGKY) hierarchy [176, 19, 79, 20].

The φ' -integral in Eq. (2.51) can be evaluated, yielding the marginal two-body density $\tilde{\psi}_2(\mathbf{r}, \mathbf{r}', \varphi, t) = \int d\varphi' \psi_2(\mathbf{r}, \mathbf{r}', \varphi, \varphi', t)$, which can be further decomposed into [67]

$$\tilde{\psi}_2(\mathbf{r}, \mathbf{r}', \varphi, t) = \psi_1(\mathbf{r}, \varphi, t) \rho(\mathbf{r}', t) g(\mathbf{r}, \mathbf{r}', \varphi, t), \tag{2.52}$$

with position-dependent density $\rho(\mathbf{r}', t) = \int d\varphi' \psi_1(\mathbf{r}', \varphi', t)$ and pair correlation function $g(\mathbf{r}, \mathbf{r}', \varphi, t)$. The product ρg is the conditional probability density to find a particle at position \mathbf{r}' given there is a particle at \mathbf{r} with orientation φ at time t . In

case of vanishing correlations (ideal gas limit) the pair correlation function evaluates to one. Applying Eq. (2.52), Eq. (2.50) turns into

$$\partial_t \psi_1 = -\nabla \cdot [(\mu_0 \mathbf{F} + v_0 \mathbf{e} - D_0 \nabla) \psi_1] + D_r \partial_\varphi^2 \psi_1, \quad (2.53)$$

where

$$\mathbf{F}(\mathbf{r}, \varphi, t) = \int d\mathbf{r}' [-\nabla u(|\mathbf{r}' - \mathbf{r}|)] \rho(\mathbf{r}', t) g(\mathbf{r}, \mathbf{r}', \varphi, t) \quad (2.54)$$

is the average force acting on a particle at position \mathbf{r} with orientation φ at time t due to the surrounding particles. Still, the product $\rho(\mathbf{r}', t) g(\mathbf{r}, \mathbf{r}', \varphi, t)$ in Eq. (2.54) can only be determined from the remaining $N - 1$ equations in the hierarchy. In order to arrive at an analytically tractable problem, Eq. (2.53) can be closed without the rest of the hierarchy via several approximations.

2.4.4 Mean-field approximations and effective speed

First, only positions \mathbf{r}' which lie inside the interaction range of the pair potential (i.e., all \mathbf{r}' for which $\nabla u(|\mathbf{r}' - \mathbf{r}|) \neq 0$) contribute to $\mathbf{F}(\mathbf{r}, \varphi, t)$. Assuming $u(r)$ to be short-ranged compared to the length scale of variations of the particle density ρ (appealing, e.g., to short-ranged repulsive interactions like the WCA potential), in Eq. (2.54) the approximation $\rho(\mathbf{r}', t) \approx \rho(\mathbf{r}, t)$ can be made [14, 146]. Further approximating the pair correlation function with that of the homogeneous steady state, i.e., $g(\mathbf{r}, \mathbf{r}', \varphi, t) \rightarrow g(\mathbf{r} - \mathbf{r}', \varphi)$, Eq. (2.54) becomes [14]

$$\mathbf{F}(\mathbf{r}, \varphi, t) \approx \rho(\mathbf{r}, t) \int_0^\infty dr \int_0^{2\pi} d\theta r [-\nabla u(r)] g(r, \theta). \quad (2.55)$$

Here, the integration is performed in polar coordinates centered at \mathbf{r} with $r = |\mathbf{r}' - \mathbf{r}|$ and θ the angle between $\mathbf{r}' - \mathbf{r}$ and \mathbf{e} , see Fig. 2.7(a) for a sketch of the geometry.

The pair correlation function $g(r, \theta)$ of the homogeneous state can, e.g., be measured in Brownian Dynamics simulations of ABPs and used as an input to Eq. (2.55), as it was done in Ref. [14]. The numerically obtained $g(r, \theta)$, as depicted in Fig. 2.7(b), shows that for a tagged particle the probability to find another particle in front is higher than in the back (and symmetric between left and right). This asymmetry does not exist for passive particles and is a result of the directed motion of ABPs. Therefore, the force $\mathbf{F}(\mathbf{r}, \varphi, t)$ is non-zero and assumed to be antiparallel to the propulsion direction \mathbf{e} of the tagged particle, i.e.,

$$\mathbf{F}(\mathbf{r}, \varphi, t) = [\mathbf{F}(\mathbf{r}, \varphi, t) \cdot \mathbf{e}] \mathbf{e} = -\rho(\mathbf{r}, t) \zeta \mathbf{e}, \quad (2.56)$$

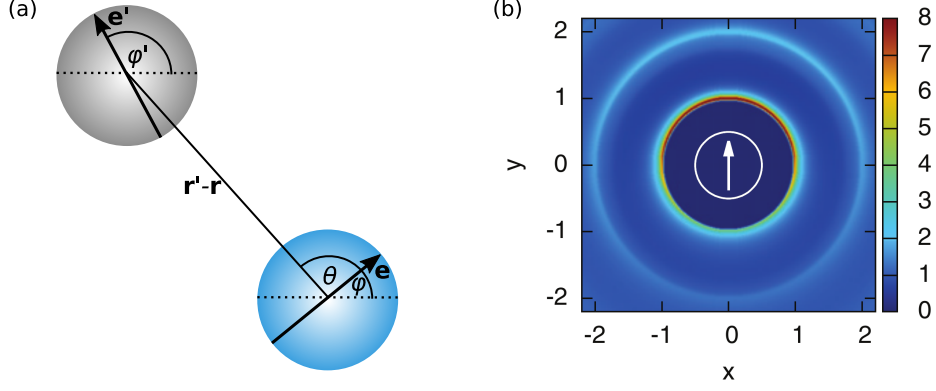


Fig. 2.7. Two-body correlations. (a) A tagged particle (blue) separated from another particle (grey) by $\mathbf{r}' - \mathbf{r}$. The propulsion direction \mathbf{e} and $\mathbf{r}' - \mathbf{r}$ enclose the angle θ . (b) Anisotropic pair-correlation function $g(r, \theta)$ determined from simulations (at packing fraction $\phi = 0.5$ and propulsion speed $v_0 = 20 D_0 \sigma^{-1}$). The white circle and arrow show the tagged particle and its orientation. The probability to find a particle in front of it is increased compared to its back. (Reprinted with permission from Ref. [14].)

with *force imbalance* coefficient [14]

$$\zeta = \int_0^\infty dr \int_0^{2\pi} d\theta r [-u'(r)] \cos \theta g(r, \theta) > 0. \quad (2.57)$$

Plugging Eq. (2.56) into Eq. (2.53) yields the *mean-field* dynamical equation

$$\partial_t \psi_1 = -\nabla \cdot [(v(\rho)\mathbf{e} - D_0 \nabla) \psi_1] + D_r \partial_\varphi^2 \psi_1, \quad (2.58)$$

for the one-body density with effective density-dependent speed

$$v(\rho) = v_0 - \mu_0 \zeta \rho. \quad (2.59)$$

Having determined $g(r, \theta)$ in simulations, the coefficient ζ can be calculated by evaluating the integral Eq. (2.57). For strongly repulsive particles, e.g., interacting via the WCA potential, it has been found that $\zeta \sim v_0$ as the asymmetry of $g(r, \theta)$ increases with the propulsion speed v_0 [14]. For softer interaction potentials, however, this relation is not necessarily true, as we will see in Sec. 3.4.

2.4.5 Moment expansion of the one-body density

It is relatively straightforward to check that the uniform distribution $\psi_1 = \rho_0 / 2\pi$, with ρ_0 the uniform particle number density, is a stationary solution of Eq. (2.58). Due to its nonlinearity and dependence on both \mathbf{r} and φ , gaining further analytical

insights from Eq. (2.58) is very challenging. An alternative approach is to switch to a representation in terms of orientational moments of the one-body density [12, 13]. Since $\psi_1(\mathbf{r}, \varphi, t)$ is a 2π -periodic function in φ , it can be expanded into a Fourier series

$$\psi_1(\mathbf{r}, \varphi, t) = \frac{1}{2\pi} \hat{\psi}_0(\mathbf{r}, t) + \frac{1}{\pi} \sum_{m=1}^{\infty} \hat{\psi}_m(\mathbf{r}, t) \cos(m\varphi) + \frac{1}{\pi} \sum_{m=1}^{\infty} \hat{\phi}_m(\mathbf{r}, t) \sin(m\varphi), \quad (2.60)$$

with Fourier coefficients (orientational moments)

$$\hat{\psi}_0(\mathbf{r}, t) = \int_0^{2\pi} d\varphi \psi_1(\mathbf{r}, \varphi, t), \quad (2.61)$$

$$\hat{\psi}_m(\mathbf{r}, t) = \int_0^{2\pi} d\varphi \psi_1(\mathbf{r}, \varphi, t) \cos(m\varphi), \quad (2.62)$$

$$\hat{\phi}_m(\mathbf{r}, t) = \int_0^{2\pi} d\varphi \psi_1(\mathbf{r}, \varphi, t) \sin(m\varphi). \quad (2.63)$$

Multiplying Eq. (2.58) by $\cos(m\varphi)$ or $\sin(m\varphi)$ and integrating over φ , dynamical equations for the moments can be derived. These equations are typically coupled and form a hierarchy, for which an appropriate closure has to be found in order to allow for further analytical treatment.

Moreover, specific combinations of the moments can be identified as familiar physical quantities. The (orientation-independent) density field is simply given by

$$\rho(\mathbf{r}, t) \equiv \hat{\psi}_0(\mathbf{r}, t). \quad (2.64)$$

The polarization field, a measure for the average orientation of particles, is defined as

$$\mathbf{p}(\mathbf{r}, t) \equiv \begin{pmatrix} \hat{\psi}_1(\mathbf{r}, t) \\ \hat{\phi}_1(\mathbf{r}, t) \end{pmatrix} = \int_0^{2\pi} d\varphi \mathbf{e} \psi_1(\mathbf{r}, \varphi, t), \quad (2.65)$$

and the nematic tensor field can be calculated as

$$\mathbf{Q}(\mathbf{r}, t) \equiv \frac{1}{2} \begin{pmatrix} \hat{\psi}_2(\mathbf{r}, t) & \hat{\phi}_2(\mathbf{r}, t) \\ \hat{\phi}_2(\mathbf{r}, t) & -\hat{\psi}_2(\mathbf{r}, t) \end{pmatrix} = \int_0^{2\pi} d\varphi (\mathbf{e} \otimes \mathbf{e} - \frac{1}{2} \mathbb{1}) \psi_1(\mathbf{r}, \varphi, t). \quad (2.66)$$

Phase separation of active Brownian particles at constant affinity

The active Brownian particle model (Sec. 2.3) describes the effective motion of active Janus particles without explicitly taking into account the physical mechanisms leading to self-propulsion. This has led to conflicting results for their entropy production as the heat exchanged with the environment along their trajectories cannot be unambiguously identified [54, 51, 143, 96]. In Ref. [144], the self-propulsion mechanism has been incorporated in a thermodynamically consistent way via a chemical reaction of an abundant chemical which allows to overcome the described shortcoming of the ABP model. While the details of this modified ABP model and its consequences for the entropy production have been discussed in Ref. [144], here we explore how it affects the motility-induced phase separation (Sec. 2.3.3) of active particles via computer simulations and mean-field theory. In Sec. 3.1, we recapitulate the main ideas of Ref. [144]. Most of the results presented in the subsequent sections have been published in Ref. [47].

3.1 Background: Active Brownian particles at constant affinity

Self-diffusiophoretic Janus particles (Sec. 2.2) are typically powered by a difference in chemical potential either between reactants and products (decomposition of hydrogen peroxide [72]) or between two phases (critical demixing of a water-lutidine mixture [161, 27]). In Ref. [144], self-propulsion of a Janus particle is modeled to arise from the conversion of two generic chemical species \bullet (reactant) and \circ (product) at fixed chemical potential difference $\Delta\mu \equiv \mu_{\bullet} - \mu_{\circ} > 0$. In response to every chemical event $\bullet \rightarrow \circ$, the particle is translated by a distance λ along its orientation vector $\mathbf{e} = (\cos \varphi, \sin \varphi)$ (and in the opposite direction in case of a backward reaction $\bullet \leftarrow \circ$), cf. Fig. 3.1. The length λ depends on diverse factors

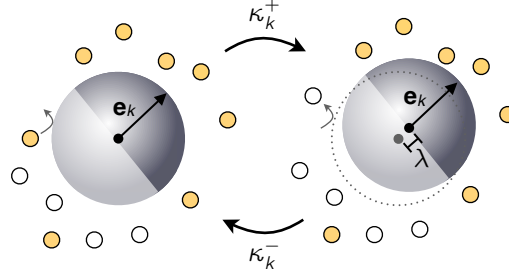


Fig. 3.1. Model of the self-propulsion mechanism of self-diffusiophoretic Janus particles. Each conversion of chemicals $\bullet \rightarrow \circ$ leads to the translation of a particle along its orientation \mathbf{e}_k by the distance λ . The corresponding transition rate κ_k^+ and the rate for a backward step κ_k^- ($\bullet \leftarrow \circ$) obey the local detailed balance condition, Eq. (3.4). Reprinted from Ref. [47], with the permission of AIP Publishing.

such as the particle geometry and surface properties [59]. Here, it is treated as a controllable parameter.

In a system of N interacting active particles, a thermodynamically consistent set of transition rates can be derived by combining the particles and the reactant and product molecules into a super-system [132] coupled to a heat bath at temperature T . The molecules can be regarded as a work reservoir with Gibbs free energy

$$G_{\text{res}}(n) = \mu_{\bullet} n_{\bullet} + \mu_{\circ} n_{\circ} = \mu_{\bullet} n_{\text{tot}} - n \Delta\mu, \quad (3.1)$$

with the total number of new product molecules $n \equiv \Delta n_{\circ} = \sum_k n_k$, the number of reactions n_k occurring on the surface of particle k and $n_{\text{tot}} = n_{\bullet} + n_{\circ}$ the (constant) total number of molecules. Here, n is an extensive quantity and $\Delta\mu$ a thermodynamic force (driving *affinity*). As $\Delta\mu > 0$, reactions $\bullet \rightarrow \circ$ triggering particle translations lead to a drain of the work reservoir.

The total energy of the combined system (active particles plus the chemicals) is $E(\{\mathbf{r}_k\}, n) = U(\{\mathbf{r}_k\}) + G_{\text{res}}(n)$ with $U(\{\mathbf{r}_k\})$ being the total potential energy arising from the particle interactions. The change in potential energy due to a single forward reaction (holding all other particle positions fixed) is

$$\delta U = U(\mathbf{r}_k + \lambda \mathbf{e}_k) - U(\mathbf{r}_k) \approx \lambda \mathbf{e}_k \cdot \nabla_k U \equiv \hat{f}_k, \quad (3.2)$$

assuming λ to be much smaller than the typical length scale set by interactions (corresponding, e.g., to the particle diameter in case of short-ranged repulsive interactions). A single reaction thus causes the change in energy

$$\delta E = \delta U + \delta G_{\text{res}} = \hat{f}_k - \Delta\mu. \quad (3.3)$$

To describe the dynamics of the particles, the (forward and backward) jump rates $\kappa_k^+(\mathbf{r}_k) = \kappa_k^+(\mathbf{r}_k \rightarrow \mathbf{r}_k + \lambda \mathbf{e}_k, n \rightarrow n + 1)$ and $\kappa_k^-(\mathbf{r}_k) = \kappa_k^-(\mathbf{r}_k + \lambda \mathbf{e}_k \rightarrow \mathbf{r}_k, n + 1 \rightarrow n)$ are required, which have to fulfill the local detailed balance condition [131]

$$\frac{\kappa_k^+(\mathbf{r}_k)}{\kappa_k^-(\mathbf{r}_k)} = \frac{\Psi_{\text{eq}}(\mathbf{r}_k + \lambda \mathbf{e}_k, n + 1)}{\Psi_{\text{eq}}(\mathbf{r}_k, n)} = e^{-\beta(\hat{f}_k - \Delta\mu)}, \quad (3.4)$$

with equilibrium distribution $\Psi_{\text{eq}}(\{\mathbf{r}_k\}, n) \propto e^{-\beta E(\{\mathbf{r}_k\}, n)}$ and $\beta = (k_B T)^{-1}$.

The evolution equation $\partial_t \Psi = \mathcal{L}_p \Psi + \mathcal{L}_a \Psi$ for the time-dependent joint probability distribution $\Psi(\{\mathbf{r}_k, \varphi_k, n_k\}, t)$ can be split up into a passive and an active contribution. Analogous to Eq. (2.43), the passive differential operator reads

$$\mathcal{L}_p = \sum_{k=1}^N \nabla_k \cdot [\mu_0 (\nabla_k U) + D_0 \nabla_k] + \partial_{\varphi_k}^2. \quad (3.5)$$

Resolving the chemical reactions and assuming them to occur independently, the active operator is given by $\mathcal{L}_a \Psi = \sum_{k=1}^N \mathcal{L}_k \Psi$ with

$$\begin{aligned} \mathcal{L}_k \Psi = & \kappa_k^+(\mathbf{r}_k - \lambda \mathbf{e}_k) \Psi(\mathbf{r}_k - \lambda \mathbf{e}_k, n_k - 1) + \kappa_k^-(\mathbf{r}_k) \Psi(\mathbf{r}_k + \lambda \mathbf{e}_k, n_k + 1) \\ & - [\kappa_k^+(\mathbf{r}_k) + \kappa_k^-(\mathbf{r}_k - \lambda \mathbf{e}_k)] \Psi(\mathbf{r}_k, n_k), \end{aligned} \quad (3.6)$$

where only the arguments of Ψ that are affected by the state transitions are indicated. Expanding the rates and the probability density around \mathbf{r}_k and n_k , and summing over the individual chemical events, to linear order in λ , one obtains

$$\mathcal{L}_k \psi \approx -\nabla_k \cdot [\lambda (\kappa_k^+ - \kappa_k^-) \mathbf{e}_k \psi], \quad (3.7)$$

with $\psi(\{\mathbf{r}_k, \varphi_k\}, t) = \int dn_1 \dots dn_N \Psi(\{\mathbf{r}_k, \varphi_k, n_k\}, t)$. Equation (3.7) describes propulsion of a particle with speed

$$\hat{v}_k(\{\mathbf{r}_k\}, \mathbf{e}_k) = \lambda (\kappa_k^+ - \kappa_k^-). \quad (3.8)$$

Through the rates κ_k^\pm , the propulsion speed \hat{v}_k of a particle depends on all particle positions and its own orientation. The corresponding Langevin equations are

$$\dot{\mathbf{r}}_k = \hat{v}_k \mathbf{e}_k - \mu_0 \nabla_k U + \boldsymbol{\xi}_k, \quad \dot{\varphi}_k = \xi_{r,k}, \quad (3.9)$$

with the same translational and rotational thermal noise $\boldsymbol{\xi}_k$ and $\xi_{r,k}$ respectively as for ABPs at constant speed. Equation (3.9) describes the dynamics of the particles' positions and orientations without explicit reference to the chemical reactions. In the following, we call this model "ABPs at constant affinity" since, here, the driving

affinity $\Delta\mu$ is kept constant, in contrast to plain ABPs which are propelled at constant speed v_0 . Note that similar Langevin equations that include additional noise on the propulsion speed of order λ^2 have been derived in Ref. [115].

3.2 Effective propulsion speed

The particle speed \hat{v}_k , Eq. (3.8), depends on the forward and backward rates κ_k^\pm , whose ratio has to fulfill the detailed balance condition (3.4). One valid choice of rates is the symmetric form

$$\kappa_k^\pm = \kappa_0 e^{\pm\beta(\Delta\mu - \hat{f}_k)/2}, \quad (3.10)$$

with attempt rate κ_0 . The particle speed then reads

$$\hat{v}_k = \kappa_0 \lambda \left(e^{\beta(\Delta\mu - \hat{f}_k)/2} - e^{-\beta(\Delta\mu - \hat{f}_k)/2} \right) = 2\kappa_0 \lambda \sinh[\beta(\Delta\mu - \hat{f}_k)/2]. \quad (3.11)$$

In the absence of a force ($\nabla_k U = 0$) or for a force perpendicular to the propulsion direction ($\nabla_k U \perp \mathbf{e}_k$), it is $\hat{f}_k = 0$ and the particle propels with the free speed

$$v_0 \equiv \hat{v}_k(\hat{f}_k = 0) = 2\kappa_0 \lambda \sinh(\beta\Delta\mu/2). \quad (3.12)$$

Thus, the three parameters κ_0 , λ and $\Delta\mu$ characterize the directed particle motion. For small $\beta\hat{f}_k \ll 1$, the particle speed [Eq. (3.11)] can be expanded as

$$\hat{v}_k \approx 2\lambda\kappa_0 \sinh(\beta\Delta\mu/2) - \kappa_0 \lambda^2 \beta \mathbf{e}_k \cdot \nabla_k U \cosh(\beta\Delta\mu/2), \quad (3.13)$$

which (employing Eq. (3.12) and $\cosh^2(x) - \sinh^2(x) = 1$) can be recast into

$$\hat{v}_k \approx v_0 - \chi \mu_0 \mathbf{e}_k \cdot \nabla_k U, \quad (3.14)$$

with dimensionless coefficient

$$\chi \equiv \frac{\kappa_0 \lambda^2}{D_0} \sqrt{1 + \left(\frac{v_0}{2\kappa_0 \lambda} \right)^2}. \quad (3.15)$$

In analogy to Sec. 2.4.2, the Langevin equations (3.9) can be represented by a Smoluchowski equation for the joint probability distribution $\psi(\{\mathbf{r}_k, \varphi_k\}, t)$ as

$$\partial_t \psi = \sum_{k=1}^N \left\{ -\nabla_k \cdot [(-\mu_0 \nabla_k U + v_0 \mathbf{e}_k - \chi \mu_0 (\mathbf{e}_k \cdot \nabla_k U) \mathbf{e}_k) \psi] + D_0 \nabla_k^2 \psi + D_r \partial_{\varphi_k}^2 \psi \right\}, \quad (3.16)$$

where expansion (3.14) has been employed. This is Eq. (2.43) plus the additional term $\propto \chi$ due to the non-constant speed. We now consider particles that interact via a repulsive pair potential $u(r)$, i.e., the potential energy is given by $U = \sum_{k,l>k} u(|\mathbf{r}_l - \mathbf{r}_k|)$. Then, integrating over positions and orientations except for a tagged particle as in Sec. 2.4.3, and dropping particle indices, yields the dynamical equation

$$\partial_t \psi_1 = -\nabla \cdot [v_0 \mathbf{e} + \mu_0 \mathbf{F} + \mu_0 \chi (\mathbf{F} \cdot \mathbf{e}) \mathbf{e} - D_0 \nabla] \psi_1 + D_r \partial_\varphi^2 \psi_1 \quad (3.17)$$

for the one-body density $\psi_1(\mathbf{r}, \varphi, t)$ with the force $\mathbf{F}(\mathbf{r}, \varphi, t)$ given by Eq. (2.54). Applying the same approximations for \mathbf{F} as in Sec. 2.4.4, we obtain

$$\partial_t \psi_1 = -\nabla \cdot [v(\rho) \mathbf{e} - D_0 \nabla] \psi_1 + D_r \partial_\varphi^2 \psi_1, \quad (3.18)$$

with effective density-dependent speed

$$v(\rho) = v_0 - \mu_0(1 + \chi) \zeta \rho \quad (3.19)$$

and force imbalance coefficient ζ given by Eq. (2.57). For ABPs at constant speed v_0 , the same expression for the effective speed with $\chi = 0$ holds [Eq. (2.59)]. Since $\chi \geq 0$ according to Eq. (3.15), here the effective speed is reduced further. The reason is that particles are not only slowed down by the repulsive forces from collisions, but also by the associated potential energy cost $\hat{f}_k > 0$ that reduces the propulsion speed \hat{v}_k (as κ_k^+ is decreased by a factor $e^{-\beta \hat{f}_k/2}$ and κ_k^- is increased by $e^{\beta \hat{f}_k/2}$).

Expression (3.19) requires the knowledge of ζ , which can be determined by measuring the pair-correlation function $g(r, \theta)$ in simulations (compare the discussion in Sec. 2.4.4). Alternatively, the density-dependent speed can be obtained directly from the particle trajectories $\{\mathbf{r}_k(t), \varphi_k(t)\}$ as

$$v(\rho) = \langle \dot{\mathbf{r}}_k \cdot \mathbf{e}_k \rangle_\rho = \langle \hat{v}_k \rangle_\rho - \mu_0 \langle \mathbf{e}_k \cdot \nabla_k U \rangle_\rho, \quad (3.20)$$

where the average $\langle \dots \rangle_\rho$ is taken over particles in an approximately homogeneous region of the system with density ρ . Applying approximation (3.14) yields

$$v(\rho) = v_0 - \mu_0(1 + \chi) \langle \mathbf{e}_k \cdot \nabla_k U \rangle_\rho, \quad (3.21)$$

for $\beta \hat{f}_k \ll 1$ showing the equivalence of $\zeta \rho$ and $\langle \mathbf{e}_k \cdot \nabla_k U \rangle_\rho$.

3.3 Hard discs

We first study suspensions of particles interacting via the WCA potential, Eq. (2.30) (with parameters ϵ and σ). As in previous studies on ABPs at constant speed [15, 135, 134], we set the potential strength to $\epsilon = 100k_B T$ modeling (almost) hard discs with an effective (Barker-Henderson) diameter $d_{\text{BH}} = 1.10688\sigma$ [Eq. (2.31)]. Equation (2.13) then implies the rotational diffusion coefficient $D_r = 3D_0/d_{\text{BH}}^2$. As units of length, time and energy we employ σ , σ^2/D_0 and $k_B T$ respectively.

3.3.1 Brownian dynamics simulations

We perform Brownian dynamics simulations of $N = 4735$ particles as described in Sec. 2.4.1 [the constant speed v_0 in Eq. (2.34) is replaced by the non-constant speed \hat{v}_k [Eq. (3.11)] with time step $\delta t = 2 \cdot 10^{-6}$. Simulations were run with a MPI-parallelized C++ simulation code developed by Alexander Winkler, Benjamin Trefz and Jonathan Siebert (available in the KOMET work group at Johannes Gutenberg-Universität Mainz), into which we have implemented the feature of non-constant speed. The computations were carried out on the Mogon II supercomputer cluster at ZDV Mainz.

We employ an elongated simulation box with dimensions $L_x = 135$, $L_y = 67.5$ (size ratio 2:1) with periodic boundary conditions, implying a global number density $\rho_0 = N/(L_x L_y) \simeq 0.52$. We fix the product $\kappa_0 \lambda = 10$ and vary the free speed v_0 [Eq. (3.12)] by changing $\Delta\mu$ for several lengths λ . We simulate at high enough speeds v_0 such that the system undergoes motility-induced phase separation into a dense cluster and a dilute gas phase (Sec. 2.3.3). The elongated simulation box encourages the dense phase to form a slab aligned perpendicular to the x -axis [15, 135, 134], cf. Fig. 3.2(b). All measurements presented in the following were performed in the steady state in a time window of duration $\Delta t = 800$ after an equilibration time of $\Delta t_{\text{eq}} = 100$.

Speed distribution

Due to the scarcity of collisions, most particles in the gas move with the free speed v_0 , see Fig. 3.2(b). In contrast, in the dense phase, the individual speeds \hat{v}_k follow a broad distribution [see Fig. 3.2(a) for $\lambda = 10^{-3}$ and $\Delta\mu = 5.5$]. Mostly, the speeds are smaller than the free speed v_0 (in particular the mean is smaller), since, due to their directed motion, particles more frequently experience forces opposing their

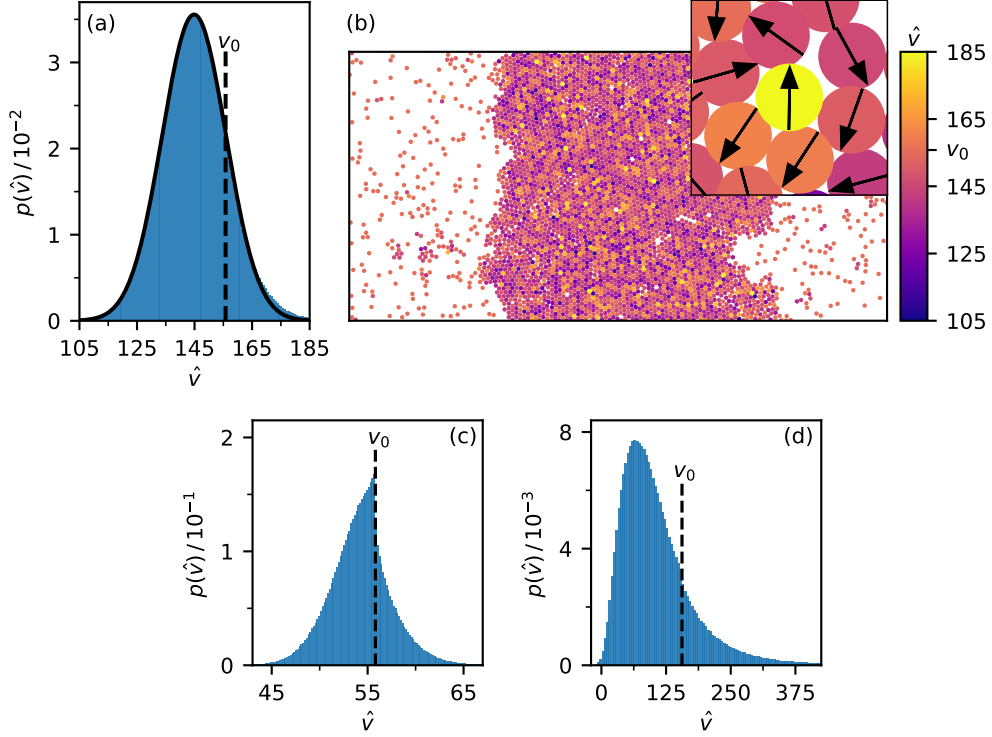


Fig. 3.2. (a) Distribution of speeds \hat{v}_k of hard discs for $\lambda = 10^{-3}$, $\Delta\mu = 5.5$. Indicated is the speed $v_0 \simeq 156$ of free particles (dashed line), which are not included in the distribution. The distribution is well fitted by a Gaussian (solid line) with mean $\langle \hat{v} \rangle \simeq 145$ and standard deviation $\simeq 11$. (b) Simulation snapshot showing the dense slab surrounded by the active gas [same parameters as in (a)], with the color indicating the propulsion speed \hat{v}_k . A particle configuration in the dense phase is shown in the inset. The speed of the tagged particle (yellow) at the center is increased ($\hat{v}_k > v_0$), since it interacts with three particles at its back and merely one at its front, implying $\mathbf{e}_k \cdot \nabla_k U < 0$. Non-Gaussian speed distributions for (c) $\lambda = 10^{-3}$, $\Delta\mu = 3.5$ ($v_0 \simeq 56$) and (d) $\lambda = 10^{-2}$, $\Delta\mu = 5.5$ ($v_0 \simeq 156$). Reprinted in slightly adapted form from Ref. [47], with the permission of AIP Publishing.

propulsion direction with $\mathbf{e}_k \cdot \nabla_k U > 0$. However, there is a tail with speeds greater v_0 , coming from particles for which the total force points along their orientation ($\mathbf{e}_k \cdot \nabla_k U < 0$). This can occur, e.g., for particles that interact with more particles in its back than its front [cf. inset of Fig. 3.2(b)]. The individual speeds \hat{v}_k are distributed quite uniformly throughout the dense phase without any visible long-range correlations, as suggested by Fig. 3.2(b).

Fig. 3.2(c) shows that when $\Delta\mu$ is reduced (i.e., for smaller v_0), the speed distribution exhibits a markedly non-Gaussian shape. At higher $\lambda = 10^{-2}$, the speed distribution becomes broader because of the higher sensitivity of the speed on the forces ($\hat{f}_k \propto \lambda$), cf. Fig. 3.2(d). In that case, the shape of the distribution is notably

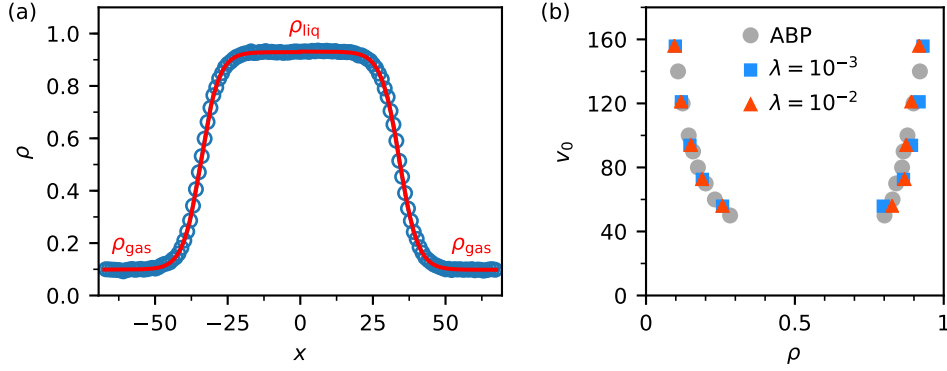


Fig. 3.3. Phase behavior. (a) Time-averaged density profile along the x -axis (circles) for $\lambda = 10^{-3}$, $\Delta\mu = 5.5$ ($v_0 \simeq 156$). Red lines: fits via Eq. (3.22) by which the coexisting densities ρ_{gas} and ρ_{liq} can be extracted. (b) Phase diagram (coexisting densities) for ABPs at constant speed v_0 (data taken from Ref. [135]) and for ABPs at constant affinity for different values of λ . (b) is reprinted from Ref. [47], with the permission of AIP Publishing.

asymmetric, since, for $\hat{v}_k \rightarrow 0$, it decays to zero very fast with only an extremely small amount of particles having negative speeds.¹

Phase diagram

In the next step, we measure the coexisting densities in the phase-separated regime using the same method as in Refs. [15, 135, 134]. Therefore, we employ discrete bins along the elongated edge of the box which allows us to measure the time-averaged density distribution $\rho(x)$. As the dense slab is free to move along the x -axis of the box, we shift the center of mass of each analyzed snapshot to $x = 0$ before performing the time average. The resulting density profile $\rho(x)$ exhibits two plateaus whose values correspond to the coexisting densities, separated by an interface of finite width, cf. Fig. 3.3(a). Since the dense slab has straight interfaces (parallel to the y -axis), this method minimizes finite-size effects. We fit both sides of the density profile individually using

$$\rho(x) = \frac{\rho_{\text{liq}} + \rho_{\text{gas}}}{2} + \frac{\rho_{\text{liq}} - \rho_{\text{gas}}}{2} \tanh\left(\frac{x - x_0}{2\omega}\right), \quad (3.22)$$

see Fig. 3.3(a), which allows us to extract the coexisting densities ρ_{gas} and ρ_{liq} by averaging the values of both sides (ω is the width of the interface and x_0 its position). In this way, we obtain the coexisting densities for different v_0 for $\lambda = 10^{-3}$

¹When the speed \hat{v}_k of a particle is close to zero due to strong forces from particles at its front, the particle is pushed away from the other particles due to the lack of propulsion. This in turn leads to a reduction of the forces and thus to an increase of \hat{v}_k . We suggest this to be the reason why it is very unlikely to observe speeds $\hat{v}_k < 0$.

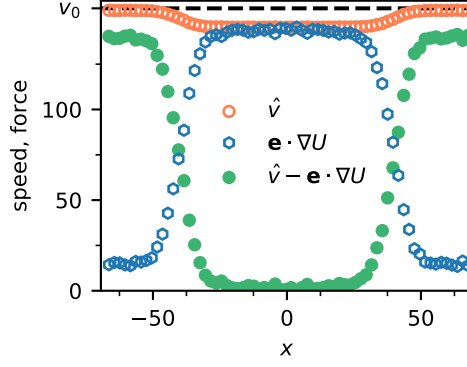


Fig. 3.4. Time-averaged profiles of the propulsion speed \hat{v} and the force opposing the propulsion direction $\mathbf{e} \cdot \nabla U$ along the x -axis (empty symbols) [$\lambda = 10^{-3}$, $\Delta\mu = 5.5$]. The effective speed is then be obtained via $v(x) = \hat{v}(x) - [\mathbf{e} \cdot \nabla U](x)$ (full symbols).

and $\lambda = 10^{-2}$, which we plot in Fig. 3.3(b) together with the values for ABPs at constant speed. The coexisting densities lie on top of each other, suggesting that the non-constant speed does not influence the phase behavior.

Effective speed

In order to obtain further insight, we determine time-averaged profiles along the x -axis for the propulsion speed $\hat{v}(x)$ and the force opposing the propulsion direction $[\mathbf{e} \cdot \nabla U](x)$. The x -dependent effective propulsion speed is then given by $v(x) = \hat{v}(x) - [\mathbf{e} \cdot \nabla U](x)$. Fig. 3.4 shows that the three quantities exhibit a similar behavior as the density profile taking constant values in the dense and dilute bulk regions ($[\mathbf{e} \cdot \nabla U](x)$ is increased in the dense region leading to a reduction of $\hat{v}(x)$). Performing fits with the same functional form as Eq. (3.22), we can therefore extract their plateau values. By relating those to the gas and liquid densities ρ_{gas} and ρ_{liq} , we can determine $\langle \hat{v}_k \rangle_\rho$, $\langle \mathbf{e}_k \cdot \nabla_k U \rangle_\rho$ and $v(\rho) = \langle \hat{v}_k \rangle_\rho - \langle \mathbf{e}_k \cdot \nabla_k U \rangle_\rho$ [Eq. (3.20)]. However, since there is a gap in our phase diagram, Fig. 3.3(b), in the range $0.3 \lesssim \rho \lesssim 0.8$ we perform additional simulations in the homogeneous regime at lower speed $v_0 = 20$ (we vary the density by changing the box size). Since the system does not phase separate at these state points, we can relate the globally averaged values of the propulsion speed and the force to the global density ρ_0 .

With decreasing $\langle \hat{v}_k \rangle_\rho$, the frequency of particle collisions diminishes, inducing a simultaneous reduction of $\langle \mathbf{e}_k \cdot \nabla_k U \rangle_\rho$. Therefore, $\langle \mathbf{e}_k \cdot \nabla_k U \rangle_\rho \propto \langle \hat{v}_k \rangle_\rho$, which is confirmed by the data presented in Fig. 3.5(a). For densities up to $\rho \lesssim 0.7$, we find

$$\langle \mathbf{e}_k \cdot \nabla_k U \rangle_\rho \approx a\rho \langle \hat{v}_k \rangle_\rho, \quad (3.23)$$

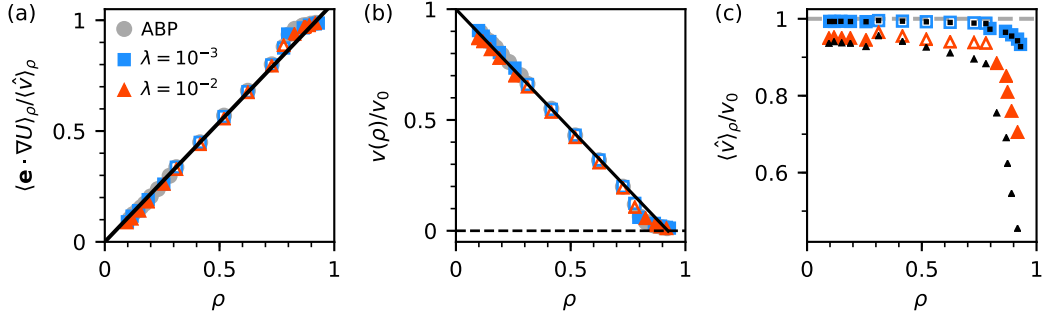


Fig. 3.5. Forces and speeds as functions of density. (a) Average force opposing the propulsion direction $\langle \mathbf{e}_k \cdot \nabla_k U \rangle_\rho$ normalized by $\langle \hat{v}_k \rangle_\rho$ for ABPs with constant speed v_0 and for ABPs at constant affinity for two values of λ . Open symbols show data acquired in the homogeneous regime at $v_0 = 20$. Black line: Fit $a\rho$ to all data points up to $\rho = 0.7$ with $a \simeq 1.1$. (b) Effective speed as defined in Eq. (3.20) and normalized by v_0 [the same color code as in (a)]. Black line: Eq. (3.27) for ABPs at constant propulsion speed ($\chi = 0$) with a as obtained in (a). (c) Speed $\langle \hat{v}_k \rangle_\rho / v_0$ for ABPs at constant affinity [the same color code as in (a)]. Larger λ and density ρ trigger a stronger reduction of the speed. Black symbols: Small \hat{f}_k -approximation of the speed, Eq. (3.24), with $\langle \mathbf{e}_k \cdot \nabla_k U \rangle_\rho$ as determined in (a). Reprinted in adapted form from Ref. [47], with the permission of AIP Publishing.

with $a \simeq 1.1$ (in good agreement with results for ABPs at constant speed [150]) independent of λ . At high densities, $\langle \mathbf{e}_k \cdot \nabla_k U \rangle_\rho / \langle \hat{v}_k \rangle_\rho$ is no longer proportional to the density and eventually saturates at $\simeq 1$, indicating arrest in the dense phase (i.e., $v(\rho) \simeq 0$). Figure 3.5(b) shows the effective speed $v(\rho)$ normalized by the free speed v_0 , which collapses on an almost linear master curve (with a small systematic dependence on λ). In contrast, the average propulsion speed $\langle \hat{v}_k \rangle_\rho$ [Fig. 3.5(c)] is affected by changing λ (it decreases for higher λ due to larger \hat{f}_k) and is reduced at high ρ (due to stronger forces). From Fig. 3.5(c), we see that the small \hat{f}_k -approximation of the propulsion speed [average of Eq. (3.14)]

$$\langle \hat{v}_k \rangle_\rho \approx v_0 - \chi \langle \mathbf{e}_k \cdot \nabla_k U \rangle_\rho \quad (3.24)$$

is accurate for $\lambda = 10^{-3}$, as well as for $\lambda = 10^{-2}$ at low densities. Combining Eqs. (3.23) and (3.24), we can express the propulsion speed and the opposing force as functions of χ and the density as

$$\langle \hat{v}_k \rangle_\rho = v_0 \frac{1}{1 + a\rho\chi}, \quad (3.25)$$

$$\langle \mathbf{e}_k \cdot \nabla_k U \rangle_\rho = v_0 \frac{a}{1 + a\rho\chi} \rho. \quad (3.26)$$

Equation (3.26) implies that the force imbalance coefficient ζ is reduced by the density-dependent factor $(1 + a\rho\chi)^{-1}$ (compared to ABPs at constant speed with

$\chi = 0$) due to the decreased average speed $\langle \hat{v}_k \rangle_\rho$. The approximate effective speed, Eq. (3.21), then reads

$$v_{\text{WCA}}(\rho) = v_0 \left[1 - \frac{a(1 + \chi)}{1 + a\rho\chi} \rho \right]. \quad (3.27)$$

3.3.2 Mean-field theory

We now turn to the dynamical equation (3.18) for the one-body density $\psi_1(\mathbf{r}, \varphi, t)$ for which we use the measured effective speed, Eq. (3.27), as input. Here, we follow a similar route as Ref. [14] for ABPs at constant speed.

Moment expansion

In the first step, we perform an expansion of the one-body density $\psi_1(\mathbf{r}, \varphi, t)$ into orientational moments as described in Sec. 2.4.5. In this way, dynamical equations for the density field $\rho(\mathbf{r}, t) = \int_0^{2\pi} d\varphi \psi_1(\mathbf{r}, \varphi, t)$ and the polarization field $\mathbf{p}(\mathbf{r}, t) = \int_0^{2\pi} d\varphi \mathbf{e} \psi_1(\mathbf{r}, \varphi, t)$ can be derived from Eq. (3.18). Integrating Eq. (3.18) over φ yields

$$\partial_t \int_0^{2\pi} d\varphi \psi_1 = -\nabla \cdot \left[v(\rho) \int_0^{2\pi} d\varphi \mathbf{e} \psi_1 \right] + \nabla^2 \int_0^{2\pi} d\varphi \psi_1 + D_r \underbrace{\int_0^{2\pi} d\varphi \partial_\varphi^2 \psi_1}_{=[\partial_\varphi \psi_1]_0^{2\pi} = 0}. \quad (3.28)$$

The last term vanishes since ψ_1 and its derivatives are 2π -periodic in φ . Identifying ρ and \mathbf{p} , we obtain the continuity equation for the density

$$\partial_t \rho = -\nabla \cdot [v(\rho)\mathbf{p} - \nabla \rho], \quad (3.29)$$

with *passive* (diffusive) current $-\nabla \rho$ and *active* current $v(\rho)\mathbf{p}$ due to self-propulsion. Multiplying Eq. (3.18) by \mathbf{e} and integrating over φ results in

$$\partial_t \int_0^{2\pi} d\varphi \mathbf{e} \psi_1 = -\nabla \cdot \left[v(\rho) \int_0^{2\pi} d\varphi \mathbf{e} \otimes \mathbf{e} \psi_1 \right] + \nabla^2 \int_0^{2\pi} d\varphi \mathbf{e} \psi_1 + D_r \int_0^{2\pi} d\varphi \mathbf{e} \partial_\varphi^2 \psi_1. \quad (3.30)$$

The integral in the rotational diffusion term can be evaluated via partial integration as

$$\int_0^{2\pi} d\varphi \mathbf{e} \partial_\varphi^2 \psi_1 = \underbrace{[\mathbf{e} \partial_\varphi \psi_1]_0^{2\pi}}_{=0} - \int_0^{2\pi} d\varphi \partial_\varphi \mathbf{e} \partial_\varphi \psi_1$$

$$\begin{aligned}
&= -\underbrace{[\partial_\varphi \mathbf{e} \psi_1]_0^{2\pi}}_{=0} + \int_0^{2\pi} d\varphi \underbrace{\partial_\varphi^2 \mathbf{e} \psi_1}_{=-\mathbf{e}} \\
&= -\mathbf{p},
\end{aligned} \tag{3.31}$$

where we have again used the periodicity of ψ_1 and its derivative. The integral in the first term on the right-hand side of Eq. (3.30) yields

$$\int_0^{2\pi} d\varphi \mathbf{e} \otimes \mathbf{e} \psi_1 = \int_0^{2\pi} d\varphi \left(\mathbf{e} \otimes \mathbf{e} - \frac{1}{2} \mathbb{1} \right) \psi_1 + \frac{1}{2} \mathbb{1} \int_0^{2\pi} d\varphi \psi_1 = \mathbf{Q} + \frac{1}{2} \rho \mathbb{1}, \tag{3.32}$$

with nematic tensor $\mathbf{Q}(\mathbf{r}, t) = \int_0^{2\pi} d\varphi \left(\mathbf{e} \otimes \mathbf{e} - \frac{1}{2} \mathbb{1} \right) \psi_1(\mathbf{r}, \varphi, t)$ [Eq. (2.66)]. Equation (3.30) can then be written as

$$\partial_t \mathbf{p} = -\nabla \cdot \left[v(\rho) \left(\mathbf{Q} + \frac{1}{2} \rho \mathbb{1} \right) \right] + \nabla^2 \mathbf{p} - D_{\mathbf{r}} \mathbf{p}, \tag{3.33}$$

which is coupled to \mathbf{Q} for which an analogous dynamical equation exists. In order to close the hierarchy, we follow Ref. [14] and set $\mathbf{Q} = 0$. This leads to

$$\partial_t \mathbf{p} = -\frac{1}{2} \nabla [v(\rho) \rho] + \nabla^2 \mathbf{p} - D_{\mathbf{r}} \mathbf{p}. \tag{3.34}$$

Drawing a formal analogy to hydrodynamics (where \mathbf{p} is the velocity field instead of the polarization), the first term on the right-hand side can be interpreted as the gradient of a “pressure” $\frac{1}{2} v(\rho) \rho$ resulting from the directed motion of particles [146] and the second term is similar to a viscosity term. The third term describes the relaxation of \mathbf{p} due to decorrelation of particle orientations. In the following, we employ the coupled equations (3.29) and (3.34) with the effective speed $v(\rho) \equiv v_{\text{WCA}}(\rho)$ of hard discs [Eq. (3.27)] to describe the system.

Linear stability analysis

The terms $\sim v(\rho) \mathbf{p}$ and $\sim v(\rho) \rho$ in Eqs. (3.29), (3.34) are non-linear (due to the density-dependent speed $v(\rho)$), which renders an analytical treatment difficult. However, following Ref. [14], from a linear stability analysis [154] we can gain insight into the onset of the instability leading to phase separation. Therefore, we consider a small perturbation about the homogeneous state $\rho(\mathbf{r}, t) = \rho_0 = \text{const.}$, $\mathbf{p}(\mathbf{r}, t) = 0$, i.e.,

$$\rho(\mathbf{r}, t) = \rho_0 + \delta\rho(\mathbf{r}, t), \quad \mathbf{p}(\mathbf{r}, t) = \delta\mathbf{p}(\mathbf{r}, t). \tag{3.35}$$

Up to linear order in $\delta\rho$, the effective speed then reads

$$v_{\text{WCA}}(\rho_0 + \delta\rho) \approx v_{\text{WCA}}(\rho_0) + \left. \frac{\partial v_{\text{WCA}}(\rho)}{\partial \rho} \right|_{\rho_0} \delta\rho = v_0 \left[1 - \frac{a(1+\chi)}{1+a\rho_0\chi} \rho_0 - \frac{a(1+\chi)}{(1+a\rho_0\chi)^2} \delta\rho \right] \quad (3.36)$$

and the linearized dynamical equations are

$$\partial_t \delta\rho = -\alpha \nabla \cdot \delta\mathbf{p} + \nabla^2 \delta\rho, \quad (3.37)$$

$$\partial_t \delta\mathbf{p} = -\gamma \nabla \delta\rho + \nabla^2 \delta\mathbf{p} - D_r \delta\mathbf{p}, \quad (3.38)$$

with coefficients

$$\alpha \equiv v_{\text{WCA}}(\rho_0) = v_0 \left[1 - \frac{a(1+\chi)}{1+a\rho_0\chi} \rho_0 \right], \quad (3.39)$$

$$\gamma \equiv \frac{1}{2} \left(v_{\text{WCA}}(\rho_0) + \rho_0 \left. \frac{\partial v_{\text{WCA}}(\rho)}{\partial \rho} \right|_{\rho_0} \right) = \frac{1}{2} v_0 \left[1 - \frac{2a(1+\chi)}{1+a\rho_0\chi} \rho_0 + \frac{a^2(1+\chi)\chi}{(1+a\rho_0\chi)^2} \rho_0^2 \right]. \quad (3.40)$$

Defining the vector $\mathbf{v}(\mathbf{r}, t) = (\delta\rho, \delta p_x, \delta p_y)$ and representing it via its Fourier transform (denoted by the tilde)

$$\mathbf{v}(\mathbf{r}, t) = \int d\mathbf{q} \tilde{\mathbf{v}}(\mathbf{q}, t) e^{i\mathbf{q}\cdot\mathbf{r}}, \quad (3.41)$$

with wave vector \mathbf{q} and $\tilde{\mathbf{v}}(\mathbf{q}, t) = (\delta\tilde{\rho}, \delta\tilde{p}_x, \delta\tilde{p}_y)$, Eqs. (3.37) and (3.38) can be written as

$$\partial_t \tilde{\mathbf{v}}(\mathbf{q}, t) = \mathbf{A}(\mathbf{q}) \cdot \tilde{\mathbf{v}}(\mathbf{q}, t). \quad (3.42)$$

The matrix $\mathbf{A}(\mathbf{q})$ is given by

$$\mathbf{A}(\mathbf{q}) = \begin{pmatrix} -q^2 & -i\alpha q_x & -i\alpha q_y \\ -i\gamma q_x & -q^2 - D_r & 0 \\ -i\gamma q_y & 0 & -q^2 - D_r \end{pmatrix}, \quad (3.43)$$

with $q^2 = q_x^2 + q_y^2$. Equation (3.42) has the general solution

$$\tilde{\mathbf{v}}(\mathbf{q}, t) = \sum_{i=1}^3 c_i(\mathbf{q}) \mathbf{a}_i(\mathbf{q}) e^{\lambda_i(\mathbf{q})t}, \quad (3.44)$$

with $\mathbf{a}_i(\mathbf{q})$ and $\lambda_i(\mathbf{q})$ the eigenvectors and eigenvalues of $\mathbf{A}(\mathbf{q})$, respectively, and coefficients $c_i(\mathbf{q})$. If the real part of one of the λ_i is positive for some range of \mathbf{q} ,

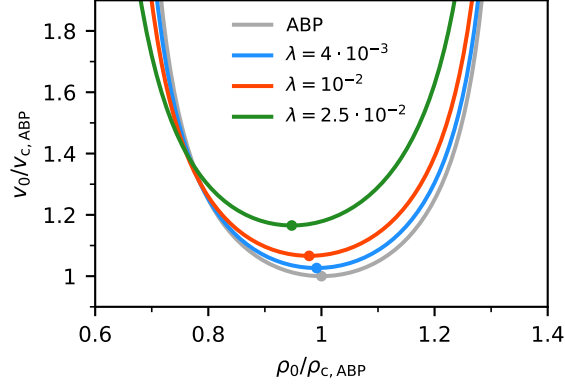


Fig. 3.6. Mean-field spinodals and critical points (circles) for ABPs at constant speed (gray) and ABPs at constant affinity for different λ .

perturbations with such wave vectors will grow exponentially, indicating the onset of an instability. The eigenvalues of $\mathbf{A}(\mathbf{q})$ can be computed as

$$\lambda_0(q) = -D_r - q^2, \quad (3.45)$$

$$\lambda_{\pm}(q) = -\frac{D_r}{2} - q^2 \pm \frac{1}{2}\sqrt{D_r^2 - 4\alpha\gamma q^2}. \quad (3.46)$$

Clearly, the real parts of λ_0 and λ_- are negative for all q , since $D_r > 0$. However, expanding the remaining eigenvalue

$$\lambda_+(q) = -\left(1 + \frac{\alpha\gamma}{D_r}\right)q^2 - \frac{\alpha^2\gamma^2}{D_r^3}q^4 + \mathcal{O}(q^6), \quad (3.47)$$

shows that for $D_r + \alpha\gamma < 0$, perturbations with small q grow, leading to a dynamical instability. For $q \rightarrow \infty$, $\lambda_+ \sim -q^2$ (as a consequence of translational diffusion) leading to damping of short wavelength perturbations and thus to a finite unstable q -range starting at $q = 0$. This instability can be associated with the phase separation observed in the simulations [14]. In case of ABPs at constant speed ($\chi = 0$), the instability condition

$$D_r + \alpha\gamma = 0 \quad (3.48)$$

can be readily solved analytically for the instability line (which corresponds to the spinodal, cf. Sec. 2.3.3) in the $\rho_0 - v_0$ plane [146]

$$\rho_{0,\pm} = \frac{3}{4a} \pm \frac{1}{4a}\sqrt{1 - \frac{16D_r}{v_0^2}}, \quad (3.49)$$

which is plotted in Fig. 3.6. Its minimum with respect to v_0 , i.e., the critical point is located at speed $v_{c,ABP} = 4\sqrt{D_r}$ and density $\rho_{c,ABP} = 3/(4a)$.

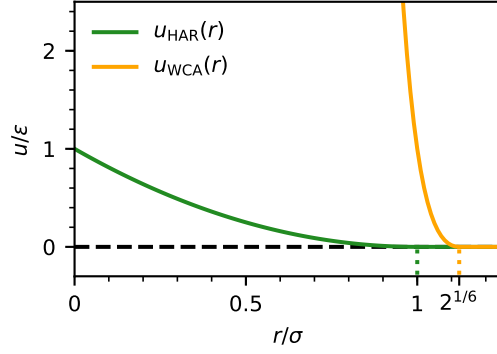


Fig. 3.7. Comparison of the harmonic potential $u_{\text{HAR}}(r)$ [Eq. (3.50)] and the WCA potential $u_{\text{WCA}}(r)$ [Eq. (2.30)].

For $\chi \neq 0$, Eq. (3.48) is a third-order polynomial in ρ_0 whose roots are very lengthy. In Figure 3.6, we therefore plot numerically calculated instability lines for different λ . Compared to ABPs at constant speed, for non-constant propulsion speeds, the critical point moves to slightly lower densities $\rho_c < \rho_{c,\text{ABP}}$ and higher speeds $v_c > v_{c,\text{ABP}}$ with the shift increasing for larger λ . In the simulations, this shift appears to be negligible, since the phase diagram, Fig. 3.3(b), is not visibly affected by changing λ .

3.4 Soft discs

In a second system, we investigate how a softer interaction potential affects the phase behavior. Therefore, we perform Brownian Dynamics simulations using the harmonic potential

$$u_{\text{HAR}}(r) = \begin{cases} \epsilon(r/\sigma - 1)^2 & (r/\sigma < 1) \\ 0 & (r/\sigma \geq 1) \end{cases}, \quad (3.50)$$

which is much softer than the WCA potential employed above [cf. Fig. 3.7], allowing particles to overlap at much smaller energy cost. Simulations are performed analogous to the case of hard discs with the same system of units. As in Ref. [14], we employ $\epsilon = 100$, a reduced rotational diffusion coefficient $D_r = 3 \cdot 10^{-3}$ and a global density $\rho_0 \simeq 0.89$.

3.4.1 Constant speed

For the harmonic potential, in contrast to hard discs, no phase diagram for ABPs at constant propulsion speed is available in literature. Therefore, we first run simulations with constant speed $\hat{v}_k = v_0$ for all particles. At speeds below $v_0 \approx 15$, we observe phase separation into a dense and dilute phase with a stable slab forming for $v_0 \gtrsim 7.5$. For speeds $v_0 \gtrsim 15$, the system reenters the homogeneous disordered state as previously reported in Ref. [14]. The coexisting densities in the phase-separated regime plotted in Fig. 3.8(a), suggest a binodal that closes in an upper critical point in agreement with the observed reentrant behavior. This is quite different from the phase separation of active hard discs, where the two-phase region extends to infinite speeds.

To get further insight, analogous to Sec. 3.3.1, we measure the effective speed $v(\rho)$ [Eq. (3.20)] in the homogeneous region of the phase diagram. The resulting reduced speeds $v(\rho)/v_0$ are plotted in Fig. 3.8(b) as a function of density ρ . In contrast to hard discs, the speeds do not decay linearly with density but curve away with a decreasing magnitude of the slope. From Fig. 3.8(c) we see that for higher densities, the first peak of the radial distribution function $g(r)$ shifts to smaller particle separations r .² At higher densities, a given particle typically interacts with more other particles, allowing for higher total forces on that particle. The increased forces lead to larger overlaps for soft particles, whereas forces of equal magnitude only lead to negligibly small overlaps for hard particles. Due to this increased ability of particles to overlap compared to hard discs, particle collisions oppose self-propulsion less, which is reflected in the deviation from the linear decay of $v(\rho)$. Moreover, for different v_0 the speeds do not collapse on a single master curve with $v(\rho)/v_0$ increasing with v_0 for fixed density. As can be seen from the broadening of $g(r)$ towards smaller separations [see Fig. 3.8(d)], particles can overlap more upon rising propulsion speed v_0 due to the softness of the interaction potential. Again, this leads to a diminishing slowdown of particles, i.e., higher $v(\rho)/v_0$. We capture this behavior with the expression

$$v_{\text{HAR}}(\rho) = v_0[(1 - a)e^{-b\rho} + a], \quad (3.51)$$

which fits the simulation data very well, cf. Fig. 3.8(b). The coefficients a and b depend on v_0 linearly [compare Fig. 3.8(e)] as

$$a \simeq 0.016v_0 - 0.57, \quad b \simeq 0.006v_0 + 0.49. \quad (3.52)$$

²The radial distribution function $g(r)$ can be obtained from the pair-correlation function $g(r, \theta)$ introduced in Sec. 2.4.4 via $g(r) = \frac{1}{2\pi} \int_0^{2\pi} d\theta g(r, \theta)$.

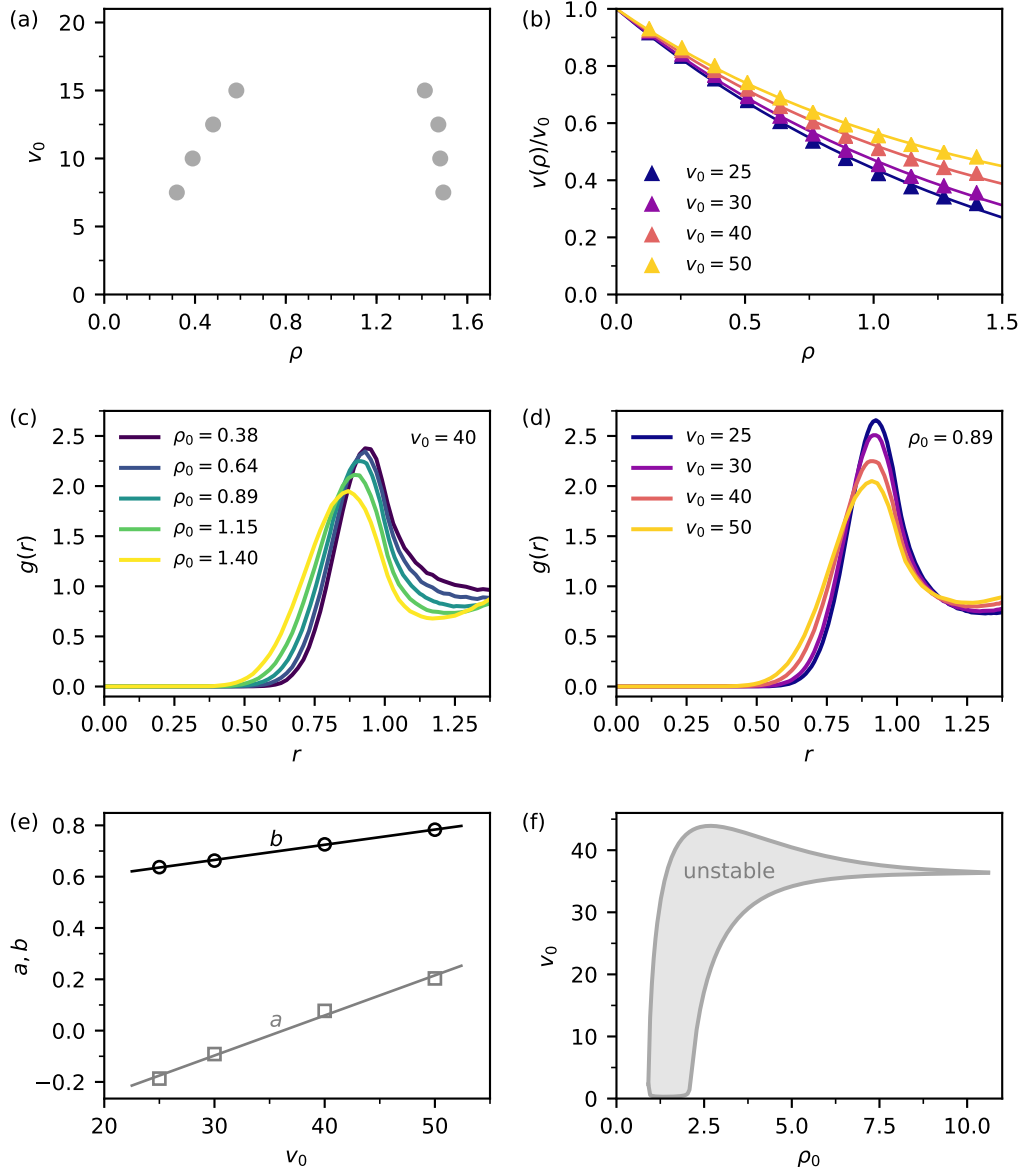


Fig. 3.8. Soft discs with constant propulsion speed. (a) Coexisting densities obtained from simulations at global density $\rho_0 = 0.89$. (b) Effective speed $v(\rho)/v_0$ for different v_0 in the homogeneous regime. The lines are fits of Eq. (3.51). (c),(d) Radial distribution function $g(r)$ at (c) $v_0 = 40$ for different global densities ρ_0 and (d) at global density $\rho_0 = 0.89$ for different propulsion speeds. (e) Values for a and b versus v_0 obtained from the fits in (b). Both can be well fitted with a linear function. The result of the fit is given in Eq. (3.52). (f) Mean-field spinodal enclosing the linearly unstable region. (a),(b),(f) are reprinted in adapted form from Ref. [47], with the permission of AIP Publishing.

For $a > 0$ (i.e., $v_0 > 36$), the effective speed would reach a non-vanishing positive value for $\rho \rightarrow \infty$, avoiding dynamic arrest. For $a < 0$ (i.e., $v_0 < 36$), however, $v_{\text{HAR}}(\rho)$ converges towards a negative value, which is probably an artifact of the lack of simulation data at very high densities.

Despite this shortcoming, we test whether the mean-field theory described in Sec. 3.3.2, modified with our expression for the effective speed $v_{\text{HAR}}(\rho)$ [Eq. (3.51)], can reproduce the reentrant behavior at high v_0 . To this end, we solve Eq. (3.48) for the instability line numerically, which is plotted in Fig. 3.8(f). Indeed, the solution exhibits a maximal speed ($v_0 \approx 44$) above which the homogeneous system is always stable in qualitative agreement with the reentrant behavior observed in the simulations. Also for small speeds ($v_0 \lesssim 0.29$), the system is predicted to be homogeneous. In order to verify the existence of a homogeneous regime at very low propulsion speeds in the simulations, one would have to perform systematic runs at speeds $0 \lesssim v_0 \lesssim 1$. For large densities, the shape of the instability region becomes somewhat implausible exhibiting a pronounced tip. Presumably, this is an artifact of employing expression (3.51) at high densities, since the position of the tip at $v_0 \simeq 36$ corresponds to the value where the high density limit of $v_{\text{HAR}}(\rho)$ changes from positive to negative.

3.4.2 Constant affinity

In the next step, we perform simulations with non-constant propulsion speed \hat{v}_k [Eq. (3.11)] at the same global density $\rho_0 \simeq 0.89$ as above. As for hard discs, we keep the product $\kappa_0\lambda = 10$ fixed and vary v_0 by adjusting $\Delta\mu$.

We now observe a notable impact of the non-constant speed on the coexisting densities which are plotted in Fig. 3.9(a). When increasing λ , the binodal is shifted to larger speeds and the difference between the coexisting densities (at fixed v_0) is enhanced. The propulsion speed $\langle \hat{v}_k \rangle_\rho$ is plotted in Fig. 3.9(b) for different λ in the homogeneous regime at $v_0 = 30$. With rising ρ , $\langle \hat{v}_k \rangle_\rho$ decays steadily from v_0 and does not exhibit the abrupt drop at high densities as observed for the hard discs [Fig. 3.5(c)]. The deviation from v_0 becomes stronger with increasing λ , as in the case of hard discs. However, as we have seen in Fig. 3.8(b), in contrast to hard discs, even for different constant speeds v_0 , the reduced effective speed $v(\rho)/v_0$ does not collapse onto a single master curve but decreases for smaller v_0 . Hence, the enhanced reduction of $\langle \hat{v}_k \rangle_\rho$ causes $v(\rho)/v_0$ to diminish upon increasing λ , cf. Fig. 3.9(c). Consequently, larger λ decreases the tendency of soft discs to avoid dynamic arrest, leading to a shift of the reentrance into the homogeneous state to higher speeds v_0 .

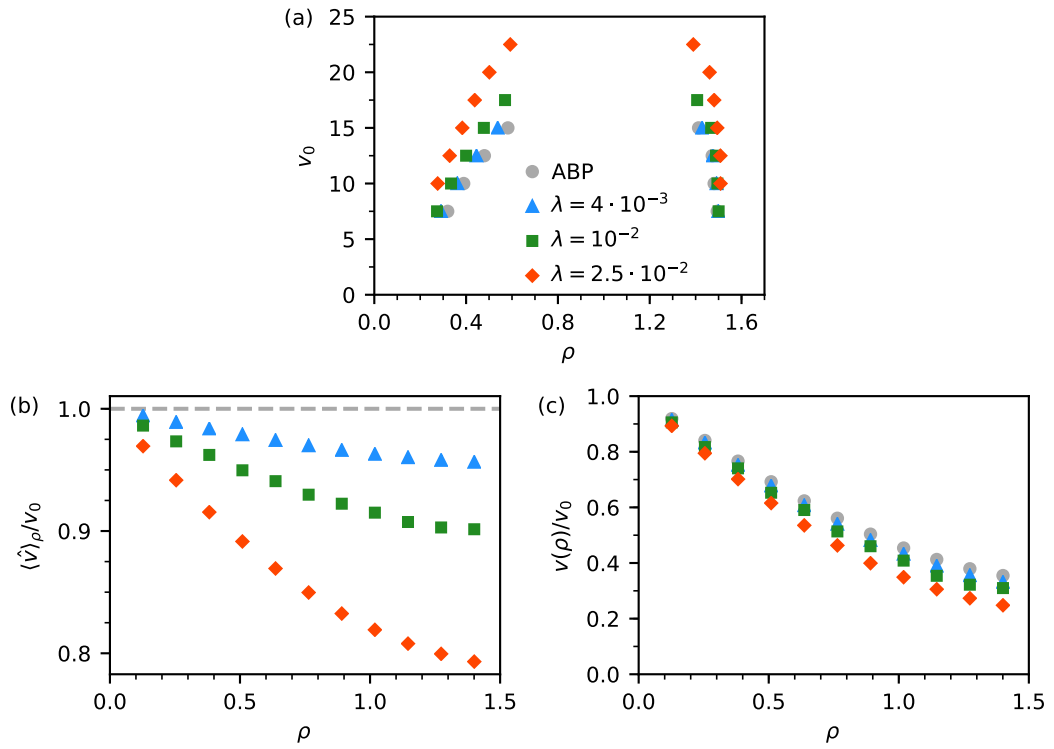


Fig. 3.9. Soft discs at constant affinity (non-constant propulsion speed). (a) Coexisting densities for different values of λ compared to those at constant speed v_0 . Speed $\langle \hat{v}_k \rangle_\rho / v_0$ (b) and effective speed $v(\rho) / v_0$ (c) as defined in Eq. (3.20) measured in the homogeneous regime at $v_0 = 30$ [same color code in (b) and (c) as in (a)]. (a),(b) are reprinted in adapted form from Ref. [47], with the permission of AIP Publishing.

Self-organization of active particles by quorum sensing rules

Many motile microorganisms adapt their behavior in response to chemical signals. For example, sperm cells can detect signaling molecules secreted by the oocyte and swim towards it by following the gradient of chemicals (“chemotaxis”) [42]. Also some bacteria are able to perform chemotaxis, which helps them to swim towards food sources or to flee from poisons [163]. Chemical signaling is also involved in cell-to-cell communication mechanisms, e.g., bacterial *quorum sensing* [98]. In a population of quorum-sensing bacteria, all members secrete signaling molecules (“autoinducers”). The resulting concentration of autoinducers in the surrounding fluid is thus a measure of the number density of bacteria. In response to the sensed concentration (typically when it surpasses a threshold value), bacteria change their behavior through the expression of certain genes. This mechanism enables the synchronized behavior of the entire bacterial population, necessary, e.g., for virulence [178], bioluminescence [93], biofilm formation [112] and motility control [147]. Moreover, there is evidence that quorum sensing plays a role in the regulation of the response of immune cells [5].

Synthetic microswimmers such as self-phoretic Janus particles, in contrast, do not possess such elaborate communication strategies, but solely interact via forces of physical origin, e.g., volume exclusion or hydrodynamic flows. However, recent advances in experimental techniques in the group of Prof. Clemens Bechinger (Fachbereich Physik, Universität Konstanz) allow for the control of speeds of light-activated phoretic swimmers on an individual level. Via a feedback-loop, this enables the implementation of new interaction rules between particles in a well-controlled experimental setup. In this chapter, we describe an interaction rule inspired by the above described bacterial quorum sensing: In response to a (virtual) self-generated concentration field of autoinducers, particles switch between two discrete states of motility (active and passive). Via numerical simulations based on the ABP model, we analyze the novel collective behavior arising from this rule and compare to

experimental results. The majority of the results presented in this chapter have been published in Ref. [9] and a minor part in Ref. [48].

4.1 Quorum-sensing active particles

We consider a collection of N active particles with self-propulsion speeds $v_k = v_0$ moving along trajectories $\mathbf{r}_k(t)$. Each particle is assumed to emit signaling molecules at a certain rate γ that diffusive with diffusion coefficient D_c and decay at rate κ . The concentration field $c(\mathbf{r}, t)$ of signaling molecules is then determined by the diffusion equation

$$\partial_t c(\mathbf{r}, t) = D_c \nabla^2 c(\mathbf{r}, t) - \kappa c(\mathbf{r}, t) + \gamma \sum_{k=1}^N \delta(\mathbf{r} - \mathbf{r}_k(t)). \quad (4.1)$$

As they are much smaller in size than the active particles, the signaling molecules can be assumed to diffusive much faster than the particles move. Thus, assuming a time scale separation, the concentration field c has already reached its steady state ($\partial_t c = 0$) within time intervals in which particles move by relevant length scales. Therefore, at every moment in time, we assume the concentration field to be determined by the steady-state equation

$$0 = D_c \nabla^2 c(\mathbf{r}) - \kappa c(\mathbf{r}) + \gamma \sum_{k=1}^N \delta(\mathbf{r} - \mathbf{r}_k(t)), \quad (4.2)$$

which has the shape of the screened Poisson equation known from electrostatics, with N source terms. In three dimensions, its Green's function (solution for one source of strength 1 at position \mathbf{r}') reads [183]

$$G(\mathbf{r}) = \frac{e^{-|\mathbf{r}-\mathbf{r}'|/\lambda}}{4\pi D_c |\mathbf{r} - \mathbf{r}'|}, \quad (4.3)$$

with decay length $\lambda = \sqrt{D_c/\kappa}$. Consequently, the solution of Eq. (4.2) is given by the superposition

$$c(\mathbf{r}) = \frac{\gamma}{4\pi D_c} \sum_{k=1}^N \frac{e^{-|\mathbf{r}-\mathbf{r}_k|/\lambda}}{|\mathbf{r} - \mathbf{r}_k|}. \quad (4.4)$$

Given a set of particle positions $\{\mathbf{r}_k\}$, the resulting concentration field $c(\mathbf{r})$ can be directly calculated via Eq. (4.4). Since the particle positions change over time, the concentration field is still implicitly time-dependent.

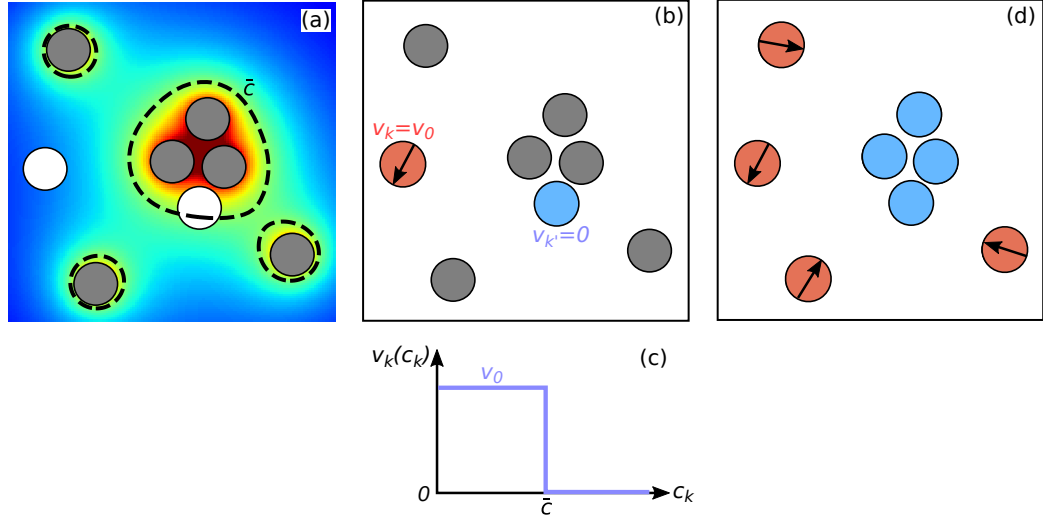


Fig. 4.1. Quorum sensing response. (a) Concentration field $c(\mathbf{r})$ [Eq. (4.4)] produced by the gray particles (blue: low c , red: high c). White circles: Test particles probing c at two different positions. Inside the dashed lines, $c(\mathbf{r})$ surpasses the threshold concentration \bar{c} above which particles turn passive, $v_k = 0$ [(c), Eq. (4.7)]. (b) Accordingly, the particle with $c_k < \bar{c}$ self-propels at $v_k = v_0$ (red), whereas the particle with $c_k > \bar{c}$ does not ($v_k = 0$, blue). (d) Resulting speeds $v_k(c_k)$ for all (gray and white) particles: $v_k = 0$ (blue) or $v_k = v_0$ (red).

Moreover, we assume that particles not only produce signaling molecules, but can also detect the concentration of molecules generated by the other particles, i.e.,

$$c_k(\mathbf{r}_k) = \frac{\gamma}{4\pi D_c} \sum_{l \neq k} \frac{e^{-|\mathbf{r}_k - \mathbf{r}_l|/\lambda}}{|\mathbf{r}_k - \mathbf{r}_l|}. \quad (4.5)$$

Introducing the reference concentration $\bar{c} = \frac{\gamma}{4\pi D_c d}$ (with particle diameter d), it can be written as

$$c_k(\mathbf{r}_k) = \bar{c} \sum_{l \neq k} \frac{e^{-|\mathbf{r}_k - \mathbf{r}_l|/\lambda}}{|\mathbf{r}_k - \mathbf{r}_l|/d}. \quad (4.6)$$

Motivated by specific systems of quorum-sensing bacteria [93, 147], we assume that particles respond to the measured concentration signal by changing their self-propulsion speed (another possibility would be the diffusion coefficient [89, 53]) in a *discontinuous* way: When the concentration c_k a particle measures surpasses a certain threshold value \bar{c} , the particle becomes passive (it stops to self-propel), i.e.,

$$v_k = \begin{cases} v_0, & \text{for } c_k < \bar{c} \\ 0, & \text{for } c_k \geq \bar{c} \end{cases}. \quad (4.7)$$

The entire quorum sensing scheme consisting of concentration production, sensing and motility response is depicted in Fig. 4.1 for a specific particle configuration. From there, it becomes clear that (depending on the threshold \bar{c}) particles typically turn passive in regions of increased particle density due to the higher concentrations they sense there.

4.1.1 Coarse-grained concentration field

The concentration a particle k located at \mathbf{r}_k measures given by Eq. (4.5) depends on the positions $\{\mathbf{r}_l\}$ ($l = 1, \dots, k-1, k+1, \dots, N$) of the remaining $N-1$ particles. However, as we will see later in this chapter and in Chap. 5, it can be useful to know the mean concentration (averaged over the positions of the other particles) a particle at a specific position senses. Therefore, we introduce the (orientation-independent) conditional probability density $\bar{\psi}(\{\mathbf{r}_l\}|\mathbf{r}_k, t)$ to find $N-1$ particles at positions $\{\mathbf{r}_l\}$ given particle k to be located at \mathbf{r}_k at time t . The mean of c_k can then be calculated as

$$\begin{aligned} \langle c_k \rangle(\mathbf{r}_k, t) &\equiv \int d\mathbf{r}_1 \dots d\mathbf{r}_{k-1} d\mathbf{r}_{k+1} \dots d\mathbf{r}_N c_k(\mathbf{r}_k) \bar{\psi}(\{\mathbf{r}_l\}|\mathbf{r}_k, t) \\ &= \frac{\gamma}{4\pi D_c} \int d\mathbf{r}_1 \dots d\mathbf{r}_{k-1} d\mathbf{r}_{k+1} \dots d\mathbf{r}_N \sum_{l \neq k} \frac{e^{-|\mathbf{r}_k - \mathbf{r}_l|/\lambda}}{|\mathbf{r}_k - \mathbf{r}_l|} \bar{\psi}(\{\mathbf{r}_l\}|\mathbf{r}_k, t). \end{aligned} \quad (4.8)$$

As particles are indistinguishable, this is a sum of $N-1$ identical integrals. Analogous to Eq. (2.45), we introduce the conditional one-body density

$$\bar{\psi}_1(\mathbf{r}'|\mathbf{r}_k, t) = (N-1) \int d\mathbf{r}_1 \dots d\mathbf{r}_{l-1} d\mathbf{r}_{l+1} \dots d\mathbf{r}_{k-1} d\mathbf{r}_{k+1} \dots d\mathbf{r}_N \bar{\psi}(\{\mathbf{r}_l\}|\mathbf{r}_k, t) \quad (4.9)$$

and rename $\mathbf{r}_k \rightarrow \mathbf{r}$ (and $c_k \rightarrow c$) and $\mathbf{r}' \rightarrow \mathbf{r}'$, which leads to

$$\langle c \rangle(\mathbf{r}, t) = \frac{\gamma}{4\pi D_c} \int d\mathbf{r}' \bar{\psi}_1(\mathbf{r}'|\mathbf{r}, t) \frac{e^{-|\mathbf{r} - \mathbf{r}'|/\lambda}}{|\mathbf{r} - \mathbf{r}'|}. \quad (4.10)$$

Decomposing the conditional density into the number density at \mathbf{r}' and the pair correlation function [analogous to Eq. (2.52)]

$$\bar{\psi}_1(\mathbf{r}'|\mathbf{r}, t) = \rho(\mathbf{r}', t) g(\mathbf{r}, \mathbf{r}', t), \quad (4.11)$$

we obtain

$$\langle c \rangle(\mathbf{r}, t) = \frac{\gamma}{4\pi D_c} \int d\mathbf{r}' \rho(\mathbf{r}', t) g(\mathbf{r}, \mathbf{r}', t) \frac{e^{-|\mathbf{r} - \mathbf{r}'|/\lambda}}{|\mathbf{r} - \mathbf{r}'|}. \quad (4.12)$$

Assuming that particles interact via volume exclusion and have a diameter d , in the steady state, we approximate

$$g(\mathbf{r}, \mathbf{r}', t) \approx \Theta(|\mathbf{r} - \mathbf{r}'| - d), \quad (4.13)$$

with $\Theta(x)$ the Heaviside step function. Performing this approximation, we have assumed that particles cannot overlap and that for $r > d$ no correlations between particle positions exist. The mean concentration a particle located at position \mathbf{r} measures in the steady state $[\rho(\mathbf{r}', t) \rightarrow \rho(\mathbf{r}')] is then given by the convolution$

$$\langle c \rangle(\mathbf{r}) = \frac{\gamma}{4\pi D_c} \int d\mathbf{r}' \rho(\mathbf{r}') \Theta(|\mathbf{r} - \mathbf{r}'| - d) \frac{e^{-|\mathbf{r} - \mathbf{r}'|/\lambda}}{|\mathbf{r} - \mathbf{r}'|}. \quad (4.14)$$

Due to the appearance of the Heaviside function, the integral can be splitted into

$$\langle c \rangle(\mathbf{r}) = \underbrace{\frac{\gamma}{4\pi D_c} \int d\mathbf{r}' \rho(\mathbf{r}') \frac{e^{-|\mathbf{r} - \mathbf{r}'|/\lambda}}{|\mathbf{r} - \mathbf{r}'|}}_{c_{\text{id}}(\mathbf{r})} - \underbrace{\frac{\gamma}{4\pi D_c} \int_{|\mathbf{r} - \mathbf{r}'| \leq d} d\mathbf{r}' \rho(\mathbf{r}') \frac{e^{-|\mathbf{r} - \mathbf{r}'|/\lambda}}{|\mathbf{r} - \mathbf{r}'|}}_{c_{\text{corr}}(\mathbf{r})}. \quad (4.15)$$

The first term $c_{\text{id}}(\mathbf{r})$ is exact for point particles, when neglecting correlations arising from the concentration-dependent speed $v_k(c_k)$. The second term $c_{\text{corr}}(\mathbf{r})$ is the correction due to the (approximated) pair-correlations arising from the excluded volume, which has to be subtracted. Assuming density variations to be negligible on length scales of order d , in the second integral we can approximate $\rho(\mathbf{r}') \approx \rho(\mathbf{r})$. Thus

$$\begin{aligned} c_{\text{corr}}(\mathbf{r}) &= \frac{\gamma}{4\pi D_c} \rho(\mathbf{r}) \int_{|\mathbf{r} - \mathbf{r}'| \leq d} d\mathbf{r}' \frac{e^{-|\mathbf{r} - \mathbf{r}'|/\lambda}}{|\mathbf{r} - \mathbf{r}'|} \\ &= \frac{\gamma}{4\pi D_c} \rho(\mathbf{r}) \int_0^{2\pi} d\theta \int_0^d dr' e^{-r'/\lambda} \\ &= \frac{\gamma\lambda}{2D_c} \rho(\mathbf{r}) (1 - e^{-d/\lambda}), \end{aligned} \quad (4.16)$$

with $r' = |\mathbf{r} - \mathbf{r}'|$. In case of a homogeneous system with $\rho(\mathbf{r}) = \rho_0 = \text{const.}$, the uniform contributions are

$$c_{0,\text{id}} \equiv \frac{\gamma\lambda}{2D_c} \rho_0, \quad (4.17)$$

$$c_{0,\text{corr}} \equiv \frac{\gamma\lambda}{2D_c} \rho_0 (1 - e^{-d/\lambda}), \quad (4.18)$$

implying that the uniform mean concentration is

$$c_0 = c_{0,\text{id}} - c_{0,\text{corr}} = \frac{\gamma\lambda}{2D_c} \rho_0 e^{-d/\lambda}. \quad (4.19)$$

4.1.2 Experimental realization

The above described quorum sensing response can be implemented experimentally for active particles driven by self-diffusiophoresis due to critical demixing of a water-lutidine mixture (Sec. 2.2). The experiment described below was designed, performed and analyzed by Tobias Bäuerle in the group of Prof. Clemens Bechinger at Universität Konstanz, Fachbereich Physik.

The particles are silica spheres with diameter $d = 4.4 \mu\text{m}$, half-coated with a 30 nm carbon film, suspended in a water-lutidine mixture at $T = 298 \text{ K}$ (several degrees below its lower critical temperature $T_c = 307 \text{ K}$). The entire suspension is contained in a thin sample cell with height $200 \mu\text{m}$, where particles form a two-dimensional system due to gravitational forces. When illuminated with green laser light at intensities above $I = 0.1 \text{ W mm}^{-2}$, the solvent around a particle heats above T_c due to heating of the carbon cap and locally demixes. This triggers particle propulsion opposite to the cap, with the propulsion speed linearly increasing with I (see Sec. 2.2 for a more detailed explanation of the underlying phoretic mechanism). Additionally, particles undergo translational and rotational Brownian motion with diffusion coefficients $D_{0,\text{exp}} = (0.0208 \pm 0.0012) \mu\text{m}^2\text{s}^{-1}$ and $D_{r,\text{exp}} = (112.6 \pm 26.1)^{-1} \text{ s}^{-1}$, respectively.¹

In preceding experiments [161, 27, 26], the sample was illuminated homogeneously, causing all particles to propel with the same speed. Here, in contrast, the propulsion speeds of the particles can be controlled independent of each other via a feedback-loop, which allows to implement the quorum sensing response: The particle positions $\{\mathbf{r}_k\}$ are determined via a video camera and a real-time image detection algorithm from which (virtual) sensed concentrations $\{c_k\}$ are calculated on a computer using Eq. (4.5). Via Eq. (4.7), the concentrations determine which particles should self-propel ($c_k < \bar{c}$) and which should not ($c_k > \bar{c}$). A laser beam with beam waist $5 \mu\text{m}$ is then selectively directed to the particles with $c_k < \bar{c}$ via an acousto-optical deflector. Each of these particle is repeatedly illuminated for a period of $8 \mu\text{s}$ every 4 ms which is fast enough to induce stable self-propulsion, as the remixing timescale of the binary mixture is of the order of 100 ms [61]. The laser intensity on a particle is set to $I = 0.2 \text{ W mm}^{-2}$ which results in a propulsion velocity $v_{0,\text{exp}} = 0.2 \mu\text{m s}^{-1}$. The remaining particles are not illuminated and undergo only Brownian motion. This cycle is repeated every 500 ms , leading to dynamical updates of the motility

¹The measured diffusion coefficients are smaller than the Stokes-Einstein values $D_{r,\text{theo}} \approx (126 \text{ s})^{-1}$ [Eq. (2.12)] and $D_{0,\text{theo}} \approx 0.051 \mu\text{m}^2\text{s}^{-1}$ [Eq. (2.8)] (using the viscosity $\eta \approx 0.002 \text{ Pa s}$ of water-lutidine at $T \lesssim T_c$ [33]). This arises from enhanced viscous friction close to the confining walls of the sample cell (compared to a bulk fluid for which the Stokes-Einstein relation holds) [22] and has also been observed in previous studies [61].

states of particles based on their calculated concentrations c_k . Typical positional changes are below 5% of the particle diameter between the updates.

To ensure a constant global particle density ρ_0 during experiments, reflective boundary conditions at the edge of a circular confinement of radius $R = 65 \mu\text{m}$ are imposed: When a particle is leaving the confinement, the illuminating laser beam is shifted relative to the particle's center by $\approx 2.6 \mu\text{m}$ which results in an intensity gradient over the particle's surface. This gradient induces a torque which reorients the particle [92, 61]. For leaving particles, the torque is applied until their swimming direction points towards the confinement's center, which guides them back to the confinement. Confining particles in this way, no accumulation of particles at the boundary occurs, as it would be the case for a hard wall [45, 137, 29]. On average the confinement contains $N = 122$ particles, corresponding to a density $\rho_0 = N/(\pi R^2) = 0.0092 \mu\text{m}^{-2}$. For the calculation of the concentrations c_k particles which have left the confinement by less than $10 \mu\text{m}$ are also taken into account in order to reduce variations due to particles leaving and reentering. Within the confinement plus the additional $10 \mu\text{m}$ rim, the average particle number is $N = 132$. To obtain steady-state conditions, the system is allowed to evolve in time for at least 30 min before measurements are performed.

4.1.3 Simulation scheme

To describe the dynamics of the particles, we employ the ABP model with repulsive interactions as introduced in Sec. 2.3.2 (neglecting hydrodynamic and phoretic interactions). The equation of motion for the particle positions read [compare Eq. (2.28)]

$$\dot{\mathbf{r}}_k = v_k \mathbf{e}_k - \mu_0 \nabla_k \sum_{l \neq k} u_{\text{WCA}}(|\mathbf{r}_l - \mathbf{r}_k|) + \boldsymbol{\xi}_k \quad (4.20)$$

and the particle orientations φ_k undergo free rotational diffusion, Eq. (2.29). The concentrations c_k are calculated using Eq. (4.5) and the particle speeds $v_k(c_k)$ via Eq. (4.7) with $v_0 = 0.2 \mu\text{m s}^{-1}$. Particles interact with the WCA potential $u_{\text{WCA}}(r)$, Eq. (2.30), with energy scale $\epsilon = 100 k_{\text{B}} T$ and length scale $\sigma = 3.98 \mu\text{m}$. Thus, the effective (Barker-Henderson) particle diameter $d_{\text{BH}} = 1.10688\sigma = 4.4 \mu\text{m}$ [Eq. (2.31)] equals the diameter d of the particles employed in the experiment. Also the translational and rotational diffusion coefficients are matched with the experimental values, i.e., $D_0 = 0.02 \mu\text{m}^2 \text{s}^{-1}$ and $D_r = (1/120) \text{s}^{-1}$. Simulations are performed with a self-written C++ code that integrates the equations of motion via the algorithm

introduced in Sec. 2.4.1 with time step $\delta t = 40$ ms. The concentrations c_k and speeds v_k are updated at every time step and the particle positions and orientations are initialized randomly inside the simulation box.

As in the experiment, particles are confined to a circular region of radius $R = (65 + 10) \mu\text{m}$ (which includes the additional $10 \mu\text{m}$ in which particles contribute to the concentrations in the experiment). Contrary to the experimental implementation, where a torque is applied to particles reaching the boundary, in the simulations, their orientation vectors are instantaneously reoriented towards the center of the confinement. The particle number is set to $N = 132$ (equaling the average number of particles in the $(65 + 10) \mu\text{m}$ zone in the experiment), which implies a density $\rho_0 = 0.0075 \mu\text{m}^{-2}$. Note that a similar geometry (with the circular boundary implemented by a hard wall instead) has been studied previously in Ref. [120] for run-and-tumble particles without translational diffusion. By performing additional simulations in a square box (with edge length L) with periodic boundary conditions, we investigate the same system without confinement. There, we simulate $N = 800$ particles at the same density ρ_0 with $L = 74.1d = 326 \mu\text{m}$.

4.2 Simulations with periodic boundary conditions

We first present results for simulations with periodic boundaries (with parameters as described above) at decay length $\lambda = 10d$ of the concentration signals. Depending on the chosen concentration threshold \bar{c} , we observe five qualitatively different steady states, see Fig. 4.2. For $\bar{c} \lesssim 5.5\bar{c}$, all particles are passive and the system is homogeneous [Fig. 4.2(a)]. For higher thresholds, the system separates into two distinct phases, a dilute phase of active particles with $c_k < \bar{c}$ (“active gas”) and a dense phase of passive particles with $c_k > \bar{c}$ (“passive cluster”) [Figs. 4.2(b-d)]. On increasing \bar{c} , the phase regions change in shape from a small active gas bubble inside the passive cluster [Fig. 4.2(b)] to two slabs of similar dimensions [Fig. 4.2(c)] and eventually to a passive (almost circular) cluster inside the active gas [Fig. 4.2(d)]. At even higher thresholds $\bar{c} \gtrsim 14.5\bar{c}$, the entire system is a homogeneous active gas [Fig. 4.2(e)]. The observed shapes of the phases (bubble, slab and droplet) are similar to those observed for the vapor-liquid transition in finite simulation boxes [95, 58, 128] and have also been reported for MIPS of ABPs at constant propulsion speed [15].

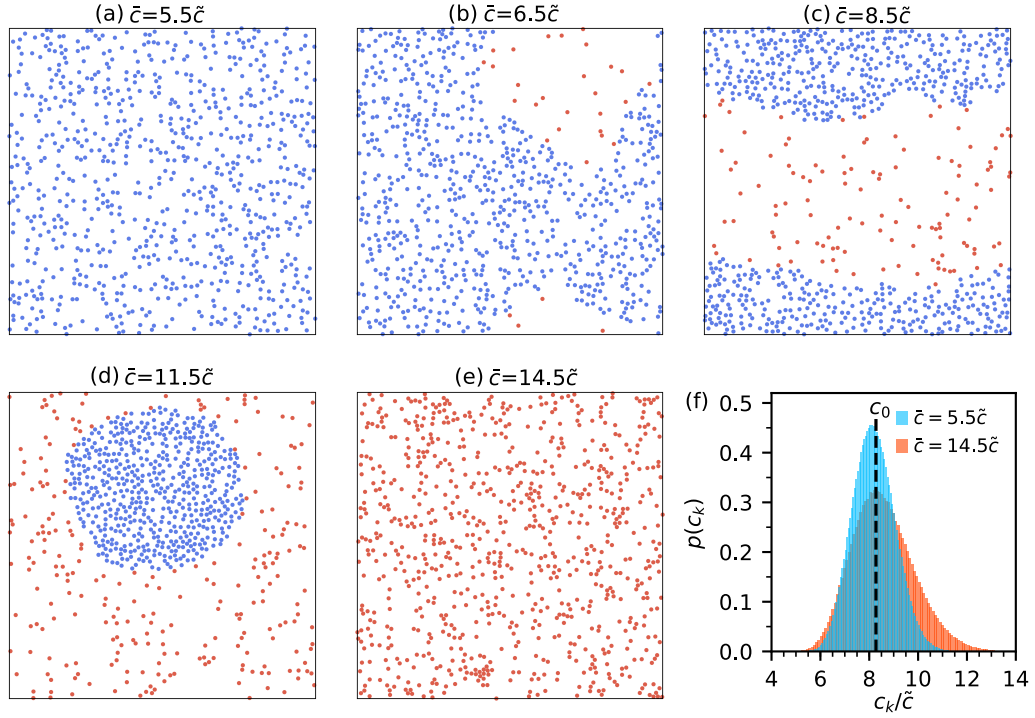


Fig. 4.2. (a-e) Steady-state snapshots of finite-size transitions in a system with periodic boundary conditions for concentration thresholds $\bar{c} = [5.5, 6.5, 8.5, 11.5, 14.5]\tilde{c}$ at decay length $\lambda = 10d$. Blue particles are passive ($v_k = 0$) and red particles are active ($v_k = v_0$). (a) Homogeneous passive system, (b) active bubble, (c) active and passive slabs, (d) passive droplet, (e) homogeneous active system. (f) Sampled distributions of measured concentrations $p(c_k)$ for $\bar{c} = 5.5\tilde{c}$ and $14.5\tilde{c}$. Dashed line: Prediction c_0 of the mean sensed concentration via Eq. (4.19).

The average sensed concentration is $\langle c \rangle / \tilde{c} = 8.18$ in the homogeneous passive system and $\langle c \rangle / \tilde{c} = 8.57$ in the homogeneous active system respectively, which is very close to the prediction $c_0 / \tilde{c} = 2\pi\lambda d\rho_0 e^{-d/\lambda} = 8.28$ from Eq. (4.19). However, both in the passive and in the active case, the sampled distribution of c_k is relatively broad, cf. Fig. 4.2(f). For the passive system, it is symmetric, whereas for the active case it is stretched towards higher c_k as activity triggers the formation of small (unstable) clusters due to self-trapping. The distribution decays to zero at $c_k \approx 5.5\tilde{c}$ for the passive system, which is close to the threshold at which an active phase starts to form. In case of the active system, the distribution reaches ≈ 0 at $c_k \approx 13\tilde{c}$. However, fluctuations to higher c_k can still occur (at a very low rate), which is confirmed by the fact that the formation of passive clusters was observed up to $\bar{c} \approx 14\tilde{c}$ (after a relatively long waiting time).

In contrast to MIPS of ABPs (Sec. 2.3.3, Chap. 3), here phase separation does not arise from collisions which slow down particles but from the motility switches (active \leftrightarrow passive) in response to the concentration signal c . Particles typically

sense higher concentrations and thus turn passive (when $c_k > \bar{c}$) in regions of higher particle density ρ . This motility reduction triggers the aggregation of passive particles into dense domains and thus the separation into a passive cluster and an active gas. As passive particles still undergo Brownian motion, particles at the interface of the cluster can turn active and enter the gas, when diffusing away from the cluster far enough where c_k becomes smaller than \bar{c} (or due to a concentration fluctuation). At the same time, active particles become part of the passive cluster when swimming sufficiently close to where $c_k > \bar{c}$. In the steady state, the average inward and outward currents through the interface between the phases compensate. A sketch visualizing the described processes leading to phase separation is shown in Fig. 4.3(a).

For the system where a circular passive cluster has formed inside the active gas [$\bar{c} = 11.5\bar{c}$, Fig. 4.2(d)], in Fig. 4.3(b,c) we provide radial steady-state profiles of the density $\rho(r)$, the average propulsion speed $\langle v \rangle(r)$ and the average sensed concentration $\langle c \rangle(r)$ (with r the distance to the center of mass of all particles). Both in the cluster ($\langle v \rangle = 0$) and in the gas ($\langle v \rangle = v_0$) the density is constant, with the cluster density being significantly higher than ρ_0 and the gas density. Inbetween, $\rho(r)$ exhibits an interface of finite width, in which $\langle v \rangle(r)$ continuously changes from 0 to v_0 (here particles switch between passive and active). As expected $\langle c \rangle$ is larger than \bar{c} in the passive and smaller than \bar{c} in the active region. The position where $\langle c \rangle = \bar{c}$ lies within the interface of the density profile.

Remarkably, the propulsion speed and density used here (corresponding to packing fraction $\phi_0 = \rho_0 \pi d^2 / 4 = 0.114$ and Péclet number $Pe = 3v_0 / (dD_r) = 16.4$) are much smaller as required for MIPS of ABPs with repulsive interactions [compare the phase diagram of ABPs in Fig. 4.4(a) which was already shown in Fig. 2.5(b)]. Also, the passive clusters observed here are considerably less dense than the closely packed aggregates observed in the MIPS region [compare Fig. 4.2 to Fig. 4.4(b)]. Applying the quorum-sensing rule in the MIPS regime can create a highly crystalline passive core inside the MIPS clusters, cf. Figs. 4.4(c,d).

Until now, we have qualitatively analyzed the steady states arising from the quorum sensing response for different concentration thresholds \bar{c} . In the next section, for the circularly confined system, we will investigate the observed phase separation in a more quantitative way and compare to experimental results.

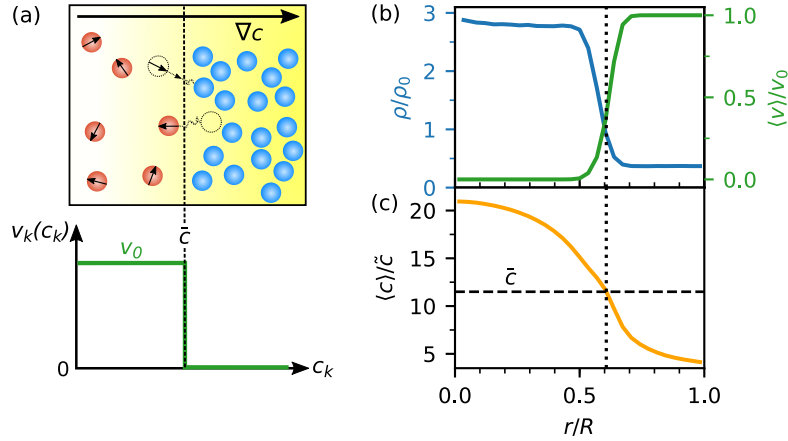


Fig. 4.3. (a) Sketch of a phase-separated system of quorum-sensing active particles. The concentration signal c_k (yellow) increases from left to right and is equal to \bar{c} at the dashed line. Left: active gas with $v_k = v_0$ and $c_k < \bar{c}$. Right: passive cluster with $v_k = 0$ and $c_k > \bar{c}$. Particles are exchanged between the phases via motility switches at the interface. Reprinted in slightly adapted form with permission from Ref. [48]. Copyright (2020) by the American Physical Society. (b,c) Radial profiles (with respect to the system's center of mass) for a passive droplet inside an active gas at $\bar{c} = 11.5\bar{c}$. (b) Normalized density $\rho(r)/\rho_0$ (blue) and mean velocity $\langle v \rangle(r)/v_0$ (green). (c) Mean sensed concentration $\langle c \rangle(r)/\bar{c}$. Dashed line: threshold concentration \bar{c} . Dotted line: position at which $\langle c \rangle = \bar{c}$.

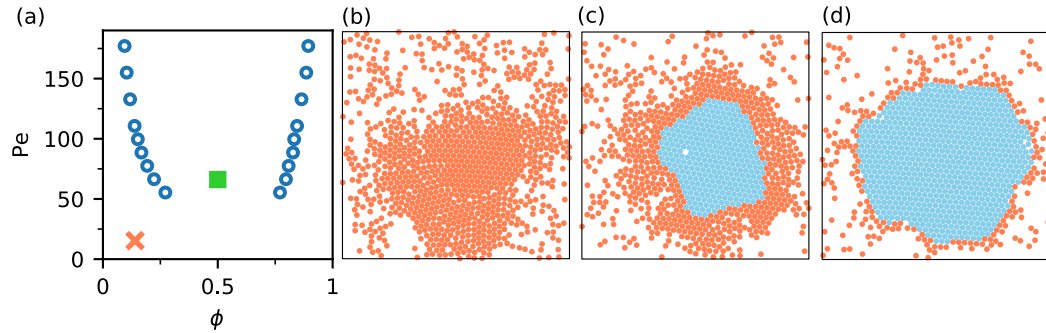


Fig. 4.4. Quorum sensing and motility-induced phase separation. (a) Circles: Numerically determined coexisting densities for ABPs with repulsive interactions (data taken from Ref. [135]) with packing fraction ϕ and Péclet number $Pe = 3v_0/(dD_r)$. Red cross: conditions studied throughout this chapter, where no clustering occurs for constant propulsion-speed. (b,c,d) Simulation snapshots of a system of $N = 1000$ particles with periodic boundary conditions. Simulations are performed within the coexistence region at propulsion speed $4v_0 = 0.8\mu\text{m s}^{-1}$ and density $4.4\rho_0$ [green square in (a)]. (b) Plain ABPs with all particles active (red). (c,d) With quorum sensing using $\lambda = 2.5d$ and (c) $\bar{c} = 13.5\bar{c}$, (d) $\bar{c} = 10\bar{c}$. An inner core of crystalline closely packed passive particles (blue) emerges, which grows as the threshold is decreased. At the same time, the dense halo of active particles shrinks. Reprinted in adapted form with permission from the Supplementary Material of Ref. [9] licensed under the Creative Commons license CC BY 4.0.

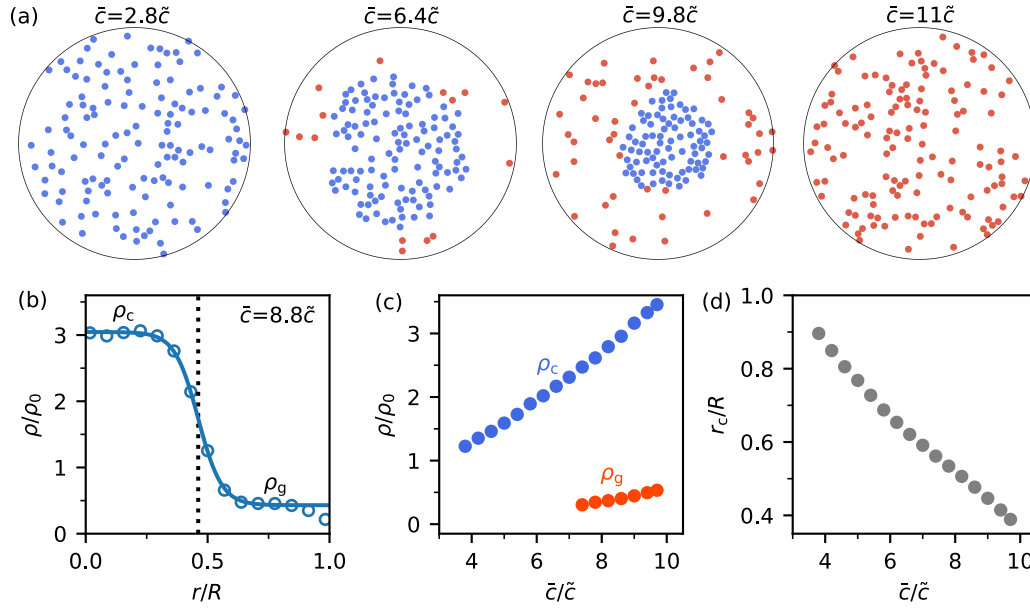


Fig. 4.5. Quorum-sensing active particles under circular confinement of radius R . (a) Steady-state snapshots at decay length $\lambda = 10d$ and concentration thresholds $\bar{c} = [2.8, 6.4, 9.8, 11]\bar{c}$. Blue: passive particles ($v_k = 0$), red: active particles ($v_k = v_0$). (b) The measured normalized radial density profile $\rho(r)/\rho_0$ (symbols, at $\bar{c} = 8.8\bar{c}$) is well fitted by expression (4.21) (line), from which the cluster density ρ_c and the gas density ρ_g can be extracted. The dotted line indicates the interface position r_c . (c) Obtained ρ_c and ρ_g versus threshold \bar{c} . (d) Cluster size r_c as a function of \bar{c} .

4.3 Circularly confined system

Similar to the system with periodic boundary conditions, in the simulations with circular confinement (as described in Sec. 4.1.3), we observe an entirely passive system for low thresholds \bar{c} and a completely active system for high \bar{c} , see Fig. 4.5(a). For intermediate thresholds, again a passive and an active domain form. In contrast to the multitude of finite-size transitions seen in Sec. 4.2, we only observe a passive circular cluster surrounded by an active gas. The cluster typically forms around the center of the confinement (and fluctuates around it), as due to the circular geometry, even for a homogeneous system, the average measured concentration $\langle c \rangle$ rises towards the center.

For the phase-separated system, the radial steady-state density profile $\rho(r)$ (with r being the distance from the particle's center of mass) [Fig. 4.5(b)] has a similar shape as that of circular clusters under periodic boundary conditions, Fig. 4.3(b). It exhibits two plateaus (corresponding to the passive and active phases) separated by a broad interface. Close to the confinement's edge ($r \rightarrow R$), the density decreases from the outer plateau value, as particles are reoriented towards the center of

the confinement at the boundary and thus preferentially escape from this region. Apart from this boundary region, the density profile can be well fitted by [compare Eq. (3.22)]

$$\rho(r) = \frac{\rho_c + \rho_g}{2} + \frac{\rho_c - \rho_g}{2} \tanh\left(\frac{r_c - r}{2\omega}\right), \quad (4.21)$$

with the cluster density ρ_c and the gas density ρ_g . The center of the interface is located at r_c , which is a measure of the cluster size. The interfacial width is given by ω . Due to the finite width of the interface, only cluster sizes $r_c \lesssim 0.9R$ can be reliably extracted. At the corresponding threshold values, clusters have typically reached a density $\rho_c \approx 1.2\rho_0$. On increasing \bar{c} , the passive clusters become smaller and denser, cf. Fig. 4.5(c,d), as higher particle densities lead to higher concentrations c_k necessary to overcome the threshold. For a decay length $\lambda = 10d$, stable clusters exist up to $\bar{c} \approx 9.8\tilde{c}$ where $\rho_c \approx 3.5\rho_0$ and $r_c \approx 0.4R$. Also, the gas becomes denser with rising \bar{c} , but only takes a plateau value ρ_g for $r_c \lesssim 0.6R$ due to boundary effects for larger r_c .

In the experimental system, formation of a passive cluster surrounded by an active gas can be observed as well, see Fig. 4.6(a). Figure 4.6(b) shows that, as in the simulations, clusters become denser and smaller with rising threshold \bar{c} and that at very high \bar{c} the system is homogeneous. The experimental radial steady-state density profiles $\rho(r)$ agree very well with those obtained from the simulations, cf. Fig. 4.6(c), although the time interval Δt_u between updates of the motility states is 12.5 times longer in the experiment ($\Delta t_{u,\text{exp}} = 500$ ms, $\Delta t_{u,\text{sim}} = 40$ ms). Simulations with shorter update intervals down to $10^{-2}\Delta t_{u,\text{exp}}$ show no change in the density profiles $\rho(r)$, see Fig. A.1.

In order to gain further insight, we perform additional simulations in which we systematically vary the decay length λ from $2.5d$ up to $20d$. The results are summarized in the phase diagram Fig. 4.7(a). In agreement with Fig. 4.5, for all λ , cluster formation only occurs within a well-defined range of thresholds \bar{c} , outside which the entire system is homogeneous and passive (blue region) or active (red region). Moreover, there are two transition regions at the boundaries of the two-phase region, both indicated in white. At the transition to the homogeneous active region, within a finite range of thresholds, unstable clusters exist that spontaneously dissolve and re-form, see also Fig. 4.8(b). Within the area between the phase-separated and the homogeneous passive region, a small amount of active particles exists close to the confinement's edge, but no passive cluster with a defined interface at $r_c \lesssim 0.9R$ forms. With increasing decay length λ , particles sense higher concentrations c_k , as they receive concentration signals from more particles. Consequently, both the upper and lower limit for the concentration threshold \bar{c} between which the system phase

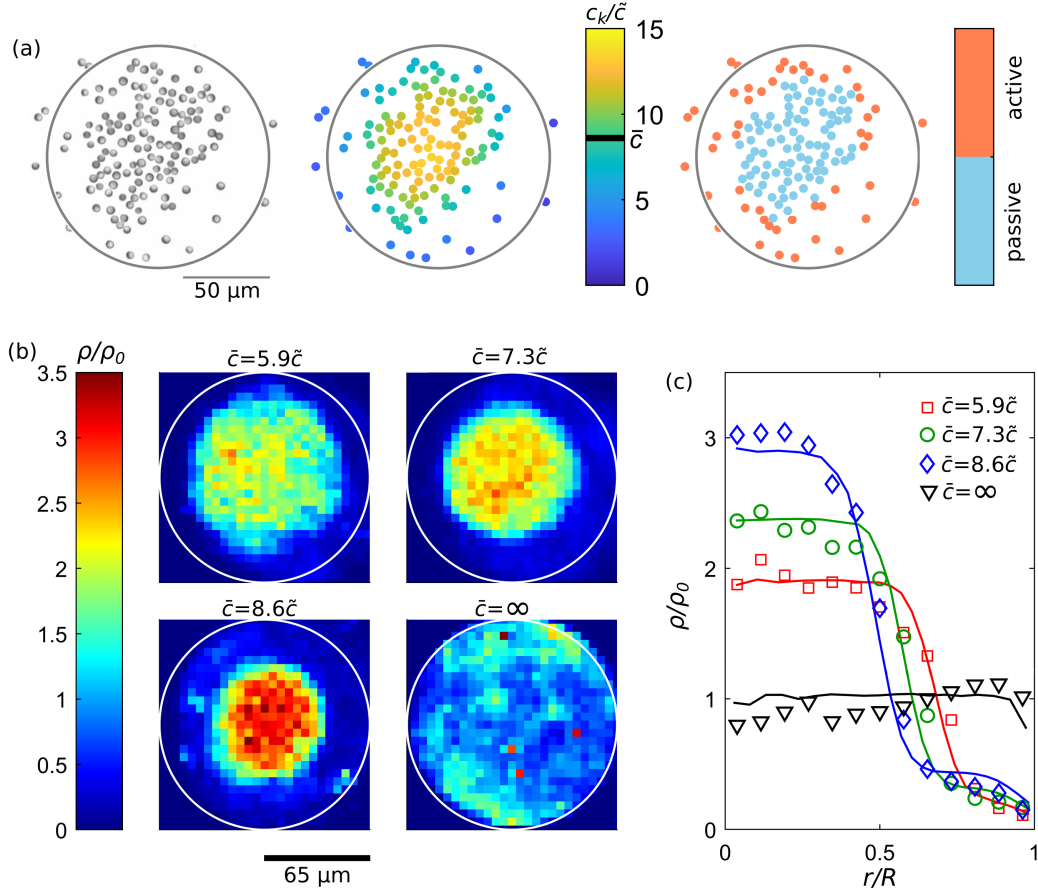


Fig. 4.6. Experimental results at decay length $\lambda = 10d$. (a) Left: Snapshot of the experimental system at concentration threshold $\bar{c} = 8.6\bar{c}$. The black circle indicates the confinement's boundary. Center: Concentrations c_k attributed to each particle according to Eq. (4.6). Right: Resulting distribution of active (red) and passive (blue) particles. (b) Normalized steady-state particle density maps ρ/ρ_0 for concentration thresholds $\bar{c} = [5.9, 7.3, 8.6, \infty]\bar{c}$. (c) Symbols: Corresponding radial density profiles $\rho(r)/\rho_0$. Lines: profiles obtained from simulations at the same threshold values. Reprinted in adapted form with permission from Ref. [9] licensed under the Creative Commons license CC BY 4.0.

separates, rise with λ . The maximal cluster density $\rho_{c,\max} \approx 3.45\rho_0$ is independent of λ [see also Fig. 4.9(c)].

The upper boundary of the homogeneous passive region can be calculated based on the mean concentration field $\langle c \rangle(\mathbf{r})$, Eq. (4.15). For a system at homogeneous density ρ_0 within a circle of radius R , the concentration field is radially symmetric, $\langle c \rangle(\mathbf{r}) = c_0(r)$, and decreases from the circle's center ($r = 0$) toward its edge. It can be calculated via

$$c_0(r) = c_{0,\text{id}}(r) - c_{0,\text{corr}}, \quad (4.22)$$

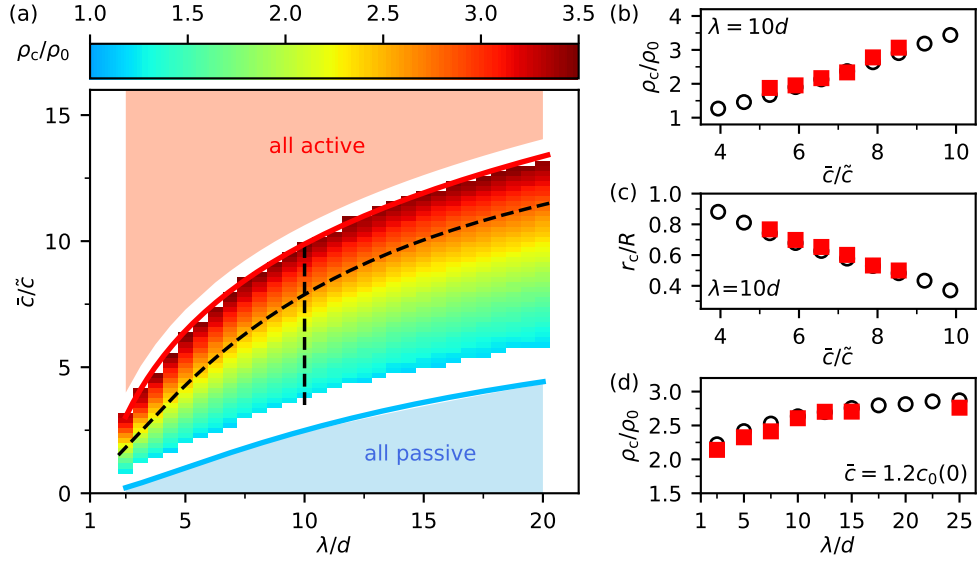


Fig. 4.7. (a) Numerical phase diagram showing the dependence of the cluster density ρ_c on the threshold \bar{c} and the interaction length λ . Stable clusters exist in the central colored region up to the red line. Shaded areas indicate regions where all particles are either active (red) or passive (blue). Black dashed lines correspond to paths along which experimental data were taken. Blue line: prediction for the boundary of the homogeneous passive region from Eq. (4.23). (b) Cluster density ρ_c and (c) cluster radius r_c as a function of threshold \bar{c} at $\lambda = 10d$ (vertical dashed line). (d) Cluster density as a function of decay length λ holding $\bar{c} = 1.2c_0(0)$ constant with $c_0(0)$ from Eq. (4.24) (horizontal dashed line). In (b–d), open symbols correspond to simulations and closed symbols to experiments. Experimental error bars (standard deviation) are comparable to the symbol size. Reprinted in adapted form with permission from Ref. [9] licensed under the Creative Commons license CC BY 4.0.

with $c_{0,\text{corr}}$ from Eq. (4.18) and $c_{0,\text{id}}(r)$ determined by integral (A.7) with $\rho(r) = \rho_0\Theta(R - r)$. Particles can turn active, when the threshold \bar{c} is higher than the concentration at the boundary $c_0(R)$, which can be obtained from Eq. (4.22) as

$$c_0(R) = \frac{1}{2}c_{0,\text{id}} [1 - I_0(2R/\lambda) + L_0(2R/\lambda)] - c_{0,\text{id}}(1 - e^{-d/\lambda}), \quad (4.23)$$

with $c_{0,\text{id}} = \frac{\gamma\lambda}{2Dc} \rho_0$ from Eq. (4.17), $I_0(x)$ the modified Bessel function of order zero of the first kind and $L_0(x)$ the modified Struve function of order zero. The condition $\bar{c} = c_0(R)$ is shown as blue line in Fig. 4.7(a) and well predicts the boundary of the homogeneous passive regime.

The dashed lines in Fig. 4.7(a) indicate the paths in the phase diagram, along which experiments were performed. Holding $\lambda = 10d$ fixed and increasing \bar{c} leads to denser and smaller clusters [Fig. 4.7(b,c)], as already seen in Fig. 4.6(b). As expected from the good agreement of the density profiles [Fig. 4.6(c)], the cluster densities ρ_c and radii r_c also agree well between experiments and simulations. Additional

experiments were performed varying λ and fixing the threshold to $\bar{c} = 1.2c_0(0)$ with

$$c_0(0) = c_{0,\text{id}}(e^{-d/\lambda} - e^{-R/\lambda}) \quad (4.24)$$

being the (λ -dependent) mean concentration at the confinement's center in a homogeneous system. Again, the agreement of ρ_c with the simulations is very good, cf. Fig. 4.7(d).

In order to understand the existence of an upper limit on \bar{c} for stable clusters to form, some insights can be obtained by looking at the number of passive particles N_p in the system (which is equal to the number of particles a cluster consists of). Figure 4.8(a) shows that upon increasing \bar{c} , clusters are made up of a decreasing average number of particles $\langle N_p \rangle$. As the major contribution to the concentration signal c_k a particle in the cluster measures comes from the other particles in the cluster (due to its higher density compared to the active gas), smaller $\langle N_p \rangle$ implies stronger fluctuations of c_k . This leads to stronger fluctuations of N_p for smaller clusters, see Fig. 4.8(b,c), as the probability that the concentration a particle at the cluster's rim senses drops below \bar{c} (or rises above it) increases. With decreasing $\langle N_p \rangle$ (i.e., rising \bar{c}), fluctuations become so strong that they can dissolve the entire cluster, see Fig. 4.8(b). Independent of λ , the minimal number of passive particles up to which we observe stable clusters is $\langle N_p \rangle_{\text{min}} \approx 65$, cf. Fig. 4.8(a). As shown in Fig. 4.9(a,b), the actual value of $\langle N_p \rangle_{\text{min}}$ depends on the number of particles N in the system (keeping the global density ρ_0 fixed) and, for larger N , decreases for smaller λ . The minimum fraction of passive particles $\langle N_p \rangle_{\text{min}}/N$ decreases with N ($\langle N_p \rangle_{\text{min}}/N = 0.49$ for $N = 132$, 0.45 for $N = 300$, 0.35 for $N = 1000$) and the maximum cluster density $\rho_{c,\text{max}}$ rises, cf. Fig. 4.9(c). This shows that in larger systems, smaller (relative to the system size) and denser clusters can be stabilized, presumably because the sensed concentrations c_k fluctuate less due to signals from more particles.

The decay length λ not only influences the range of thresholds where stable clusters exist [Fig. 4.7(a)], but also affects the shape of the interface between cluster and gas. For large λ , the interface is almost circular. For small λ , the shape of the interface can fluctuate strongly, see Fig. 4.10(a) for snapshots with $\lambda = 2.5d$ and $20d$. This can be explained by fluctuations of the concentration signal: For smaller λ , a particle receives chemical signals from fewer particles and thus the total signal it measures fluctuates stronger. Consequently, the strength of density fluctuations required for a particle at the cluster surface to switch from passive to active (or reverse) is decreased, which leads to a rougher and broader interface. This effect can be quantified via the interfacial width ω [as extracted by fitting the radial density

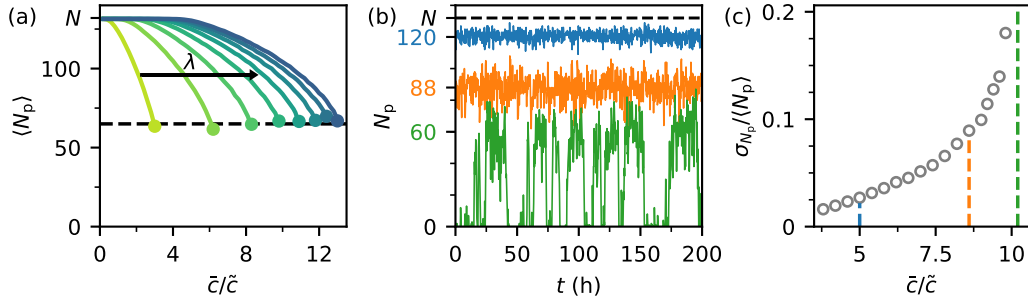


Fig. 4.8. Cluster fluctuations and stability. (a) Average number of passive particles $\langle N_p \rangle$ from simulations with $N = 132$ particles as a function of threshold \bar{c} for $\lambda = [2.5, 5, 7.5, 10, 12.5, 15, 17.5, 20]d$ (from left to right). For each value of λ , the circle indicates the maximum value of \bar{c} up to which we observe stable clusters. Independent of λ , the circles lie well on the $\langle N_p \rangle_{\min} = 65$ (dashed) line. (b) Time series $N_p(t)$ at $\lambda = 10d$ for concentration thresholds $\bar{c} = [5.0, 8.6, 10.2]\tilde{c}$ (from top to bottom) with averages indicated on the left (for $\bar{c} = 10.2\tilde{c}$ the time frames in which no cluster existed were excluded from the averaging). (c) Standard deviation of $N_p(t)$ divided by the average, $\sigma_{N_p}/\langle N_p \rangle$, which rises with \bar{c} (only shown in the regime where stable clusters exist). Dashed lines indicate the threshold values employed in (b). Reprinted in adapted form with permission from Ref. [9] licensed under the Creative Commons license CC BY 4.0.

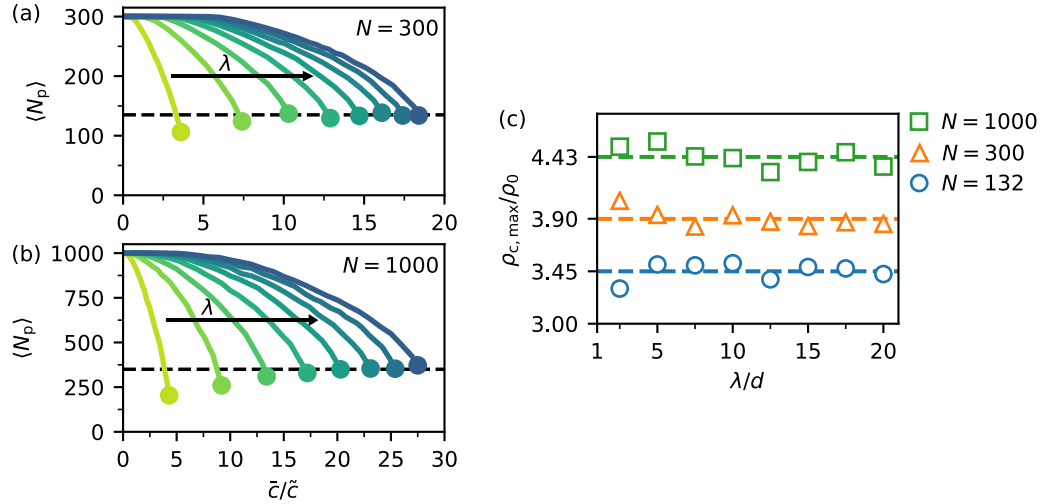


Fig. 4.9. Finite-size behavior. (a,b) Average number of passive particles $\langle N_p \rangle$ versus threshold \bar{c} for interaction lengths $\lambda = [2.5, 5, 7.5, 10, 12.5, 15, 17.5, 20]d$ (from left to right) for the circularly confined system at fixed global density $\rho_0 = 0.0075 \mu\text{m}^{-2}$ and particle numbers (a) $N = 300$, (b) $N = 1000$. The dashed lines indicate the minimal number of passive particles up to which stable cluster are observed ($\langle N_p \rangle_{\min} \approx 135$ for $N = 300$ and $\langle N_p \rangle_{\min} \approx 350$ for $N = 1000$). For small λ , the minimal particle number is slightly lower. (c) Maximum cluster densities $\rho_{c,\max}/\rho_0$ (at the highest \bar{c} where stable clusters were observed) versus λ for the different system sizes. The dashed lines indicate the averages. (a,b) are reprinted in adapted form with permission from Ref. [9] licensed under the Creative Commons license CC BY 4.0.

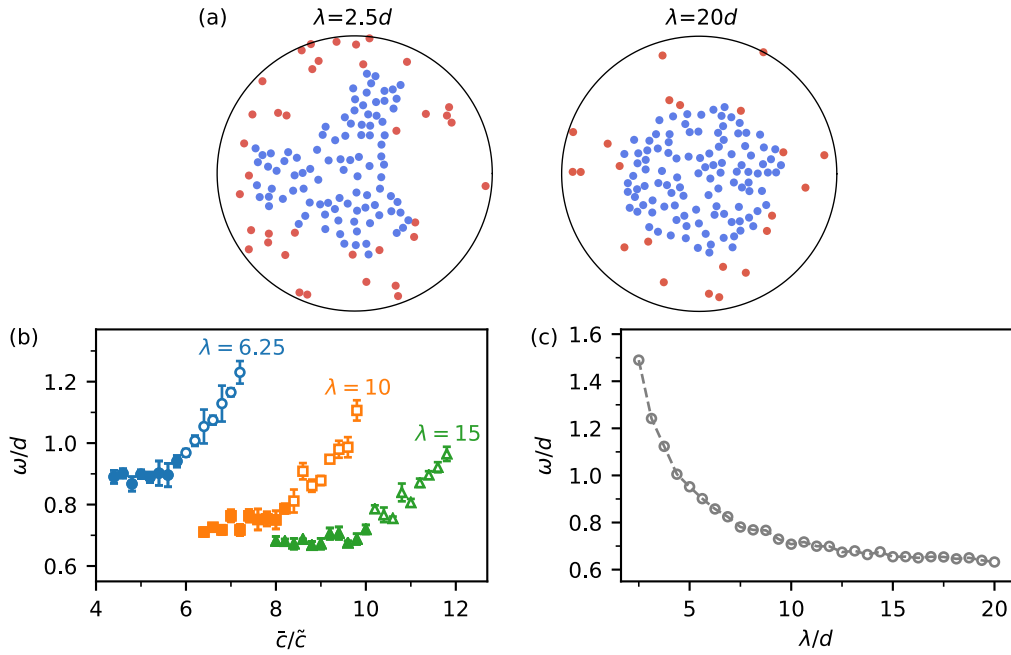


Fig. 4.10. Interfacial fluctuations and interfacial width. (a) Snapshots of the system at $\lambda = 2.5d$, $\bar{c} = 2\bar{c}$ (left) and $\lambda = 20d$, $\bar{c} = 10.6\bar{c}$ (right). For smaller λ , the shape of the interface is fluctuating stronger. (b) Interfacial width ω versus threshold \bar{c} for different λ (in units of d). Data is shown for stable clusters with radius $r_c < 0.65R$. Solid symbols: values used for averaging in (c). Error bars show standard errors. (c) Interfacial width ω against decay length λ .

profiles with Eq. (4.21)] which increases for smaller λ , see Figs. 4.10(b,c). There is also a dependence of ω on the threshold \bar{c} , cf. Fig. 4.10(b). For small \bar{c} , $\omega(\bar{c})$ exhibits a plateau. These plateau values were used for calculating the average interfacial widths, shown in Fig. 4.10(c) for each λ . For thresholds closer to the upper limit of cluster stability, $\omega(\bar{c})$ increases. We attribute this to the above discussed enhanced fluctuations of the number of particles N_p in the cluster closer to the maximal threshold. As a consequence, cluster size fluctuations are stronger which in turn leads to an effective increase of ω .

Mean-field theory for quorum-sensing active particles

In the previous chapter, we have seen that systems of quorum-sensing active particles can separate into an active gas phase and a passive cluster phase. In contrast to MIPS of ABPs, this phenomenon does not arise due to particle collisions, but is a result of the particles' motility response towards a self-generated concentration field. The sizes and densities of the coexisting domains can be controlled by the concentration threshold \bar{c} at which particles switch between active and passive states. The range of thresholds in which phase coexistence is possible (and the width of the interface between the two phases) depends on the decay length λ of the chemical profiles of particles.

The goal of this chapter is to develop a comprehensive theoretical framework that describes the findings from Chap. 4, as well as their dependence on the propulsion speed v_0 and the global density ρ_0 . As in Chap. 3, we treat the particle dynamics in terms of a (mean-field) one-body Smoluchowski equation, which, through the propulsion speed, is now coupled to the concentration field of chemicals. Interestingly, the discontinuous motility response of particles simplifies the theoretical treatment (in contrast to MIPS) as the resulting equations are linear. This allows us to obtain analytical results for two different geometries: a planar and a circular interface. Moreover, we compare to numerical simulations. Quantitative agreement can be achieved when incorporating fluctuations into the mean-field theory via an increased diffusive current out of the passive phase.

Going beyond a pure motility response, we also explore the effect of an additional coupling of the particles' orientations to the chemical field. Specifically, we consider particles that align *perpendicular* to the gradient of the chemical concentration. This response is different from well-studied chemotaxis where particles align *parallel* to the gradient [116, 125, 88, 148, 85], and gives rise to a circular particle current inside clusters ("vortex clusters").

Most of the results presented in this chapter have been published in Ref. [48].

5.1 Derivation of the one-body Smoluchowski equation

We consider N active particles with positions \mathbf{r}_k and orientations $\mathbf{e}_k = (\cos \varphi_k, \sin \varphi_k)$ with equations of motion

$$\dot{\mathbf{r}}_k = v_k \mathbf{e}_k + \boldsymbol{\xi}_k, \quad (5.1)$$

$$\dot{\varphi}_k = \chi_k \mathbf{e}_k \cdot \mathbf{s}_k + \xi_{r,k}, \quad (5.2)$$

where the translational and rotational noise $\boldsymbol{\xi}_k$ and $\xi_{r,k}$ respectively, have the same properties as before. However, there are two differences to the equations of motion considered in the previous chapter. First, particle interactions via a repulsive potential are neglected. This approximation is justified by the dilute conditions studied in Chap. 4 where particle collisions only occur at a low rate and simplifies the analytical calculations throughout this chapter. Secondly, the particle orientations do not only undergo free rotational diffusion, but are additionally coupled to the vector \mathbf{s}_k . The term $\chi_k \mathbf{e}_k \cdot \mathbf{s}_k$ is a torque (times a rotational mobility which is absorbed into χ_k) that orients particles perpendicular to \mathbf{s}_k with its strength set by χ_k . The torque does not play a role in the description of the phase separation via quorum sensing discussed in the previous chapter ($\chi_k = 0$). Its influence on the collective behavior of quorum-sensing active particles will be discussed in Sec. 5.5. In the following, we develop a mean-field theory that covers both cases, $\chi_k \neq 0$ and $\chi_k = 0$.

The particle properties, viz., v_k , χ_k and \mathbf{s}_k are functions of the measured concentrations c_k , calculated according to Eq. (4.5). Particularly, we assume a speed and coupling strength that jump between two constant values at the concentration threshold \bar{c}

$$v_k(c_k) = v^> \Theta(\bar{c} - c_k) + v^< \Theta(c_k - \bar{c}), \quad (5.3)$$

$$\chi_k(c_k) = \chi^> \Theta(\bar{c} - c_k) + \chi^< \Theta(c_k - \bar{c}). \quad (5.4)$$

Moreover, we consider the case $\mathbf{s}_k = \nabla_k c_k / |\nabla_k c_k|$, i.e., the torque orients particles perpendicular to the concentration gradient. The concentration c_k a particle measures depends on its own position \mathbf{r}_k and on the positions of all the other $N - 1$ particles. In order to allow for an analytical treatment, we assume that v_k , χ_k and \mathbf{s}_k of a particle k only depend on its mean sensed concentration $\langle c_k \rangle(\mathbf{r}_k, t)$ averaged over the other particle's positions, as given by Eq. (4.8).

To obtain a coarse-grained description of the particle dynamics, as in Sec. 3.2, we start out by rewriting the Langevin equations (5.1), (5.2) into the Smoluchowski equation for the N -body probability density $\psi(\{\mathbf{r}_k\}, \{\varphi_k\}, t)$. Applying the scheme introduced in Sec. (2.4.2) yields

$$\partial_t \psi = \sum_{k=1}^N \left\{ -\nabla_k \cdot (v_k \mathbf{e}_k \psi) + D_0 \nabla_k^2 \psi - \chi_k \partial_{\varphi_k} (\mathbf{e}_k \cdot \mathbf{s}_k \psi) + D_r \partial_{\varphi_k}^2 \psi \right\}. \quad (5.5)$$

Following Sec. 2.4.3, we integrate out the degrees of freedom of $N - 1$ particles and derive a dynamical equation for the one-body density ψ_1 , Eq. (2.45). The diffusion and propulsion terms can be treated as before and the torque term yields¹

$$\begin{aligned} & \int d\mathbf{r}_2 \dots d\mathbf{r}_N \int d\varphi_2 \dots d\varphi_N N \sum_{k=1}^N \chi_k \partial_{\varphi_k} (\mathbf{e}_k \cdot \mathbf{s}_k \psi) \\ &= \chi_1 \partial_{\varphi_1} (\mathbf{e}_1 \cdot \mathbf{s}_1 \psi_1) + \sum_{k=2}^N \int d\mathbf{r}_2 \dots d\mathbf{r}_{k-1} d\mathbf{r}_{k+1} \dots d\mathbf{r}_N \int d\varphi_2 \dots d\varphi_N N \chi_k \mathbf{s}_k \cdot \underbrace{[\mathbf{e}_k \psi]_0^{2\pi}}_{=0} \\ &= \chi_1 \partial_{\varphi_1} (\mathbf{e}_1 \cdot \mathbf{s}_1 \psi_1), \end{aligned} \quad (5.6)$$

since ψ and \mathbf{e}_k are 2π -periodic in φ_k . Dropping indices, the final equation for $\psi_1(\mathbf{r}, \varphi, t)$ reads

$$\partial_t \psi_1 = -\nabla \cdot [(v\mathbf{e} - D_0 \nabla) \psi_1] - \chi \partial_{\varphi} (\mathbf{e} \cdot \mathbf{s} \psi_1) + D_r \partial_{\varphi}^2 \psi_1, \quad (5.7)$$

with

$$v(\langle c \rangle) = v^> \Theta(\bar{c} - \langle c \rangle) + v^< \Theta(\langle c \rangle - \bar{c}), \quad (5.8)$$

$$\chi(\langle c \rangle) = \chi^> \Theta(\bar{c} - \langle c \rangle) + \chi^< \Theta(\langle c \rangle - \bar{c}), \quad (5.9)$$

and $\mathbf{s} = \nabla \langle c \rangle / |\nabla \langle c \rangle|$, depending on the mean concentration field

$$\langle c \rangle(\mathbf{r}, t) = \frac{\gamma}{4\pi D_c} \int d\mathbf{r}' \rho(\mathbf{r}', t) \frac{e^{-|\mathbf{r}-\mathbf{r}'|/\lambda}}{|\mathbf{r}-\mathbf{r}'|}, \quad (5.10)$$

which is Eq. (4.14) for point particles. In a homogeneous system, Eq. (5.10) implies the uniform concentration

$$c_0 = \frac{\gamma \lambda}{2D_c} \rho_0, \quad (5.11)$$

which is equal to $c_{0,\text{id}}$, as defined in Eq. (4.17).

¹ $\int d\mathbf{r}_2 \dots d\mathbf{r}_{k-1} d\mathbf{r}_{k+1} \dots d\mathbf{r}_N$ is defined as in Sec. 2.4.3.

5.2 Moment expansion

As in Sec. 3.3.2, from Eq. (5.7) we derive dynamical equations for the orientational moments $\hat{\psi}_m(\mathbf{r}, t)$ and $\hat{\phi}_m(\mathbf{r}, t)$ [Eqs. (2.62, 2.63)] of the one-body density $\psi_1(\mathbf{r}, \varphi, t)$. For $m = 0$, we obtain

$$\partial_t \hat{\psi}_0 = -\partial_x(v\hat{\psi}_1) - \partial_y(v\hat{\phi}_1) + D_0 \nabla^2 \hat{\psi}_0. \quad (5.12)$$

For $m = 1$, we have

$$\begin{aligned} \partial_t \hat{\psi}_1 = & -\frac{1}{2} \left[\partial_x(v\hat{\psi}_0) + \partial_x(v\hat{\psi}_2) + \partial_y(v\hat{\phi}_2) \right] + \frac{1}{2} \chi \left[s_y(\hat{\psi}_2 - \hat{\psi}_0) - s_x \hat{\phi}_2 \right] \\ & + D_0 \nabla^2 \hat{\psi}_1 - D_r \hat{\psi}_1, \end{aligned} \quad (5.13)$$

$$\begin{aligned} \partial_t \hat{\phi}_1 = & -\frac{1}{2} \left[\partial_y(v\hat{\psi}_0) + \partial_x(v\hat{\phi}_2) - \partial_y(v\hat{\psi}_2) \right] + \frac{1}{2} \chi \left[s_y \hat{\phi}_2 + s_x(\hat{\psi}_2 + \hat{\psi}_0) \right] \\ & + D_0 \nabla^2 \hat{\phi}_1 - D_r \hat{\phi}_1. \end{aligned} \quad (5.14)$$

At the next order $m = 2$, we find

$$\begin{aligned} \partial_t \hat{\psi}_2 = & -\frac{1}{2} \partial_x(v\hat{\psi}_1) + \frac{1}{2} \partial_y(v\hat{\phi}_1) - \frac{1}{2} \partial_x(v\hat{\psi}_3) - \frac{1}{2} \partial_y(v\hat{\phi}_3) - \chi s_x(\hat{\phi}_3 + \hat{\phi}_1) \\ & + \chi s_y(\hat{\psi}_3 - \hat{\psi}_1) + D_0 \nabla^2 \hat{\psi}_2 - 4D_r \hat{\psi}_2, \end{aligned} \quad (5.15)$$

$$\begin{aligned} \partial_t \hat{\phi}_2 = & -\frac{1}{2} \partial_x(v\hat{\phi}_1) - \frac{1}{2} \partial_y(v\hat{\psi}_1) - \frac{1}{2} \partial_x(v\hat{\phi}_3) + \frac{1}{2} \partial_y(v\hat{\psi}_3) + \chi s_x(\hat{\psi}_3 + \hat{\psi}_1) \\ & + \chi s_y(\hat{\phi}_3 - \hat{\phi}_1) + D_0 \nabla^2 \hat{\phi}_2 - 4D_r \hat{\phi}_2. \end{aligned} \quad (5.16)$$

In Sec. 3.3.2, we have closed the hierarchy at order $m = 1$ by setting $\hat{\psi}_2 = \hat{\phi}_2 = 0$. Here, due to the additional aligning torque, entirely neglecting the second moments leads to a deficient description [116, 87]. We therefore only set the third moments to zero, $\hat{\psi}_3 = \hat{\phi}_3 = 0$, and neglect time and spatial derivatives of $\hat{\psi}_2$ and $\hat{\phi}_2$ in Eqs. (5.15, 5.16) [13, 116, 87]. The second moments are then

$$\hat{\psi}_2 = \frac{1}{4D_r} \left[-\frac{1}{2} \partial_x(v\hat{\psi}_1) + \frac{1}{2} \partial_y(v\hat{\phi}_1) - \chi(s_x \hat{\phi}_1 + s_y \hat{\psi}_1) \right], \quad (5.17)$$

$$\hat{\phi}_2 = \frac{1}{4D_r} \left[-\frac{1}{2} \partial_x(v\hat{\phi}_1) - \frac{1}{2} \partial_y(v\hat{\psi}_1) - \chi(s_y \hat{\phi}_1 - s_x \hat{\psi}_1) \right], \quad (5.18)$$

which now only couple to the $m = 1$ modes. Plugging Eqs. (5.17, 5.18) into Eqs. (5.13, 5.14), we obtain

$$\begin{aligned} \partial_t \hat{\psi}_1 = & -\frac{1}{2} \partial_x(v\hat{\psi}_0) + D_0 \nabla^2 \hat{\psi}_1 - \frac{1}{2} \chi s_y \hat{\psi}_0 - D_r \hat{\psi}_1 - \frac{\chi^2}{8D_r} \left[s_x^2 + s_y^2 \right] \hat{\psi}_1 \\ & + \frac{1}{16D_r} \left[\partial_x(v\partial_x(v\hat{\psi}_1)) - \partial_x(v\partial_y(v\hat{\phi}_1)) + \partial_y(v\partial_x(v\hat{\phi}_1)) + \partial_y(v\partial_y(v\hat{\psi}_1)) \right] \end{aligned}$$

$$\begin{aligned}
& + \frac{1}{8D_r} \left[\partial_x(v\chi s_x \hat{\phi}_1) + \partial_x(v\chi s_y \hat{\psi}_1) - \partial_y(v\chi s_x \hat{\psi}_1) + \partial_y(v\chi s_y \hat{\phi}_1) \right] \\
& + \frac{\chi}{16D_r} \left[s_x \partial_x(v\hat{\phi}_1) + s_x \partial_y(v\hat{\psi}_1) - s_y \partial_x(v\hat{\psi}_1) + s_y \partial_y(v\hat{\phi}_1) \right] \quad (5.19)
\end{aligned}$$

and

$$\begin{aligned}
\partial_t \hat{\phi}_1 = & -\frac{1}{2} \partial_y(v\hat{\psi}_0) + D_0 \nabla^2 \hat{\phi}_1 + \frac{1}{2} \chi s_x \hat{\psi}_0 - D_r \hat{\phi}_1 - \frac{\chi^2}{8D_r} [s_x^2 + s_y^2] \hat{\phi}_1 \\
& + \frac{1}{16D_r} \left[\partial_x(v\partial_x(v\hat{\phi}_1)) + \partial_x(v\partial_y(v\hat{\psi}_1)) - \partial_y(v\partial_x(v\hat{\psi}_1)) + \partial_y(v\partial_y(v\hat{\phi}_1)) \right] \\
& - \frac{1}{8D_r} \left[\partial_x(v\chi s_x \hat{\psi}_1) - \partial_x(v\chi s_y \hat{\phi}_1) + \partial_y(v\chi s_x \hat{\phi}_1) + \partial_y(v\chi s_y \hat{\psi}_1) \right] \\
& - \frac{\chi}{16D_r} \left[s_x \partial_x(v\hat{\psi}_1) - s_x \partial_y(v\hat{\phi}_1) + s_y \partial_x(v\hat{\phi}_1) + s_y \partial_y(v\hat{\psi}_1) \right]. \quad (5.20)
\end{aligned}$$

Eqs. (5.12, 5.19, 5.20) constitute a closed set of equations for $\hat{\psi}_0$, $\hat{\psi}_1$ and $\hat{\phi}_1$. Identifying density $\rho \equiv \hat{\psi}_0$ and polarization $\mathbf{p} \equiv (\hat{\psi}_1, \hat{\phi}_1)$ [as introduced in Sec. 2.4.5], Eq. (5.12) becomes the continuity equation for the density

$$\partial_t \rho = -\nabla \cdot \mathbf{j}, \quad (5.21)$$

with particle current

$$\mathbf{j} = v\mathbf{p} - D_0 \nabla \rho. \quad (5.22)$$

Eqs. (5.19, 5.20) can be rewritten into the dynamical equation for the polarization as

$$\begin{aligned}
\partial_t \mathbf{p} = & \frac{1}{2} \chi \rho \mathbf{R} \cdot \mathbf{s} - \left(D_r + \frac{\chi^2}{8D_r} |\mathbf{s}|^2 \right) \mathbf{p} + \frac{v}{16D_r} [\nabla \cdot (\chi \mathbf{s}) \mathbf{R} \cdot \mathbf{p} - \nabla \cdot (\mathbf{R} \cdot \chi \mathbf{s}) \mathbf{p}] \\
& + \nabla \cdot \mathbf{M}, \quad (5.23)
\end{aligned}$$

with matrices

$$\begin{aligned}
\mathbf{M} \equiv & \frac{v}{16D_r} [\nabla(v\mathbf{p}) + \mathbf{R} \cdot \nabla(v\mathbf{p}) \cdot \mathbf{R}] + \frac{\chi v}{16D_r} [3(\mathbf{s} \otimes \mathbf{p}) \cdot \mathbf{R} - \mathbf{R} \cdot (\mathbf{s} \otimes \mathbf{p})] \\
& - \frac{1}{2} v \rho \mathbb{1} + D_0 \nabla \mathbf{p} \quad (5.24)
\end{aligned}$$

and

$$\mathbf{R} \equiv \begin{pmatrix} 0 & -1 \\ 1 & 0 \end{pmatrix} \quad (5.25)$$

describing a rotation by $\pi/2$. Here, we use the conventions $(\nabla \mathbf{a})_{ij} = \partial_i a_j$ (with vector \mathbf{a}) and $(\nabla \cdot \mathbf{M})_j = \partial_i M_{ij}$ (with matrix \mathbf{M}). In the next sections, we employ the coupled equations (5.21), (5.23) to describe different steady states of the system.

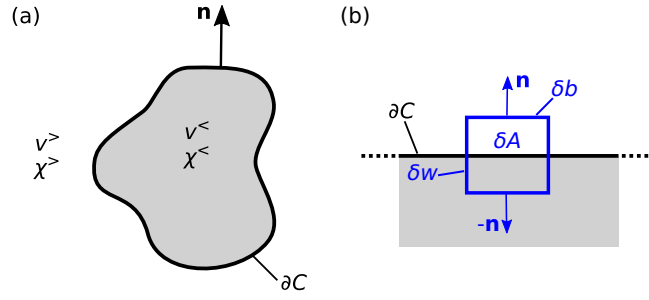


Fig. 5.1. Jump conditions. (a) Domain \mathcal{C} inside which $\langle c \rangle > \bar{c}$ bounded by the curve $\partial\mathcal{C}$. Along this curve, the speed $v(\langle c \rangle)$ and coupling $\chi(\langle c \rangle)$ are discontinuous. (b) Zoom to part of the boundary curve $\partial\mathcal{C}$ with integration area $\delta A = \delta b \delta w$. Reprinted in adapted form with permission from Ref. [48]. Copyright 2020 by the American Physical Society.

5.3 Jump conditions

We now assume that the system has reached a steady state ($\partial_t \rho = \partial_t \mathbf{p} = 0$, $\langle c \rangle(\mathbf{r}, t) = \langle c \rangle(\mathbf{r})$), in which a closed domain \mathcal{C} has formed with speed $v^<$ and coupling $\chi^<$ inside, and $v^>$ and $\chi^>$ outside, see Fig. 5.1(a). The concentration profile $\langle c \rangle(\mathbf{r})$ remains a continuous function everywhere, but it is $\langle c \rangle > \bar{c}$ inside and $\langle c \rangle < \bar{c}$ outside \mathcal{C} . The domain is bounded by the curve $\partial\mathcal{C}$, on which the concentration field fulfills $\langle c \rangle = \bar{c}$, with normal vector \mathbf{n} pointing outwards. For this situation, we can draw an analogy with a problem encountered in electrostatics: A dielectric constant that jumps at the interface between different media. Consequently, the discontinuity of v and χ imposes jump conditions at $\partial\mathcal{C}$ for $\mathbf{j}(\mathbf{r})$ and $\mathbf{M}(\mathbf{r})$ [and thus for $\rho(\mathbf{r})$ and $\mathbf{p}(\mathbf{r})$] via Eqs. (5.21,5.23).² In the following, we determine these conditions analogous to the derivation of the jump conditions for the electromagnetic fields [75].

Therefore, we consider an infinitesimally small area element $\delta A = \delta b \delta w$ with one half inside and one half outside \mathcal{C} , as shown in Fig. 5.1(b). Due to the infinitesimal size of δA , the bounding curve $\partial\mathcal{C}$ can be assumed to be locally straight and the jumping quantities $\mathbf{X}(\mathbf{r})$ (\mathbf{j} , \mathbf{M} , ρ and \mathbf{p}) to take constant values $\mathbf{X}^<$ and $\mathbf{X}^>$ in the inner and outer half of δA , respectively. We denote continuous quantities $\mathbf{Y}(\mathbf{r})$ evaluated on $\partial\mathcal{C}$ by \mathbf{Y}_c . The jump conditions can then be derived by integrating equations (5.21) and (5.23) over δA .

²In electrostatics the Maxwell equations set jump conditions for the electric field $\mathbf{E}(\mathbf{r})$ and the electric displacement field $\mathbf{D}(\mathbf{r})$.

Density

We start out by integrating Eq. (5.21) with $\partial_t \rho = 0$ over δA , which, using the divergence theorem, can be written as

$$\int_{\delta A} dS \nabla \cdot \mathbf{j} = \int_{\partial A} dl \mathbf{n}_A \cdot \mathbf{j} = 0, \quad (5.26)$$

with area element dS , line element dl , the bounding curve ∂A of the area δA and \mathbf{n}_A its outer normal. The normal is equal to \mathbf{n} and $-\mathbf{n}$ on the outer edge and inner edge of δA , respectively. On the edges penetrating $\partial \mathcal{C}$ it is $\pm \mathbf{R} \cdot \mathbf{n}$. We can split up the line integral into integrals over the four individual edges of δA as

$$\begin{aligned} \int_{\partial A} dl \mathbf{n}_A \cdot \mathbf{j} &= \delta b \mathbf{n} \cdot \mathbf{j}^> - \delta b \mathbf{n} \cdot \mathbf{j}^< + \frac{\delta w}{2} \mathbf{R} \cdot \mathbf{n} \cdot (\mathbf{j}^> + \mathbf{j}^<) - \frac{\delta w}{2} \mathbf{R} \cdot \mathbf{n} \cdot (\mathbf{j}^> + \mathbf{j}^<) \\ &= \delta b \mathbf{n} \cdot (\mathbf{j}^> - \mathbf{j}^<). \end{aligned} \quad (5.27)$$

This implies that the normal component of the current \mathbf{j} is continuous at $\partial \mathcal{C}$

$$\mathbf{n} \cdot (\mathbf{j}^> - \mathbf{j}^<) = 0. \quad (5.28)$$

Polarization

We now integrate the individual terms in Eq. (5.23) over δA . The integral over $\nabla \cdot \mathbf{M}$ can be evaluated analogous to the integral over $\nabla \cdot \mathbf{j}$ [Eq. (5.27)], since the divergence theorem can also be applied to higher order tensor fields. We obtain

$$\int_{\delta A} dS \nabla \cdot \mathbf{M} = \int_{\partial A} dl \mathbf{n}_A \cdot \mathbf{M} = \delta b \mathbf{n} \cdot (\mathbf{M}^> - \mathbf{M}^<). \quad (5.29)$$

As the divergence term cannot be applied to the remaining terms in Eq. (5.23), these have to be evaluated in the halves of δA inside \mathcal{C} and outside \mathcal{C} individually. For the first of these terms we find

$$\begin{aligned} &\int_{\delta A} dS \left[\frac{1}{2} \chi \rho \mathbf{R} \cdot \mathbf{s} - \left(D_r + \frac{\chi^2}{8 D_r} |\mathbf{s}|^2 \right) \mathbf{p} \right] \\ &= \delta b \frac{\delta w}{2} \left[\frac{1}{2} \mathbf{R} \cdot \mathbf{s}_c (\chi^> \rho^> + \chi^< \rho^<) - D_r (\mathbf{p}^> + \mathbf{p}^<) - \frac{|\mathbf{s}_c|^2}{8 D_r} (\chi^>{}^2 \mathbf{p}^> + \chi^<{}^2 \mathbf{p}^<) \right]. \end{aligned} \quad (5.30)$$

The next term

$$\int_{\delta A} dS \frac{v}{16 D_r} \nabla \cdot (\chi \mathbf{s}) \mathbf{R} \cdot \mathbf{p} \quad (5.31)$$

can be split up into two terms using $\nabla \cdot (\chi \mathbf{s}) = \chi \nabla \cdot \mathbf{s} + \mathbf{s} \cdot \nabla \chi$ as

$$\int_{\delta A} dS \frac{v}{16D_r} \chi (\nabla \cdot \mathbf{s}) \mathbf{R} \cdot \mathbf{p} = \delta b \frac{\delta w}{2} \frac{1}{16D_r} (\nabla \cdot \mathbf{s})_c [v^> \chi^> \mathbf{R} \cdot \mathbf{p}^> + v^< \chi^< \mathbf{R} \cdot \mathbf{p}^<] \quad (5.32)$$

and

$$\begin{aligned} \int_{\delta A} dS \frac{v}{16D_r} (\mathbf{s} \cdot \nabla \chi) \mathbf{R} \cdot \mathbf{p} &= \delta b \int_{w_c - \delta w/2}^{w_c + \delta w/2} dw \frac{v}{16D_r} (\mathbf{s} \cdot \nabla \chi) \mathbf{R} \cdot \mathbf{p} \\ &= \delta b \int_{w_c - \delta w/2}^{w_c + \delta w/2} dw \frac{v}{16D_r} \mathbf{s} \cdot \mathbf{n} (\chi^> - \chi^<) \delta(w - w_c) \mathbf{R} \cdot \mathbf{p} \\ &= \delta b \frac{1}{16D_r} (\mathbf{s}_c \cdot \mathbf{n}) (\chi^> - \chi^<) \frac{1}{2\epsilon} \int_{w_c - \epsilon}^{w_c + \epsilon} dw v \mathbf{R} \cdot \mathbf{p} \\ &= \delta b \frac{1}{16D_r} (\mathbf{s}_c \cdot \mathbf{n}) (\chi^> - \chi^<) \frac{1}{2} (v^> \mathbf{R} \cdot \mathbf{p}^> - v^< \mathbf{R} \cdot \mathbf{p}^<). \end{aligned} \quad (5.33)$$

In line two of Eq. (5.33), we have used

$$\nabla \chi(w) = \nabla [\chi^> \Theta(w - w_c) + \chi^< \Theta(w_c - w)] = \mathbf{n} (\chi^> - \chi^<) \delta(w - w_c), \quad (5.34)$$

with w the coordinate locally (inside δA) perpendicular to $\partial \mathcal{C}$. Following Ref. [63], in line three of Eq. (5.33) we have employed the explicit representation of the delta distribution

$$\delta(w - w_c) = \begin{cases} 1/(2\epsilon), & \text{for } -\epsilon < w - w_c < \epsilon \\ 0, & \text{otherwise} \end{cases}, \quad (5.35)$$

with $\epsilon \rightarrow 0$ ($\epsilon < \delta w/2$), in order to evaluate the delta distribution at the discontinuity of v . The remaining term can be integrated analogous to term (5.31) as

$$\begin{aligned} \int_{\delta A} dS \frac{v}{16D_r} \nabla \cdot (\mathbf{R} \cdot \chi \mathbf{s}) \mathbf{p} &= \delta b \frac{\delta w}{2} \frac{1}{16D_r} [\nabla \cdot (\mathbf{R} \cdot \mathbf{s})]_c [v^> \chi^> \mathbf{p}^> + v^< \chi^< \mathbf{p}^<] \\ &\quad + \delta b \frac{1}{16D_r} (\mathbf{R} \cdot \mathbf{s}_c \cdot \mathbf{n}) (\chi^> - \chi^<) \frac{1}{2} (v^> \mathbf{p}^> - v^< \mathbf{p}^<). \end{aligned} \quad (5.36)$$

In case of $\mathbf{s} = \nabla \langle c \rangle / |\nabla \langle c \rangle|$ and $v^< < v^>$, $\mathbf{s}_c = -\mathbf{n}$ and thus $\mathbf{R} \cdot \mathbf{s}_c \cdot \mathbf{n} = 0$. Therefore, the second term in Eq. (5.36) vanishes. Collecting the evaluated integrals (5.29,5.30,5.32,5.33,5.36), we arrive at an expression of the form

$$\delta b[\dots] + \delta b \delta w[\dots] = 0. \quad (5.37)$$

Dividing by δb and performing the limit $\delta w \rightarrow 0$, only the terms $\sim \delta b$ remain, i.e.,

$$\mathbf{n} \cdot (\mathbf{M}^> - \mathbf{M}^<) + \frac{1}{16D_r} (\mathbf{s}_c \cdot \mathbf{n}) (\chi^> - \chi^<) \frac{1}{2} (v^> \mathbf{R} \cdot \mathbf{p}^> - v^< \mathbf{R} \cdot \mathbf{p}^<) = 0. \quad (5.38)$$

5.4 No orientational coupling: Phase separation

We now turn to the case of vanishing orientational coupling through setting $\chi = 0$. Moreover, we introduce the typical length and speed scales

$$\ell \equiv \sqrt{D_0/D_r}, \quad v_* \equiv 4\sqrt{D_0 D_r}. \quad (5.39)$$

We consider a steady state ($\partial_t \rho = 0$, $\partial_t \mathbf{p} = 0$) with no-flux boundary conditions. Assuming that $\nabla \times \mathbf{j} = 0$, $\nabla \cdot \mathbf{j} = 0$ [Eq. (5.21)] implies a vanishing particle current everywhere, i.e., $\mathbf{j} = 0$. Then Eq. (5.22) can be written as

$$\nabla \rho = \frac{v}{D_0} \mathbf{p}, \quad (5.40)$$

which directly connects the density gradient and the polarization. For $\chi = 0$, the matrix \mathbf{M} [Eq. (5.24)] simplifies into

$$\mathbf{M}_0 = -\frac{1}{2} v \rho \mathbb{1} + D_0 \left(1 + \frac{v^2}{v_*^2} \right) \nabla \mathbf{p} \quad (5.41)$$

and the equation for the polarization, Eq. (5.23), becomes

$$0 = -\frac{1}{2} \nabla(v\rho) + D_0 \left(1 + \frac{v^2}{v_*^2} \right) \nabla^2 \mathbf{p} - D_r \mathbf{p}. \quad (5.42)$$

Since, in each of the two regions (inside and outside \mathcal{C}), v is constant everywhere except at $\partial\mathcal{C}$, $\nabla(v\rho) = v\nabla\rho$. Then, the density gradient [Eq. (5.40)] can be inserted and Eq. (5.42) turns into a differential equation for \mathbf{p} alone

$$0 = D_0 \left(1 + \frac{v^2}{v_*^2} \right) \nabla^2 \mathbf{p} - \left(D_r + \frac{v^2}{2D_0} \right) \mathbf{p}, \quad (5.43)$$

which is valid in the individual regions where $v = v^<$ and $v = v^>$, respectively. Clearly, $\mathbf{p} = 0$ is one solution which corresponds to a homogeneous system since it implies $\nabla\rho = 0$ according to Eq. (5.40). In the following, we study inhomogeneous

solutions by solving Eqs. (5.40) and (5.43) for ρ and \mathbf{p} in the two regions separately and applying appropriate jump conditions.

For $\chi = 0$, the jump condition (5.38) simplifies into

$$\mathbf{n} \cdot (\mathbf{M}_0^> - \mathbf{M}_0^<) = 0. \quad (5.44)$$

As we require $\mathbf{j} = 0$, however, the jump condition for the current [Eq. (5.28)] does not provide any information. Though $\mathbf{j} = 0$ has led us to Eq. (5.40) for which we can derive another jump condition via the scheme introduced in the preceding section. Integrating Eq. (5.40) over an infinitesimal area δA with one half inside and one half outside \mathcal{C} , yields

$$\int_{\delta A} dS \nabla \rho = \int_{\delta A} dS \frac{v}{D_0} \mathbf{p}. \quad (5.45)$$

Assuming $\nabla \rho = \mathbf{n} \partial_w \rho$ inside δA , Eq. (5.45) turns into

$$\delta b \mathbf{n} \underbrace{\int_{w_c - \delta w/2}^{w_c + \delta w/2} dw \partial_w \rho}_{=\rho^> - \rho^<} = \delta b \frac{\delta w}{2} \frac{1}{D_0} (v^> \mathbf{p}^> + v^< \mathbf{p}^<). \quad (5.46)$$

Dividing by δb and taking the limit $\delta w \rightarrow 0$, we arrive at

$$\rho^> = \rho^<, \quad (5.47)$$

implying that the density is continuous at $\partial \mathcal{C}$.

Note that for a vanishing translational diffusion coefficient $D_0 = 0$, $\mathbf{p} = 0$ everywhere [Eq. (5.40)] and thus $v\rho = \text{const.}$, i.e., $v^>\rho^> = v^<\rho^<$, according to Eq. (5.42). In Refs. [151, 52], this relationship has been exploited to create complex density patterns of active particles by spatial modulations of their propulsion speed and has also been studied in Ref. [120]. In that case, $v^< = 0$ implies $\rho^> = 0$ which means that all particles condense into a cluster and stop moving. In the following, for two different geometries, we consider the coexistence of motile ($v^> > 0$) and passive ($v^< = 0$) particles with non-vanishing diffusion coefficient $D_0 > 0$ which corresponds to the situation studied in Chap. 4.

5.4.1 Planar interface

We first consider a geometry with a planar interface at $x = 0$ with normal vector $\mathbf{n} = \mathbf{e}_x$ of the bounding curve $\partial \mathcal{C}$, see Fig. 5.2(a). Along the transversal y -direction, the system is translationally invariant, implying that the density $\rho(x)$ only depends

on x and the polarization is $\mathbf{p}(x) = p(x)\mathbf{e}_x$. For $x < 0$, we set $v^< = 0$ so that $\rho(x) = \rho_c = \text{const.}$ [according to Eq. (5.40)] and $p(x) = 0$. For $x > 0$ with $v^> = v_0 > 0$, the differential equation (5.43) can be written as

$$\partial_x^2 p(x) - \frac{p(x)}{\xi_0^2} = 0, \quad (5.48)$$

with decay length

$$\xi_0 \equiv \ell \left[\frac{1 + (v_0/v_*)^2}{1 + 8(v_0/v_*)^2} \right]^{1/2}, \quad (5.49)$$

which equals ℓ for $v_0 = 0$ and drops to $\ell/\sqrt{8}$ for $v_0 \rightarrow \infty$. The solution of Eq. (5.48) is

$$p(x) = ae^{-x/\xi_0} \quad (5.50)$$

with integration constant a .³ Integrating Eq. (5.40), the density for $x > 0$ is [requiring its continuity at $x = 0$ according to Eq. (5.47)]

$$\rho(x) = \rho_c - \frac{v_0 \xi_0}{D_0} a \left(e^{-x/\xi_0} - 1 \right). \quad (5.51)$$

Since the density must be lower in the region with finite self-propulsion speed (as seen in Chap. 4), from Eq. (5.51), it follows $a < 0$. Consequently, the polarization [Eq. (5.50)] has a discontinuity at $x = 0$, where it jumps from zero to $a < 0$. The density decays into the active gas reaching

$$\rho_g = \rho_c + \frac{v_0 \xi_0}{D_0} a \quad (5.52)$$

for $x \gg \xi_0$. In order to connect the solutions for $x < 0$ and $x > 0$, we evaluate the jump condition (5.44), which reads

$$\begin{aligned} 0 &= \mathbf{e}_x \cdot \left[-\frac{1}{2} v_0 \rho_c \mathbb{1} + D_0 \left(1 + \frac{v_0^2}{v_*^2} \right) (\partial_x p(x))^> \mathbf{e}_x \otimes \mathbf{e}_x \right] \\ \Leftrightarrow 0 &= \frac{1}{2} v_0 \rho_c + D_0 \left(1 + \frac{v_0^2}{v_*^2} \right) \frac{a}{\xi_0}, \end{aligned} \quad (5.53)$$

and relates the yet unknown constants a and ρ_c . Using relation (5.52), Eq. (5.53) can be recast into

$$\frac{\rho_c}{\rho_g} = 1 + 8 \frac{v_0^2}{v_*^2}, \quad (5.54)$$

³Another solution would be $p(x) = \tilde{a}e^{x/\xi_0}$, which, however, is unphysical in our system, as it would imply $|p(x)| \rightarrow \infty$ for $x \rightarrow \infty$.

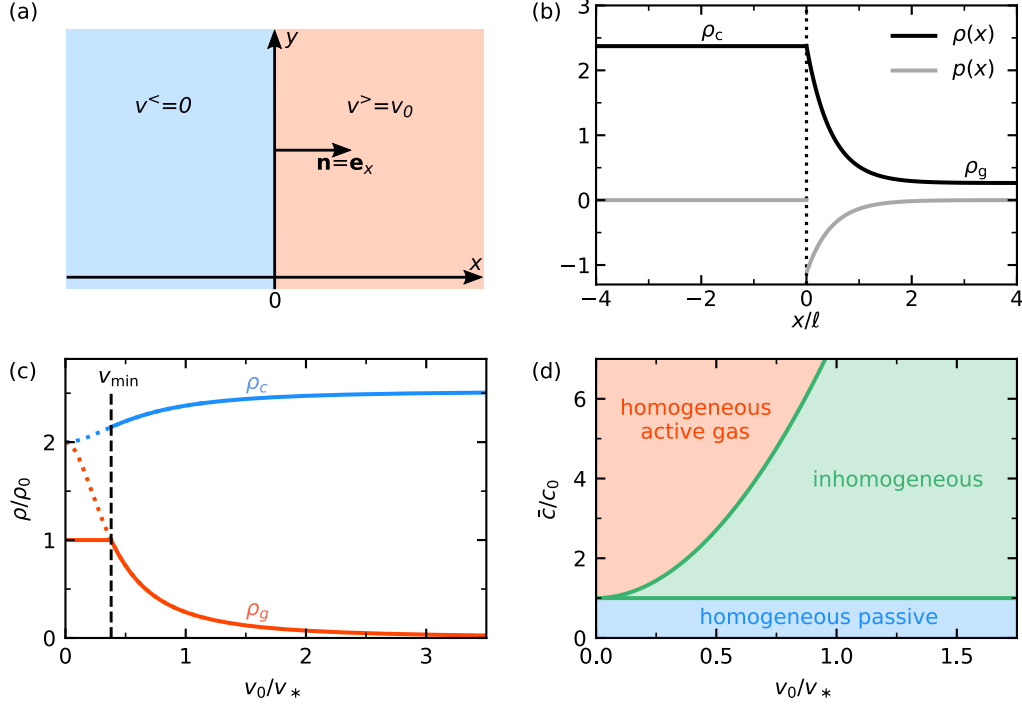


Fig. 5.2. Phase separation with a planar interface. (a) Sketch of the geometry. A planar interface with normal vector $\mathbf{n} = \mathbf{e}_x$ separates the domains with speeds $v^< = 0$ and $v^> = v_0$. (b) Profiles $\rho(x)$ and $p(x)$ at $v_0/v_* = 1$, $\bar{c}/c_0 = 2$ and $\lambda/\ell = 0.45$. (c) Passive (ρ_c) and active gas (ρ_g) densities as a function of propulsion speed for $\bar{c}/c_0 = 2$ and $\lambda/\ell = 0.45$ with respect to a uniform system at density ρ_0 . There is a minimal speed v_{\min} below which the system remains a homogeneous active gas. (d) Corresponding \bar{c} - v_0 phase diagram. As the threshold \bar{c} is increased, v_{\min} rises (upper green line). For thresholds below the concentration of the uniform system c_0 , another homogeneous region exists in which all particles become passive. (b-d) are reprinted in adapted form with permission from Ref. [48]. Copyright 2020 by the American Physical Society.

showing that the ratio of cluster and gas density rises quadratically with the propulsion speed v_0 .

Moreover, the concentration $\langle c \rangle(\mathbf{r})$ [Eq. (5.10)] has to be equal to the threshold \bar{c} at the interface, i.e.,

$$\langle c \rangle(x=0) = \frac{\gamma}{4\pi D_c} \int_{-\infty}^{\infty} dx' \int_{-\infty}^{\infty} dy' \rho(\mathbf{r}') \frac{e^{-|y\mathbf{e}_y - \mathbf{r}'|/\lambda}}{|\mathbf{r}'|} \stackrel{!}{=} \bar{c}. \quad (5.55)$$

Setting $y = 0$ due to translational invariance along the interface and changing to polar coordinates (r', θ) around the origin, we obtain

$$\bar{c} = \frac{\gamma}{4\pi D_c} \int_0^{\infty} dr' e^{-r'/\lambda} \int_{-\pi}^{\pi} d\theta \rho(r' \cos \theta)$$

$$\begin{aligned}
&= \frac{\gamma}{4\pi D_c} \int_0^\infty dr' e^{-r'/\lambda} \left\{ \int_{\pi/2}^{-\pi/2} d\theta \rho_c + \int_{-\pi/2}^{\pi/2} d\theta \left[\rho_c - \frac{v_0 \xi_0}{D_0} a \left(e^{-r' \cos \theta / \xi_0} - 1 \right) \right] \right\} \\
&= \frac{\gamma \lambda}{2D_c} \left[\rho_c + \frac{v_0 \xi_0}{2D_0} a \left(1 - \frac{2}{\pi} \frac{\cos^{-1}(\lambda/\xi_0)}{\sqrt{1 - (\lambda/\xi_0)^2}} \right) \right]. \tag{5.56}
\end{aligned}$$

Equations (5.53) and (5.56) can be solved for a and the cluster density ρ_c , which reads

$$\rho_c = \bar{\rho} \left[1 - \frac{v_0^2 \xi_0^2}{4D_0^2 (1 + v_0^2/v_*^2)} \left(1 - \frac{2}{\pi} \frac{\cos^{-1}(\lambda/\xi_0)}{\sqrt{1 - (\lambda/\xi_0)^2}} \right) \right]^{-1}, \tag{5.57}$$

with $\bar{\rho} \equiv \frac{2D_c}{\gamma \lambda} \bar{c}$.

For a given outer speed v_0 , threshold \bar{c} and decay length λ , the density and polarization profiles can now be constructed via Eqs. (5.50) and (5.51), see Fig. 5.2(b). In Fig. 5.2(c), we plot ρ_c [Eq. (5.57)] and ρ_g [combining Eqs. (5.54), (5.57)] normalized by the global density ρ_0 as a function of the reduced outer speed v_0/v_* . The coexistence of a passive and an active domain is only possible for propulsion speeds v_0 higher than a minimal speed v_{\min} set by the condition $\rho_g = \rho_0$. For speeds $v_0 < v_{\min}$, Eqs. (5.54) and (5.57) would predict a gas density ρ_g higher than the homogeneous density ρ_0 , which is unphysical in our system given the shape of the density profile [Fig. 5.2(b)]. Consequently, for these speeds, the remaining solution $\rho(x) = \rho_0$ describing a homogeneous active gas (all particles have speed v_0) is selected by the system. With rising speed, the cluster density ρ_c saturates at

$$\rho_c(v_0 \rightarrow \infty) = \bar{\rho} \left[\frac{1}{2} + \frac{\cos^{-1}(\sqrt{8}\lambda/\ell)}{\pi \sqrt{1 - 8(\lambda/\ell)^2}} \right]^{-1} \tag{5.58}$$

and the gas density ρ_g converges to zero as a consequence of the enhanced active current into the passive region.

The \bar{c} - v_0 phase diagram in Fig. 5.2(d) summarizes the results and displays the three different states already reported in Chap. 4. For thresholds smaller than the concentration c_0 [Eq. (5.11)] of the uniform system ($\bar{c} < c_0$), the system is homogeneous and all particles are passive. For $\bar{c} > c_0$, the system is either a homogeneous active gas ($v_0 < v_{\min}$) or becomes spatially inhomogeneous developing an interface between a dense passive and a dilute active domain ($v_0 > v_{\min}$). In order to enable phase coexistence at greater thresholds \bar{c} , a higher speed v_{\min} is required.

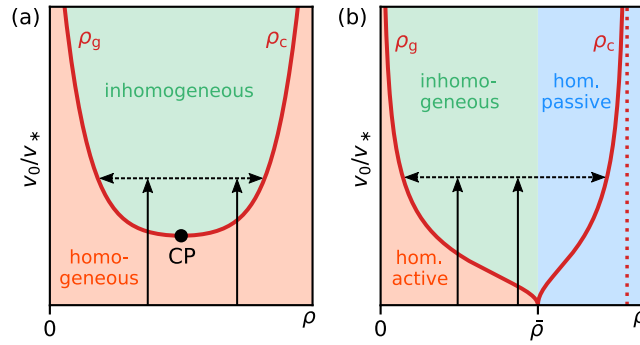


Fig. 5.3. $v_0 - \rho$ phase diagrams. (a) Schematic phase diagram for active Brownian particles with repulsive interactions. The coexistence region is bounded by the binodal (red line), which terminates in the critical point (CP). Vertical arrows show two quenches to the same speed but at different global densities ρ_0 yielding the same coexisting densities (but different relative size of dilute to dense regions). (b) Phase diagram at fixed threshold \bar{c} for the discontinuous motility response, exhibiting no critical point. The system becomes homogeneous and passive for $\rho_0 > \bar{\rho}$ at all speeds. The prediction Eq. (5.58) for the maximal cluster density is shown as dashed line. Reprinted with permission from Ref. [48]. Copyright 2020 by the American Physical Society.

Comparison to MIPS

In Fig. 5.3, we plot the $v_0 - \rho$ phase diagram for a fixed threshold \bar{c} [without normalizing ρ with the global density ρ_0 as in Fig. 5.2(c)] and a schematic phase diagram of MIPS of ABPs with repulsive interactions that was discussed in Sec. 2.3.3 and Chap. 3. In case of MIPS, on quenching the system into the two-phase region, the stable steady state is inhomogeneous and the coexisting densities lie on the binodal. Varying the global density, the coexisting densities remain the same but the relative size of the domains changes according to the lever rule [140]. The coexisting densities meet at the critical point below which the system is homogeneous irrespective of the global density. For the discontinuous motility response studied here, a state of coexistence can be reached as well and we suspect that the lever rule that sets the size of the domains applies. However, there are important differences to the MIPS phase diagram. First, the two-phase region cannot be entered for all global densities ρ_0 between ρ_g and ρ_c , but only for $\rho_0 < \bar{\rho}$ when crossing the gas density at $v_0 > v_{\min}$. For $\rho_0 > \bar{\rho}$, the entire system becomes passive and homogeneous as $c_0 > \bar{c}$. Secondly, there is no critical point setting a lower bound of the coexistence region at finite v_0 as for MIPS. On decreasing v_0 , the two-phase region becomes narrower and ends at a single point at $v_0 = 0$ with density $\bar{\rho}$ [cf. Eqs. (5.54), (5.57)]. Therefore, stable aggregation can be achieved even at very low propulsion speeds in a region of parameter space primarily determined by the threshold \bar{c} .

5.4.2 Circular interface

We now consider a steady state with a circular cluster of radius r_c with speed $v^<$ surrounded by a region with speed $v^>$. Going to polar coordinates (r, θ) with $r = 0$ at the system's center of mass, the normal vector of the bounding curve $\partial\mathcal{C}$ is $\mathbf{n} = \mathbf{e}_r$. Due to symmetry, we anticipate a radially symmetric density profile $\rho(r)$ and polarization $\mathbf{p} = p(r)\mathbf{e}_r$. In polar coordinates, Eqs. (5.40) and (5.42) read

$$\partial_r \rho = \frac{v}{D_0} p, \quad (5.59)$$

$$0 = -\frac{1}{2} \partial_r (v\rho) + D_0 \left(1 + \frac{v^2}{v_*^2} \right) \left(\partial_r^2 p + \frac{1}{r} \partial_r p - \frac{p}{r^2} \right) - D_{\Gamma} p. \quad (5.60)$$

Within the individual regions of constant speed, these two equations can be combined into (the prime denotes the derivative with respect to r)

$$0 = p'' + \frac{p'}{r} - \frac{p}{r^2} - \frac{p}{\xi^2}, \quad (5.61)$$

with length scale ξ as defined in Eq. (5.49) (depending on $v^<$ or $v^>$ instead of v_0). Equation (5.61) is the modified Bessel equation, whose general solution reads [183]

$$p(r) = a_1 I_1(r/\xi) + a_2 K_1(r/\xi), \quad (5.62)$$

with $I_n(x)$ and $K_n(x)$ modified Bessel functions of order n of the first and second kind respectively. To determine the integration constants a_1 and a_2 , it is important to keep in mind the following limits of the modified Bessel functions

$$\lim_{x \rightarrow 0} I_n(x) = 0, \quad \lim_{x \rightarrow \infty} I_n(x) = \infty, \quad (5.63)$$

$$\lim_{x \rightarrow 0} K_n(x) = \infty, \quad \lim_{x \rightarrow \infty} K_n(x) = 0. \quad (5.64)$$

In the outer region, we require $p \rightarrow 0$ as $r \rightarrow \infty$ and thus $a_1^> = 0$. The density profile can be obtained through integrating Eq. (5.59) as

$$\rho(r) = \frac{v\xi}{D_0} [a_1 I_0(r/\xi) - a_2 K_0(r/\xi)] + b, \quad (5.65)$$

with another integration constant b . As $r_c \rightarrow 0$, the integral over the density (i.e., number of particles) in the inner region should vanish. Therefore $a_2^< = 0$, since $K_0(r/\xi)$ diverges at the origin [Eq. (5.64)]. Furthermore, $b^> = \rho_g$ as, for $r \rightarrow \infty$, the density is that of the active gas.

Passive circular clusters

In the next step, we set $v^< = 0$ and $v^> = v_0$, turning to the situation of a circular cluster of passive particles surrounded by an active gas, as discussed in Chap. 4. As for the planar interface, this implies $p = 0$ ($a_1^< = 0$) and a constant density ρ_c ($b^< = \rho_c$) inside the cluster. Summarizing, the density and polarization profiles read

$$\rho(r) = \begin{cases} \rho_c, & \text{for } r < r_c \\ -\frac{v_0 \xi_0}{D_0} a_2^> K_0(r/\xi_0) + \rho_g, & \text{for } r > r_c \end{cases}, \quad (5.66)$$

$$p(r) = \begin{cases} 0, & \text{for } r < r_c \\ a_2^> K_1(r/\xi_0), & \text{for } r > r_c \end{cases}, \quad (5.67)$$

for which we need to determine ρ_c , ρ_g , r_c and $a_2^>$. To this end, we need four additional equations fixing these parameters.

The first condition is the continuity of the density [Eq. (5.47)], requiring

$$\rho_c = -\frac{v_0 \xi_0}{D_0} a_2^> K_0(r_c/\xi_0) + \rho_g, \quad (5.68)$$

from which we see that $a_2^> < 0$ in order to ensure $\rho_c > \rho_g$. Moreover, the jump condition (5.44) has to be fulfilled. Here, it reads

$$0 = -\frac{1}{2} v_0 \rho^> + D_0 \left(1 + \frac{v_0^2}{v_*^2} \right) p'^>. \quad (5.69)$$

Using

$$\begin{aligned} p'^> &= -a_2^> \left[\frac{K_0(r_c/\xi_0)}{\xi_0} + \frac{K_1(r_c/\xi_0)}{r_c} \right] \\ &= \frac{D_0}{v_0 \xi_0^2} (\rho^> - \rho_g) - \frac{p^>}{r_c}, \end{aligned} \quad (5.70)$$

Eq. (5.69) can be recast into (using $\rho^> = \rho_c$)

$$\rho_c = \left(1 + 8 \frac{v_0^2}{v_*^2} \right) \rho_g + \frac{v_0}{D_r} \left(1 + \frac{v_0^2}{v_*^2} \right) \frac{p^>}{r_c}, \quad (5.71)$$

with the polarization at (the outer side of) the cluster boundary

$$p^> = a_2^> K_1(r_c/\xi_0) < 0. \quad (5.72)$$

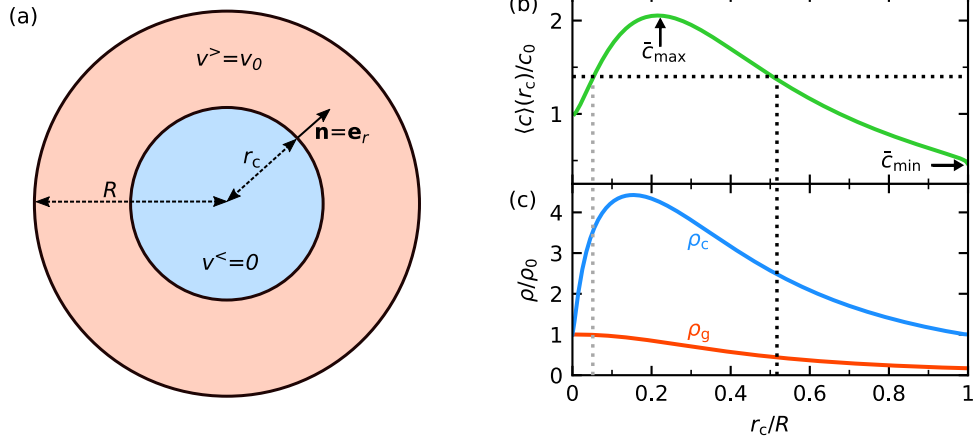


Fig. 5.4. Phase separation with a circular interface. (a) Sketch of the geometry. Inside a circular confinement of radius R , a circular passive region ($v^< = 0$) of radius r_c with surface normal $\mathbf{n} = \mathbf{e}_r$ coexists with an active phase ($v^> = v_0$). (b) Concentration at cluster boundary $\langle c \rangle(r_c)$ [solution of Eq. (5.75)] and (c) coexisting densities as function of cluster size r_c for $R = 66.4\ell$, $\lambda = 15.6\ell$, $v_0 = 0.8v_*$. For a given threshold $\bar{c} > c_0$ (dotted line $\bar{c} = 1.4c_0$) there are two solutions for r_c with different coexisting densities $\rho_{c,g}$ (only the solution with larger r_c is stable). The maximum \bar{c}_{\max} sets the maximal threshold at which passive clusters can exist. The value of $\langle c \rangle(r_c = R)$ sets the minimum threshold \bar{c}_{\min} below which the system is entirely passive. (b),(c) are reprinted in adapted form with permission from Ref. [48]. Copyright 2020 by the American Physical Society.

Note that Eq. (5.71) is equal to Eq. (5.54), which was obtained for a planar interface, plus an additional correction term $\sim 1/r_c$. Consequently, as one might have expected, for an infinitely large cluster ($r_c \rightarrow \infty$), the results for a circular and planar interface become equal.

In order to get closer to the situation studied in Chap. 4, we additionally assume a circular confinement of radius R around the system with the particles' center of mass located at the center of the confinement (i.e., $\rho(r) = 0$ for $r > R$), see Fig. 5.4(a). Imposing no-flux boundary conditions, the number of particles in the confinement has to be conserved implying

$$\int d\mathbf{r} \rho(\mathbf{r}) = \rho_0 A, \quad (5.73)$$

with $A = \pi R^2$ the area of the system. Inserting the density profile (5.66) and evaluating the integral leads to

$$\rho_c = \rho_0 - \frac{R^2 - r_c^2}{R^2} \frac{\xi_0 v_0}{D_0} a_2^> K_0(r_c/\xi_0) - \frac{2\xi_0^2 v_0}{D_0 R^2} a_2^> [R K_1(R/\xi_0) - r_c K_1(r_c/\xi_0)]. \quad (5.74)$$

Through Eqs. (5.68, 5.71, 5.74), ρ_c , ρ_g and $a_2^>$ are fixed as functions of the cluster radius r_c . Thus, we know the density profile $\rho(r, r_c)$ as function of r and r_c .

Using expression (A.7) from the appendix, the concentration at r_c is given by

$$\frac{\langle c \rangle(r_c)}{c_0} = \int_0^R dr' r' \frac{\rho(r', r_c)}{\rho_0} \int_0^\infty dk \frac{k}{\sqrt{1 + (k\lambda)^2}} J_0(kr_c) J_0(kr'), \quad (5.75)$$

with $J_0(x)$ the Bessel function of first kind and order zero. For given v_0 , λ , ρ_0 and R , the integral (5.75) can be calculated numerically in the range $0 \leq r_c \leq R$. Figures 5.4(b,c) show a typical plot of the function $\langle c \rangle(r_c)$ and the corresponding coexisting densities $\rho_{c,g}(r_c)$ obtained in this way, which give a good overview of the possible steady states of the system. For $r_c = 0$, the entire system is an active gas with density $\rho_g = \rho_0$ and the concentration $\langle c \rangle(0)$ is given by Eq. (4.24) with $d = 0$. In the plot, $\langle c \rangle(0) \approx c_0$ since $\lambda \ll R$. In the opposite limit $r_c = R$, the system is completely passive with $\rho_c = \rho_0$ and minimal boundary concentration [Eq. (4.23) with $d = 0$]

$$\langle c \rangle(R) = \frac{1}{2} c_0 [1 - I_0(2R/\lambda) + L_0(2R/\lambda)] < \langle c \rangle(0), \quad (5.76)$$

with $L_0(x)$ the modified Struve function of order zero. For values $0 < r_c < R$, a passive and an active region coexist. With rising r_c , the gas density decreases from $\rho_g = \rho_0$, while the cluster density first increases and then decays towards $\rho_c = \rho_0$. Similarly, the boundary concentration $\langle c \rangle(r_c)$ rises from $\langle c \rangle(0) \approx c_0$, before it reaches a maximum at a radius r_c^* and decreases.

The value r_c the system takes for a given threshold \bar{c} , is then set by the condition [compare Eq. (5.55)]

$$\bar{c} \stackrel{!}{=} \langle c \rangle(r_c), \quad (5.77)$$

which eventually fully determines the profiles $\rho(r)$ and $p(r)$. As already seen in Chap. 4, the minimal threshold required for an inhomogeneous system is set by $\bar{c}_{\min} = \langle c \rangle(R)$ [Eq. (5.76)]. For $\bar{c} < \bar{c}_{\min}$, the system is uniform and passive. The maximal threshold \bar{c}_{\max} above which no phase-separated system can exist is given by the maximum of $\langle c \rangle(r_c)$ at r_c^* . For $\bar{c} > \bar{c}_{\max}$, the system is a homogeneous active gas. Inbetween these bounds, phase coexistence is possible and, interestingly, for $\bar{c} > \langle c \rangle(0)$, two solutions $r_c^{(1)}$ and $r_c^{(2)}$ (with $r_c^{(1)} < r_c^{(2)}$) exist. However, we argue that the smaller solution $r_c^{(1)}$ is unstable, since the slope $\langle c \rangle'(r_c^{(1)}) > 0$: increasing r_c by a small amount, the boundary concentration rises above \bar{c} and additional particles at the boundary turn passive, leading to further cluster growth. Similarly, a decrease of r_c triggers cluster shrinkage. For the larger solution $r_c^{(2)}$, the reverse holds as $\langle c \rangle'(r_c^{(2)}) < 0$. An increase of r_c lowers $\langle c \rangle(r_c)$ below \bar{c} and particles at the rim turn active, thus stabilizing the cluster. Indeed, in simulations, only steady states corresponding to the stable solution $r_c^{(2)}$ are observed, as we will see in the next section.

5.4.3 Simulations

Simulation details

We now turn to numerical simulations in order to test our analytical predictions. Simulations are performed analogous to those described in Sec. 4.1.3. Using the same simulation code, we solve Eqs. (5.1),(5.2) with $\chi = 0$ for $N = 800$ particles, additionally interacting via the repulsive WCA potential, Eq. (2.30), with length scale σ and strength $\epsilon = 100k_B T$. The rotational diffusion coefficient is set to $D_r = 3D_0/d_{\text{BH}}^2$ [Eq. (2.13)] with Barker-Handerson particle diameter $d_{\text{BH}} = 1.10688\sigma$. As units of length, time and energy we use σ , σ^2/D_0 and $k_B T$ respectively. As in Sec. 4.3, we impose a circular confinement of radius R by instantaneously redirecting the orientation of particles that reach the boundary towards the confinement's center. We set $R = 42.4$ implying a packing fraction $\phi_0 = N \frac{(d_{\text{BH}}/2)^2}{R^2} = 0.136$ (which corresponds to a particle number density $\rho_0 = 0.141$). Particles are randomly initialized inside the confinement and simulations are run for a time frame $\Delta t = 600$. As in Chap. 4, every particle k acts as a point source of signaling molecules and senses the concentration of molecules at its position $c_k(\mathbf{r}_k)$ generated by the other particles according to Eq. (4.5). When c_k is smaller than the threshold value \bar{c} , the particle propels with speed v_0 . For $c_k > \bar{c}$, its propulsion speed is set to zero. Note that in the analytical theory presented above, we have assumed that particles only sense the *mean* concentration $\langle c_k \rangle$, Eq. (4.8).

We perform simulations for different decay lengths of the chemical λ , varying the threshold \bar{c} and the propulsion speed v_0 (the latter was kept constant in Chap. 4) in the parameter range where the system separates into a dense passive cluster and a dilute active gas, see Fig. 5.5(a) for a snapshot. Again, we measure the radial steady-state density profile $\rho(r)$ with respect to the particles' center of mass [an example is shown in Fig. 5.5(b)], which we fit with expression (4.21) to extract the coexisting densities ρ_c and ρ_g , as well as the cluster radius r_c and the interfacial width ω . In agreement with the findings from Chap. 4 [Fig. 4.5(c)], with rising \bar{c} , both the cluster and the gas become denser while the cluster size decreases, cf. 5.5(c,d). On increasing v_0 (at fixed \bar{c}), the clusters become denser (and larger), while the gas density is reduced due to a stronger active current into the cluster, as predicted by the theoretical results [Fig. 5.2 and Eq. (5.71)]. Moreover, the maximal threshold up to which the formation of stable clusters is observed increases with v_0 . The interfacial width ω is plotted in Fig. 5.5(e) versus v_0 for different λ (as in Fig. 4.10, ω is averaged over runs in the range of thresholds where it is \bar{c} -independent), showing a notable increase for smaller v_0 . Presumably, this can be attributed to enhanced

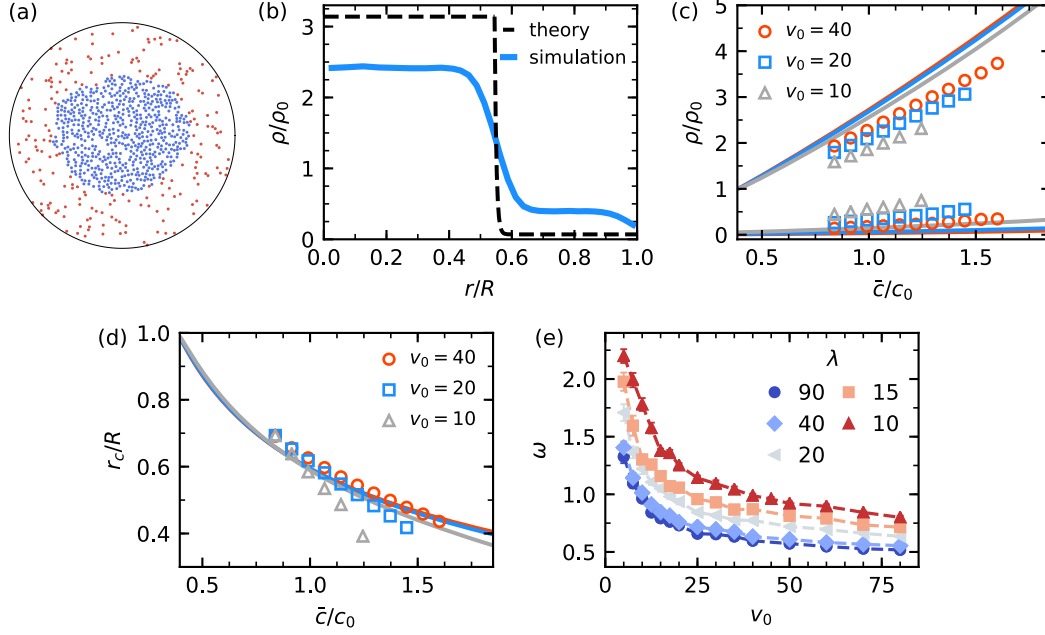


Fig. 5.5. (a) Simulation snapshot for $v_0 = 20$, $\lambda = 10$, $\bar{c} = 1.1c_0$ showing a passive cluster (blue) surrounded by an active gas (red). (b) Corresponding radial density profile $\rho(r)$ from simulations (blue) and theory [Eq. (5.66)]. (c,d) Cluster and gas densities (c) and cluster radius r_c (d) versus threshold \bar{c} for different propulsion speeds v_0 at $\lambda = 10$ (symbols: simulations, lines: theory). Stable clusters also exist at lower \bar{c} than shown here, but in that case the gas density cannot be measured reliably due to the influence of the confinement. Standard errors are smaller than symbol size. (e) Interfacial width ω between cluster and gas versus v_0 for different λ . Error bars show standard errors. Reprinted in adapted form with permission from Ref. [48]. Copyright 2020 by the American Physical Society.

fluctuations of particle currents for lower speeds (random diffusive motion of active particles becomes more important). Additionally, the interface becomes broader for shorter decay lengths λ due to stronger fluctuations of the concentration signal, as already discussed in Sec. 4.3 [Fig 4.10(c)].

Comparison with mean-field theory

For a quantitative comparison with the analytical results, the excluded volume of the particles has to be taken into account in the mean-field theory (in which particles are treated as points) since it affects the mean concentration measured by particles, as discussed in Sec. 4.1.1. To this end, the correction term [Eq. (4.16) evaluated at r_c]

$$\frac{c_{\text{corr}}(r_c)}{c_0} = \frac{\rho_c}{\rho_0} \left(1 - e^{-d_{\text{BH}}/\lambda}\right) \quad (5.78)$$

must be subtracted from $\langle c \rangle(r_c)$ [Eq. (5.75)], when condition (5.77) is solved for the cluster radius r_c .

Fig. 5.5(b) compares the density profile for $\lambda = 10$, $v_0 = 20$ and $\bar{c} = 1.1c_0$ from the simulations to the theoretically predicted stable solution. The latter decays sharply at the interface between the regions of speed zero and v_0 , i.e., the decay length ξ_0 is very small. This is in contrast to the broad interface observed in the simulations that arise from fluctuations that are not accounted for in the mean-field theory.

Moreover, the theory considerably overestimates the cluster density and underestimates the gas density, which also holds for different thresholds and propulsion speeds, cf. Fig. 5.5(c). This suggests that the particle current through the interface from the cluster into gas is considerably smaller in the theory than in the simulations. Within the mean-field theory, a particle leaves the cluster (it turns from passive to active), when it moves from $r < r_c$ to $r > r_c$, which is only possible via translational diffusion of the particle itself (the current out of the cluster is $-D_0 \nabla \rho$), see Fig. 5.6(a). However, this picture is based on the assumption that particles sense mean concentrations, which is not valid in the simulations. There, due to the motion of the surrounding particles, the concentration signal a particle senses fluctuates (even if the particle would be held fixed). Hence, the particles at the boundary of the cluster keep changing between sensing super- and sub-threshold concentrations and thus constantly switch between passive and active. When a passive particle at the interface turns active due to a concentration fluctuation and is oriented towards the gas, it can leave the cluster (if it swims sufficiently far away from the surface before turning passive again due to another fluctuation), cf. Fig. 5.6(a). As this additional fluctuation-induced particle current is not included in the mean-field theory, the disagreement with the simulations is not surprising.

Effective diffusion coefficient

In order to include this process into the theory, we assume that its dominant effect is an additional diffusive current $\mathbf{j}_{\text{fluc}} = -D_{\text{fluc}} \nabla \rho$ through the interface. As the density gradient is small away from the interface, this current is of importance only in its vicinity, in agreement with the above described mechanism. We therefore replace D_0 by an increased effective translational diffusion coefficient $D_{\text{eff}} = D_0 + D_{\text{fluc}}$. Solving the theory for $\rho(r)$ for different values of D_{eff} , we find that upon increasing D_{eff} , indeed, the cluster density decreases and the gas density rises (also the decay length ξ_0 becomes larger), as shown in Fig. 5.6(b). For $D_{\text{eff}} = 10.2D_0$ (at $v_0 = 20$, $\lambda = 10$, $\bar{c} = 1.1c_0$) we find very good agreement with the numerical density profile,

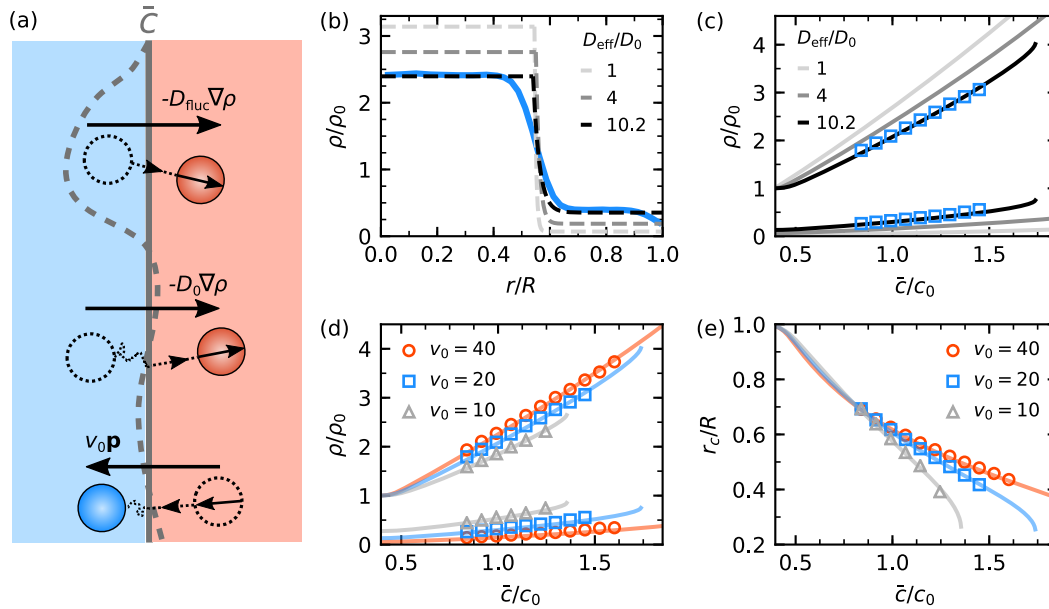


Fig. 5.6. Fitting via effective diffusion coefficient D_{eff} . (a) Sketch illustrating the mechanisms behind the different currents through the interface between passive cluster (blue) and active gas (red). Bottom: Active current $v_0\mathbf{p}$ into the cluster due to self-propelled motion. Center: Translational diffusion leads to the diffusive current $-D_0\nabla\rho$ into the gas. Top: Passive particles close to the mean interface position (solid gray line with $\langle c \rangle = \bar{c}$) can turn active due to concentration fluctuations (the dashed line is the fluctuating interface with $c_k = \bar{c}$) and swim into the gas. This leads to an additional fluctuation-induced current $-D_{\text{fluc}}\nabla\rho$ and thus to an effective diffusion coefficient $D_{\text{eff}} = D_0 + D_{\text{fluc}}$. (b) Radial density profile $\rho(r)$ at $v_0 = 20$, $\lambda = 10$, $\bar{c} = 1.1c_0$ from simulations (solid blue line) compared to the theoretical prediction for different values of D_{eff} (dashed lines). (c) Coexisting densities versus \bar{c} at $v_0 = 20$, $\lambda = 10$ (symbols: simulations, lines: theory for different D_{eff}). (d,e) Coexisting densities (d) and cluster radius r_c (e) versus \bar{c} for $\lambda = 10$ and different velocities. Symbols: simulations, lines: theory with D_{eff} obtained from fits ($v_0 = 10$: $D_{\text{eff}} = 7.1D_0$, $v_0 = 20$: $D_{\text{eff}} = 10.2D_0$, $v_0 = 40$: $D_{\text{eff}} = 11.4D_0$). (b,d,e) are reprinted in adapted form with permission from Ref. [48]. Copyright 2020 by the American Physical Society.

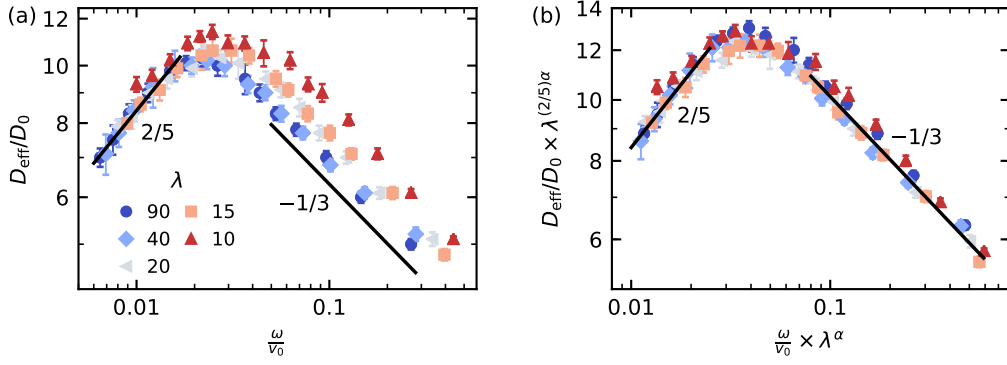


Fig. 5.7. (a) Fitted effective diffusion coefficients D_{eff} versus the ratio of interfacial width and propulsion speed ω/v_0 for different λ as double-logarithmic plot. The solid lines indicate scalings $\sim (\omega/v_0)^{2/5}$ (left) and $\sim (\omega/v_0)^{-1/3}$ (right). Errorbars show standard deviations of fits. (b) Plotting $D_{\text{eff}}\lambda^{(2/5)\alpha}$ versus $(\omega/v_0)\lambda^\alpha$ with $\alpha = 0.13$, the data collapses, which implies relation (5.80). (b) is reprinted with permission from Ref. [48]. Copyright 2020 by the American Physical Society.

which demonstrates the relevance of the fluctuation-induced current. Interestingly, with the same value of D_{eff} , the theory still predicts the coexisting densities ρ_c and ρ_g at different thresholds \bar{c} (at fixed v_0 and λ) well, see Fig. 5.6(c). Therefore, we treat $D_{\text{eff}}(v_0, \lambda)$ as an effective parameter, by which we simultaneously fit the theory curves $\rho_c(\bar{c})$ and $\rho_g(\bar{c})$ to the simulation data. To perform the fit, for given v_0 and λ , we first solve the theory for $\rho_{c,g}(\bar{c})$ (as described in Sec. 5.4.2) for a range of D_{eff} values with step width $0.1D_0$. The best fit minimizes the objective function $L(D_{\text{eff}})$, for which we choose the sum of squared errors [68]

$$L(D_{\text{eff}}) = \frac{1}{2} \sum_{i=1}^{N_{\bar{c}}} \left[(\rho_{c,\text{theo}}(\bar{c}_i, D_{\text{eff}}) - \rho_{c,\text{sim}}(\bar{c}_i))^2 + (\rho_{g,\text{theo}}(\bar{c}_i, D_{\text{eff}}) - \rho_{g,\text{sim}}(\bar{c}_i))^2 \right] \quad (5.79)$$

of the cluster and gas densities at the $N_{\bar{c}}$ thresholds \bar{c}_i where data has been obtained.⁴ Figure 5.6(d,e) shows that via this fitting procedure, even for parameters different from that used in Fig. 5.6(b,c), good agreement for the coexisting densities and the cluster radius between theory and simulations can be obtained.

Combining the fitted values $D_{\text{eff}}(v_0, \lambda)$ with the measured interfacial widths $\omega(v_0, \lambda)$ [Fig. 5.5(e)], we plot D_{eff} versus ω/v_0 in Fig. 5.7(a). The quantity ω/v_0 can be regarded as a measure for the time a particle that has switched from passive to active at the cluster's surface needs to travel through the interface (of width ω) with propulsion speed v_0 to enter the active gas. When a particle has to spend a longer

⁴The standard deviation of the thus obtained best fit parameter D_{eff}^* can be estimated as $\sigma(D_{\text{eff}}^*) = \sigma_\rho \left(\frac{\partial^2 L}{\partial D_{\text{eff}}^2} \Big|_{D_{\text{eff}}^*} \right)^{-1/2}$, with σ_ρ the standard deviation of the measurements of cluster and gas density [68].

time in the interfacial region in order to escape from the cluster, the probability that it turns passive again due to another concentration fluctuation (and thus reenters the cluster before reaching the gas) is increased. Therefore, a diminishing number of particles successfully leave the cluster, which implies a lower outward particle current. This picture is confirmed by the fitted values of D_{eff} , which for all λ decrease monotonously for $\omega/v_0 \gtrsim 0.03$, cf. Fig. 5.7(a). In this regime, the effective diffusion coefficient scales $\sim (\omega/v_0)^{-1/3}$ and is higher for smaller λ . The latter can presumably be attributed to increased concentration fluctuations in case of a smaller interaction range. For $\omega/v_0 \rightarrow 0$, i.e., sharp interfaces and high propulsion speeds [cf. Fig. 5.5(e)], the effective diffusion coefficient becomes independent of λ and decreases $\sim (\omega/v_0)^{2/5}$, indicating that fluctuations are less important. Interestingly, we observe a collapse of the entire data when rescaling it appropriately, cf. Fig. 5.7(b), implying

$$\frac{D_{\text{eff}}}{D_0} = \lambda^{-(2/5)\alpha} f\left(\lambda^\alpha \frac{\omega}{v_0}\right), \quad (5.80)$$

with exponent $\alpha \simeq 0.13$ and scaling function $f(x)$. Fig. 5.7(b) suggests that for small x , it is $f(x) \sim x^{2/5}$ and thus $D_{\text{eff}} \sim (\omega/v_0)^{2/5}$ as already seen before. In the opposite limit of large x , $f(x)$ scales $\sim x^{-1/3}$, from which we can conclude $D_{\text{eff}} \sim \lambda^{-(11/15)\alpha} (\omega/v_0)^{-1/3}$.

Phase diagrams

In the next step, we employ the obtained D_{eff} values to construct the theoretical $v_0 - \rho$ and $v_0 - \bar{c}$ phase diagrams which we quantitatively compare to the simulation results. As already seen in Fig. 5.4(b), the theory curve $\langle c \rangle(r_c)$ [Eq. (5.75)] for the concentration at the cluster boundary exhibits a maximum, which defines the maximal threshold \bar{c}_{max} up to which stable clusters can exist. This maximal value decreases for lower propulsion speeds v_0 , as shown in Fig. 5.8(a). Consequently (as for the planar interface in Sec. 5.4.1), there is a minimal speed v_{min} (determined by $\bar{c}_{\text{max}}(v_0) = \bar{c}$), only above which a stable phase-separated state exists. In the simulations [Fig. 5.5(c,d)], we have observed the existence of a maximal threshold \bar{c}_{max} that depends on v_0 . In Fig. 5.8(b), we plot the coexisting densities versus v_0 for different thresholds, showing an increase of v_{min} with \bar{c} . The minimal speeds from the simulations are in quantitative agreement with the theoretical predictions, which was not to be expected, as they are not an input to the fit for D_{eff} .

In Fig. 5.8(c), we finally plot the $v_0 - \bar{c}$ phase diagram. In the inhomogeneous region, at small thresholds \bar{c} , we observe the instantaneous formation of a dense

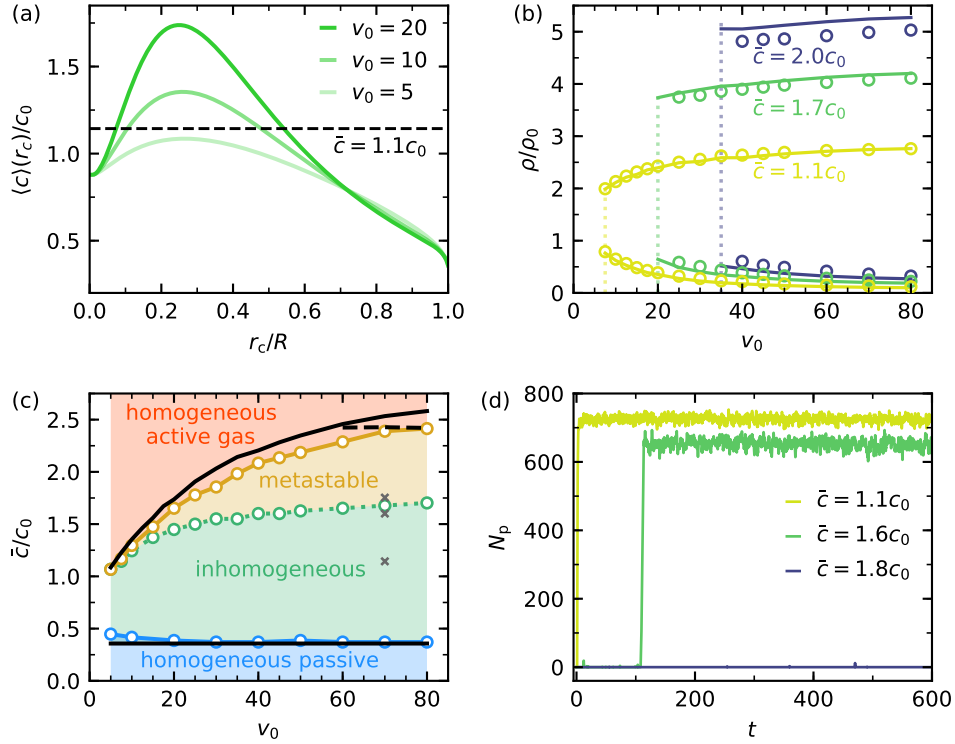


Fig. 5.8. Cluster stability and phase diagrams for circular clusters (at $\lambda = 10$). (a) Concentration at cluster boundary $\langle c \rangle(r_c)$ versus cluster size r_c [Eq. (5.75)] for different propulsion speeds v_0 . The maximum \bar{c}_{\max} (setting the maximal threshold at which passive clusters can exist) decreases for smaller speeds. Dashed line: threshold $\bar{c} = 1.1c_0$. (b) Coexisting densities for different \bar{c} versus v_0 from simulations (symbols) and theory (lines). There is a minimal speed v_{\min} below which no stable clusters exist in the simulations. Dotted lines: theory predictions for v_{\min} [given by $\bar{c}_{\max}(v_0) = \bar{c}$]. For $\bar{c} = 1.7, 2.0c_0$ the system was initialized in a crystalline configuration. (c) $v_0 - \bar{c}$ phase diagram from simulations. Blue: Passive homogeneous system (defined by $\rho_c < 1.02\rho_0$). Green: Passive clusters surrounded by an active gas form from a random initial configuration. Orange: Metastable clusters that only form from a crystalline starting configuration. Red: Homogeneous active gas. Upper black line: Maximal threshold $\bar{c}_{\max}(v_0)$ from theory. Clusters denser than dense packing are predicted above the dashed line. Lower black line: Minimal threshold $\bar{c}_{\min} = \langle c \rangle(R)$ [Eq. (5.76)]. (d) Time series of the number of passive particles N_p over the entire simulation time (started from a random initial configuration) at $v_0 = 70$ for three different thresholds (the state points are indicated in (c) as gray crosses). (b,c) are reprinted in adapted form with permission from Ref. [48]. Copyright 2020 by the American Physical Society.

cluster from a random starting configuration [green region in Fig. 5.8(c), yellow line in Fig. 5.8(d)] resembling spinodal decomposition (Sec. 2.3.3). Increasing \bar{c} , a transition to a nucleation-like behavior occurs, i.e., clusters only form after a waiting time when a sufficiently strong density fluctuation has occurred [green line in Fig. 5.8(d)]. Increasing the threshold further, the average nucleation time prolongs until no cluster formation can be observed anymore within simulation time [blue line in Fig. 5.8(d)]. In order to access the steady state within reasonable simulation time, in this metastable regime [orange region in Fig. 5.8(c)], we initialize the system in a crystalline configuration. Thereby, we do not have to wait for a nucleation event to occur. Although no sharp transition from instantaneous phase separation to nucleation exists in the simulations, in Fig. 5.8(c), we nonetheless draw a boundary separating the two regions.⁵ This line is supposed to convey a rough impression of where cluster formation takes longer than the duration of the simulations, rather than being a quantitative statement about nucleation times.

Through the simulations in the metastable regime, we find that the (speed-dependent) maximum threshold \bar{c} up to which stable clusters exist, is indeed very close to the theoretical prediction $\bar{c}_{\max}(v_0)$, cf. Fig. 5.8(c). Figure 5.8(b) shows that even at thresholds in the metastable region, the coexisting densities are well predicted by the theory (although they have not been taken into account in the fitting procedure). Presumably, the remaining discrepancies can be explained by fluctuations and the influence of the excluded volume of the particles, both of which are not included in the theory. Since there is no upper boundary for the cluster density in the theory, it can rise above the maximal packing fraction $\phi_{\max} = \pi\sqrt{3}/6$ of spheres in two dimensions [157] (corresponding to $\rho_c \approx 6.66\rho_0$), see Fig. 5.8(c). At the highest v_0 and \bar{c} we have probed in the simulations, the cluster density reaches $\sim 90\%$ of dense packing. Moreover, the prediction for the lower boundary \bar{c}_{\min} [Eq. (5.76)] below which the system is passive and homogeneous agrees well with the simulations.

⁵If not in all out of three independent simulations (for a given speed and threshold) a cluster has formed after the simulation time $\Delta t = 600$, we consider the state point to be metastable.

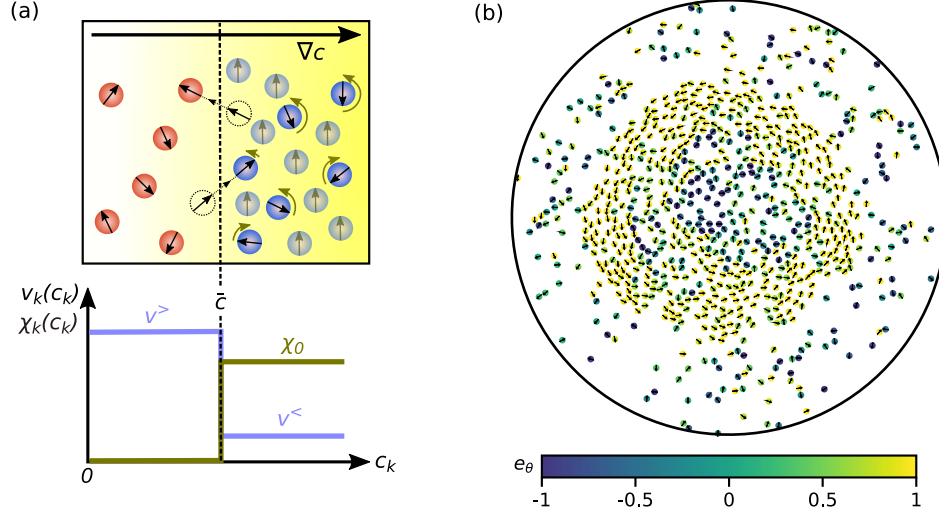


Fig. 5.9. Quorum-sensing active particles with orientational coupling. (a) Motility response $v_k(c_k)$ and orientational response $\chi_k(c_k)$ to the sensed concentration c_k (yellow): Particles switch from high speed $v^>$ to small speed $v^<$ and orient perpendicular to $\nabla_k c_k$, when c_k exceeds the threshold \bar{c} . (b) Representative snapshot of the system under circular confinement with $\lambda = 20$, $\bar{c} = 0.86c_0$, $v^> = 30$, $v^< = \frac{1}{8}v^>$ and coupling strength $\chi_0 = -32.7D_T$. Particles are colored by their angular alignment, $e_{k,\theta} = \mathbf{e}_k \cdot \mathbf{e}_\theta$. Reprinted in adapted form with permission from Ref. [48]. Copyright 2020 by the American Physical Society.

5.5 With orientational coupling: Vortex clusters

We now consider the case $\chi \neq 0$, i.e., the particle orientations φ_k couple to the direction of the concentration gradient $\mathbf{s}_k = \nabla_k c_k / |\nabla_k c_k|$ evaluated at the particle positions \mathbf{r}_k with [calculating the gradient of Eq. (4.5)]

$$\nabla_k c_k(\mathbf{r}_k) = \frac{\gamma}{4\pi D_c} \sum_{l \neq k} e^{-|\mathbf{r}_{kl}|/\lambda} \left(\frac{1}{|\mathbf{r}_{kl}|} + \frac{1}{\lambda} \right) \frac{\mathbf{r}_{kl}}{|\mathbf{r}_{kl}|^2}, \quad (5.81)$$

where $\mathbf{r}_{kl} = \mathbf{r}_l - \mathbf{r}_k$. We set $\chi^< = \chi_0 \neq 0$, $\chi^> = 0$, implying that, according to Eq. (5.2), particles with $c_k > \bar{c}$ experience a torque that aligns them perpendicular to \mathbf{s}_k [cf. Fig. 5.9(a)]. Moreover, we consider finite speeds $v^< > 0$ (with $v^< < v^>$).

5.5.1 Simulations

To get insight on how the particles' collective behavior is affected, we first perform simulations (as described in Sec. 5.4.3) with additional orientational coupling. We

set $\lambda = 20$, $\bar{c} = 0.86c_0$, $v^> = 30$ and use a slightly smaller confinement radius $R = 36.7$ as in Sec. 5.4.3, which implies a packing fraction $\phi_0 = 0.182$ and number density $\rho_0 = 0.189$.

As without orientational coupling, for $\chi_0 \neq 0$, a single, almost circular dense cluster forms at the center of the confinement (now with finite speed $v^< > 0$ instead of $v^< = 0$), which is surrounded by a dilute gas. Furthermore, inside the cluster a circular particle current arises due to orientational coupling (“vortex cluster”), cf. Fig. 5.9(b) for a snapshot at $\chi_0 = -32.7D_r$ and $v^< = \frac{1}{8}v^>$. The reason for the circular current is that the concentration gradient $\nabla_k c_k$ a particle measures, on average points towards the cluster’s center [see Fig. 5.10(a,b)]. As particles in the cluster are oriented perpendicular to the gradient due to the aligning torque, they (on average) swim along regions of constant c_k , i.e., circles around the center of the cluster, cf. Fig. 5.10(a). The direction of the current is set by the sign of χ_0 : clockwise for $\chi_0 > 0$ and anti-clockwise for $\chi_0 < 0$. Note that the observed vortex formation is not linked to the circular confinement, but also occurs in extended systems with periodic boundary conditions, see Fig. A.2.

In the next step, we quantify the orientational order in the system. Therefore, we change to polar coordinates with unit vectors \mathbf{e}_r and \mathbf{e}_θ and the origin located at the particles’ center of mass. Projecting the orientations on the unit vectors, we measure the average radial and angular component of the particle orientations

$$\langle e_r \rangle = \langle \mathbf{e}_k \cdot \mathbf{e}_r \rangle, \quad \langle e_\theta \rangle = \langle \mathbf{e}_k \cdot \mathbf{e}_\theta \rangle \quad (5.82)$$

as a function of the distance r from the center of mass. Due to the competing effects of rotational diffusion and aligning torque, $\langle e_\theta \rangle$ rises with increasing torque strength χ_0 , cf. Fig. 5.10(d). Moreover, $\langle e_\theta \rangle$ exhibits a maximum at the inner side of the interface between cluster and gas, and decays both into the gas (where $\chi_0 = 0$) and towards the center of the cluster. The latter can be explained by fluctuations of the concentration field: the average gradient a particle senses points towards the cluster’s center, $\langle \nabla c \rangle = -|\langle \partial_r c \rangle| \mathbf{e}_r$, but the magnitude $|\langle \partial_r c \rangle|$ diminishes closer to the center, see Fig. 5.10(b). This leads to enhanced fluctuations of the gradient direction, quantified by the distribution of angles δ_k between the actual direction $\nabla_k c_k / |\nabla_k c_k|$ and the mean direction $-\mathbf{e}_r$, which broadens for smaller r [compare Fig. 5.10(b)]. In turn, the direction along which a particle aligns (perpendicular to $\mathbf{s}_k = \nabla_k c_k / |\nabla_k c_k|$) fluctuates stronger, which leads to the drop of $\langle e_\theta \rangle$. As regions of increased angular alignment $\langle e_\theta \rangle$ have a lower outgoing particle current in radial direction, the density profile $\rho(r)$ is no more constant in the cluster, but has a peak close to the position of maximal $\langle e_\theta \rangle$, cf. Fig. 5.10(c).

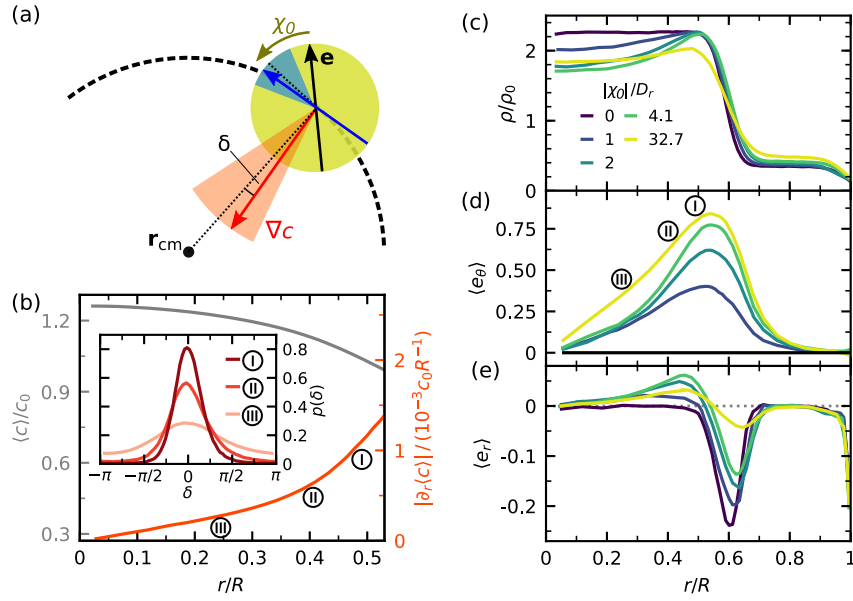


Fig. 5.10. Analysis of vortex clusters at $\lambda = 20$, $\bar{c} = 0.86c_0$, $v^> = 30$, $v^< = \frac{1}{8}v^>$. (a) Schematic illustration of the mechanism leading to the circular particle current. The concentration gradient ∇c (red) on average points towards the particles' center of mass \mathbf{r}_{cm} . The torque of strength χ_0 (brown) aligns the particle orientation \mathbf{e} perpendicular to ∇c (blue), triggering motion on a circle around \mathbf{r}_{cm} (dashed line). As the direction of ∇c fluctuates around $-\mathbf{e}_r$ (red cone, angle δ), the preferred orientation fluctuates as well (blue cone). (b) Radial profile of mean concentration $\langle c \rangle$ and magnitude of the radial component of its gradient $|\partial_r \langle c \rangle|$ inside the cluster for $\chi_0 = -32.7D_r$. Inset: Distribution of angle δ for different distances r from the center of mass (indicated by Roman numerals). (c-e) Radial profiles of (c) density ρ , (d) average angular orientation $\langle e_\theta \rangle$, and (e) radial orientation $\langle e_r \rangle$ for different χ_0 [labels in (d) refer to (b)]. Reprinted in adapted form with permission from Ref. [48]. Copyright 2020 by the American Physical Society.

Figure 5.10(e) shows that the $\langle e_r \rangle$ -profile is influenced by the orientational coupling as well. For $\chi_0 = 0$, it exhibits a negative peak at the interface between the regions of small and high propulsion speed where particle orientations on average point into the cluster. With rising torque strength χ_0 , this peak diminishes, which results in a stronger current of particles out of the cluster and thus in a higher gas density, cf. Fig. 5.10(c). Additionally, a weaker positive peak of $\langle e_r \rangle$ arises at the inner side of the density maximum.

5.5.2 Theory

We now generalize the theory for circular clusters from Sec. 5.4.2 to the case of additional orientational coupling. We set $\chi^< = \chi_0$ and $\chi^> = 0$ and use the mean direction of the concentration gradient $\mathbf{s} = -\mathbf{e}_r$ pointing towards the origin. The

polarization $\mathbf{p}(r) = p_r(r)\mathbf{e}_r + p_\theta(r)\mathbf{e}_\theta$ now has an additional angular component. In the steady state, the radial component of the current \mathbf{j} [Eq. (5.22)] still has to vanish, $j_r = 0$, implying

$$D_0 \partial_r \rho = v p_r. \quad (5.83)$$

However, the angular current is now non-zero and given by $j_\theta = v p_\theta$ ($\partial_\theta \rho = 0$ due to the radial symmetry of the density profile).

In order to write the polarization equation (5.23) in polar coordinates, we need the matrix \mathbf{M} [Eq. (5.24)], which reads $\mathbf{M} = \mathbf{M}_0 + \mathbf{M}_\chi$ with \mathbf{M}_0 from Eq. (5.41) and

$$\begin{aligned} \mathbf{M}_\chi &= \frac{\chi v}{16D_r} [3(\mathbf{s} \otimes \mathbf{p}) \cdot \mathbf{R} - \mathbf{R} \cdot (\mathbf{s} \otimes \mathbf{p})] \\ &= \frac{\chi v}{16D_r} [-3(p_r \mathbf{e}_r \otimes \mathbf{e}_r + p_\theta \mathbf{e}_r \otimes \mathbf{e}_\theta) \cdot \mathbf{R} + \mathbf{R} \cdot (p_r \mathbf{e}_r \otimes \mathbf{e}_r + p_\theta \mathbf{e}_r \otimes \mathbf{e}_\theta)] \\ &= \frac{\chi v}{16D_r} (-3p_\theta \mathbf{e}_r \otimes \mathbf{e}_r + 3p_r \mathbf{e}_r \otimes \mathbf{e}_\theta + p_r \mathbf{e}_\theta \otimes \mathbf{e}_r + p_\theta \mathbf{e}_\theta \otimes \mathbf{e}_\theta), \end{aligned} \quad (5.84)$$

where $\mathbf{R} \cdot \mathbf{e}_r = -\mathbf{e}_r \cdot \mathbf{R} = \mathbf{e}_\theta$ and $\mathbf{e}_\theta \cdot \mathbf{R} = -\mathbf{R} \cdot \mathbf{e}_\theta = \mathbf{e}_r$. For Eq. (5.23), we need the divergence of \mathbf{M}_χ , which, away from the jump in χ and v , is given by⁶

$$\nabla \cdot \mathbf{M}_\chi = \frac{\chi v}{16D_r} \left[- \left(3\partial_r p_\theta + \frac{4p_\theta}{r} \right) \mathbf{e}_r + \left(3\partial_r p_r + \frac{4p_r}{r} \right) \mathbf{e}_\theta \right]. \quad (5.85)$$

Moreover, it is

$$\frac{v}{16D_r} [\nabla \cdot (\chi \mathbf{s}) \mathbf{R} \cdot \mathbf{p} - \nabla \cdot (\mathbf{R} \cdot \chi \mathbf{s}) \mathbf{p}] = \frac{\chi v}{16D_r} \left(\frac{p_\theta}{r} \mathbf{e}_r - \frac{p_r}{r} \mathbf{e}_\theta \right). \quad (5.86)$$

Plugging Eqs. (5.85) and (5.86) into Eq. (5.23) (with $\partial_t \mathbf{p} = 0$) and collecting terms in direction of \mathbf{e}_r and \mathbf{e}_θ , yields the two coupled equations (which are valid away from the jump in χ and v)

$$0 = -\frac{1}{2} v \partial_r \rho + D_0 \left(1 + \frac{v^2}{v_*^2} \right) \nabla^2 p_r - \left(D_r + \frac{\chi^2}{8D_r} \right) p_r - \frac{3\chi v}{16D_r} \left(p'_\theta + \frac{p_\theta}{r} \right), \quad (5.87)$$

$$0 = -\frac{1}{2} \chi \rho + D_0 \left(1 + \frac{v^2}{v_*^2} \right) \nabla^2 p_\theta - \left(D_r + \frac{\chi^2}{8D_r} \right) p_\theta + \frac{3\chi v}{16D_r} \left(p'_r + \frac{p_r}{r} \right). \quad (5.88)$$

On rearranging terms and inserting Eq. (5.83), we arrive at the two coupled inhomogeneous modified Bessel equations

$$0 = p_r'' + \frac{p_r'}{r} - \frac{p_r}{r^2} - \frac{p_r}{\xi_\chi^2} - \frac{3\chi v}{v_*^2 + v^2} \left(p'_\theta + \frac{p_\theta}{r} \right), \quad (5.89)$$

⁶In polar coordinates the divergence of a tensor of rank two \mathbf{S} reads [6]
 $\nabla \cdot \mathbf{S} = [\partial_r S_{rr} + \frac{1}{r} \partial_\theta S_{\theta r} + \frac{1}{r} (S_{rr} - S_{\theta\theta})] \mathbf{e}_r + [\partial_r S_{r\theta} + \frac{1}{r} \partial_\theta S_{\theta\theta} + \frac{1}{r} (S_{r\theta} + S_{\theta r})] \mathbf{e}_\theta.$

$$0 = p_\theta'' + \frac{p_\theta'}{r} - \frac{p_\theta}{r^2} - \frac{p_\theta}{\xi_\chi^2} + \frac{3\chi v}{v_*^2 + v^2} \left(p_r' + \frac{p_r}{r} \right) - \frac{\chi}{2D_0[1 + (v/v_*)^2]} \rho, \quad (5.90)$$

with radial decay length

$$\xi_\chi \equiv \ell \left[\frac{1 + (v/v_*)^2}{1 + 8(v/v_*)^2 + \frac{1}{8}(\chi/D_r)^2} \right]^{1/2} \quad (5.91)$$

and angular decay length

$$\tilde{\xi}_\chi \equiv \ell \left[\frac{1 + (v/v_*)^2}{1 + \frac{1}{8}(\chi/D_r)^2} \right]^{1/2}, \quad (5.92)$$

generalizing the decay length ξ_0 [Eq. (5.49)] obtained without orientational coupling. Determining a closed solution of Eqs. (5.89), (5.90) is a considerable challenge. Instead, here we try to obtain some qualitative insights by studying the limit of vanishing translational diffusion ($D_0 = 0$), which significantly simplifies the analytical treatment. Under this assumption, it is $p_r = 0$ everywhere [Eq. (5.83)]. Then, Eq. (5.88) implies the following relation between density and angular polarization

$$p_\theta(r) = -\frac{1}{2} \frac{\chi/D_r}{1 + \chi^2/(8D_r^2)} \rho(r). \quad (5.93)$$

In the outer region with $\chi = 0$, we thus have $p_\theta = 0$ and a constant density ρ_g [Eq. (5.87)]. In the inner region with $\chi = \chi_0$, plugging Eq. (5.93) into Eq. (5.87) leads to a differential equation for the density

$$\partial_r \rho = \alpha \frac{\rho}{r}, \quad \alpha = \frac{3\chi_0^2/D_r^2}{16 - \chi_0^2/D_r^2}, \quad (5.94)$$

the solution of which reads

$$\rho(r) = ar^\alpha, \quad (5.95)$$

with constant a . For $\chi_0/D_r < 4$, $\alpha > 0$, implying that the density rises from $\rho = 0$ at the origin up to ar_c^α at the border of the cluster. The value of a can be determined via the jump condition Eq. (5.38). Irrespective of the functional form of $\rho(r)$, Eq. (5.93) implies a constant mean angular orientation

$$\langle e_\theta \rangle = \frac{p_\theta}{\rho} = -\frac{1}{2} \frac{\chi_0/D_r}{1 + \chi_0^2/(8D_r^2)} \quad (5.96)$$

inside the cluster, which we compare to the maximum $\langle e_\theta \rangle_{\max}$ of the angular orientation profiles from the simulations [Fig. 5.10(d)]. In case of small $v^<$ and χ_0 , we find good agreement, cf. Fig. 5.11. For higher $v^<$, density and concentration fluctuations

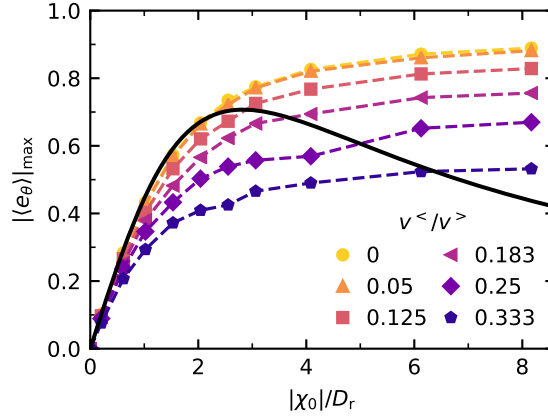


Fig. 5.11. Maximum $|\langle e_\theta \rangle|_{\max}$ of the radial angular orientation profiles $|\langle e_\theta \rangle|(r)$ against torque strength $|\chi_0|$ for different velocities $v^<$ in the cluster at $\lambda = 20$, $v^> = 30$, $\bar{c} = 0.86c_0$ from simulations (standard errors are smaller than symbol size). The ($v^<$ -independent) theory prediction, Eq. (5.96), is shown in black and decays to zero for higher $|\chi_0|$. Reprinted in adapted form with permission from Ref. [48]. Copyright 2020 by the American Physical Society.

become more important, which presumably explain the stronger deviations from the mean-field prediction. In the simulations, for $\chi_0/D_r \gtrsim 3$, $\langle e_\theta \rangle_{\max}$ saturates whereas the theoretical prediction goes to zero in the limit $\chi_0 \rightarrow \infty$. Taking into account higher orientational moments of the one-body density ψ_1 might help to capture the high χ_0 -behavior.

Dynamics of binary active clusters driven by ion-exchange particles

Up to now, we have been dealing with systems in which the individual interacting constituents are active, e.g., diffusiophoretic Janus colloids, for which the interaction of the solvent with their nonuniform surface leads to self-propulsion. Introducing strong attractive interactions between individual active colloids can lead to the formation of colloidal clusters composed of several particles (also referred to as “colloidal molecules” [91]) that, depending on their composition and structure, swim linearly or exhibit different motion patterns such as circular or spinning motion [40, 35, 162]. Such active colloidal clusters can also be created out of both active and passive particles [165, 55, 136]. Following a different route, it is possible to assemble active colloidal clusters from uniform passive particles only. This requires particles of at least two different types that, when assembled into a cluster, are propelled by *nonreciprocal* effective forces between unlike particles. This concept has first been discussed theoretically in Ref. [142] for phoretically interacting particles where nonreciprocal interactions arise from different surface activities and phoretic mobilities.¹ In experiments, clusters composed of (individually passive) dielectric colloidal particles of different diameters perform directed motion in a perpendicular electric field due to asymmetric electrohydrodynamic flows [94, 103]. In these approaches, the assembly process of colloidal molecules is assisted by external fields or patterned substrates.

The first experimental realization of *self-assembling* active clusters was provided by the group of Prof. Thomas Palberg (Johannes Gutenberg-Universität Mainz, Institut für Physik), who studied suspensions of cationic ion-exchange particles (IEXs) that interact over long distances (compared to the particle diameter) via self-generated electroosmotic flows close to a substrate [108]. When all particles are of the same type, the long-range attractive interactions lead to the formation of passive colloidal clusters. On adding anionic ion-exchange particles or passive particles to the system,

¹It is important to stress that although the *effective* interactions between colloids are nonreciprocal, Newton’s third law of force reciprocity is not broken on the level of ions and molecules.

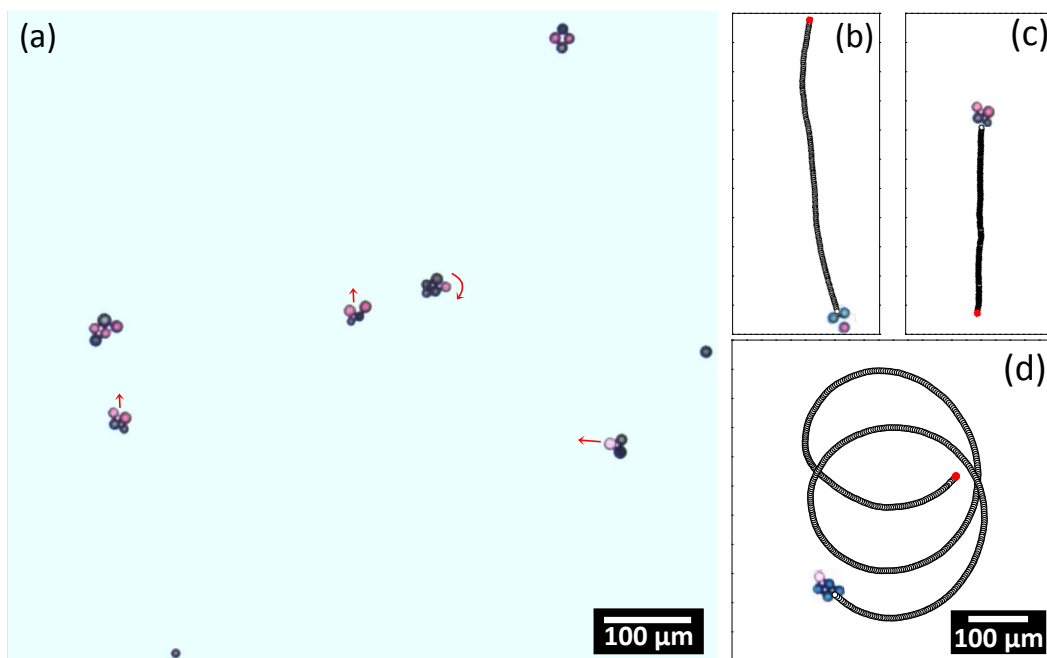


Fig. 6.1. Binary active clusters composed of IEXs. (a) Snapshot of the experimental system showing several clusters with different sizes, compositions and structures (cationic IEXs appear red or white and anionic IEXs blue). (b,c) Trajectories of (b) a trimer with one cationic IEX and (c) a tetramer with two cationic IEXs. Both undergo linear motion because of their reflection symmetry. (d) The pentamer breaks this symmetry and in addition rotates, which leads to circular motion. Reprinted with permission from Ref. [105]. Copyright 2018 by the American Chemical Society.

clusters that consist of particles of different types undergo directed motion due to nonreciprocal interactions with different symmetry-dependent motion patterns, see Fig. 6.1.²

In this chapter, we develop a model to predict the dynamic properties of these clusters. An accurate microscopic description of the system based on first-principles is very challenging due to the complex interplay of field gradients, hydrodynamics, surface properties and boundary conditions. Therefore, we follow a different approach based on effective interaction potentials that can be constructed from relatively simple measurements of approach speeds between components. This chapter, to a large extent, presents results published in Ref. [105] that were obtained in close collaboration with Dr. Ran Niu from the group of Prof. Thomas Palberg, who performed all the experiments discussed here (including particle tracking and speed measurements).

²An alternative approach based on absorbing and nonabsorbing particles in a near-critical binary solution is given in Ref. [126].

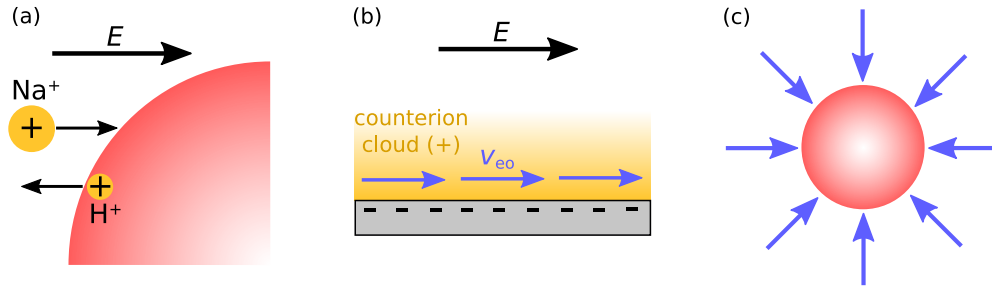


Fig. 6.2. Flow generation of a cationic IEX. (a) A cationic IEX (red) exchanges stored H^+ ions for Na^+ ions. Due to the difference in ion diffusivities, an electric field pointing towards the IEX is generated. (b) The negatively charged substrate (gray) is screened by a counterion cloud of positive charges (yellow), inside which the electric field induces an electroosmotic flow. (c) Resulting radially symmetric flow profile pointing towards the IEX (top view). (a) and (b) are adapted from Ref. [108].

6.1 Experimental setup

The experimental system is a dilute, deionized aqueous suspension of uniform, spherical cationic ion-exchange particles of diameter $d = 15 \mu\text{m}$ mixed with either anionic IEXs or passive particles of the same diameter, contained in a sample cell of height 1 mm. The solvent contains a small amount ($\sim 10^{-7} \text{ mol/L}$) of residual non-protonic cations [107, 108] as well as residual anions. The IEXs are made of porous ion-exchange resin and exchange stored protons (H^+) for residual Na^+ ions of the solvent (cationic) or OH^- for residual Cl^- ions (anionic). The passive particles are negatively charged polystyrene spheres. Due to gravity, the particles sediment onto the negatively charged substrate and form a quasi two-dimensional system.

Close to the substrate, the cationic IEXs generate a converging (pointing towards the IEXs) long-ranged solvent flow measurable for about $150 \mu\text{m}$ with flow velocity $\sim 1/r$ in the far field [108]. The origin of this flow can be understood as follows [107, 108]: Due to the release of protons, cationic IEXs generate a concentration profile $c(r)$ of H^+ that (in the stationary case) in the far field decays $c(r) \sim 1/r$ away from the particles as shown by pH measurements [108]. This scaling is consistent with the assumption that protons freely diffuse in three dimensions after being released (closer to the particles $c(r)$ is more complicated due to additional effects). The protons moving away from an IEX have a higher diffusion coefficient than the to-be-exchanged Na^+ cations.³ This gives rise to local electric fields pointing towards the IEX that prevent charge separation by slowing down the outward drift of H^+

³ $D_{\text{H}^+} = 9.3 \cdot 10^{-9} \text{ m}^2/\text{s}$ [70], $D_{\text{Na}^+} \approx 2 \cdot 10^{-9} \text{ m}^2/\text{s}$ [107].

and accelerating the inward drift of Na^+ [4], cf. Fig. 6.2(a). The negatively charged substrate is screened by an excess of positive charges in its vicinity, which experience a force towards the IEX due to the electric field. As these forces are transmitted to the fluid, a flow towards the particle is generated, see Fig. 6.2(b,c). A detailed discussion of such *electroosmotic* flows can be found in Ref. [4]. The ion-exchange rate and the flow strength stay constant for several hours before the ion-exchange capacity is exhausted [108], which is long enough to ensure stable conditions during the experiments.

The anionic IEXs create an electroosmotic flow as well due to the same mechanism as the cationic IEXs. However, since the charge of the exchanged ions is opposite, the resulting flow is diverging (pointing away from the IEXs). As the difference in diffusion coefficients of OH^- and Cl^- is much smaller than that of the cations, the generated flow is expected to be weaker and shorter in range.

6.2 Particle interactions

The flows generated by the IEXs lead to interactions between individual particles. For two cationic IEXs, the converging electroosmotic flows induce a long-range attraction between them due to the asymmetry in the superposed flow [108]. When the particles come closer, backflow out of the plane of the substrate (due to the incompressibility of the solvent) and probably electrophoretic flows around particles become important, leading to an effective repulsion. At a distance of $\approx 35 \mu\text{m}$, attraction and repulsion compensate and the particles become bonded, forming a dimer. On a coarse-grained level (instead of modeling all the involved microscopic processes), the effects in both regimes can be well captured via the effective pair potential [108]

$$u(r) = -\frac{\gamma}{r} + \frac{\alpha}{r} e^{-r/\xi}, \quad (6.1)$$

with r the distance between the cationic IEXs and parameters γ , α and ξ . The term $\sim -1/r$ describes the long-range attraction and the term $\sim e^{-r/\xi}/r$ captures the short-range repulsion. Assuming overdamped motion, the dynamics of cationic IEX i is then simply determined by the equation of motion

$$\dot{\mathbf{r}}_i = -\nabla_i \sum_{j \neq i} u(r_{ij}). \quad (6.2)$$

with $r_{ij} = |\mathbf{r}_j - \mathbf{r}_i|$. For overdamped motion, usually the product of particle mobility μ and the gradient of the potential energy appears. Here, the mobility is absorbed

into the effective potential $u(r)$ (which has units of a diffusion coefficient), since in the experiment one does not have access to μ and $u(r)$ separately. In Ref. [108], an additional noise term was included in Eq. (6.2), which is not thermal⁴, but arises from fluctuations of the flow. As we are interested only in average speeds throughout this chapter noise is neglected here. This model well captures the effective interaction between cationic IEXs and is able to describe the formation of passive colloidal clusters of different sizes and structures observed in suspensions of cationic IEXs [108]. The parameters of the potential can be determined by fitting the experimentally measured approach speed of two IEXs with the model prediction.

In suspensions additionally containing either passive particles or anionic IEXs, further interactions between the different particle types arise, which lead to the formation of clusters that perform self-propelled motion. Following a similar route as for cationic IEXs, we model these interactions via effective pair potentials, the parameters of which we extract from comparing model predictions to experimental speed measurements of interacting particle pairs. The obtained potentials are the basis for our predictions of the dynamic properties of larger clusters in Sec. 6.3.

6.2.1 A cationic IEX and a passive particle

While passive particles mainly interact sterically, they are advected by the flow generated by a cationic IEX [107]. To study the particle motion induced by the flow, we first consider an isolated pair (in the experiment all other particles have to be at least 10 times their diameter away) of one passive particle and one cationic IEX. At large separations, the passive particle approaches the stationary IEX, see Fig. 6.3(a). This implies that the effective interaction between the particles is *nonreciprocal*. In contrast to a pair of cationic IEXs, as the particles come closer, the IEX starts to move away from the passive particle. Eventually, both particles move together with a small exclusion zone inbetween forming a dimer that performs linear directed motion along its symmetry axis, cf. 6.3(a). In order to explain this behavior on a qualitative level, we postulate an additional *reciprocal* component of the solvent flow which couples the particles hydrodynamically. This flow pushes the IEX forward as the passive particle comes close to it while the passive particle is pushed backward against the direction of advection. In the assembled dimer, where the distance between the particles remains constant, both particles move with the same speed.

⁴Due to the size of the particles ($d = 15 \mu\text{m}$), thermal Brownian motion is practically negligible on time scales of the experiment.

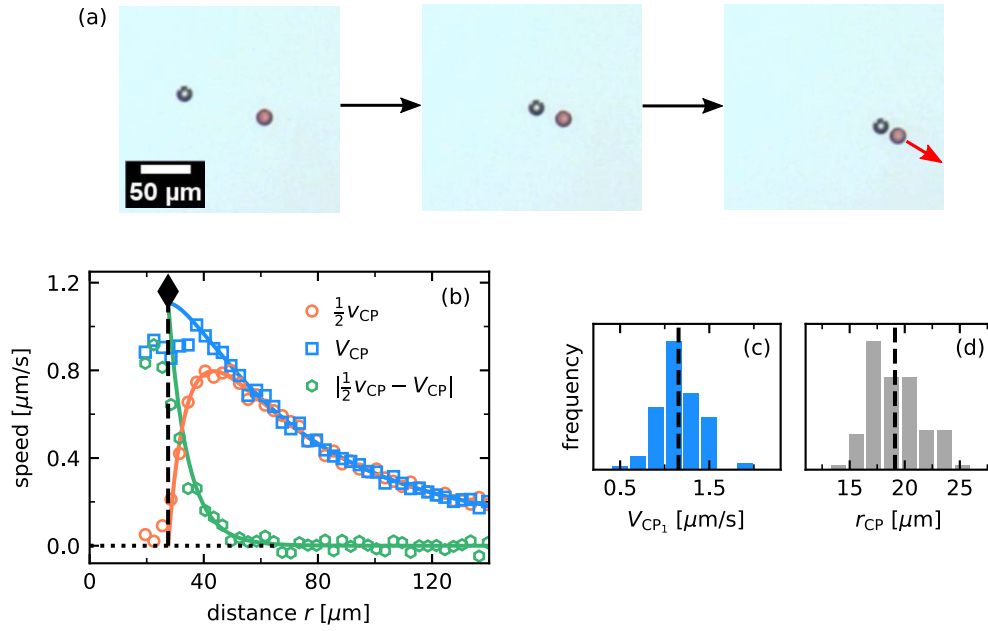


Fig. 6.3. Pair of a cationic IEX and a passive particle. (a) A passive particle (gray) and a cationic IEX (red) assembling into a dimer (from left to right) that moves along its symmetry axis (red arrow). (b) Measured relative drift speed $v_{CP}(r)$ (red symbols, divided by two) and center-of-mass speed $V_{CP}(r)$ (blue symbols) as functions of the particle separation r . Green symbols show the magnitude of the differential speed $\frac{1}{2}v_{CP}(r) - V_{CP}(r)$, representing the reciprocal contribution. The average measured speed of the assembled dimers V_{CP1} is indicated by the black diamond and the dashed line is the model prediction for the dimer separation r_{CP} . The blue and green lines are fits to the experimental data via Eqs. (6.8), (6.9) with effective potentials (6.10), (6.11). The red line is obtained by adding the two fits [Eq. (6.7)]. (c,d) Experimental histograms of (c) the speed and (d) the particle separation of assembled dimers (the black line indicates the mean values). (b-d) Reprinted with permission from Ref. [105]. Copyright 2018 by the American Chemical Society.

For a more quantitative analysis, the particle positions \mathbf{r}_P (passive particle) and \mathbf{r}_C (cationic IEX) of the pair of interest were tracked over time. This allows to determine the relative drift speed

$$v_{CP}(r) = |\dot{\mathbf{r}}| = |\dot{\mathbf{r}}_C - \dot{\mathbf{r}}_P|, \quad (6.3)$$

with separation vector $\mathbf{r} = \mathbf{r}_C - \mathbf{r}_P$, and the speed of the center of mass $\mathbf{R} = \frac{1}{2}(\mathbf{r}_C + \mathbf{r}_P)$,

$$V_{CP}(r) = |\dot{\mathbf{R}}| = \frac{1}{2}|\dot{\mathbf{r}}_C + \dot{\mathbf{r}}_P|, \quad (6.4)$$

as a function of the separation $r = |\mathbf{r}|$. The measured speeds were averaged over 160 independent trajectories and are plotted in Fig. 6.3(b). For large distances, both the drift and the center-of-mass speed increase and for $r \gtrsim 50 \mu\text{m}$, $\frac{1}{2}v_{CP}(r) = V_{CP}(r)$, implying that the IEX is at rest [Eqs. (6.3), (6.4) with $\dot{\mathbf{r}}_C = 0$]. For smaller r , the center-of-mass speed further rises as the IEX starts to move, whereas the drift speed

decreases due to the slow-down of the passive particle. This suggests that the interaction range of the reciprocal solvent flow is $\sim 50 \mu\text{m}$. For smaller distances, the drift speed drops to zero indicating binding into the dimer. The average center-of-mass (swimming) speed of assembled dimers is $V_{\text{CP}_1} \simeq 1.16 \mu\text{m/s}$ with average steady-state separation $r_{\text{CP}} \simeq 19 \mu\text{m}$. These values are not the same for all dimers but follow a distribution, cf. Fig. 6.3(c,d).

Based on these observations, we extend the above presented scheme for two cationic IEXs from Ref. [108] to model the dynamics of the particles. We assume the equations of motion

$$\dot{\mathbf{r}}_{\text{P}} = -\nabla_{\text{P}}[u_{\text{C}}(r) + U_{\text{P}}(r)] = [u'_{\text{C}}(r) + U'_{\text{P}}(r)]\frac{\mathbf{r}}{r}, \quad (6.5)$$

$$\dot{\mathbf{r}}_{\text{C}} = -\nabla_{\text{C}}U_{\text{P}}(r) = -U'_{\text{P}}(r)\frac{\mathbf{r}}{r}, \quad (6.6)$$

with ∇_k the gradient with respect to the position of particle k . The effective potentials (absorbing the particle mobilities) $u_{\text{C}}(r)$ and $U_{\text{P}}(r)$ account for the electroosmotic flow generated by the cationic IEX and the additional flow arising from the presence of the passive particle, respectively. Since $u_{\text{C}}(r)$ acts only on the passive particle, it describes a nonreciprocal interaction, whereas $U_{\text{P}}(r)$ is reciprocal, as it acts on both particles. Equations (6.5), (6.6) imply that the drift and center-of-mass speeds are

$$v_{\text{CP}}(r) = u'_{\text{C}}(r) + 2U'_{\text{P}}(r), \quad (6.7)$$

$$V_{\text{CP}}(r) = \frac{1}{2}u'_{\text{C}}(r). \quad (6.8)$$

The derivative of the reciprocal potential can therefore be expressed in terms of the speeds as

$$U'_{\text{P}}(r) = \frac{1}{2}v_{\text{CP}}(r) - V_{\text{CP}}(r). \quad (6.9)$$

We now assume the following forms for the effective potentials

$$u_{\text{C}}(r) = -\frac{\gamma}{r} + \frac{\alpha}{r}e^{-r/\xi}, \quad (6.10)$$

$$U_{\text{P}}(r) = \frac{\alpha_{\text{P}}}{r}e^{-r/\xi_{\text{P}}}. \quad (6.11)$$

The ansatz for $u_{\text{C}}(r)$ is motivated by the potential (6.1) used in Ref. [108] describing the long-range attraction $\sim 1/r$ and the more complicated flow closer to the particle via the additional Yukawa-like repulsive contribution with decay length ξ . Using relation (6.8), this form of $u_{\text{C}}(r)$ can be excellently fitted to the measured center-of-mass speed $V_{\text{CP}}(r)$, as shown in Fig. 6.3(b) (blue curve). The reciprocal contribution

(6.9) is also plotted in Fig. 6.3(b) and is well described by the repulsive Yukawa ansatz (6.11) (green curve). Adding the fits for $u_C(r)$ and $U_P(r)$ [Eq. (6.7)], indeed captures the experimentally measured drift speed $v_{CP}(r)$ (red line). This good agreement justifies both the equations of motion (6.5), (6.6) and our choice for the effective potentials (6.10), (6.11). The parameters of the potentials obtained from the fits are $\gamma \simeq 7328 \mu\text{m}^3/\text{s}$, $\alpha \simeq 8106 \mu\text{m}^3/\text{s}$, $\xi \simeq 24.9 \mu\text{m}$ for $u_C(r)$ and $\alpha_P \simeq 4008 \mu\text{m}^3/\text{s}$, $\xi_P = 9.4 \mu\text{m}$ for $U_P(r)$.

This analysis in terms of effective potentials allows a prediction of the steady-state particle separation r_{CP} via the condition $v_{CP}(r_{CP}) = 0$, yielding $r_{CP} \simeq 27 \mu\text{m}$, compare Fig. 6.3(b). This value is $8 \mu\text{m}$ larger than the average separation measured in the experiment, which probably can be explained as an effect of the distortion of the pH gradient of the cationic IEX in the moving dimer [106]. Due to this effect, the pH gradient becomes asymmetric, allowing the passive particle to be closer. In contrast, the prediction for the steady-state center-of-mass speed $V_{CP_1} \equiv V_{CP}(r_{CP}) \simeq 1.11 \mu\text{m}/\text{s}$ is very close to the experimental value $1.16 \mu\text{m}/\text{s}$, suggesting that the distortion of the pH gradient does not substantially affect the dimer speed.

6.2.2 A cationic IEX and an anionic IEX

We now move to mixtures of cationic and anionic IEXs. As their generated flow is diverging, two anionic IEXs repel each other. Focusing on their interaction with cationic IEXs, analogous to the case of passive particles, we consider isolated pairs of one anionic IEX and one cationic IEX. It can be observed that in its flow range ($\sim 120 \mu\text{m}$) a cationic IEX attracts anionic IEXs towards it. As the particles come close, the same qualitative behavior as for a passive particle holds: their motion couples and they start to self-propel in the direction of the cationic IEX. For the assembled dimers, the average particle separation is $r_{CA} \simeq 18 \mu\text{m}$ and the average propulsion speed is $V_{CA_1} \simeq 1.14 \mu\text{m}/\text{s}$. As in case of the passive particles, the relative drift speed $v_{CA}(r)$ and the center-of-mass speed $V_{CA}(r)$ were measured experimentally as a function of the separation $r = |\mathbf{r}_C - \mathbf{r}_A|$ and are plotted in Fig. 6.4. We find that for $r \gtrsim 50 \mu\text{m}$, the center-of-mass speed is the same as that of the pair with a passive particle reduced by a factor $\mu_A \simeq 0.76$, i.e., $V_{CA}(r) = \mu_A V_{CP}(r)$ [see inset of Fig. 6.4]. This leads us to the conclusion that the electroosmotic flow of the cationic IEX is the same as before, but the mobility of the anionic IEX is smaller by a factor μ_A than that of the passive particle (due to diverse factors as, e.g., a different surface charge).

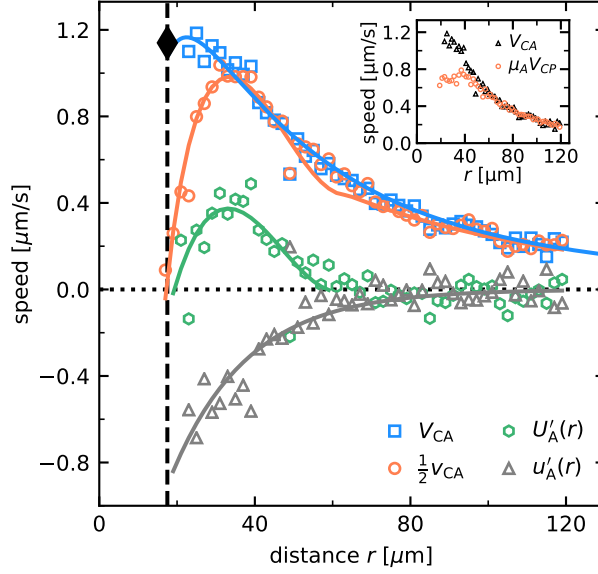


Fig. 6.4. Cationic-anionic IEX pair. Measured relative drift speed $v_{CA}(r)$ (red symbols, divided by two) and center-of-mass speed $V_{CA}(r)$ (blue symbols) as a function of the particle separation r . The measured dimer speed V_{CA_1} is indicated by the black diamond and the dashed black line shows the measured dimer separation r_{CA} . Gray symbols show the flow generated by the anionic IEX $u'_A(r)$ and green symbols the reciprocal interaction $U'_A(r)$. Gray and green lines represent fits as described in the main text, whereas the red and blue lines are model predictions (6.14), (6.15) based on the fitted potentials. The inset shows the measured center-of-mass speed of the cationic-anionic pair and that of the cationic-passive pair multiplied by $\mu_A = 0.76$. For $r \gtrsim 50 \mu\text{m}$ the curves collapse. Reprinted in adapted form with permission from Ref. [105]. Copyright 2018 by the American Chemical Society.

Based on these findings, we extend the previous model [Eqs. (6.5), (6.6)] into

$$\dot{\mathbf{r}}_A = -\nabla_A[\mu_A u_C(r) + U_A(r)] = [\mu_A u'_C(r) + U'_A(r)] \frac{\mathbf{r}}{r}, \quad (6.12)$$

$$\dot{\mathbf{r}}_C = -\nabla_C[u_A(r) + U_A(r)] = -[u'_A(r) + U'_A(r)] \frac{\mathbf{r}}{r}, \quad (6.13)$$

with separation vector $\mathbf{r} = \mathbf{r}_C - \mathbf{r}_A$. Here, $u_C(r)$ is the same potential as above, describing the flow of the cationic IEX with its strength reduced by the prefactor μ_A . Moreover, $u_A(r)$ accounts for the flow generated by the anionic IEX and $U_A(r)$ is the additional reciprocal contribution. The relative drift and center-of-mass speed can be expressed in terms of the effective potentials as

$$v_{CA}(r) = \mu_A u'_C(r) + u'_A(r) + 2U'_A(r), \quad (6.14)$$

$$V_{CA}(r) = \frac{1}{2}[\mu_A u'_C(r) - u'_A(r)]. \quad (6.15)$$

Combining Eqs. (6.8), (6.14) and (6.15), the derivatives of the potentials can be written in terms of the measured speeds as

$$u'_A(r) = 2[\mu_A V_{CP}(r) - V_{CA}(r)], \quad (6.16)$$

$$U'_A(r) = \frac{1}{2}v_{CA}(r) + V_{CA}(r) - 2\mu_A V_{CP}(r). \quad (6.17)$$

These expressions are also plotted in Fig. 6.4. As expected, the flow generated by the anionic IEX, represented by $u'_A(r)$, is weaker than that of the cationic IEX and shorter in range. Furthermore, the flow is diverging (pointing away from the anionic IEX) as the cationic IEX is repelled by the flow ($u'_A(r) < 0$). It can be well fitted with $u_A(r) = \alpha_A \exp(-r/\xi_A)$ (gray line) with $\alpha_A \simeq 43.4 \mu\text{m}^2/\text{s}$ and $\xi_A \simeq 19.7 \mu\text{m}$. Combining this expression with the fit of $u_C(r)$ from Sec. 6.2.1, Eq. (6.15) well captures the measured center-of-mass speed $V_{CA}(r)$ (blue line). The reciprocal flow contribution $U'_A(r)$ is short-ranged, but now attractive and vanishes as the particles reach their steady-state separation. We fit it with a cubic function $U'_A(r) = \alpha_3 r^3 + \alpha_2 r^2 + \alpha_1 r + \alpha_0$ (green line), yielding $\alpha_3 \simeq 3.5 \cdot 10^{-5} \mu\text{m}^{-1}\text{s}^{-1}$, $\alpha_2 \simeq -0.005 \text{s}^{-1}$, $\alpha_1 \simeq 0.2 \mu\text{m}\text{s}^{-1}$, $\alpha_0 \simeq -2.5 \mu\text{m}^2\text{s}^{-1}$. Combining all three potentials into the prediction for the drift speed $v_{CA}(r)$ [Eq. (6.14), red line] yields good agreement with the experimental data [except for a kink in the region $50 \mu\text{m} \lesssim r \lesssim 70 \mu\text{m}$ which is an artifact of the polynomial fit of $U'_A(r)$]. The prediction for the steady-state separation $r_{CA} \simeq 18 \mu\text{m}$ (determined by $v_{CA}(r_{CA}) = 0$) agrees well with the measured value. Also the prediction of the dimer speed $V_{CA_1} \equiv V_{CA}(r_{CA}) \simeq 1.09 \mu\text{m}/\text{s}$ is very close to the measured speed $\simeq 1.14 \mu\text{m}/\text{s}$.

6.3 Larger clusters

The dimers are only metastable, since the cationic IEXs attract particles over long distances which leads to growth of the clusters. Nonetheless, due to the dilute conditions at which the experiment is performed, single clusters (with a fixed number of particles) can be observed for at least five minutes, which allows to gather sufficient statistics. The motion pattern of a cluster depends on its symmetry: clusters with a reflection symmetry move linearly [Fig. 6.1(b,c)], while clusters without this symmetry perform circular motion [Fig. 6.1(d)]. Clusters with an inversion symmetry are inert, not undergoing directed motion [for example the cluster composed of four particles at the top of Fig. 6.1(a)]. Although clusters with several cationic IEXs exist, in the following, we focus on clusters containing only one cationic IEX. From the clusters' trajectories, their linear and angular speeds and

the inter-particle distances of particles in the clusters (describing their structure), were extracted. For each cluster type, data of at least 40 independent clusters was collected. In the following, we attempt to predict the dynamic properties of clusters based on their structure and our model of the pair interactions described in Sec. 6.2.

6.3.1 Cationic-passive clusters

In mixtures with passive particles, after a dimer has started moving, the following passive particles always assemble on the side of the passive particle. Consequently, no inert clusters were observed in the experiment. Circularly moving clusters were only observed for short times as they (due to particle rearrangement) transform into linearly moving structures with reflection symmetry. Hence, the only stable structures are linear swimmers. In Fig. 6.5(a), the measured swimming speeds V_{CP_N} of clusters composed of one cationic IEX and N passive particles are shown. The speeds are very similar $\simeq 1.5 \mu\text{m/s}$ and almost independent of cluster size and structure. The largest dependence is on the number N_1 of passive particles that are direct neighbors of the cationic IEX, which is either two or three.

In order to calculate the cluster speeds within our model, we now generalize the analysis from Sec. 6.2.1 to one cationic IEX and N passive particles. Their center-of-mass velocity is given by

$$\mathbf{V}_{CP_N} = \frac{1}{N+1} \left(\dot{\mathbf{r}}_C + \sum_{i=1}^N \dot{\mathbf{r}}_{P_i} \right). \quad (6.18)$$

Since all particles must move with the same velocity to maintain the cluster structure ($\dot{\mathbf{r}}_C = \dot{\mathbf{r}}_{P_i} \forall i$), the center-of-mass speed turns into the sum over all reciprocal contributions on the cationic IEX

$$\mathbf{V}_{CP_N} = \dot{\mathbf{r}}_C = - \sum_{i=1}^N U'_P(r_i) \frac{\mathbf{r}_i}{r_i}, \quad (6.19)$$

with $\mathbf{r}_i = \mathbf{r}_C - \mathbf{r}_{P_i}$ and $r_i = |\mathbf{r}_i|$. As the measured speeds V_{CP_N} mainly depend on N_1 , we assume that the reciprocal interactions between the particles in the second and third layer and the cationic IEX are screened ($U'_P = 0$) by the passive particles inbetween. For each passive particle j in the first layer, $\dot{\mathbf{r}}_C = \dot{\mathbf{r}}_{P_j}$ implies

$$- \sum_{i=1}^{N_1} U'_P(r_i) \frac{\mathbf{r}_i}{r_i} = [U'_P(r_j) + u'_C(r_j)] \frac{\mathbf{r}_j}{r_j}. \quad (6.20)$$

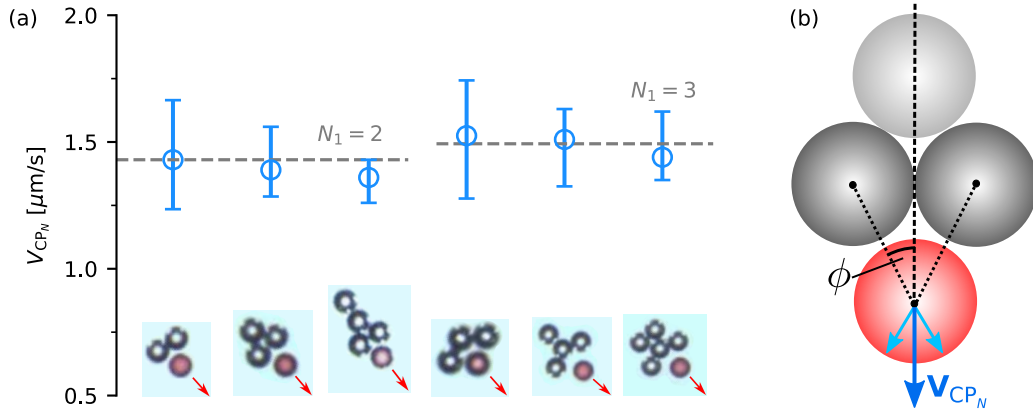


Fig. 6.5. Larger cationic-passive clusters. (a) Center-of-mass speeds of clusters CP_N with $N \geq 2$ shown in the snapshots below (the red particle is the cationic IEX). Medians (blue symbols) and first-to-third quartiles (bars) represent the experimental speed distributions. The statistical uncertainty of the median is comparable to the symbol size. The speeds predicted by the model via Eq. (6.24) are shown as dashed lines and only depend on the number N_1 of direct neighbors of the cationic IEX. Reprinted with permission from Ref. [105]. Copyright 2018 by the American Chemical Society. (b) Sketch illustrating the calculation of the cluster speed in the model. The two passive particles (gray) next to the cationic IEX (red), push the latter forward due to the reciprocal interaction (light blue arrows), which leads to propulsion with speed V_{CP_N} (blue arrow) along the cluster's symmetry axis (dashed line). The passive particle in the second layer (light gray) does not contribute to the cluster's propulsion.

Adding the conditions, Eq. (6.20), for all N_1 passive particles yields

$$-N_1 \sum_{i=1}^{N_1} U'_P(r_i) \frac{\mathbf{r}_i}{r_i} = \sum_{i=1}^{N_1} U'_P(r_i) \frac{\mathbf{r}_i}{r_i} + \sum_{i=1}^{N_1} u'_C(r_i) \frac{\mathbf{r}_i}{r_i}, \quad (6.21)$$

from which we conclude

$$U'_P(r_i) = -\frac{1}{N_1 + 1} u'_C(r_i). \quad (6.22)$$

Since, for the passive particles in the first layer, measurements confirm $r_i \simeq r_{CP} = 19 \mu\text{m}$, we can identify the dimer speed $V_{CP_1} = \frac{1}{2} u'_C(r_{CP})$ [Eq. (6.8)] and thus write the cluster speed, Eq. (6.19), as

$$\mathbf{V}_{CP_N} = \frac{2}{N_1 + 1} \sum_{i=1}^{N_1} V_{CP_1} \frac{\mathbf{r}_i}{r_i}. \quad (6.23)$$

The cluster speed therefore depends on the number of passive particles in the first layer N_1 , the dimer speed V_{CP_1} and the structure of the cluster through the separation vectors \mathbf{r}_i . For the reflectionally symmetric clusters observed in the

experiment, Eq. (6.23) implies that the speed points along the symmetry axis and has the magnitude

$$V_{\text{CP}_N} = \frac{2}{N_1 + 1} \sum_{i=1}^{N_1} V_{\text{CP}_1} \cos \phi_i, \quad (6.24)$$

with ϕ_i the average angle between the symmetry axis and \mathbf{r}_i [see Fig. 6.5(b)], which can be extracted from the measured particle separations. For the cluster with $N = N_1 = 2$ it is $\phi \simeq 21.6^\circ$ for both passive particles and thus $V_{\text{CP}_2} \simeq 1.43 \mu\text{m/s}$ according to Eq. (6.24) (employing the measured dimer speed $V_{\text{CP}_1} \simeq 1.16 \mu\text{m/s}$). For the cluster with $N = N_1 = 3$, it is $\phi = 0$ for one particle and $\phi \simeq 37.8^\circ$ for the other two particles, for which Eq. (6.24) predicts $V_{\text{CP}_3} \simeq 1.49 \mu\text{m/s}$. Both predictions agree well with the measured speeds even for the clusters with additional layers of passive particles, cf. Fig. 6.5(a). However, the data suggests that particles that are not direct neighbors of the IEX slightly lower the swimming speed, presumably indirectly, by influencing the cluster structure.

6.3.2 Cationic-anionic clusters

In mixtures of cationic and anionic IEXs, linearly and circularly swimming clusters and inert clusters were observed. In Fig. 6.6(a), the most commonly observed clusters (not including inert ones) with one cationic IEX are depicted. The bond length between anionic and cationic IEXs decreases for larger clusters (which was not observed for cationic-passive clusters), which may result from a stronger neutralization of the pH gradient by a higher number of anionic IEXs. The clusters with $N = 2$ or $N = 3$ anionic IEXs are linear swimmers, whereas for $N = 4$, one linearly and two circularly swimming structures exist. The three different clusters with $N = 5$ are all circle swimmers. Clusters with $N > 5$ typically contain more than one cationic IEX.

To predict the clusters' center-of-mass speeds, we follow similar arguments as in Sec. 6.3.1. The center-of-mass speed has to be equal to $\dot{\mathbf{r}}_C$, which yields

$$\mathbf{V}_{\text{CA}_N} = - \sum_{i=1}^N [u'_A(r_i) + U'_A(r_i)] \frac{\mathbf{r}_i}{r_i}. \quad (6.25)$$

From summing over all N conditions $\dot{\mathbf{r}}_C = \dot{\mathbf{r}}_{A_i}$ [now including also the particles not neighboring the cationic IEX and using Eqs. (6.12), (6.13)], the reciprocal contributions $U'_A(r_i)$ can be expressed via the nonreciprocal interactions as

$$U'_A(r_i) = - \frac{1}{N + 1} [N u'_A(r_i) + \mu_A u'_C(r_i)]. \quad (6.26)$$

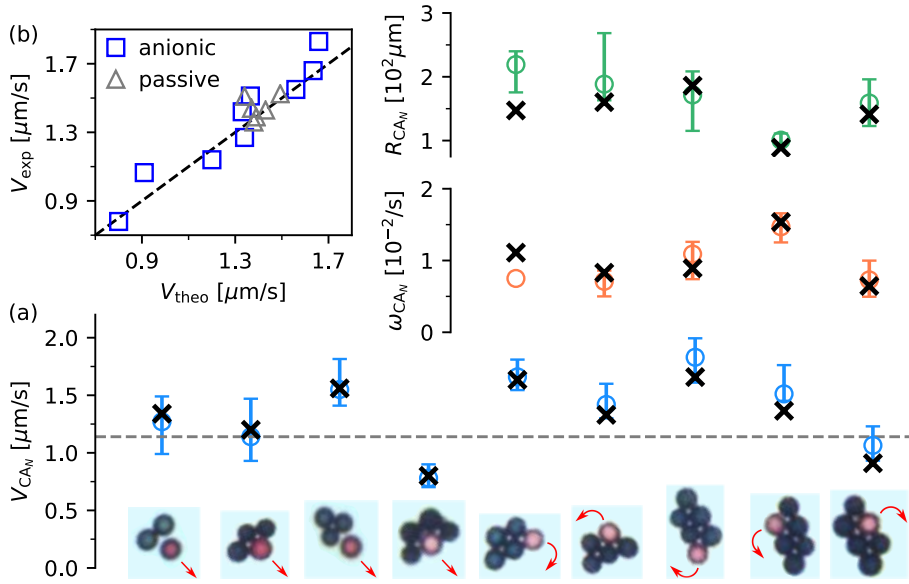


Fig. 6.6. Larger cationic-anionic clusters. (a) Center-of-mass speeds V_{CA_N} obtained from experimental measurements (circles) and model predictions Eq. (6.27). Symbols and bars show median and first-to-third quartile of experimental speed distributions. The average dimer speed V_{CA_1} is indicated by the dashed line. For circle swimmers, the angular velocities ω_{CA_N} and trajectory radii R_{CA_N} are shown as well, together with the model predictions Eq. (6.31). In the snapshots of the clusters, cationic IEXs appear red and anionic IEXs dark blue. The linear and circular swimming directions are indicated as red arrows. (b) Global comparison of the linear speeds of all clusters between measurements and model predictions. Reprinted with permission from Ref. [105]. Copyright 2018 by the American Chemical Society.

Plugging this result back into Eq. (6.25) and identifying the pair speed $V_{CA}(r_i)$ [Eq. (6.15)], we arrive at

$$\mathbf{V}_{CA_N} = \frac{2}{N+1} \sum_{i=1}^N V_{CA}(r_i) \frac{\mathbf{r}_i}{r_i}. \quad (6.27)$$

A prediction for the angular velocities ω of circle swimmers within our model can be derived as follows. The dynamical equation for any particle $\alpha \in \{A_1, \dots, A_N, C\}$ in the cluster can be written as $\dot{\mathbf{r}}_\alpha = \mathbf{F}_\alpha$, where the effective force \mathbf{F}_α (absorbing the mobility) summarizes all interactions due to effective potentials. Taking the cross product with the distance $\mathbf{x}_\alpha = \mathbf{r}_\alpha - \mathbf{R}$ from the cluster's center of mass and summing over the equations for all particles, yields the (effective) torque balance equation

$$\sum_{\alpha} \mathbf{x}_\alpha \times \dot{\mathbf{r}}_\alpha = \sum_{\alpha} \mathbf{x}_\alpha \times \mathbf{F}_\alpha. \quad (6.28)$$

Introducing polar coordinates (x, φ, z) (with the center of mass at the origin) and using $\mathbf{r}_\alpha = \mathbf{x}_\alpha + \mathbf{R}$, the left-hand side can be written as

$$\sum_{\alpha} (x_{\alpha} \mathbf{e}_{x_{\alpha}}) \times (x_{\alpha} \mathbf{e}_{\varphi_{\alpha}} \dot{\varphi}_{\alpha}) + \underbrace{\sum_{\alpha} \mathbf{x}_{\alpha} \times \dot{\mathbf{R}}}_{=0} = \dot{\varphi} \mathbf{e}_z \sum_{\alpha} \mathbf{x}_{\alpha}^2, \quad (6.29)$$

where we have used $\dot{\varphi}_{\alpha} = \dot{\varphi}$ which follows from assuming the cluster to be a rigid body. Inserting the explicit expressions for the forces \mathbf{F}_{α} , the right-hand side of Eq. (6.28) turns into

$$\begin{aligned} & \sum_{i=1}^N \mathbf{x}_{A_i} \times [\mu_A u'_C(r_i) + U'_A(r_i)] \frac{\mathbf{r}_i}{r_i} + \mathbf{x}_C \times \sum_{i=1}^N [-u'_A(r_i) - U'_A(r_i)] \frac{\mathbf{r}_i}{r_i} \\ &= \sum_{i=1}^N [\mu_A u'_C(r_i) \mathbf{x}_{A_i} - u'_A(r_i) \mathbf{x}_C] \times \frac{\mathbf{r}_i}{r_i} + \sum_{i=1}^N U'_A(r_i) \mathbf{r}_i \times \frac{\mathbf{r}_i}{r_i} \\ &= \sum_{i=1}^N [\mu_A u'_C(r_i) \mathbf{x}_{A_i} - u'_A(r_i) \mathbf{x}_C] \times \frac{\mathbf{r}_i}{r_i}. \end{aligned} \quad (6.30)$$

Thus, Eq. (6.28) can be solved for the angular velocity $\boldsymbol{\omega}_{CA_N} = \dot{\varphi} \mathbf{e}_z$ as

$$\boldsymbol{\omega}_{CA_N} = \frac{\sum_{i=1}^N [\mu_A u'_C(r_i) \mathbf{x}_{A_i} - u'_A(r_i) \mathbf{x}_C] \times (\mathbf{r}_i/r_i)}{\mathbf{x}_C^2 + \sum_{i=1}^N \mathbf{x}_{A_i}^2}. \quad (6.31)$$

The numerator is the total effective torque with respect to \mathbf{R} and the denominator reflects the higher resistance to rotation of a larger cluster. The average relative positions of the particles within clusters were measured in the experiment and are used as inputs for Eqs. (6.27) and (6.31) together with the effective potentials determined in Sec. 6.2.2. Moreover, the radii of the trajectories of circle swimmers can be calculated as $R_{CA_N} = v_{CA_N}/\omega_{CA_N}$.

In Fig. 6.6(a), the measured center-of-mass and angular speeds are plotted together with the radii R_{CA_N} . Although the values seem to be scattered without any apparent pattern, our model predictions agree very well with the experimental values. This, together with the results for the cationic-passive clusters, shows that it is sufficient to know the effective two-body interactions, extracted from experiments with particle pairs, and the cluster geometry to accurately predict the properties of the motion of larger clusters via a superposition of the interactions (see Fig. 6.6(b) for a global comparison of the linear speeds).

Conclusion and outlook

In this thesis, we have investigated several self-organized phenomena in active matter systems via computer simulations and analytical theory. In Chaps. 3-5, we have seen how different inter-particle interactions lead to various collective behaviors of motile particles and in Chap. 6 we have analyzed self-assembling aggregates of passive particles that gain activity due to nonreciprocal interactions.

Going beyond the standard model of active Brownian particles propelled at constant speed, in Chap. 3, we have dealt with particles driven by a difference in chemical potential implying a non-constant propulsion speed that depends on potential energy. In simulations, this leads to large fluctuations of particle speeds. For hard particles, however, the influence on the effective density-dependent speed $v(\rho)$ is rather weak and the small impact on the phase diagram of MIPS predicted by mean-field theory could not be confirmed in simulations. This suggests that for the description of the collective behavior of self-phoretic Janus colloids, the influence of the non-constant propulsion speed can be neglected. Already at constant propulsion speed, systems of soft particles reenter the homogeneous state at high speeds, as their tendency to overlap (and thus to avoid dynamic arrest) increases considerably with density and speed. Using their measured effective speed as input, the reentrant behavior is qualitatively confirmed by mean-field theory. In that case, the non-constant propulsion speed has a notable impact on the phase diagram. To understand the collective behavior of microorganisms, many of which are deformable, employing a constant propulsion speed might thus lead to deficient results. Therefore, precise estimates of the step length λ , the attempt rate κ_0 and the affinity $\Delta\mu$ would be required to make quantitative statements about such systems.

In Chap. 4, we have shown via simulations that a motility response of active particles towards self-generated chemical signals inspired by bacterial quorum sensing can trigger the separation into a dense passive cluster and a dilute active gas at much lower speeds and densities compared to those required for MIPS. Via the concentration threshold at which particles switch between active and passive, the densities and relative sizes of the phases can be controlled. This interaction rule has also been implemented for real systems of light-activated self-phoretic colloids in which the propulsion speed can be controlled at the level of individual particles.

The properties of the resulting steady states obtained in simulations agree very well with experiments, which shows that such externally imposed interaction rules are able to control the collective behavior of synthetic active matter well. Via slight modifications of the response scheme, in addition to the density and size of aggregates, the shape can also be controlled: A non-isotropic concentration profile of signaling molecules can lead to the formation of elliptical or square-like clusters [9]. Introducing a second (higher) threshold at which particles turn active again, the formation of ring-like structures with a reduced particle density at the center can be observed [9]. Moreover, narrowing the “vision cone” of particles, i.e., the range of angles relative to their orientation from which they can receive signals, can trigger the formation of cohesive flocks [84]. Another promising route could be “inverse” design, i.e., to first define a target state and then to determine interaction rules that give rise to it (instead of studying the emergent collective behavior of a given model). Techniques from the field of reinforcement learning [153], which have already been applied to optimize the behavior of individual active particles in specific environments [34, 100], might serve as powerful tools for this task.

Investigating the quorum-sensing induced phase separation in more detail, in Chap. 5 we have developed a mean-field theory that describes the system in terms of the coupled dynamical equations for density and polarization. As these equations are linear, it is possible to obtain analytical steady-state solutions. Excellent agreement with numerical simulations is achieved by introducing as single fit parameter an effective diffusion coefficient that accounts for the additional current due to concentration fluctuations within the interface. The effective diffusion coefficient is independent of the concentration threshold and is found to obey a scaling law. Due to the discontinuity of the concentration-dependent propulsion speed $v(\langle c \rangle)$ no critical point exists in this system, which is in contrast to MIPS of ABPs, where the effective density-dependent speed $v(\rho)$ continuously decreases. The absence of a critical point, which would be characterized by diverging fluctuations leading to the break-down of mean-field approximations in its vicinity, might be the very reason for the success of mean-field theory here. Furthermore, we have explored a novel route to the formation of vortex clusters based on an additional orientational response of particles to the gradient of the concentration field. For colloidal Janus particles, the necessary torques on particles can be implemented experimentally [92]. Typically, in active matter, vortices arise from the combination of aligning inter-particle interactions and confinement [65, 172, 23] (or are related to active turbulence [155]). On the other hand, the approach presented here also works in extended systems with periodic boundary conditions. Such vortex formation in the absence of a confinement has been observed experimentally for magnetic rollers [80].

Finally, in Chap. 6, we have analyzed the dynamics of ion-exchange particles (IEXs) in dilute, binary suspensions. Cationic IEXs generate long-ranged, converging electroosmotic flows over submillimeter ranges that attract other particles and lead to the formation of small clusters. As a result of nonreciprocal flow-induced interactions, depending on their structure, these clusters undergo linear or circular directed motion. Instead of attempting to model the microscopic mechanisms of the electroosmotic flow which are highly complex and strongly dependent on various microscopic parameters, we have developed a model that only requires a single experimental input, the approach speed of a pair of particles (which is accessible rather easily). Thereby, it is possible to disentangle the interplay of reciprocal and nonreciprocal interactions that gives rise to self-propulsion. The properties of the motion of larger clusters can be predicted via a superposition of the thus obtained pair-interactions. As our approach is rather generic, it would be interesting to see, if it is also applicable to other phoretic mechanisms. One straightforward extension might be to incorporate particles with different diameters [104, 105]. Another route is to include external factors such as patterned substrates, magnetic fields and gravity into the model, which could improve the control of the assembled structures.

A.1 Supplementary Figures

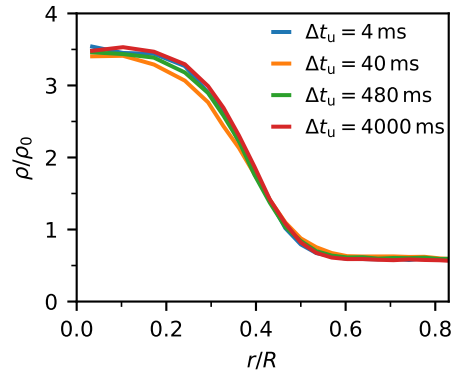


Fig. A.1. Radial density profiles for different time intervals Δt_u between motility updates (at $\lambda = 10d$, $\bar{c} = 9.9\bar{c}$). There is no visible difference observed on varying the interval from 4 ms to 4000 ms (40 ms was used in the simulations in Chap. 4, 500 ms in the experiments). Reprinted with permission from the Supplementary Material of Ref. [9] licensed under the Creative Commons license CC BY 4.0.

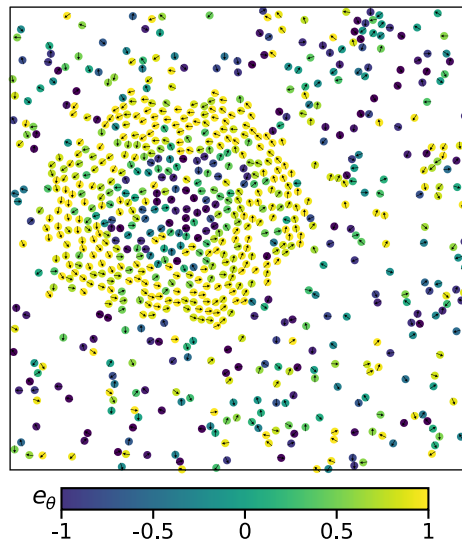


Fig. A.2. Vortex cluster in a system of $N = 800$ particles in a simulation box with periodic boundary conditions and edge length $L = 65$ at $v^> = 30$, $v^< = \frac{1}{8}v^>$, $\lambda = 10$, $\bar{c} = 1.22c_0$ and $\chi_0 = -32.7D_T$. Particles are colored by their angular alignment $e_{k,\theta} = \mathbf{e}_k \cdot \mathbf{e}_\theta$.

A.2 Concentration profile of a radially symmetric density distribution

Here, we calculate the ideal part $c_{\text{id}}(\mathbf{r})$ of the mean concentration profile $\langle c \rangle(\mathbf{r})$, Eq. (4.15), generated by a radially symmetric steady-state density distribution $\rho(|\mathbf{r}|)$, as it appears in Secs. 4.3 and 5.4.2. We write $c_{\text{id}}(\mathbf{r})$ as convolution

$$c_{\text{id}}(\mathbf{r}) = \int d\mathbf{r}' \rho(\mathbf{r}') \mathbb{U}(\mathbf{r} - \mathbf{r}'), \quad (\text{A.1})$$

with kernel

$$\mathbb{U}(\mathbf{x}) = \frac{\gamma}{4\pi D_c} \frac{e^{-|\mathbf{x}|/\lambda}}{|\mathbf{x}|}. \quad (\text{A.2})$$

According to the convolution theorem, the Fourier transform (denoted by the tilde) of the concentration profile is

$$\tilde{c}_{\text{id}}(\mathbf{k}) = \tilde{\rho}(\mathbf{k}) \tilde{\mathbb{U}}(\mathbf{k}). \quad (\text{A.3})$$

Since both $\rho(\mathbf{r}) = \rho(r)$ and $\mathbb{U}(\mathbf{r}) = \mathbb{U}(r)$ (with $r = |\mathbf{r}|$) are radially symmetric functions, their Fourier transforms are given by the Hankel transform via [24]

$$\tilde{f}(\mathbf{k}) = \tilde{f}(k) = 2\pi \int_0^\infty dr r f(r) J_0(kr), \quad (\text{A.4})$$

where $f(\mathbf{r}) = f(r)$ is a radially symmetric function, $k = |\mathbf{k}|$ and $J_0(x)$ is the Bessel function of first kind and order zero. Specifically

$$\tilde{\mathbb{U}}(k) = 2\pi \int_0^\infty dr \frac{\gamma}{4\pi D_c} e^{-r/\lambda} J_0(kr) = \frac{\gamma}{2D_c} \frac{\lambda}{\sqrt{1 + (k\lambda)^2}}. \quad (\text{A.5})$$

We now represent $c_{\text{id}}(\mathbf{r}) = c_{\text{id}}(r)$ by its Fourier transform (using the inverse Hankel transform)

$$c_{\text{id}}(r) = \frac{1}{2\pi} \int_0^\infty dk k \tilde{\rho}(k) \tilde{\mathbb{U}}(k) J_0(kr). \quad (\text{A.6})$$

Then, calculating the Fourier transform of $\rho(r)$ via Eq. (A.4) and inserting $\tilde{\mathbb{U}}(k)$ from Eq. (A.5) leads to the result

$$c_{\text{id}}(r) = \frac{\gamma\lambda}{2D_c} \int_0^\infty dr' r' \rho(r') \int_0^\infty dk \frac{k}{\sqrt{1 + (k\lambda)^2}} J_0(kr) J_0(kr'). \quad (\text{A.7})$$

Bibliography

- [1]M. Abercrombie. “The Croonian Lecture, 1978 - The crawling movement of metazoan cells”. In: *Proc. R. Soc. B* 207.1167 (1980), pp. 129–147. DOI: 10.1098/rspb.1980.0017.
- [2]M. Allen and D. Tildesley. *Computer Simulation of Liquids*. Oxford science publications. Clarendon Press, 1987.
- [3]R. D. Allen. “Motility”. In: *J. Cell Biol.* 91.3 (1981), p. 148. DOI: 10.1083/jcb.91.3.148s.
- [4]J. L. Anderson. “Colloid Transport by Interfacial Forces”. In: *Annu. Rev. Fluid Mech.* 21.1 (1989), pp. 61–99. DOI: 10.1146/annurev.fl.21.010189.000425.
- [5]L. Antonioli, C. Blandizzi, P. Pacher, M. Williams, and G. Haskó. “Rethinking Communication in the Immune System: The Quorum Sensing Concept”. In: *Trends Immunol.* 40.2 (2019), pp. 88–97. DOI: 10.1016/j.it.2018.12.002.
- [6]G. Arfken and H. Weber. *Mathematical Methods for Physicists*. Elsevier Science, 2013.
- [7]L. Bai and D. Breen. “Calculating Center of Mass in an Unbounded 2D Environment”. In: *J. Graph. Tools* 13.4 (2008), pp. 53–60. DOI: 10.1080/2151237X.2008.10129266.
- [8]J. A. Barker and D. Henderson. “Perturbation Theory and Equation of State for Fluids. II. A Successful Theory of Liquids”. In: *J. Chem. Phys.* 47.11 (1967), pp. 4714–4721. DOI: 10.1063/1.1701689.
- [9]T. Bäuerle, A. Fischer, T. Speck, and C. Bechinger. “Self-organization of active particles by quorum sensing rules”. In: *Nat. Commun.* 9.1 (2018), p. 3232. DOI: 10.1038/s41467-018-05675-7.
- [10]C. Bechinger, R. Di Leonardo, H. Löwen, et al. “Active particles in complex and crowded environments”. In: *Rev. Mod. Phys.* 88 (4 2016), p. 045006. DOI: 10.1103/RevModPhys.88.045006.
- [11]H. Berg. *Random Walks in Biology*. Princeton paperbacks. Princeton University Press, 1993.
- [12]E. Bertin, M. Droz, and G. Grégoire. “Boltzmann and hydrodynamic description for self-propelled particles”. In: *Phys. Rev. E* 74 (2 2006), p. 022101. DOI: 10.1103/PhysRevE.74.022101.
- [13]E. Bertin, M. Droz, and G. Grégoire. “Hydrodynamic equations for self-propelled particles: microscopic derivation and stability analysis”. In: *J. Phys. A* 42.44 (2009), p. 445001. DOI: 10.1088/1751-8113/42/44/445001.

- [14] J. Bialké, H. Löwen, and T. Speck. “Microscopic theory for the phase separation of self-propelled repulsive disks”. In: *EPL* 103.3 (2013), p. 30008. DOI: 10.1209/0295-5075/103/30008.
- [15] J. Bialké, J. T. Siebert, H. Löwen, and T. Speck. “Negative Interfacial Tension in Phase-Separated Active Brownian Particles”. In: *Phys. Rev. Lett.* 115 (9 2015), p. 098301. DOI: 10.1103/PhysRevLett.115.098301.
- [16] J. Bialké, T. Speck, and H. Löwen. “Active colloidal suspensions: Clustering and phase behavior”. In: *J. Non-Cryst. Solids* 407 (2015), pp. 367–375. DOI: 10.1016/j.jnoncrysol.2014.08.011.
- [17] J. Bialké, T. Speck, and H. Löwen. “Crystallization in a Dense Suspension of Self-Propelled Particles”. In: *Phys. Rev. Lett.* 108 (16 2012), p. 168301. DOI: 10.1103/PhysRevLett.108.168301.
- [18] J. Blaschke, M. Maurer, K. Menon, A. Zöttl, and H. Stark. “Phase separation and coexistence of hydrodynamically interacting microswimmers”. In: *Soft Matter* 12 (48 2016), pp. 9821–9831. DOI: 10.1039/C6SM02042A.
- [19] N. N. Bogoliubov. “Kinetic Equations”. In: *Journal of Physics-USSR* 10 (3 1946), pp. 265–274.
- [20] M. Born and H. S. Green. “A general kinetic theory of liquids I. The molecular distribution functions”. In: *Proc. R. Soc. Lond. A.* 188 (1012 1946). DOI: 10.1098/rspa.1946.0093.
- [21] C. Brennen and H. Winet. “Fluid Mechanics of Propulsion by Cilia and Flagella”. In: *Annu. Rev. Fluid Mech.* 9.1 (1977), pp. 339–398. DOI: 10.1146/annurev.fl.09.010177.002011.
- [22] H. Brenner. “The slow motion of a sphere through a viscous fluid towards a plane surface”. In: *Chem. Eng. Sci.* 16.3 (1961), pp. 242–251. DOI: 10.1016/0009-2509(61)80035-3.
- [23] A. Bricard, J.-B. Caussin, D. Das, et al. “Emergent vortices in populations of colloidal rollers”. In: *Nat. Commun.* 6 (2015), p. 7470. DOI: 10.1038/ncomms8470.
- [24] I. Bronshtein. *Handbook of Mathematics*. Springer, 2004.
- [25] R. Brown. “XXVII. A brief account of microscopical observations made in the months of June, July and August 1827, on the particles contained in the pollen of plants; and on the general existence of active molecules in organic and inorganic bodies”. In: *Philos. Mag.* 4.21 (1828), pp. 161–173.
- [26] I. Buttinoni, J. Bialké, F. Kümmel, et al. “Dynamical clustering and phase separation in suspensions of self-propelled colloidal particles”. In: *Phys. Rev. Lett.* 110.23 (2013). Article Number: 238301. DOI: 10.1103/PhysRevLett.110.238301.
- [27] I. Buttinoni, G. Volpe, F. Kümmel, G. Volpe, and C. Bechinger. “Active Brownian motion tunable by light”. In: *J. Phys. Condens. Matter* 24.28 (2012), p. 284129. DOI: 10.1088/0953-8984/24/28/284129.

- [28] S. Camazine, J. Deneubourg, N. Franks, et al. *Self-organization in Biological Systems*. Princeton Studies in Complexity. Princeton University Press, 2003.
- [29] L. Caprini and U. Marini Bettolo Marconi. “Active particles under confinement and effective force generation among surfaces”. In: *Soft Matter* 14 (44 2018), pp. 9044–9054. DOI: 10.1039/C8SM01840E.
- [30] M. E. Cates and J. Tailleur. “When are active Brownian particles and run-and-tumble particles equivalent? Consequences for motility-induced phase separation”. In: *EPL* 101.2 (2013), p. 20010. DOI: 10.1209/0295-5075/101/20010.
- [31] M. E. Cates and J. Tailleur. “Motility-Induced Phase Separation”. In: *Annu. Rev. Condens. Matter Phys.* 6.1 (2015), pp. 219–244. DOI: 10.1146/annurev-conmatphys-031214-014710.
- [32] P. Chaikin and T. Lubensky. *Principles of Condensed Matter Physics*. Cambridge University Press, 2000.
- [33] J. C. Clunie and J. K. Baird. “Interdiffusion Coefficient and Dynamic Viscosity for the Mixture 2,6-Lutidine + Water near the Lower Consolute Point”. In: *Phys. Chem. Liq.* 37.4 (1999), pp. 357–371. DOI: 10.1080/00319109908031441.
- [34] S. Colabrese, K. Gustavsson, A. Celani, and L. Biferale. “Flow Navigation by Smart Microswimmers via Reinforcement Learning”. In: *Phys. Rev. Lett.* 118 (15 2017), p. 158004. DOI: 10.1103/PhysRevLett.118.158004.
- [35] M. S. Davies Wykes, J. Palacci, T. Adachi, et al. “Dynamic self-assembly of microscale rotors and swimmers”. In: *Soft Matter* 12 (20 2016), pp. 4584–4589. DOI: 10.1039/C5SM03127C.
- [36] R. Dreyfus, J. Baudry, M. L. Roper, et al. “Microscopic artificial swimmers”. In: *Nature* 437.7060 (2005), pp. 862–865. DOI: 10.1038/nature04090.
- [37] D. Dusenbery. *Living at Micro Scale: The Unexpected Physics of Being Small*. Harvard University Press, 2009.
- [38] S. J. Ebbens and J. R. Howse. “In pursuit of propulsion at the nanoscale”. In: *Soft Matter* 6 (4 2010), pp. 726–738. DOI: 10.1039/B918598D.
- [39] S. J. Ebbens and J. R. Howse. “Direct Observation of the Direction of Motion for Spherical Catalytic Swimmers”. In: *Langmuir* 27.20 (2011), pp. 12293–12296. DOI: 10.1021/1a2033127.
- [40] S. Ebbens, R. A. L. Jones, A. J. Ryan, R. Golestanian, and J. R. Howse. “Self-assembled autonomous runners and tumblers”. In: *Phys. Rev. E* 82 (1 2010), p. 015304. DOI: 10.1103/PhysRevE.82.015304.
- [41] A. Einstein. “Über die von der molekularkinetischen Theorie der Wärme geforderte Bewegung von in ruhenden Flüssigkeiten suspendierten Teilchen”. In: *Ann. Phys.* 322 (1905), pp. 549–560. DOI: 10.1002/andp.19053220806.
- [42] M. Eisenbach and L. Giojalas. “Sperm guidance in mammals - An unpaved road to the egg”. In: *Nat. Rev. Mol. Cell Biol.* 7 (2006), pp. 276–85. DOI: 10.1038/nrm1893.

- [43] J. Elgeti, R. G. Winkler, and G. Gompper. “Physics of microswimmers—single particle motion and collective behavior: a review”. In: *Rep. Prog. Phys.* 78.5 (2015), p. 056601. DOI: 10.1088/0034-4885/78/5/056601.
- [44] J. Emlen John T. “Flocking Behavior in Birds”. In: *Auk* 69.2 (1952), pp. 160–170. DOI: 10.2307/4081266.
- [45] Y. Fily, A. Baskaran, and M. F. Hagan. “Dynamics of self-propelled particles under strong confinement”. In: *Soft Matter* 10 (30 2014), pp. 5609–5617. DOI: 10.1039/C4SM00975D.
- [46] Y. Fily and M. C. Marchetti. “Athermal Phase Separation of Self-Propelled Particles with No Alignment”. In: *Phys. Rev. Lett.* 108 (23 2012), p. 235702. DOI: 10.1103/PhysRevLett.108.235702.
- [47] A. Fischer, A. Chatterjee, and T. Speck. “Aggregation and sedimentation of active Brownian particles at constant affinity”. In: *J. Chem. Phys.* 150.6 (2019), p. 064910. DOI: 10.1063/1.5081115.
- [48] A. Fischer, F. Schmid, and T. Speck. “Quorum-sensing active particles with discontinuous motility”. In: *Phys. Rev. E* 101 (1 2020), p. 012601. DOI: 10.1103/PhysRevE.101.012601.
- [49] Flickr. <https://www.flickr.com/photos/47353092@N00/8498002874>. Accessed: 2020-01-15.
- [50] Flickr. <https://www.flickr.com/photos/robinhughes/404457553>. Accessed: 2020-01-15.
- [51] É. Fodor, C. Nardini, M. E. Cates, et al. “How Far from Equilibrium Is Active Matter?” In: *Phys. Rev. Lett.* 117 (3 2016), p. 038103. DOI: 10.1103/PhysRevLett.117.038103.
- [52] G. Frangipane, D. Dell’Arciprete, S. Petracchini, et al. “Dynamic density shaping of photokinetic *E. coli*”. In: *eLife* 7 (2018), e36608. DOI: 10.7554/eLife.36608.
- [53] X. Fu, L.-H. Tang, C. Liu, et al. “Stripe Formation in Bacterial Systems with Density-Suppressed Motility”. In: *Phys. Rev. Lett.* 108 (19 2012), p. 198102. DOI: 10.1103/PhysRevLett.108.198102.
- [54] C. Ganguly and D. Chaudhuri. “Stochastic thermodynamics of active Brownian particles”. In: *Phys. Rev. E* 88 (3 2013), p. 032102. DOI: 10.1103/PhysRevE.88.032102.
- [55] W. Gao, A. Pei, X. Feng, C. Hennessy, and J. Wang. “Organized Self-Assembly of Janus Micromotors with Hydrophobic Hemispheres”. In: *J. Am. Chem. Soc.* 135.3 (2013), pp. 998–1001. DOI: 10.1021/ja311455k.
- [56] C. Gardiner. *Handbook of stochastic methods for physics, chemistry, and the natural sciences*. Springer-Verlag, 1985.
- [57] A. Ghosh and P. Fischer. “Controlled Propulsion of Artificial Magnetic Nanostructured Propellers”. In: *Nano Lett.* 9.6 (2009), pp. 2243–2245. DOI: 10.1021/nl900186w.

- [58]R. Godawat, S. N. Jamadagni, J. R. Errington, and S. Garde. “Structure, Stability, and Rupture of Free and Supported Liquid Films and Assemblies in Molecular Simulations”. In: *Ind. Eng. Chem. Res.* 47.10 (2008), pp. 3582–3590. DOI: 10.1021/ie7017383.
- [59]R. Golestanian, T. B. Liverpool, and A. Ajdari. “Designing phoretic micro- and nano-swimmers”. In: *New J. Phys.* 9.5 (2007), pp. 126–126. DOI: 10.1088/1367-2630/9/5/126.
- [60]R. Golestanian, T. B. Liverpool, and A. Ajdari. “Propulsion of a Molecular Machine by Asymmetric Distribution of Reaction Products”. In: *Phys. Rev. Lett.* 94 (22 2005), p. 220801. DOI: 10.1103/PhysRevLett.94.220801.
- [61]J. Gomez-Solano, S. Samin, C. Lozano, et al. “Tuning the motility and directionality of self-propelled colloids”. In: *Sci. Rep.* 7 (2017), p. 14891. DOI: 10.1038/s41598-017-14126-0.
- [62]C. A. Grattoni, R. A. Dawe, C. Y. Seah, and J. D. Gray. “Lower critical solution coexistence curve and physical properties (density, viscosity, surface tension, and interfacial tension) of 2,6-lutidine + water”. In: *J. Chem. Eng. Data* 38.4 (1993), pp. 516–519. DOI: 10.1021/je00012a008.
- [63]D. Griffiths and S. Walborn. “Dirac deltas and discontinuous functions”. In: *Am. J. Phys.* 67 (1999), pp. 446–447. DOI: 10.1119/1.19283.
- [64]R. Groß, M. Bonani, F. Mondada, and M. Dorigo. “Autonomous Self-Assembly in Swarm-Bots”. In: *IEEE Trans. Robot.* 22 (2007), pp. 1115–1130. DOI: 10.1109/TR0.2006.882919.
- [65]D. Grossman, I. S. Aranson, and E. B. Jacob. “Emergence of agent swarm migration and vortex formation through inelastic collisions”. In: *New J. Phys.* 10.2 (2008), p. 023036. DOI: 10.1088/1367-2630/10/2/023036.
- [66]B. ten Hagen, S. van Teeffelen, and H. Löwen. “Brownian motion of a self-propelled particle”. In: *J. Phys. Condens. Matter* 23.19 (2011), p. 194119. DOI: 10.1088/0953-8984/23/19/194119.
- [67]J. Hansen and I. McDonald. *Theory of Simple Liquids*. Elsevier Science, 1990.
- [68]P. C. Hansen, V. Pereyra, and G. Scherer. *Least Squares Data Fitting with Applications*. Johns Hopkins University Press, 2012.
- [69]J. Happel and H. Brenner. *Low Reynolds number hydrodynamics: with special applications to particulate media*. Mechanics of Fluids and Transport Processes. Springer Netherlands, 1983.
- [70]W. M. Haynes. *CRC handbook of chemistry and physics*. 93rd edn. CRC Press, Boca Raton, 2013.
- [71]D. Higham. “An Algorithmic Introduction to Numerical Simulation of Stochastic Differential Equations”. In: *SIAM Review* 43.3 (2001), pp. 525–546. DOI: 10.1137/S0036144500378302.

- [72]J. R. Howse, R. A. L. Jones, A. J. Ryan, et al. “Self-Motile Colloidal Particles: From Directed Propulsion to Random Walk”. In: *Phys. Rev. Lett.* 99 (4 2007), p. 048102. DOI: 10.1103/PhysRevLett.99.048102.
- [73]M.-J. Huang, J. Schofield, and R. Kapral. “Chemotactic and hydrodynamic effects on collective dynamics of self-diffusiophoretic Janus motors”. In: *New J. Phys.* 19.12 (2017), p. 125003. DOI: 10.1088/1367-2630/aa958c.
- [74]Z. Izri, M. N. van der Linden, S. Michelin, and O. Dauchot. “Self-Propulsion of Pure Water Droplets by Spontaneous Marangoni-Stress-Driven Motion”. In: *Phys. Rev. Lett.* 113 (24 2014), p. 248302. DOI: 10.1103/PhysRevLett.113.248302.
- [75]J. Jackson. *Classical electrodynamics*. Wiley, 1975.
- [76]H.-R. Jiang, N. Yoshinaga, and M. Sano. “Active Motion of a Janus Particle by Self-Thermophoresis in a Defocused Laser Beam”. In: *Phys. Rev. Lett.* 105 (26 2010), p. 268302. DOI: 10.1103/PhysRevLett.105.268302.
- [77]D. Kaiser. “Bacterial Swarming: A Re-examination of Cell-Movement Patterns”. In: *Curr. Biol.* 17.14 (2007), R561–R570. DOI: 10.1016/j.cub.2007.04.050.
- [78]A. S. Khair. “Diffusiophoresis of colloidal particles in neutral solute gradients at finite Péclet number”. In: *J. Fluid Mech.* 731 (2013), pp. 64–94. DOI: 10.1017/jfm.2013.364.
- [79]J. G. Kirkwood. “The Statistical Mechanical Theory of Transport Processes I. General Theory”. In: *J. Chem. Phys.* 14.3 (1946), pp. 180–201. DOI: 10.1063/1.1724117.
- [80]G. Kokot and A. Snezhko. “Manipulation of emergent vortices in swarms of magnetic rollers”. In: *Nat. Commun.* 9 (2018), p. 2344. DOI: 10.1038/s41467-018-04765-w.
- [81]P. Krinninger and M. Schmidt. “Power functional theory for active Brownian particles: General formulation and power sum rules”. In: *J. Chem. Phys.* 150.7 (2019), p. 074112. DOI: 10.1063/1.5061764.
- [82]R. Kubo. “The fluctuation-dissipation theorem”. In: *Rep. Prog. Phys.* 29.1 (1966), pp. 255–284. DOI: 10.1088/0034-4885/29/1/306.
- [83]P. Langevin. “Sur la théorie du mouvement brownien”. In: *C. R. Acad. Sci. Paris* 146 (1908), pp. 530–533.
- [84]F. A. Lavergne, H. Wendehenne, T. Bäuerle, and C. Bechinger. “Group formation and cohesion of active particles with visual perception-dependent motility”. In: *Science* 364.6435 (2019), pp. 70–74. DOI: 10.1126/science.aau5347.
- [85]B. Liebchen and H. Löwen. “Synthetic Chemotaxis and Collective Behavior in Active Matter”. In: *Acc. Chem. Res.* 51.12 (2018), pp. 2982–2990. DOI: 10.1021/acs.accounts.8b00215.
- [86]B. Liebchen and H. Löwen. “Which interactions dominate in active colloids?” In: *J. Chem. Phys.* 150.6 (2019), p. 061102. DOI: 10.1063/1.5082284.

- [87]B. Liebchen, D. Marenduzzo, and M. E. Cates. “Phoretic Interactions Generically Induce Dynamic Clusters and Wave Patterns in Active Colloids”. In: *Phys. Rev. Lett.* 118 (26 2017), p. 268001. DOI: 10.1103/PhysRevLett.118.268001.
- [88]B. Liebchen, D. Marenduzzo, I. Pagonabarraga, and M. E. Cates. “Clustering and Pattern Formation in Chemorepulsive Active Colloids”. In: *Phys. Rev. Lett.* 115 (25 2015), p. 258301. DOI: 10.1103/PhysRevLett.115.258301.
- [89]C. Liu, X. Fu, L. Liu, et al. “Sequential Establishment of Stripe Patterns in an Expanding Cell Population”. In: *Science* 334.6053 (2011), pp. 238–241. DOI: 10.1126/science.1209042.
- [90]H. M. López, J. Gachelin, C. Douarche, H. Auradou, and E. Clément. “Turning Bacteria Suspensions into Superfluids”. In: *Phys. Rev. Lett.* 115 (2 2015), p. 028301. DOI: 10.1103/PhysRevLett.115.028301.
- [91]H. Löwen. “Active colloidal molecules”. In: *EPL* 121.5 (2018), p. 58001. DOI: 10.1209/0295-5075/121/58001.
- [92]C. Lozano, B. ten Hagen, H. Löwen, and C. Bechinger. “Phototaxis of synthetic microswimmers in optical landscapes”. In: *Nat. Commun.* 7 (2016). Article Number: 12828. DOI: 10.1038/ncomms12828.
- [93]C. Lupp and E. G. Ruby. “*Vibrio fischeri* Uses Two Quorum-Sensing Systems for the Regulation of Early and Late Colonization Factors”. In: *J. Bacteriol.* 187.11 (2005), pp. 3620–3629. DOI: 10.1128/JB.187.11.3620-3629.2005.
- [94]F. Ma, X. Yang, H. Zhao, and N. Wu. “Inducing Propulsion of Colloidal Dimers by Breaking the Symmetry in Electrohydrodynamic Flow”. In: *Phys. Rev. Lett.* 115 (20 2015), p. 208302. DOI: 10.1103/PhysRevLett.115.208302.
- [95]L. G. MacDowell, V. K. Shen, and J. R. Errington. “Nucleation and cavitation of spherical, cylindrical, and slablike droplets and bubbles in small systems”. In: *J. Chem. Phys.* 125.3 (2006), p. 034705. DOI: 10.1063/1.2218845.
- [96]D. Mandal, K. Klymko, and M. R. DeWeese. “Entropy Production and Fluctuation Theorems for Active Matter”. In: *Phys. Rev. Lett.* 119 (25 2017), p. 258001. DOI: 10.1103/PhysRevLett.119.258001.
- [97]M. C. Marchetti, J. F. Joanny, S. Ramaswamy, et al. “Hydrodynamics of soft active matter”. In: *Rev. Mod. Phys.* 85 (3 2013), pp. 1143–1189. DOI: 10.1103/RevModPhys.85.1143.
- [98]M. B. Miller and B. L. Bassler. “Quorum Sensing in Bacteria”. In: *Annu. Rev. Microbiol.* 55.1 (2001), pp. 165–199. DOI: 10.1146/annurev.micro.55.1.165.
- [99]H. Mori. “Transport, Collective Motion, and Brownian Motion*”). In: *Prog. Theor. Phys.* 33.3 (1965), pp. 423–455. DOI: 10.1143/PTP.33.423.
- [100]S. Muiños-Landin, K. Ghazi-Zahedi, and F. Cichos. *Reinforcement Learning of Artificial Microswimmers*. 2018. arXiv: 1803.06425 [cond-mat.soft].

- [101]V. Narayan, S. Ramaswamy, and N. Menon. “Long-Lived Giant Number Fluctuations in a Swarming Granular Nematic”. In: *Science* 317.5834 (2007), pp. 105–108. DOI: 10.1126/science.1140414.
- [102]D. Needleman and Z. Dogic. “Active matter at the interface between materials science and cell biology”. In: *Nat. Rev. Mater.* 2 (2017), p. 17048. DOI: 10.1038/natrevmats.2017.48.
- [103]S. Ni, E. Marini, I. Buttinoni, H. Wolf, and L. Isa. “Hybrid colloidal microswimmers through sequential capillary assembly”. In: *Soft Matter* 13 (23 2017), pp. 4252–4259. DOI: 10.1039/C7SM00443E.
- [104]R. Niu, D. Botin, J. Weber, A. Reinmüller, and T. Palberg. “Assembly and Speed in Ion-Exchange-Based Modular Phoretic Microswimmers”. In: *Langmuir* 33.14 (2017), pp. 3450–3457. DOI: 10.1021/acs.langmuir.7b00288.
- [105]R. Niu, A. Fischer, T. Palberg, and T. Speck. “Dynamics of Binary Active Clusters Driven by Ion-Exchange Particles”. In: *ACS Nano* 12.11 (2018), pp. 10932–10938. DOI: 10.1021/acsnano.8b04221.
- [106]R. Niu, S. Khodorov, J. Weber, A. Reinmüller, and T. Palberg. “Large scale microphotometry for high resolution pH-characterization during electro-osmotic pumping and modular micro-swimming”. In: *New J. Phys.* 19.11 (2017), p. 115014. DOI: 10.1088/1367-2630/aa9545.
- [107]R. Niu, P. Kreissl, A. T. Brown, et al. “Microfluidic pumping by micromolar salt concentrations”. In: *Soft Matter* 13 (7 2017), pp. 1505–1518. DOI: 10.1039/C6SM02240E.
- [108]R. Niu, T. Palberg, and T. Speck. “Self-Assembly of Colloidal Molecules due to Self-Generated Flow”. In: *Phys. Rev. Lett.* 119 (2 2017), p. 028001. DOI: 10.1103/PhysRevLett.119.028001.
- [109]J. Palacci, C. Cottin-Bizonne, C. Ybert, and L. Bocquet. “Sedimentation and Effective Temperature of Active Colloidal Suspensions”. In: *Phys. Rev. Lett.* 105 (8 2010), p. 088304. DOI: 10.1103/PhysRevLett.105.088304.
- [110]J. Palacci, S. Sacanna, A. P. Steinberg, D. J. Pine, and P. M. Chaikin. “Living Crystals of Light-Activated Colloidal Surfers”. In: *Science* 339.6122 (2013), pp. 936–940. DOI: 10.1126/science.1230020.
- [111]E. Palik. *Handbook of Optical Constants of Solids*. Academic Press handbook series. Academic Press, 1985.
- [112]M. R. Parsek and E. Greenberg. “Sociomicrobiology: the connections between quorum sensing and biofilms”. In: *Trends Microbiol.* 13.1 (2005), pp. 27–33. DOI: 10.1016/j.tim.2004.11.007.
- [113]R. Pathria and P. Beale. *Statistical Mechanics*. Elsevier Science, 2011.
- [114]W. F. Paxton, K. C. Kistler, C. C. Olmeda, et al. “Catalytic Nanomotors: Autonomous Movement of Striped Nanorods”. In: *J. Am. Chem. Soc.* 126.41 (2004), pp. 13424–13431. DOI: 10.1021/ja047697z.

- [115]P. Pietzonka and U. Seifert. “Entropy production of active particles and for particles in active baths”. In: *J. Phys. A* 51.1 (2017), 01LT01. DOI: 10.1088/1751-8121/aa91b9.
- [116]O. Pohl and H. Stark. “Dynamic Clustering and Chemotactic Collapse of Self-Phoretic Active Particles”. In: *Phys. Rev. Lett.* 112 (23 2014), p. 238303. DOI: 10.1103/PhysRevLett.112.238303.
- [117]E. M. Purcell. “Life at low Reynolds number”. In: *Am. J. Phys.* 45.1 (1977), pp. 3–11. DOI: 10.1119/1.10903.
- [118]S. Ramaswamy. “The Mechanics and Statistics of Active Matter”. In: *Annu. Rev. Condens. Matter Phys.* 1.1 (2010), pp. 323–345. DOI: 10.1146/annurev-conmatphys-070909-104101.
- [119]G. S. Redner, M. F. Hagan, and A. Baskaran. “Structure and Dynamics of a Phase-Separating Active Colloidal Fluid”. In: *Phys. Rev. Lett.* 110 (5 2013), p. 055701. DOI: 10.1103/PhysRevLett.110.055701.
- [120]M. Rein, N. Heinß, F. Schmid, and T. Speck. “Collective Behavior of Quorum-Sensing Run-and-Tumble Particles under Confinement”. In: *Phys. Rev. Lett.* 116 (2016), p. 058102. DOI: 10.1103/PhysRevLett.116.058102.
- [121]C. W. Reynolds. “Flocks, Herds and Schools: A Distributed Behavioral Model”. In: *Proceedings of the 14th Annual Conference on Computer Graphics and Interactive Techniques*. 1987, pp. 25–34. DOI: 10.1145/37401.37406.
- [122]P. Romanczuk, M. Bär, W. Ebeling, B. Lindner, and L. Schimansky-Geier. “Active Brownian particles”. In: *Eur. Phys. J. Special Topics* 202.1 (2012), pp. 1–162. DOI: 10.1140/epjst/e2012-01529-y.
- [123]P. Rørth. “Collective Cell Migration”. In: *Annu. Rev. Cell Dev. Biol.* 25.1 (2009), pp. 407–429. DOI: 10.1146/annurev.cellbio.042308.113231.
- [124]M. Rubenstein, A. Cornejo, and R. Nagpal. “Programmable self-assembly in a thousand-robot swarm”. In: *Science* 345.6198 (2014), pp. 795–799. DOI: 10.1126/science.1254295.
- [125]S. Saha, R. Golestanian, and S. Ramaswamy. “Clusters, asters, and collective oscillations in chemotactic colloids”. In: *Phys. Rev. E* 89 (6 2014), p. 062316. DOI: 10.1103/PhysRevE.89.062316.
- [126]F. Schmidt, B. Liebchen, H. Löwen, and G. Volpe. “Light-controlled assembly of active colloidal molecules”. In: *J. Chem. Phys.* 150.9 (2019), p. 094905. DOI: 10.1063/1.5079861.
- [127]M. J. Schnitzer. “Theory of continuum random walks and application to chemotaxis”. In: *Phys. Rev. E* 48 (4 1993), pp. 2553–2568. DOI: 10.1103/PhysRevE.48.2553.
- [128]M. Schrader, P. Virnau, and K. Binder. “Simulation of vapor-liquid coexistence in finite volumes: A method to compute the surface free energy of droplets”. In: *Phys. Rev. E* 79 (6 2009), p. 061104. DOI: 10.1103/PhysRevE.79.061104.
- [129]F. Schwabl. *Statistische Mechanik*. Springer-Lehrbuch. Springer Berlin Heidelberg, 2013.

- [130]F. Schweitzer and J. Farmer. *Brownian Agents and Active Particles: Collective Dynamics in the Natural and Social Sciences*. Physics and astronomy online library. Springer Berlin Heidelberg, 2003.
- [131]U. Seifert. “Stochastic thermodynamics, fluctuation theorems and molecular machines”. In: *Rep. Prog. Phys.* 75.12 (2012), p. 126001. DOI: 10.1088/0034-4885/75/12/126001.
- [132]U. Seifert. “Stochastic thermodynamics: From principles to the cost of precision”. In: *Physica A* 504 (2018), pp. 176–191. DOI: 10.1016/j.physa.2017.10.024.
- [133]E. Shaw. “Schooling Fishes”. In: *Am. Sci.* 66.2 (1978), pp. 166–175.
- [134]J. T. Siebert, F. Dittrich, F. Schmid, et al. “Critical behavior of active Brownian particles”. In: *Phys. Rev. E* 98 (3 2018), p. 030601. DOI: 10.1103/PhysRevE.98.030601.
- [135]J. T. Siebert, J. Letz, T. Speck, and P. Virnau. “Phase behavior of active Brownian disks, spheres, and dimers”. In: *Soft Matter* 13 (5 2017), pp. 1020–1026. DOI: 10.1039/C6SM02622B.
- [136]D. P. Singh, U. Choudhury, P. Fischer, and A. G. Mark. “Non-Equilibrium Assembly of Light-Activated Colloidal Mixtures”. In: *Adv. Mater.* 29.32 (2017), p. 1701328. DOI: 10.1002/adma.201701328.
- [137]F. Smallenburg and H. Löwen. “Swim pressure on walls with curves and corners”. In: *Phys. Rev. E* 92 (3 2015), p. 032304. DOI: 10.1103/PhysRevE.92.032304.
- [138]M. v. Smoluchowski. “Über Brownsche Molekularbewegung unter Einwirkung äußerer Kräfte und deren Zusammenhang mit der verallgemeinerten Diffusionsgleichung”. In: *Ann. Physik* 353.1103-1102 (24 1915).
- [139]A. Sokolov and I. S. Aranson. “Reduction of Viscosity in Suspension of Swimming Bacteria”. In: *Phys. Rev. Lett.* 103 (14 2009), p. 148101. DOI: 10.1103/PhysRevLett.103.148101.
- [140]A. P. Solon, J. Stenhammar, M. E. Cates, Y. Kafri, and J. Tailleur. “Generalized thermodynamics of phase equilibria in scalar active matter”. In: *Phys. Rev. E* 97 (2 2018), p. 020602. DOI: 10.1103/PhysRevE.97.020602.
- [141]A. P. Solon, J. Stenhammar, R. Wittkowski, et al. “Pressure and Phase Equilibria in Interacting Active Brownian Spheres”. In: *Phys. Rev. Lett.* 114 (19 2015), p. 198301. DOI: 10.1103/PhysRevLett.114.198301.
- [142]R. Soto and R. Golestanian. “Self-Assembly of Catalytically Active Colloidal Molecules: Tailoring Activity Through Surface Chemistry”. In: *Phys. Rev. Lett.* 112 (6 2014), p. 068301. DOI: 10.1103/PhysRevLett.112.068301.
- [143]T. Speck. “Stochastic thermodynamics for active matter”. In: *EPL* 114.3 (2016), p. 30006. DOI: 10.1209/0295-5075/114/30006.
- [144]T. Speck. “Active Brownian particles driven by constant affinity”. In: *EPL* 123.2 (2018), p. 20007. DOI: 10.1209/0295-5075/123/20007.

- [145]T. Speck. “Thermodynamic approach to the self-diffusiophoresis of colloidal Janus particles”. In: *Phys. Rev. E* 99 (6 2019), p. 060602. DOI: 10.1103/PhysRevE.99.060602.
- [146]T. Speck, A. M. Menzel, J. Bialké, and H. Löwen. “Dynamical mean-field theory and weakly non-linear analysis for the phase separation of active Brownian particles”. In: *J. Chem. Phys.* 142.22 (2015), p. 224109. DOI: 10.1063/1.4922324.
- [147]V. Sperandio, A. G. Torres, and J. B. Kaper. “Quorum sensing Escherichia coli regulators B and C (QseBC): a novel two-component regulatory system involved in the regulation of flagella and motility by quorum sensing in E. coli”. In: *Mol. Microbiol.* 43.3 (2002), pp. 809–821. DOI: 10.1046/j.1365-2958.2002.02803.x.
- [148]H. Stark. “Artificial Chemotaxis of Self-Phoretic Active Colloids: Collective Behavior”. In: *Acc. Chem. Res.* 51.11 (2018), pp. 2681–2688. DOI: 10.1021/acs.accounts.8b00259.
- [149]J. Stenhammar, D. Marenduzzo, R. J. Allen, and M. E. Cates. “Phase behaviour of active Brownian particles: the role of dimensionality”. In: *Soft Matter* 10 (10 2014), pp. 1489–1499. DOI: 10.1039/C3SM52813H.
- [150]J. Stenhammar, A. Tiribocchi, R. J. Allen, D. Marenduzzo, and M. E. Cates. “Continuum Theory of Phase Separation Kinetics for Active Brownian Particles”. In: *Phys. Rev. Lett.* 111 (14 2013), p. 145702. DOI: 10.1103/PhysRevLett.111.145702.
- [151]J. Stenhammar, R. Wittkowski, D. Marenduzzo, and M. E. Cates. “Light-induced self-assembly of active rectification devices”. In: *Sci. Adv.* 2.4 (2016). DOI: 10.1126/sciadv.1501850.
- [152]G. Stokes. “On the Effect of the Internal Friction of Fluids on the Motion of Pendulums”. In: *Transactions of the Cambridge Philosophical Society* 9 (Part II 1851), pp. 8–106.
- [153]R. S. Sutton and A. G. Barto. *Reinforcement Learning: An Introduction*. MIT Press, 1998.
- [154]M. Tabor. *Chaos and integrability in nonlinear dynamics: an introduction*. Wiley-Interscience publication. Wiley, 1989.
- [155]S. P. Thampi, R. Golestanian, and J. M. Yeomans. “Vorticity, defects and correlations in active turbulence”. In: *Philos. Trans. Royal Soc. A* 372.2029 (2014), p. 20130366. DOI: 10.1098/rsta.2013.0366.
- [156]I. Theurkauff, C. Cottin-Bizonne, J. Palacci, C. Ybert, and L. Bocquet. “Dynamic Clustering in Active Colloidal Suspensions with Chemical Signaling”. In: *Phys. Rev. Lett.* 108 (26 2012), p. 268303. DOI: 10.1103/PhysRevLett.108.268303.
- [157]L. F. Tóth. “Über die dichteste Kugellagerung”. In: *Math. Z.* 48 (1940), pp. 676–684.
- [158]G. E. Uhlenbeck and L. S. Ornstein. “On the Theory of the Brownian Motion”. In: *Phys. Rev.* 36 (5 1930), pp. 823–841. DOI: 10.1103/PhysRev.36.823.
- [159]T. Vicsek, A. Czirók, E. Ben-Jacob, I. Cohen, and O. Shochet. “Novel Type of Phase Transition in a System of Self-Driven Particles”. In: *Phys. Rev. Lett.* 75 (6 1995), pp. 1226–1229. DOI: 10.1103/PhysRevLett.75.1226.

- [160]G. Vizsnyiczai, G. Frangipane, C. Maggi, et al. “Light controlled 3D micromotors powered by bacteria”. In: *Nat. Commun.* 8 (2017). DOI: 10.1038/ncomms15974.
- [161]G. Volpe, I. Buttinoni, D. Vogt, H.-J. Kümmerer, and C. Bechinger. “Microswimmers in patterned environments”. In: *Soft Matter* 7 (19 2011), pp. 8810–8815. DOI: 10.1039/C1SM05960B.
- [162]H. Vutukuri, B. Bet, R. Roij, M. Dijkstra, and W. Huck. “Rational design and dynamics of self-propelled colloidal bead chains: From rotators to flagella”. In: *Sci. Rep.* 7 (2017). DOI: 10.1038/s41598-017-16731-5.
- [163]G. Wadhams and J. Armitage. “Making sense of it all: bacterial chemotaxis”. In: *Nat. Rev. Mol. Cell Bio.* 5 (2005), pp. 1024–37. DOI: 10.1038/nrm1524.
- [164]W. Wang, L. A. Castro, M. Hoyos, and T. E. Mallouk. “Autonomous Motion of Metallic Microrods Propelled by Ultrasound”. In: *ACS Nano* 6.7 (2012), pp. 6122–6132. DOI: 10.1021/nn301312z.
- [165]W. Wang, W. Duan, A. Sen, and T. E. Mallouk. “Catalytically powered dynamic assembly of rod-shaped nanomotors and passive tracer particles”. In: *Proc. Natl. Acad. Sci. U.S.A.* 110.44 (2013), pp. 17744–17749. DOI: 10.1073/pnas.1311543110.
- [166]J. D. Weeks, D. Chandler, and H. C. Andersen. “Role of Repulsive Forces in Determining the Equilibrium Structure of Simple Liquids”. In: *J. Chem. Phys.* 54 (1971), p. 5237. DOI: 10.1063/1.1674820.
- [167]H. H. Wensink, J. Dunkel, S. Heidenreich, et al. “Meso-scale turbulence in living fluids”. In: *Proc. Natl. Acad. Sci. U.S.A.* 109.36 (2012), pp. 14308–14313. DOI: 10.1073/pnas.1202032109.
- [168]Wikimedia Commons. <https://commons.wikimedia.org/wiki/File:Sperm-20051108.jpg>. Accessed: 2020-01-15.
- [169]Wikimedia Commons. https://commons.wikimedia.org/wiki/File:Rosy_starling_swarm2.jpg. Accessed: 2020-01-15.
- [170]Wikipedia. https://en.wikipedia.org/wiki/File:P_vortex_colony1.png. Accessed: 2020-01-15.
- [171]B. Williams, S. Anand, J. Rajagopalan, and M. Saif. “A self-propelled biohybrid swimmer at low Reynolds number”. In: *Nat. Commun.* 5 (2014), p. 3081. DOI: 10.1038/ncomms4081.
- [172]H. Wioland, F. G. Woodhouse, J. Dunkel, J. O. Kessler, and R. E. Goldstein. “Confinement Stabilizes a Bacterial Suspension into a Spiral Vortex”. In: *Phys. Rev. Lett.* 110 (26 2013), p. 268102. DOI: 10.1103/PhysRevLett.110.268102.
- [173]R. Wittkowski, A. Tiribocchi, J. Stenhammar, et al. “Scalar φ^4 field theory for active-particle phase separation”. In: *Nat. Commun.* 5 (2014), p. 4351. DOI: 10.1038/ncomms5351.
- [174]A. Würger. “Self-Diffusiophoresis of Janus Particles in Near-Critical Mixtures”. In: *Phys. Rev. Lett.* 115 (18 2015), p. 188304. DOI: 10.1103/PhysRevLett.115.188304.

- [175]A. Wysocki, R. G. Winkler, and G. Gompper. “Cooperative motion of active Brownian spheres in three-dimensional dense suspensions”. In: *EPL* 105.4 (2014), p. 48004. DOI: 10.1209/0295-5075/105/48004.
- [176]J. Yvon. *La théorie statistique des fluides et l'équation d'état*. Hermann, Paris, 1935.
- [177]H. P. Zhang, A. Be'er, E.-L. Florin, and H. L. Swinney. “Collective motion and density fluctuations in bacterial colonies”. In: *Proc. Natl. Acad. Sci. U.S.A.* 107.31 (2010), pp. 13626–13630. DOI: 10.1073/pnas.1001651107.
- [178]J. Zhu, M. B. Miller, R. E. Vance, et al. “Quorum-sensing regulators control virulence gene expression in *Vibrio cholerae*”. In: *Proc. Natl. Acad. Sci. U.S.A.* 99.5 (2002), pp. 3129–3134. DOI: 10.1073/pnas.052694299.
- [179]A. Zöttl and H. Stark. “Hydrodynamics Determines Collective Motion and Phase Behavior of Active Colloids in Quasi-Two-Dimensional Confinement”. In: *Phys. Rev. Lett.* 112 (11 2014), p. 118101. DOI: 10.1103/PhysRevLett.112.118101.
- [180]A. Zöttl and H. Stark. “Emergent behavior in active colloids”. In: *J. Phys. Condens. Matter* 28.25 (2016), p. 253001. DOI: 10.1088/0953-8984/28/25/253001.
- [181]R. Zwanzig. *Nonequilibrium Statistical Mechanics*. Oxford University Press, 2001.
- [182]R. Zwanzig. “Memory Effects in Irreversible Thermodynamics”. In: *Phys. Rev.* 124 (4 1961), pp. 983–992. DOI: 10.1103/PhysRev.124.983.
- [183]D. Zwillinger. *Handbook of Differential Equations*. Elsevier Science, 1998.

Colophon

This thesis was typeset with $\text{\LaTeX}2_{\epsilon}$. It uses the *Clean Thesis* style developed by Ricardo Langner. The design of the *Clean Thesis* style is inspired by user guide documents from Apple Inc.

Download the *Clean Thesis* style at <http://cleanthesis.der-ric.de/>.

